Synthesis and Properties of some Doped Lithium Transition-Metal Phosphates

A thesis submitted in partial fulfilment
of the requirements for the degree of

Doctor of Philosophy

in Materials and Process Engineering
by

Garrett Phillip Butt

The
University
of Waikato
Te Whare Wānanga
o Waikato

20 November 2000

Acknowledgements

I would like to thank the following people:

My Mum, Wally and Vicki, Theresa and Angela. Also my nephews and nieces Sean, Keith, Connor, Jason, Jordan, Jesse and Alex for being so entertaining.

Kathryn Allen and her family for their support, encouragement and understanding in the last five years.

Dr Nigel Sammes and Assoc. Prof. Janis Swan, for advice and support throughout my years at Waikato University. Also Professor Osamu Yamamoto and Professor Yasuo Takeda for all the help during my time researching in Japan.

The Pacific Lithium crew: Paul, Phil, Rudi, Hans, Jadranka, Jens, Dave, Tania, Alex, Mike, Nobby, Judith, Sonya, Shu Yi, Jan and Grant for all the help and advice over the last year. Special thanks go to Dr Brett Ammundsen, for the invaluable time and effort he provided as a supervisor.

Cheers to the Technology People: Mike P, Mike B, Mattress, Geoff T, Bob, Wei, Yuanji, and Charlie.

Cheers to the lads at Yamamoto Lab, Mie University, Japan. Thanks go to Arachi, Katsuyuki, Atsuko, Keiji, Mori, Fujioshi, Mariko, Ai, Sakai and Miki.

Special thanks to Te Kauhanganui and the Tainui Maaori Trust Board for the Tumate Mahuta Memorial Waikato Raupatu Postgraduate Scholarship.

Abstract

Four structurally related materials; $LiNiPO_4$, $LiCoPO_4$, $Li_3Fe_2(PO_4)_3$ and $Li_3V_2(PO_4)_3$, were synthesised, characterised and evaluated as potential cathode materials for lithium secondary batteries.

The materials were synthesized using mainly solid-state techniques. Structural characterisation was performed using powder XRD with Rietveld refinement and Raman spectroscopy. Results showed that the pure forms of $LiNiPO_4$, $LiCoPO_4$ and $Li_3Fe_2(PO_4)_3$ could be synthesised in air at various temperatures. $Li_3V_2(PO_4)_3$ required a reducing atmosphere of $2\%H_2/98\%N_2$ to achieve phase purity. Attempts were made to substitute all four materials with aliovalent dopants. $Li_3Fe_2(PO_4)_3$ and $Li_3V_2(PO_4)_3$ underwent a phase change depending on dopant content to a higher ionic conducting phase.

AC impedance spectroscopy was used to determine conductivity of the materials. In general the phosphates are poor conductors. There was a significant increase in conductivity when substituting the transition metal Ti^{4+} for M^{3+} in $Li_3Fe_2(PO_4)_3$ and $Li_3V_2(PO_4)_3$, and $V^{3+}$for Co^{2+} in $LiCoPO_4$.

The four materials and their highest conducting doped analogues were evaluated as cathodes in coin type lithium cells to determine their viability in Li secondary batteries. $LiCoPO_4$ showed a first discharge capacity of 130 mAh/g at 4.6V, but could be cycled over only a limited number of charge-discharge cycles owing to electrolyte instability at the high oxidation potentials (>5V) required for full charge. $LiNiPO_4$ could not be charged at all to accessible voltages. Ti doped $Li_3Fe_2(PO_4)_3$ had a relatively low discharge capacity of 60 mAh/g. $Li_3V_2(PO_4)_3$ and Ti doped $Li_3V_2(PO_4)_3$ showed a discharge capacity of 130 and 110 mAh/g respectively, although the Ti doped $Li_3V_2(PO_4)_3$ showed better cycling characteristics. Therefore, although aliovalent doping could increase the total conductivity of the phosphate materials, the accessible capacities of these materials remained limited.

Contents

List of Figures:

List of Tables:

1 Introduction

1 Introduction

1.1 Advanced Power Sources

Environmental issues are the major factor currently influencing the direction of the development of battery and power source technology. Environmental concerns, such as pollution and dwindling fossil fuel reserves, have caused the push behind the massive research efforts into the production of environmentally clean electricity and power packs for electric vehicle propulsion, both of which are later discussed in detail. More recently, the considerable increase in the cost of crude oil is stimulating interest in renewable technologies. The difference between capital investment costs for non-renewable and renewable resources is getting closer to reaching a crossover point, maybe even within the next decade.

Over the past two decades there has also been a revolution in portable consumer electronics, coupled with changing lifestyles, that is placing greater demand on battery technology. The various applications for battery technology have led to the development of many different types of materials, with the majority of investigations being in the development of electrolytes and other components for power storage and conversion systems.[1,2,3] Consumer demand has kept pace with the miniaturisation of many electrically driven devices and continually requires batteries to become smaller, lighter and to improve performance.

This chapter discusses the main incentives behind the research into advanced materials for power sources. These include various types of batteries especially lithium, and fuel cells. The chapter details those powers sources which have been commercialised and some that are under development for commercialisation. It also discusses the materials examined in this thesis and their applications.

1.2 Environmental Issues

Over the last 200 years the planets' CO_2 levels have increased by 25%. This corresponds to a temperature rise of 1 °C in this century. Normally, as an ice age approaches or recedes, temperatures change at a rate of 0.1 °C per century. This rate has been multiplied ten times by man and the natural environment is having trouble coping.

There has already been a rise in sea levels of 0.1m this century. Some predictions for the next century include sea level rises by more than 1m due to melting glaciers and ice-caps and global warming increasing temperatures by 3 to 4.5%.

If all the fossil fuels on earth were consumed, evidence for the worst-case scenario suggests that temperatures could increase by 5 – 10 °C. This could result in the Greenland and West Antarctic ice sheets melting, which hold the equivalent of 5 – 10m of sea level. Even though this could take several centuries to occur, the results could be very profound.

The nations of the world officially recognised the problem of greenhouse gases at the Rio de Janeiro Earth Summit for Climate Change. Together with the international community, New Zealand has to seek ways to reduce its net release of CO_2 into the atmosphere down to 1990 levels by the year 2000.

However, this is very difficult to do. Currently, New Zealand is looking at burning more natural gas to satisfy our growing electricity demands, making it more difficult all the time. New Zealand is looking to plant more trees as a possible solution to this problem. However, in 25 years time when the trees are ready for cropping that carbon will just be released again.

One solution proposed is to impose carbon taxes on industry to try to encourage efficiency. These taxes could also be levied on sulphur oxides, nitrogen oxides, particulate matter and reactive organic gases. If the taxes were severe enough, this would encourage industry to deal with their wastes in a more environmentally friendly manner. For example, the smokestacks of thermal stations can be adapted so that sulphur from coal is not emitted.

1.3 Electric Vehicle Development

In 1990 the state of California passed a law requiring that 2% of all new vehicles in 1997 were to have zero emissions, and that this percentage was to increase by 2% per annum until 2001. This has since been changed to 10% of all new vehicles by 2003. Nine other states and the District of Columbia soon passed the same law, in an effort to try to reduce the increasing pollution problem. Other avenues have been investigated to solve the Californian pollution problem, with critics believing that more could be done by encouraging mass transit, retiring unclean cars, promoting vehicles that are cleaner running (natural gas for example) and other more environmentally friendly measures. However, the Californian regulators have concluded that these measures would not be sufficient and continue to require zero emissions.

The majority of investigations have revolved around electric vehicle (EV) technology, because the EV is the only practical and commercially viable zero-emission vehicle that both complies with the Californian Clean Air Act and will be available in the foreseeable future.

Many industries already use EVs in areas that require pollution-free environments, and where space is limited and confined. The advantages of EVs include:

- less noise and fumes, no idling
- easy starting
- safe operation
- low maintenance
- low running costs
- better manoeuvrability
- longer operating life

These advantages would also benefit other potential users of EVs. However, the weight, size, performance and cost of batteries along with the cost of an EV, have hindered the popularity of owning an EV for personal transportation when compared to conventional transportation. Besides the problems presented above, there are a number of other critical issues to be addressed. These are discussed later.

EVs have been developed over the last decade or so that are coming closer to competing with the performance of the internal combustion engine. It is likely that the rich and fashion conscious will drive these at first because they are very expensive. However, as production methods improve in EV technology, these costs will decrease.

1.3.1 Batteries and the Automotive Market

In over 100 years of rechargeable battery usage, the lead acid battery ($Pb-PbO_2$ - chemistry) and the Ni-Cd battery (Cd-NiOOH - chemistry) have dominated more than 90% of the market.[4] Since the Californian Clean Air Act was passed, battery development has flourished as battery scientists and engineers take on the challenge to develop an improved battery that will support the commercialisation of the EV. It is expected that the global automotive battery market will continue to grow in size, assisting the EV's entry into the $500 billion global auto industry.[5] The progress being made in automotive battery technology is having spin-offs for other battery and electronic technologies worldwide.

1.3.2 Alternative Power Sources

The interest in electrically propelled vehicles is reflected by the growing investment put into power storage units. Some of these devices that are presently under intense research and development include:

- Fuel cells
- Solar cells *
- Ultra-Capacitors
- Flywheels
- Hybrids *
- Batteries

(* generally depend on storage batteries)

1.3.2.1 Fuel Cells

A fuel cell is an electrochemical device that converts the chemical energy of a fuel directly into electrical energy (Figure 1.1). The most important feature of a fuel cell is its high-energy conversion efficiency. It is not limited by the Carnot cycle because it converts the chemical energy of the fuel directly to electrical energy, without the intermediate step of thermal energy. Fuel cells have several advantages over conventional methods of power generation, such as lower production of pollutants, modular construction, minimal siting restrictions, higher conversion efficiency and the potential for cogeneration.

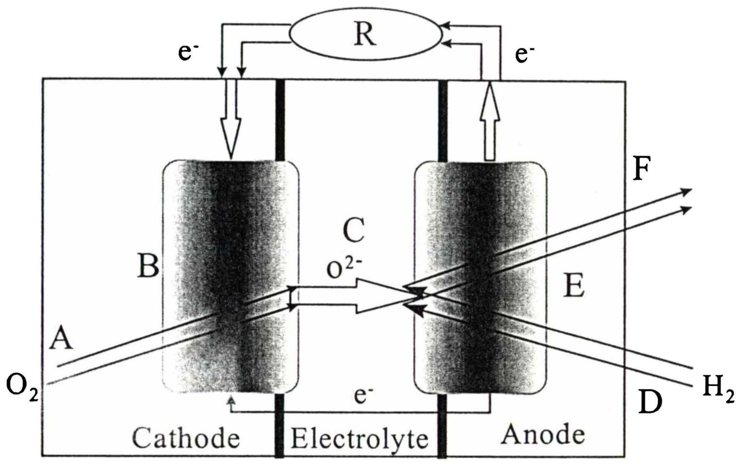

A Diffusion of O_2 though porous cathode
B Charge transfer to O^{2-} at cathode
C Diffusion of O^{2-} through electrolyte
D Diffusion of H_2 through porous anode
E Oxidation reaction of H_2 at anode
F Diffusion of H_2O through anode

Figure 1.1 Schematic of Fuel Cell

The principles of fuel cell operation were first reported by Sir William Grove in 1839.[6] His fuel cell used dilute sulphuric acid as the electrolyte and operated at room temperature. Ceramic fuel cells came much later and began with Nernst's discovery of solid oxide electrolytes in 1899,[7] and the operation of the first solid oxide fuel cell at 1000 °C by Bauer and Preis in 1937.[8] Since then, ceramic fuel cell technology has advanced considerably. Multi-kilowatt fuel cells based on the zirconia electrolyte, have been operated for thousands of hours and have shown excellent performance.[10]

The application of fuel cells to EVs to date, has generally been to public transportation, particularly buses.[9,10] These are still at the prototype stage and tend to be expensive to produce and run. Some low temperature polymer membrane-based fuel cell systems have been applied to cars, but are also in their infancy. Fuel cells emit trace air pollutants and therefore may not meet the zero emission standards. However, the fuel cell is far cleaner than the Internal Combustion Engine (ICE).

1.3.2.2 Solar Cells

The photovoltaic effect was first described by Becquerel in 1839 and studied in more detail by Hertz in 1870. When photons strike a solar cell, some are absorbed, transferring the energy to an electron in an atom of the cell. With its newfound energy, the electron is able to escape from its normal position associated with that atom to become part of the current in an electrical circuit. By leaving this position, the electron causes a hole to form. To induce an electric field within a solar cell, two separate semiconductors, a p- and n- type are sandwiched together. The excess electrons in the n-type material flow to the p-type, and the holes thereby vacated during this process flow to the n-type. This provides the voltage needed to drive the current through an external load.

Solar cells do not deliver enough energy to power directly, a ‘practical’ EV. They are also restricted to use during sunlight hours only, which tends to rule out solar technology as a viable power source. However, the solar cell does offer potential as a method of trickle charging battery packs. Events like the World Solar Challenge, a 3000 km solar car race from Darwin to Adelaide (Australia) held every three years, are fast becoming recognised as a proving ground for new EV technologies.[11]

1.3.2.3 Ultra-Capacitors

Electrochemical capacitors; or ultra-capacitors, are being developed for hybrid vehicle systems as a power-assist device for the fast response engine’s energy storage requirements.[12,13] Ultra-capacitors are higher specific energy and power versions of electrolytic capacitors — devices that store energy as an electrostatic charge. They are electrochemical systems that store energy in a polarised liquid layer at the interface between an ionically conducting electrolyte and a conducting electrode. Energy storage capacity increases by increasing the surface area of the interface. Ultra-capacitors are being developed as primary energy devices for power assist during acceleration and hill climbing, as well as recovery of braking energy. They are also potentially useful as secondary energy storage devices in hybrid electric vehicles (HEVs), providing load-levelling power to chemical batteries. Additional electronics are required to maintain a constant voltage, because the voltage drops as energy is discharged. Ultra-capacitors have shown some promise toward being able to accept high regenerative pulses while exhibiting high cycle life. However, before ultra-capacitors can achieve widespread use, they need to overcome several technical barriers such as comparatively low specific energy, high cost, low reliability in a multiple string configuration and efficient packaging of multi-cell high-voltage modules. Their low volumetric density and relatively high cost has resulted in the US Department of Energy (DOE) de-emphasising this research in favour of other power sources since the beginning of 1998. This is due mainly to the US DOE assigning a set timeframe to the technical targets which will be discussed later.

1.3.2.4 Flywheels

Chrysler, Ford and General Motors have completed preliminary work on the development of Flywheel system technologies for automotive applications.[12,13] Flywheels store kinetic energy within a rapidly spinning wheel-like rotor or disk. Ultimately, flywheels could store comparable amounts of energy to batteries. They contain no acids or other potentially hazardous materials. Flywheels are not affected by temperature extremes in contrast to most batteries. Although flywheels are being used in some bus applications today, more work needs to be done to make flywheels safe and effective for HEV automotive applications. Current flywheels are still very complex, heavy, and large for personal vehicles. For them to have success in EVs, they would need to provide higher energy densities than what is now available. In addition, there are some concerns regarding the safety of a device that spins mass at high speeds.

Flywheels have been used in various forms for centuries, and have a long history of use in automotive applications. Early cars used a hand crank connected to a flywheel to start the engine, and all of today's internal combustion engines use flywheels to store energy and deliver a smooth flow of power from the abrupt power pulses of the engine. Modern flywheels employ a high-strength composite rotor, which rotates in a vacuum chamber to minimize aerodynamic losses. A motor/generator is mounted on the rotor's shaft both to spin the rotor up to speed (charging) and to convert the rotor's kinetic energy to electrical energy (discharging). A high-strength containment structure houses the rotating elements and low-energy-loss bearings stabilize the shaft. Interface electronics are needed to convert the alternating current to direct current, condition the power, and monitor and control the flywheel.

1.3.2.5 Hybrids

A hybrid electric vehicle is an optimised mix of two or more components. The vehicle drive-train consists of:

- Electric traction motors/controllers
- Electric energy storage systems, such as batteries, ultra-capacitors, and flywheels
- Hybrid power units such as spark ignition engines, compression ignition direct injection (diesel) engines, gas turbines, and fuel cells
- Fuel systems for hybrid power units
- Transmissions

There are other key developments being made to help reduce emissions and improve the efficiency of HEVs, including:

- Emission control systems
- Energy management and systems control
- Thermal management of components
- Light weight and aerodynamic body/chassis
- Low rolling resistance (including tyres)
- Reduction of accessory loads in the vehicle

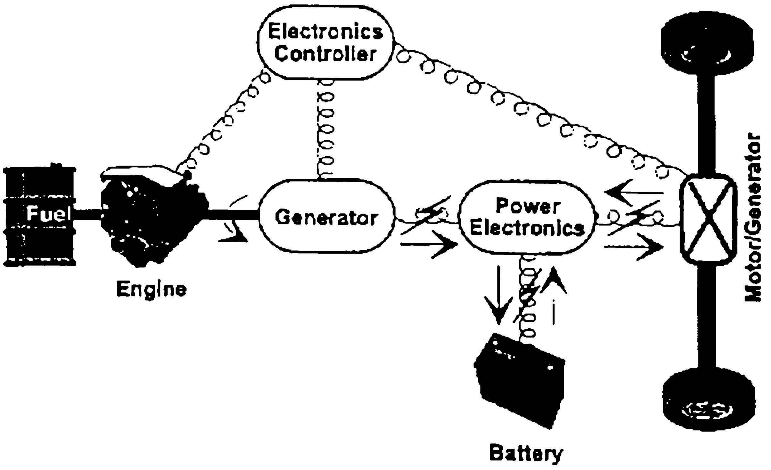

Series Hybrid Configuration

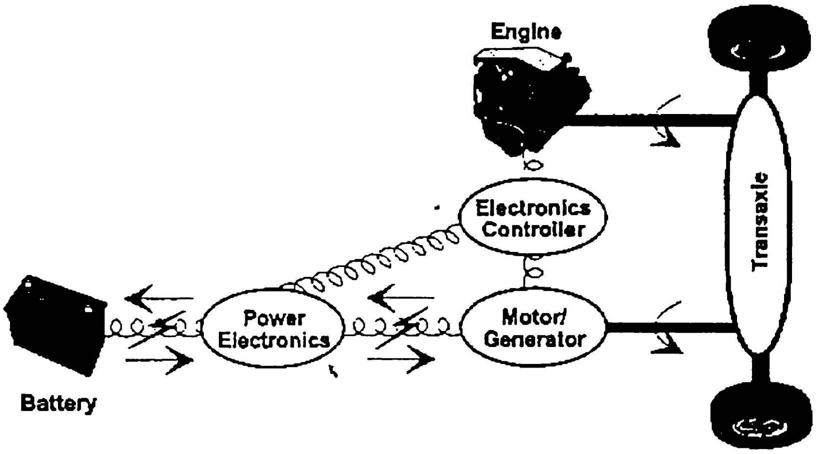

Parallel Hybrid Configuration

Figure 1.2 Schematics of Typical HEV Series and Parallel Configurations

The two or more types of power supply used in a hybrid to support the drive may be employed independently, in parallel, or in series (Figure 1.2), or in a combination of the two to increase the vehicle's range or performance.[14] The most common combinations include: batteries plus mains power, as used in trains and trams for example; and batteries plus internal combustion engine, which is essentially a cross between an EV and a conventional vehicle. Hybrid vehicles generally require a battery pack. When more power is required, the internal combustion engine starts up and can run a generator to provide electricity directly to the electric motors, top up the battery pack, or provide extra power directly through a purpose built transmission.[15] It is believed that the hybrid could be a viable short-term solution to the performance problems facing EVs, and may help to bridge the gap from the conventional motor car to the cleaner, greener car. Hybrids have already been released on the market; one example is the Toyota Prius, first released in 1997. The 2000 hybrid model boasts performances of approximately 16–20 km/l, and a maximum range of about 1000 km. Another is the soon to be released 2001 Honda Insight, which boasts an impressive 36 km/l. These are ICE battery hybrids but the benefits over a normal ICE are significant, without any loss of power or maximum speed.

1.3.2.6 Batteries

The battery is by far the most researched power storage device. Note however that the title 'battery' covers a large range of electro-chemical and some electro-physical devices.

1.4 Automotive Battery Technologies

The performances of batteries used for automotive applications are usually measured using two quantities; energy density and power density. The energy density (watt-hours per kilogram) affects the vehicle range, and the power density (watts per kilogram) affects the vehicle acceleration.

Another unit to consider when comparing battery technologies is dollars per kilowatt-hour, which gives an idea of the economic viability of a given battery.

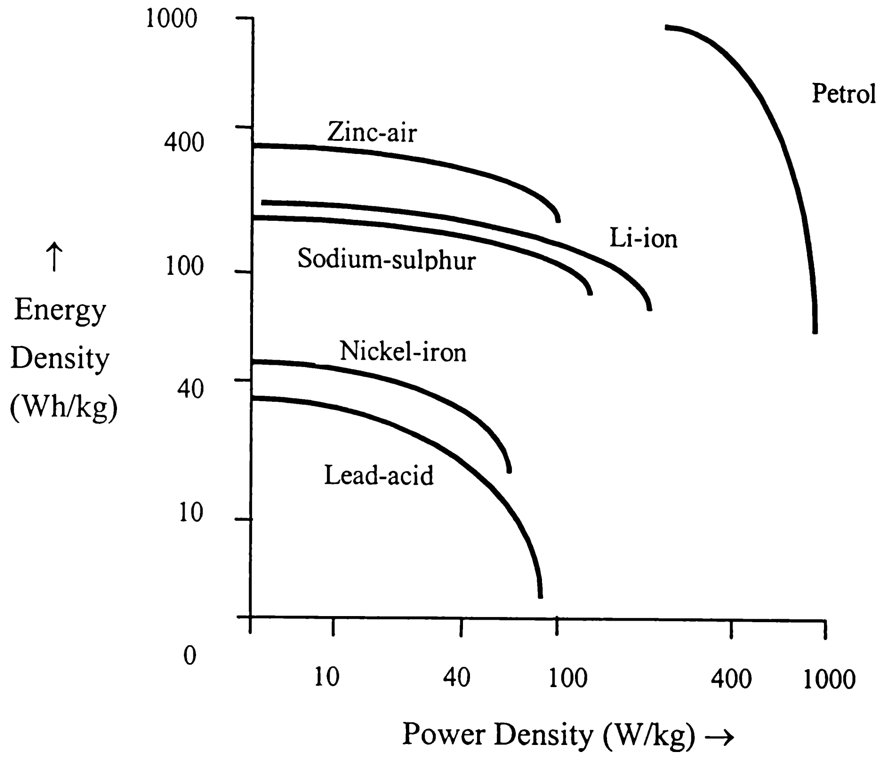

Figure 1.3 Batteries Fail to Rival Petrol on Energy Density and Power Density.

Figure 1.3 illustrates that petrol delivers greater power and energy densities than any high performance batteries presently available.[13] Therefore, the conventional vehicle continues to have greater range and acceleration than the EV.

Technological advances in electric motor design, controllers, recharging techniques, aerodynamics, tyres and other aspects of the EV have continued to increase the efficiency of the EV over the conventional vehicle. Therefore the required power and energy densities of the batteries can be less than that for petrol.

For example, acceleration of a heavy vehicle requires an engine with 100-200 horsepower (high power density required), but only 20% of its power is needed for highway cruising and only 4% for city driving (lower power density required).[15] This over-sizing makes the engine inefficient for the majority of the time. Hence, petrol vehicles are commonly used in circumstances which only require a small part of the range offered by these vehicles. This is the primary market that the EV would be able to fulfil.

Table 1.1 Performance Comparison of ICE vs EV

	ICE Vehicle	Electric Vehicle	Electric Vehicle
Quantity (one kg)	Petrol	Lead acid battery	Nickel metal hydride
Energy Density (ED) (Wh/kg)	2700	22	70
Efficiency or ED at the wheels (%)	15	75	75
ED at the wheels (Wh/kg)	400	17	53

From the figures presented in Table 1.1, a battery with an energy density of 540 Wh/kg will deliver 400 Wh/kg at the wheels; this would be competitive with an ICE running on petrol.

Table 1.2 Key Targets for Batteries in Electric Vehicles

Key Characteristics	Units	Mid-Term Battery	Long-Term Battery
Power to Weight Ratio	W/kg	150-200	300
Energy to Weight Ratio	Wh/kg	80-100	150
Cycle Life	Cycles	600	1000
Calendar Life	Years	5	10
Production Cost	$/kWh	< 250	< 150

In order to give battery developers some guidelines for research, the Advanced Battery Consortium (ABC), the Partnership for a New Generation of Vehicles (PNGV) along with the US DOE set up the following key targets for battery performance, (Table 1.2)[12,13,16]

To date, a number of high performance batteries have achieved energy densities of approximately 150-200 Wh/kg, with similar power densities. These high performance batteries tend to vary significantly in price from battery to battery, ranging from $50 (US) to $1,200 (US) per kilowatt-hour.[5] Some of the main contenders are listed in Table 1.3.[17,18]

Table 1.3 Competing EV Battery Technologies

Technology	Energy Wh/kg	Power W/kg	Cost $/kWh
Lead Acid	33-50	65-300	70-200
Nickel-Cadmium	55-105	90-100	150-300
Nickel Metal Hydride	55-70	150-200	230-1000
Sodium Sulphur	80-140	90-175	200-1200
Zinc-Air	185-200	60-225	100
Zinc-Bromine	75-85	35-60	150-300
Li-ion	150	100	50-500

Besides the performance of a battery, other important considerations include cost, safety, robustness to abuse, reliability, cycle life, recharging time and ease of manufacture. For larger batteries, safety, thermal stability, overcharge and over-discharge protection and reliability become even more important. All batteries which are now available, or soon to become so contain at least one undesirable property. Sodium sulphur batteries for example, require molten sodium-sulphur to be maintained at 300 °C, which has obvious safety concerns, especially in an accident situation. Sodium sulphur batteries also require a recharge every four days, or else the liquid sodium-sulphur will solidify and the batteries cannot be reused.

1.5 Solid State Electrochemistry

High Ionic conductivity in solids is a widely recognised, but relatively rare phenomena. Usually ionic solids are electrical insulators that only conduct ionically at high temperatures. Solid-state electrochemistry may be divided into two broad topics[19]:

A. *Solid electrolytes*, which conduct electricity by the motions of ions, and exhibit negligible electronic transport. Included in this group are crystalline and amorphous inorganic solids as well as ionically conducting polymers.
B. *Intercalation electrodes*, which conduct both ions and electrons. Again there are numerous examples based mainly on inorganic solids and polymers.

Large proportions of existing battery technologies are based on ion-conducting materials. The trend for emerging battery technologies is toward replacing liquid components with solid-state materials. The proven benefits include decreased weight (higher energy densities), increased safety (particularly with respect to lithium-based systems) and greater design flexibility.

1.5.1 History

Traditionally, the study of ion-conducting materials has focused on liquid solutions composed of an electrolyte in a low molecular weight polar solvent (for example, water). Since 1834, parallel investigations of molten salts and crystalline vitreous solid electrolytes were undertaken. The first of these investigations was carried out by Faraday.[20] Faraday showed that solid PbF_2, at red heat, had strange electrical properties. This was later determined to be due to ion motion through the solid. Tubandt,[21] by studying the AgI system, produced direct evidence that ions carry an electrical current in solids. The apparatus Tubandt used is illustrated in Figure 1.4.

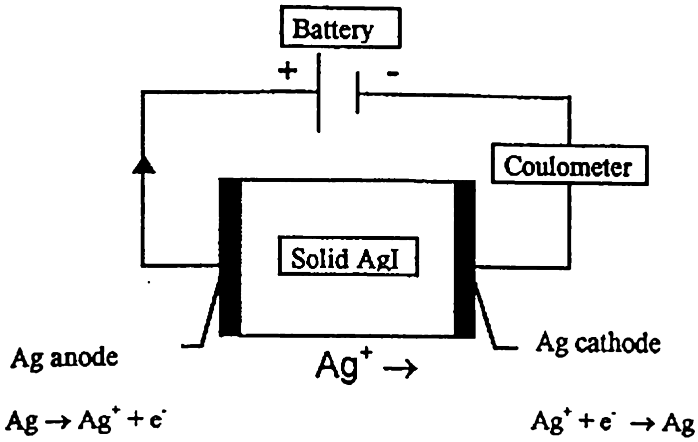

Figure 1.4 Apparatus Used to Show that Ag^+ Carries Current in Solid AgI.

At above 150 °C, an external battery imposes a potential across the cell, oxidation occurs at the anode and the silver ions move through the solid AgI electrolyte. The silver ions are reduced and deposited as metal on the cathode. The coulometer measures the total flow of electrons through the circuit. Tubandt found that the weight changes of the anode and cathode corresponded to one equivalent of silver being transported between the electrodes. Hence proof that Ag^+ is the charge carrier therefore ionic conduction had taken place.[20]

Some milestones in the development of solid-state ionic materials are listed in Table 1.4. Research into polymer electrolyte materials has been in progress for the past thirty years.[22,23] One of the important properties separating polymer electrolyte materials from hard, crystalline solid electrolytes is the ability of a polymer electrolyte to flow (a viscoelastic property) and thus maintain interfacial contact with the electrodes while the battery is being discharged, whereas the hard crystalline solid electrolytes tend to lose interfacial contact with the electrodes. It is this problem which has resulted in a large number of solid-state batteries being unsuccessful. However, research into insertion (lithium intercalation type) compounds for use as electrode materials, coupled with a polymeric-based electrolyte, has begun to overcome these problems.[23,24]

Table 1.4 Development of Solid State Ionic Materials

Year	**Researcher**	**Milestone**
1834	M. Faraday[20]	-Discovers solid PbF_2 at red heat gives strange electrical properties.
1884	E. Warburg[25]	-Alkali cation conductivity for oxide glasses proved.
1899	Nernst Glower[7]	-Realises application of zirconia as an electrolyte.
1910	C.Tubandt[21]	-Proof that ions carry electrical current in solids. -Recognition that other ionic solids have measurable conductivities, such as NaCl.
1900s	Y.I. Frenkel	-Propose hopping of ions through a series of interstitial sites (Frenkel disorder).
	W. Schottky	-Propose hopping of vacancies among normal lattice positions (Schottky disorder). -Basis for modern day theories on defect chemistry.[26]
1930	J.A.A. Ketelaar	-With the development of x-ray diffraction techniques, made it possible to study disorder of mobile ions in conducting solids such as Ag and Hg in Ag_2HgI_4.
1965	Yung FanY. You and J.T. Kummer	-Recognise the potential application for β-alumina as an electrolyte.
1970	Wright[22]& Armand[23]	-Pioneering work into the first extensively studied polymer electrolyte material, poly(ethylene oxide).

The historical development of ionically conducting materials is also reflected by the chronology of solid electrolytes used in solid state batteries, which is illustrated in Table 1.5. The electrolyte, conductivity (log(Scm^{-1})) and typical cell system is also shown.[11]

Table 1.5 Chronology of Solid Electrolyte Batteries

Date	**Electrolyte**	**Log (Scm^{-1})**	**Typical cell system**
1950-60	AgI	-5	Ag/V_2O_5
1960-65	Ag_3SI	-2	AgI_2
1965-70	$RbAg_4I_5$	-0.5	Ag/Me_4NI_5
1970-75	LiI	-7	Li/I_2(P2VP)
1970-75	LiI(Al_2O_3)	-5	Li/PbI_2
1965-75	β-Alumina	-1.5	Na-Hg/I_2,PC
1980-85	$LiI_aO_bS_cP_d$	-3	Li/TiS_2
1978-85	LiX-PEO	-7	Li/V_2O_5
1983-87	MEEP	-4	Li/TiS_2
1985-90	plasticised SPE	-3	Li/V_6O_{13}
PEO = polyethylene oxide.		SPE = solid polymer electrolyte.	

Useful solid electrolyte materials typically display conductivities in the range of 10^{-5} to 1 Scm^{-1} (at room temperature), which fall between semiconductors, such as silicon and aqueous electrolytes such as $NaCl_{(aq)}$.

1.6 Applications

The solid-state ionic materials discussed above, have also been found to be potentially suitable for many other applications. Some of these potential applications are displayed in Table 1.6.

Investigations into the application of solid-state materials, such as stabilised zirconia, in fuel cells and sensors have been fairly successful over the past decade, while the investigations into the application of polymeric materials to these situations are more recent. This leads to a more detailed examination of an application of specific interest to this thesis.

Table 1.6 Applications of Solid State Ionic Materials

Application	**Example (material)**	**Reference**
Fuel cells	perfluorosulfonate "based" ionomers, such as NAFION®.	27
Sensors	biosensor, siloxane and ethylene polymers with ferrocene.	28
Lasers and phosphors	β -alumina combined with rare-earth ions.	20
Electrochromic displays and electrochromic windows	Li^+ conductors based on PEO, PPG, and PMM for example.	29,30
	Li_xWO_3 and H_xWO_3 compounds.	31
Data storage devices	2,3-bis-(2,3,5-trimethyl-3-thienyl)-maleic anhydride.	29

1.7 Current Battery Configurations

There are many different battery configurations currently being researched. Some of the more significant ones are listed below, along with discussion of their advantages and drawbacks:

- Pb/PbO_2
- MH/KOH/NiOOH
- Zn/KOH/NiOOH
- Zn/KOH/Air
- $Na\beta\text{-}Al_2O_3/NaAlCl_4/NiCl_2$

The lead-acid battery has too low an energy density to be considered as a potential EV battery, but due to its low cost it is used in all commercial EVs. The nickel metal hydrides are probably the best competitor to the lithium ion technology, with their main disadvantages being their lower energy density, a need for temperature control during charge, high cost, and hydrogen pressure in large systems. The Zn-air battery has great potential for fleet vehicles or special purpose vehicles. The disadvantages which will limit its use include its low specific power, low energy efficiency, and the need for a battery exchange centre as the recharge is performed chemically.

Li Variants:

- $Li/LiAgF_6$:2Me-THF-EC/TiS_2
- $Li/LiCF_3SO_3$:PEO/$LiMn_2O_4$
- $Li/LiCF_3SO_3$:PEO/V_6O_{13}
- $LiC_6/LiPF_6$:EC-DEC/$LiCoO_2$ (Sony)
- Other Li ion/polymer combinations

The Li/TiS_2 battery has been used extensively in the space shuttle. It has a reasonable specific energy and a low cost, but is limited by a low power density and the short cycle life of Li. The $LiCF_3SO_3$ organo-disulphide polymer is attractive as an electrolyte due to its low comparative toxicity and higher conductivity. However, it does have severe disadvantages. Cathodes in combination with this battery include $LiMn_2O_4$ and its variants, as well as V_6O_{13}. Potentially cheap batteries with reasonable specific power and energy densities, they are limited due to a short cycle life, a low Li^+ transport number and electrolyte instability. There are also the problems of scaling up, bipolar assemblies, overcharge/overdischarge and thermal management. The Sony cell, first released in 1990 utilizes $LiCoO_2$ as a cathode.[32] Currently the most popular Li-ion battery since its inception, it has problems of intolerance to overcharge/overdischarge, a high cost, a flammable solvent electrolyte and engineering issues when going for specific shape and scale up.

Potentially successful mid-term batteries include:

- MH/NiOOH
- Na/$NiCl_2$
- Li-Ion

Prospective long-term batteries include:

- Zn/Air
- $LiAlFeS_2$
- Li Polymer

The mid-term and long-term batteries will be chosen for specific purposes. The Na/$NiCl_2$ shows good cycle life but operates at high temperature. Li-ion will become cheaper as new materials like the doped spinel $LiMn_2O_4$ are commercialised. The $LiAlFeS_2$ is a high-temperature battery, which has good specific energy and power density, and excellent cycle life, but is currently limited by its operating temperature (hence problems with thermal sealing). The lithium polymer battery probably shows the best long-term potential, and is currently under intense research as a third generation battery.

Presently there is no ideal battery chemistry. To accelerate a vehicle, a battery that releases electrons quickly is required. Usually batteries of this type are not effective at storing energy for long range. The most obvious mid-term solution is the HEV, which most major car companies are producing, however, most of these still operate primarily on an ICE. This will have to change in order to meet zero emission vehicle (ZEV) guidelines.

Lithium-based battery technology is the most promising candidate to achieve these targets, even with safety and performance considerations.

1.8 Lithium Batteries and Component Material Requirements

Lithium batteries have rapidly entered mainstream electronic designs, with the most common area of application being in portable equipment and non-volatile memory backup applications.

In the 1960s, significant advances were made in materials processing, handling, and non-aqueous electrolytes. These advances have enabled manufacturers to apply the electrochemical possibilities of lithium to practical cell hardware.

1.8.1 The Electrochemical Cell

A battery or electrochemical cell is an electrochemical device that produces electrical energy from oxidation/reduction reactions. Batteries can be classed as either primary (non-rechargeable or disposable), or secondary (rechargeable or reusable) which are also referred to as storage batteries or accumulators. The battery (cell) is composed of three main components: the cathode, anode and the electrolyte joined via an external circuit. The functioning of a cell/battery process can be described by using the Li/TiS$_2$ example shown in Figure 1.5.[33]

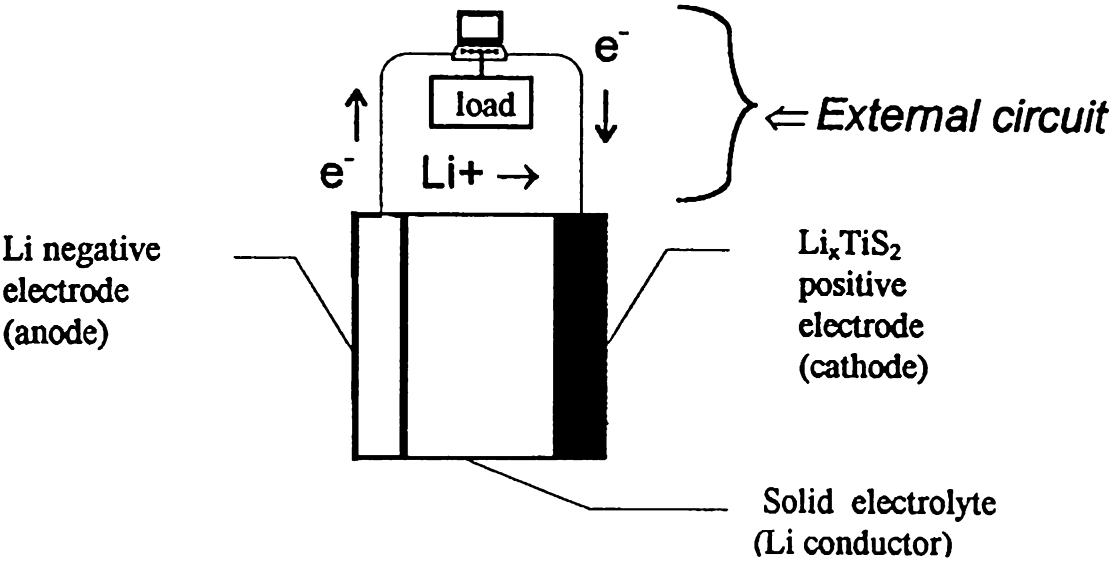

Figure 1.5 Li/TiS$_2$ Solid-Electrolyte Battery (one cell)

Each cell has two electronically-conducting electrodes, through which electrons enter or leave the cell. It is at the surface of these electrodes, at the interface between the electrolyte and the electrode, that the primary electrochemistry takes place. In Figure 1.5, the Li-metal is oxidised to a metal ion Li$^+$ at the anode-electrolyte interface. The Li$^+$ then enters the electrolyte. During the oxidation process, electrons are released into the external circuit available to do useful work, and to balance the flow of charge carried by ions through the electrolyte. At the electrolyte-cathode interface, Li^+ is reduced (obtaining electrons from the external circuit) and is incorporated into the cathode. The above process also applies to liquid and crystalline salt electrolytes.

In summary, three reactions must occur in a functioning cell:[34]

- redox reactions must take place at the electrodes
- electrons flow through an external conductor
- ions flow in the electrolyte.

1.8.2 Historical Development of Lithium Secondary Batteries

Research into lithium batteries began in the 1950s when it was noticed that Li metal was stable in a number of non-aqueous electrolytes such as fused salts, liquid SO_2 or organic electrolytes such as $LiClO_4$ in propylene carbonate.[35] This stability was attributed to the formation of a passive layer that prevents the direct electrochemical reaction between lithium metal and the electrolyte but still allows for lithium to go into solution during cell discharge.

The commercialisation of lithium primary batteries followed relatively quickly in the late 1960s and 1970s. Some of the room temperature systems (some still in use today) are lithium/sulphur oxide Li/SO_2,[36] lithium/manganese dioxide Li/MnO_2,[37] lithium polycarbon monoflouride ($Li(CF_x)_n$),[38] and lithium/iodine-polyvinylpyridine Li/I(PVP).[39] These primary systems have found a variety of applications from military to medical with Li/MnO_2 being dominant in the consumer market.

Not surprisingly, the development of rechargeable batteries was much slower. Cycling of the metallic lithium anode in organic electrolytes showed that this anode was not completely reversible. Lithium was lost during each cycle. Metal deposited during charging could only be partially stripped during discharge due to corrosion and passivation.[40] In order to avoid a capacity fade, cells were built with a relatively large excess of lithium compared to the stoichiometric amount required for a single cycle. The average lithium cycling efficiency is usually defined as:

$$E = \frac{Q_s - Q_{ex}/n}{Q_s}$$ Equation 1.1

Where Q_s is the charge of lithium stripped, Q_{ex} the amount of excess Li, n the number of cycles. Equation 1.1 can also be used to calculate the relative excess $R = Q_{ex}/Q_s$ of lithium required to achieve a certain cycle number N:

$$R = N(1-E)$$ Equation 1.2

From the early 1970s, this problem was solved by using a molten salt systems (LiCl – KCl) with a Li-Al alloy anode and a FeS cathode. This is a high temperature-system.[41]

Room temperature systems became viable when Exxon commercialised its Li/TiS_2 system in the mid 1970s as a coin cell for electronic watches.[42] Since then, large numbers of rechargeable systems with different cathode materials, different lithium metal- or lithium compound-based anodes and electrolytes have been investigated and developed (Table 1.7).[43]

The commercial success of the Sony Li-ion battery is considered a triumph of materials electrochemistry that has encouraged continued development of the next generation lithium battery.[45]

Table 1.7 Development of Rechargeable Lithium Batteries

Year	Development of Components			Systems
	Anode	Cathode	Electrolyte	
1970s	Lithium metal Lithium alloys	Transition metal sulphides TiS_2, MoS_2 Transition metal oxides V_2O_5, and V_6O_{13} Liquid cathodes SO_2	Liquid organic electrolytes Solid inorganic electrolytes Li_3N	$Li/LE/TiS_2$ Li/SO_2
1980s	Li intercalation $LiWO_2$ Li-carbon (LiC_{12}) (coke)	Selenides $NbSe_3$ Discharged cathodes $LiCoO_2$, $LiNiO_2$ Manganese oxides (Li_xMnO_2)	Polymer electrolytes Plasticised polymer electrolytes	$Li/LE/MoS_2$ $Li/LE/NbSe_3$ $Li/LE/LiCoO_2$ $Li/PE/V_2O_5$ $Li/PE/V_6O_{13}$ $Li/LE/MnO_2$ $C/LE/LiCoO_2$
1990s	Li-carbon (LiC_6) Graphite	Manganese spinels ($LiMn_2O_4$)		$C/LE/LiCoO_2$ $C/LE/LiMn_2O_4$

1.8.3 Rechargeable Lithium Battery Design

Lithium batteries can generally be classed into four basic designs as represented in Figure 1.6, two of which use metallic lithium.[44] The first and oldest utilises a negative electrode comprised of lithium metal, a metal oxide intercalation compound as the positive electrode, and a non-aqueous liquid or solid polymer electrolyte. In more recent years, the lithium metal has been replaced with a second intercalation electrode based on carbon, and is known variously as a lithium ion, shuttlecock, rocking-chair or a swing battery.

The lithium ion battery is fabricated in the discharged state with the lithium located in the positive electrode. On initial charging, lithium ions diffuse along channels in the carbon host.

The charge compensating electrons pass around the external circuit. Discharge reverses this process. As a result, cycling of the cell only involves the exchange of lithium ions between two otherwise inert hosts. In contrast, discharge and charging of the lithium metal cell involves stripping and plating lithium metal at the negative electrode. Characteristics of cells with lithium metal as an anode and typical lithium ion cells are compared in Table 1.8.[45]

Table 1.8 Comparison of Lithium Metal and Lithium-ion Batteries

Lithium metal battery	Lithium-ion battery
Potential safety problems	Excellent safety – no lithium metal
Plating/stripping lithium limits cycle life	High cycling efficiency
Very high gravimetric energy density	Modest-high gravimetric density
Very high volumetric density	High volumetric density
High cell potential	Modest-high cell potential
Very low self discharge	Modest self discharge
No memory effect	No memory effect

The most important difference is the absence of lithium metal in the lithium ion battery. The deposition of lithium on charging the lithium metal results in a very reactive surface, often with dendrites, which may grow enough to cross the electrolyte and short circuit the cell. Consequently, the lithium ion battery is, in principle, a safer design since lithium is inserted not plated.

Because it is fabricated in the discharged state, the Li ion battery may be transported to the point of sale in a safe condition and without need for special precautions, unlike lithium metal cells. The absence of lithium metal at the negative electrode ensures good reversibility, and therefore cycle life. Since lithium metal cannot be stripped and plated with an efficiency of 99%, a three- to six-fold excess of lithium is required to achieve several hundred cycles from a lithium metal battery.

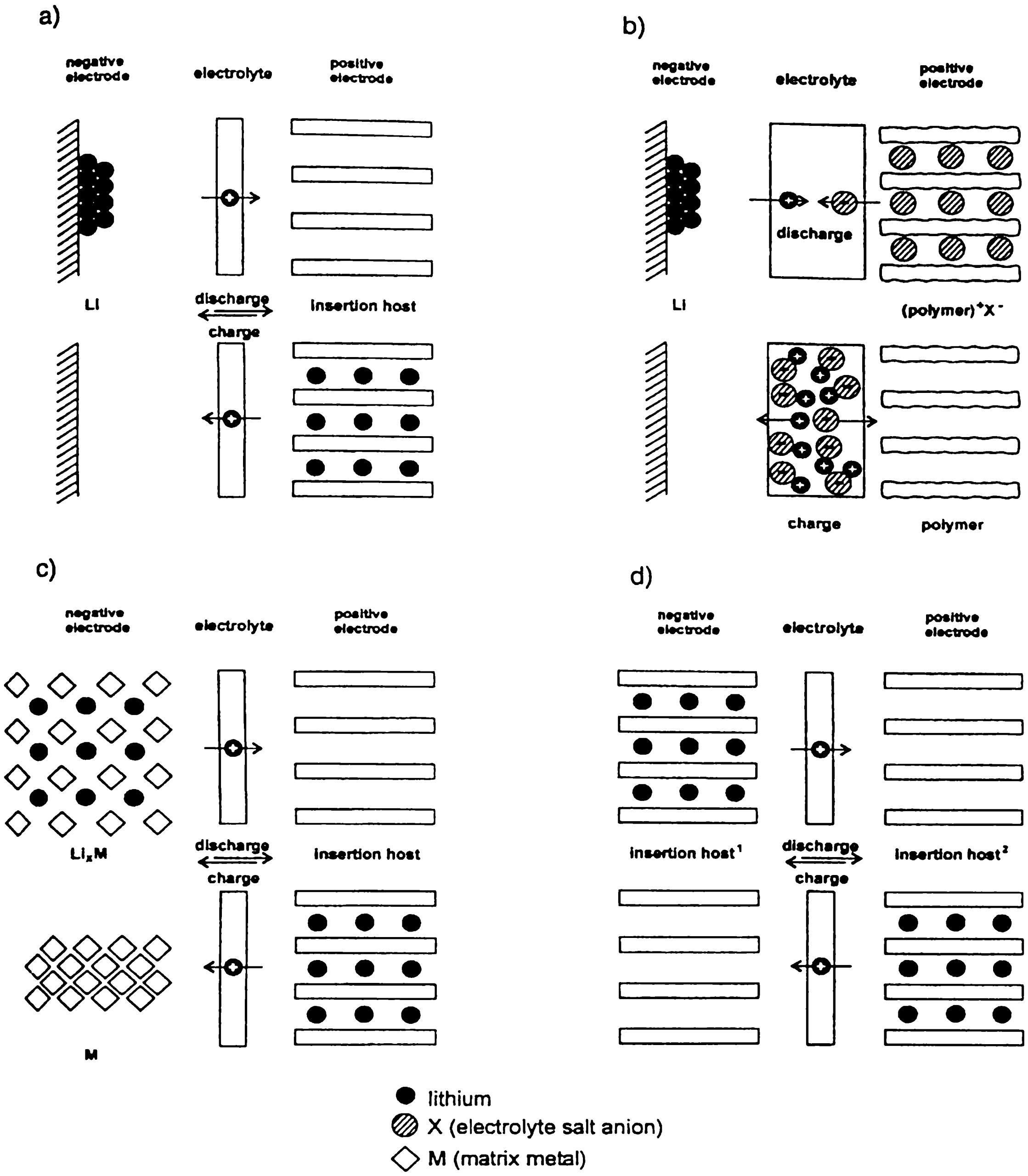

A) Anode – metallic Li, Cathode – insertion host

B) Anode – metallic Li, Cathode – anion-exchanging electroactive polymer

C) Anode – Li alloy (dimensionally unstable), Cathode – dimensionally stable insertion host

D) Anode – dimensionally stable insertion host, Cathode – dimensionally stable insertion host

Figure 1.6 Schematic Representation of the Main Li Battery Configurations

These features have made Li ion batteries the favoured choice for commercial batteries in the consumer market. However, when applying battery technology to an EV, a very high gravimetric energy density is required. The carbon anode used in the Sony cell[32] has a significantly lower gravimetric and volumetric energy density than lithium metal.[46] Higher-capacity carbons are available but have their own safety problems due to the internal surface area of the material containing large quantities of lithium, which increase the overall surface area. Another problem is that the voltage of the Li ion battery will always be lower than that of the lithium metal battery due to the more positive redox potential of carbon when compared to lithium. The lower voltage again leads to a reduction in specific energy. If the cycling performance of lithium metal can be improved so that the requirement for a large excess of lithium on the anode can be removed, and provided a safe design can be engineered, then lithium metal may still provide the best battery for EV applications.

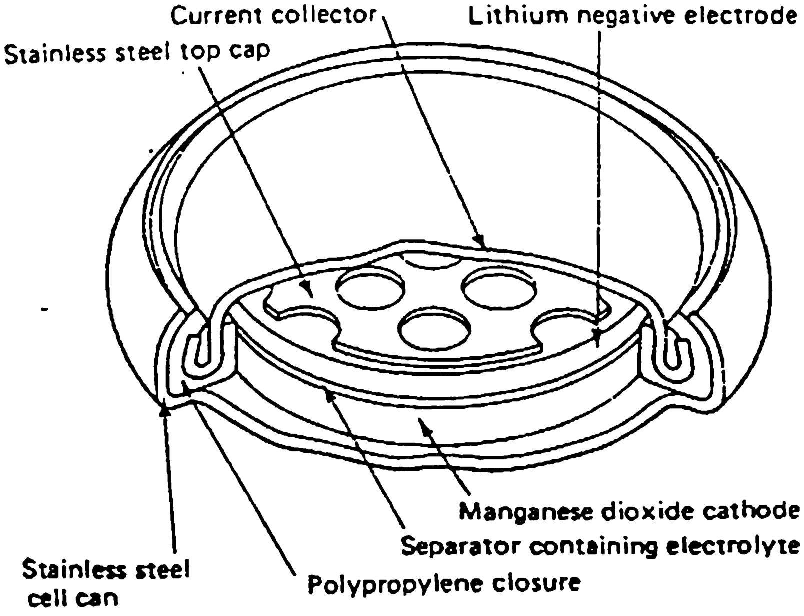

Figure 1.7 Lithium-Manganese Dioxide Button Cell

There are a large variety of lithium battery designs that cater for many different applications. Figure 1.7 shows a common button cell,[47] Figure 1.8 a complex cylindrical cell[48] and a prismatic battery Figure 1.9.[49]

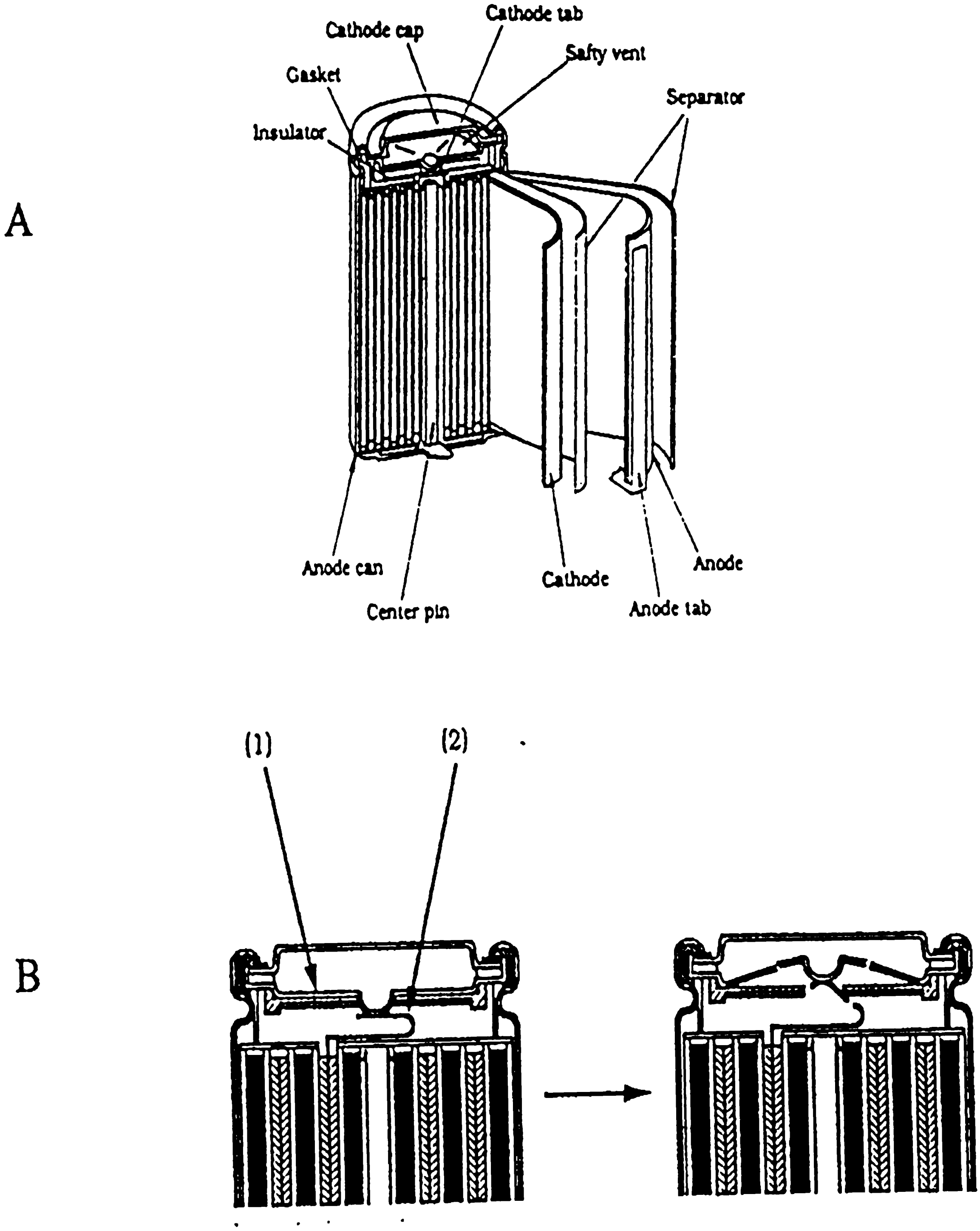

(**A**) cell construction, and (**B**) current breaker

(**1**) vent mechanism (**2**), to protect/safety against over-charging.

Figure 1.8 $LiCoO_2/C$ Cylindrical Cell

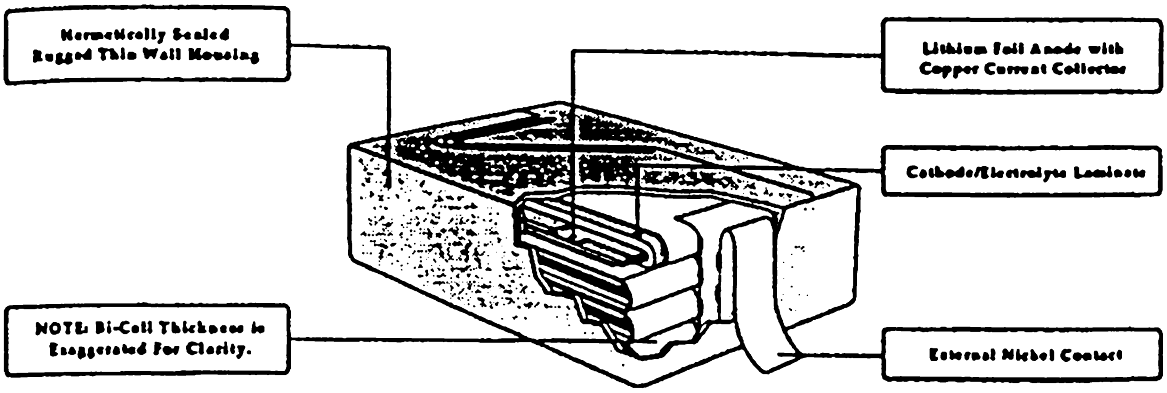

Figure 1.9 Typical Prismatic Battery

1.8.4 Design and Fabrication Considerations

Goodenough has outlined some design considerations for the electrochemical cell: [16]

The internal resistance of the cell is R:

$$R = (L/\sigma_i A) + R_{\text{int}} + R_e \qquad \text{Equation 1.3}$$

Where L/A = thickness/area ratio of an electrolyte membrane,

σ_i = ionic conductivity of the electrolyte,

R_{int} = resistance to ionic transfer across the reactant-electrolyte interface, and

R_e = internal resistance to electronic current collection within the electrodes.

The operating voltage V, Equation 1.4, is limited by the open-circuit voltage V_{oc}, Equation 1.5:

$$V = V_{oc} - IR \qquad \text{Equation 1.4}$$

$$V_{oc} = (\mu_A - \mu_C) / (-nF) \qquad \text{Equation 1.5}$$

where $\mu_A - \mu_C$ = difference in the electrochemical potential of the anode and the cathode, n = number of electrons involved in the chemical reaction of the cell, and

F = Faraday's constant.

The consequences of Equations 1.3, 1.4, and 1.5 are:

- If the voltage is less than 4 V, a high current through the cell would be required to deliver high power (P=IV). To obtain a low I^2 R loss and a high maximum power ($P_{max}=I_{max}V_{max}$), a small resistance (R) is required.
- Generally, the electrolyte conductivity is fairly low (σ_i usually less than 1 Scm^{-2} at the operating temperature. To achieve a small resistance (R) requires a small thickness/area (L / A) ratio. The practical lower limit for L / A is set by R_e, which increases with area (A). In other words, presently available electrolytes are required to be thin, to minimise the resistance to ion flow through the electrolyte.
- Batteries also require metallic electrode current collectors, hence when designing a power cell, the designer not only aims to optimise σ_i and minimise L (thickness) of the electrolyte, but also needs to minimise interfacial resistance R_{int} from metal current collectors.

A typical cell polarisation curve (Figure 1.10) has three regions:

- Region (i) represents a voltage drop (V_{oc} - V) at low current drain due to an increase in the interfacial resistance (R_{int}), referred to as the electrode polarisation over-voltage. In lithium batteries, the polarisation over-voltage is a result of the formation of a passive film at the lithium-electrolyte interface.
- Region (ii) is mainly the ionic conductivity (σ_i) in the electrolyte, as well as R_{int}.
- Region (iii) is due to a depletion in acceptor sites and/or mobile ions at interfacial regions in the cell. Region (iii) is referred to as the "diffusion-limited" region. Region (iii) will move to higher currents, if an increase in ionic conductivity (σ_I) is observed for either side of the interfaces.[14,16]

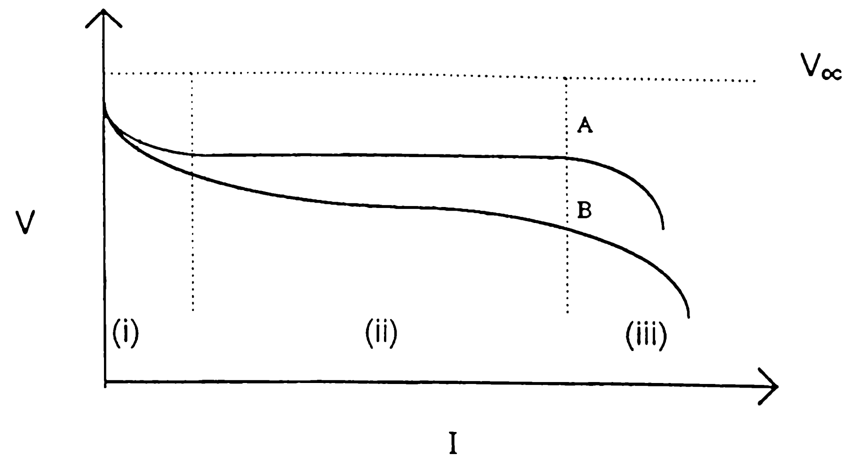

A Solid-state system

B Liquid system.

Figure 1.10 Typical Polarisation Curves for an Electrochemical Cell.

1.9 The Electrolyte

The electrolyte is an essential component of an electrochemical cell, such as battery, fuel cell, or sensor. The requirement of a battery electrolyte is that it must be a good ionic conductor and an electronic insulator; otherwise it would short and lose charge on standing. It should not react with the reactants of the cell other than to donate/accept the working ions to and from the electrodes.

The voltage of rechargeable lithium cells may be as high as 5V; hence a wide electrochemical stability window for the electrolyte is crucial for the cells shelf life and cycle life. This limits the number of potential electrolytes, as many aqueous and non-aqueous electrolytes have too narrow a thermodynamic and/or kinetic electrochemical stability window. Aprotic electrolytes seem to be the only choice that has been employed commercially so far, but these have their own disadvantages; they are expensive, generally flammable, often toxic and have lower ionic conductivity.[49]

In non-aqueous electrolytes the Li^+ ion transference number is typically only about 0.3, which means that only approximately 1/3 of the ionic charge is transported due to the movement of Li ions.[50] This is because in an electrolyte solution, the solvation of the smaller Li^+ cation is usually stronger than the solvation of the corresponding bigger anion X^-, for example PF_6^-,

ClO_4^-, or $N(SO_2CF_3)_2^-$. This results in the mobility of the anions being greater than that of the solvated Li^+ cations. This limits the power density of a lithium cell, the electrochemistry of which strongly depends on Li^+ transport in the electrolyte. In order to try to minimise this effect, it is necessary to make the electrolyte as thin as possible, so that Li^+ pathways are short.

Suitable non-aqueous electrolytes for secondary lithium batteries can be roughly divided into three groups: liquid, solid and polymer. Liquid electrolytes require the presence of a separator that maintains the separation of the two electrodes and yet is permeable to the working ions. It also immobilises the liquid electrolyte. It is more effective if the immobilising agent also fixes the counter ion of a liquid electrolyte, and also allows easy fabrication of a thin, flexible membrane. A solid electrolyte acts as a separator on its own as does a polymer.

The reactants of an electrochemical cell may be gaseous, liquid or solid. Solid electrolytes are useful in the case of gaseous or liquid reactants, but in the case of solid reactants, a solid electrolyte creates a solid-solid interface that causes problems with the changing volumes of both solids during repeated charge/discharge. Loss of interfacial contact not only increases the internal resistance for ion transport across the electrode-electrolyte interface, it also lowers the capacity of the cell as parts of the electrode concerned lose contact with the electrolyte. This means that liquid or polymer electrolytes are preferred if the reactants are solids.

Besides determining the nature of the reactants, the choice of electrolytes determines the limiting electrochemical potentials μ_A and μ_C and hence the magnitude of the open circuit voltage (Equation 1.5). The highest electron donor state in the anode should lie below the lowest electron acceptor state in the electrolyte if the electrolyte is not to be reduced or to react chemically with the anode. Also, the lowest electron acceptor state in the cathode should lie above the highest electron donor state of the electrolyte if the electrolyte is not to be oxidised or to react chemically with the cathode.

As shown in Figure 1.11, in the case of a solid electrolyte, the highest occupied molecular orbital (HOMO) of the gaseous or liquid reductant at the anode should lie below the bottom of the conduction band of the electrolyte if the reductant is not to inject electrons in to the conduction band. The lowest unoccupied molecular orbital (LUMO) of the oxidant at the cathode should lie above the top of the valence band of the electrolyte if the oxidant is not to inject holes into the valence band. The LUMO of a liquid electrolyte should lie above the Fermi energy of a metallic anode reductant and its HOMO should lie below the Fermi energy of a metallic cathode oxidant.[16] Maximising V_{oc} requires matching of the μ_A and μ_C to the electrolyte window E_g.

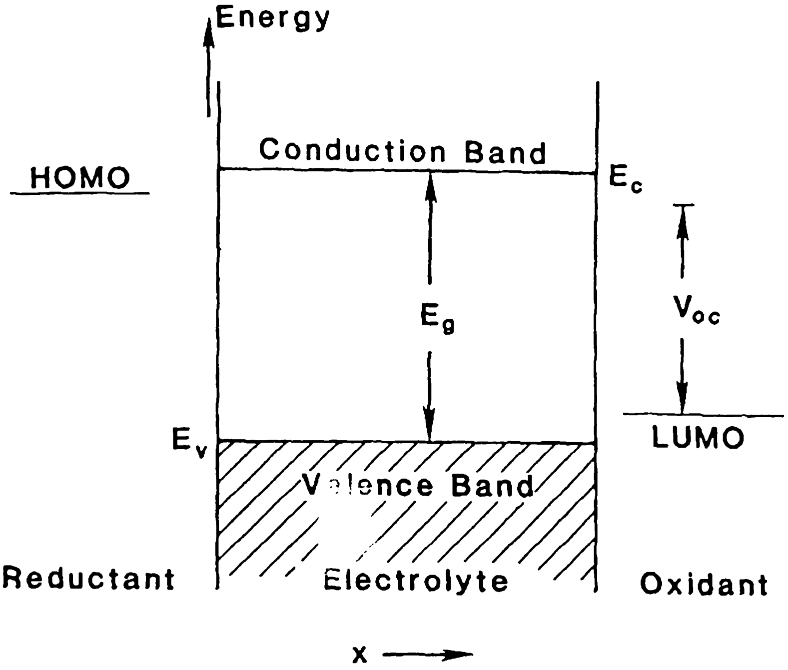

Figure 1.11 Placement of Reactant Energies

1.9.1 Liquid Electrolytes

Typical liquid electrolytes consist of a lithium salt Li^+X^- dissolved in an aprotic organic solvent or a mixture of esters or ethers. To obtain a good liquid electrolyte the following properties need to be examined:

- High Li ion mobility.
- Li^+ transference number near 1.0 (in practice most are less than 0.5).
- High ionic conductivity (to minimise polarisation due to low Li ion transference number.

- Must have intrinsic stability.
- Is unreactive with cell contents or forms a passivating film with high ionic conductivity.
- Safety aspects – flash point, solvent volatility, toxicity, and thermodynamics of solvent reaction with other cell components under thermal abuse situations.

1.9.1.1 Ethers

The electrochemistry of the Li electrode during cycling with electrolytes such as $LiAsF_6$ in cyclic ethers 2-methyltetrahydrofuran (2-MeTHF), tetrahydrofuran (THF), 4-methyldioxolane (4-MeDIOX) and 1,3 Dioxolane (DIOX) have been studied extensively.[51,52,53] 2-MeTHF/ $LiAsF_6$ is the most stable of these compounds, and has particularly high cycling efficiency. 2-MeTHF cannot spontaneously rearrange unlike other substituted 5-membered cyclic ethers such as 4-MeDIOX, and DIOX. These ethers need to be inhibited otherwise they rearrange to propyl formate and ethyl formate respectively. 2-MeTHF exhibits the slowest reaction kinetics with Li, 5 times slower than THF,[54] and it also contains the naturally occurring contaminant 2-methylfuran which actually enhances Li cycling efficiency.

1,2-Dimethoxyethane (DME) is commonly used in conjunction with $LiClO_4$ and a high dielectric solvent such as PC in primary Li batteries. Its chelating nature, presumed high donor number and low viscosity all contribute to the high conductivity of blended electrolytes that contain it.

1.9.1.2 Organic Carbonates

Cyclic carbonates such as propylene carbonate (PC) and ethylene carbonate (EC) are amongst the oldest known solvents for use as blended electrolytes. EC solutions are typically more highly conductive than analogous PC solutions. This is mainly due to the higher dielectric constant of EC and also to the slightly lower viscosity of EC solutions.[55] Electrolytes that contain only EC however are unsatisfactory for use much below room temperature as the EC often crystallises due to a freezing point of 36 °C. Several different systems have been found to benefit from the addition of EC. It is believed that EC reduction products on Li or C anodes enhance the compactness and integrity of the passive film, and this increases cycling efficiency.

Acyclic carbonates such as dimethyl carbonate (DMC) and diethyl carbonate (DEC) are much less polar and less viscous than the cyclic PC and EC. The main effect of this lower polarity is a significant decrease in the solvent-solvent interaction energy. The weaker dipole-dipole attractive forces result in much lower viscosities and boiling points than those of the cyclic counterparts.

The low toxicity of EC and the essentially non-toxic nature of PC have resulted in their extensive evaluation as possible Li battery electrolyte solvents, and most commercial lithium ion cells use a mixture of EC and DEC as this combination has good wetting properties.

1.9.1.3 Other Solvents

Sulfolane and other sulfones are typically solids at room temperature. They generally exhibit excellent oxidative stability, but they are limited in high rate capability situations due to their high viscosity. Many co-solvents and salts have been examined in an attempt to lower the viscosity, but this only results in lowering the cycling efficiency.[56] Acetonitrile and higher nitriles have been examined but tend to be too reactive with Li, and glymes with higher molecular weight than DME offer lower vapour pressures and flash solvent points but have lower conductivities.

Blended solvents are now the standard due to a synergistic effect on conductivity, which results from the blending of a low-polarity and a high-polarity solvent. The resulting electrolyte has a higher conductivity than that of either solvent individually, and this is possibly due to a low viscosity enhancement, resulting in higher ion mobility, and hence enhanced conductivity.[57,58]

1.9.1.4 Lithium Salts

Of the many factors that are considered in the choice of the best Li salt, or solute for a battery, performance, price and safety top the list. The important performance factors are conductivity, thermal stability and chemical stability at both anode and cathode interfaces, solubility and cycling efficiency. A significant limiting relationship between the mutually exclusive demands of a highly dissociated salt and low viscosity is due to highly dissociated salts being limited to compounds with weak electrostatic attractions i.e. spatially large anions. Large anions have increased mass and consequently produce denser, more viscous electrolytes.

$LiClO_4$ has one of the longest histories of any Li solute. It is moderately conductive, thermally stable, oxidatively robust and cycles relatively well. However, it is limited by its tendency to detonate in the presence of low-concentration organic solvents.[59] Perflourinated Li salts such as $LiMF_x$, have received extensive study due to the high conductivity solutions that they form. The order of conductivity for the monovalent anions is $LiSbF_6 > LiAsF_6 \approx LiPF_6 > LiBF_4$. The order of reductive stability is $LiPF_6 > LiAsF_6 > LiSbF_6$, and is the reverse of the thermal stability order.[60,61] $LiSbF_6$ and $LiTaF_6$ have been observed to readily polymerise cyclic ethers and to spontaneously reduce to the parent metal in the presence of Li metal.[62] The oxidative stability of $LiPF_6$ is outstanding, and though its electrochemical performance is less than that of $LiAsF_6$, its much lower toxicity has established its significant presence in the Li ion battery market.[63]

Other salts that have been considered are the organic anions $LiN(SO_2CF_3)_2$ (HQ-115 from Hydro-Quebec/3M) and $LiC(SO_2CF_3)_3$ (Li Methide from Covalent Associates). These exhibit high conductivities in typical organic solvents and HQ-115 has been commercialised for use in primary batteries for some time.

1.9.2 Solid Electrolytes

The solid electrolyte functions both as an electrolyte and a separator between the anode and the cathode. This twin function requires that solid electrolytes be designed not only with good ionic conduction, but also have the physical properties to function effectively as a separator. If these requirements are not met, the consequences include poor performance and compromise of safety considerations, especially when dealing with lithium. It should be noted that at this stage there are no commercial lithium batteries utilising solid electrolytes, due to lower performances at room temperature.

The potential benefits from using solid-state lithium ion-conducting materials for electrolytes in batteries include:

- high open circuit potential
- high energy density
- long service and shelf life
- stable flat discharge voltage
- wide operating temperature range
- safe and environment friendly, excludes heavy metals and other toxic substances from the environment
- no leakage problem related to gas/liquids; therefore increased safety
- design benefits when working with solid state materials
- cost effectiveness

1.9.2.1 LISICONS

The lithium analogues of NASICONs (sodium super ion conductors) are solid solutions based on Stoichiometric phases such as γ-Li_2ZnGeO_4 or γ-$Li_3(P, As, V)O_4$, but containing interstitial Li^+ ions.[64] These are introduced by aliovalent substitutions $Zn \rightleftarrows 2Li$ in Li_2ZnGeO_4 or $P \rightleftarrows Si$ in Li_3PO_4, to give the solid solution formulae:

$Li_{2+2x}Zn_{1-x}GeO_4$ $0.3 < x < 0.8$

$Li_{3+x}(P_{1-x}Si_x)O_4$ $0 < x < 0.4$

The crystal structures of the end-members with $x = 0$ are so-called γ-tetrahedral structures with distorted hexagonal close-packed oxide arrays and cations distributed over various tetrahedral sites. It has been found by neutron powder diffraction that the Li^+ ions in the solid solutions occupy partially various tetrahedral and octahedral interstitial sites, which link up to form an essentially three-dimensional conduction pathway.

The conductivities increase dramatically with x, from basically insulating behaviour in the stoichiometric $x = 0$, to reach a maximum at $x = 0.5$. For the system given above the conductivity reaches values of 0.1 Scm^{-1} at 300 °C, but decreases rapidly at lower temperatures.

1.9.2.2 Li_4SiO_4 Derivatives

Stoichiometric Li_4SiO_4 is a modest Li^+ ion conductor but is a very good host material for doping.[64] Both Li^+ interstitials and Li^+ vacancies can be created resulting in high conductivities. In the substitution $Si \rightleftharpoons Al$, the Al ions occupy Si sites with Li entering interstitial sites to give:

$Li_{4+x}(Si_{1-x}Al_x)O_4$ $0 < x < 0.4$

Another substitution $3Li \rightleftharpoons Al$ leads to the creation of Li^+ vacancies with the general formula:

$Li_{4-3x}Al_xSiO_4$ $0 < x < 0.5$

This results in a system where the conductivity varies dramatically with x.

The crystal structure of Li_4SiO_4 and its solid solutions are particularly favourable for Li^+ ion conduction because it has an oxide ion array which approximates to tetragonal packing. The structure is not only permeated with open channels that enable Li^+ ion migration along the channels, Li^+ ions can also move through the channel walls which allows three dimensional conduction.

1.9.2.3 Li_3N

H-doped lithium nitride is the highest Li^+ ion conducting crystalline material known to date.[65] It is essentially a vacancy conductor because the substituting hydrogen atoms in the formula $Li_{3-x}H_xN$ are tightly bound as NH^{2-} groups. These are located in such a way as to leave vacancies in the Li^+ ion conduction pathway.

Li_3N has a layered structure in which sheets of Li_2N are separated from each other by additional Li^+ ions, which act to bridge the N atoms in adjacent sheets (Figure 1.12). In H-doped Li_3N, 1-2% of the Li^+ ions in the Li_2N sheets are vacant, giving rise to a high in-plane conductivity of 1×10^{-3} Scm^{-1} at 25 °C, but with a much lower cross plane conductivity of 1×10^{-5} Scm^{-1}.

Unfortunately, Li_3N has a low decomposition potential 0.445V, which limits its usefulness as a practical solid electrolyte in batteries.

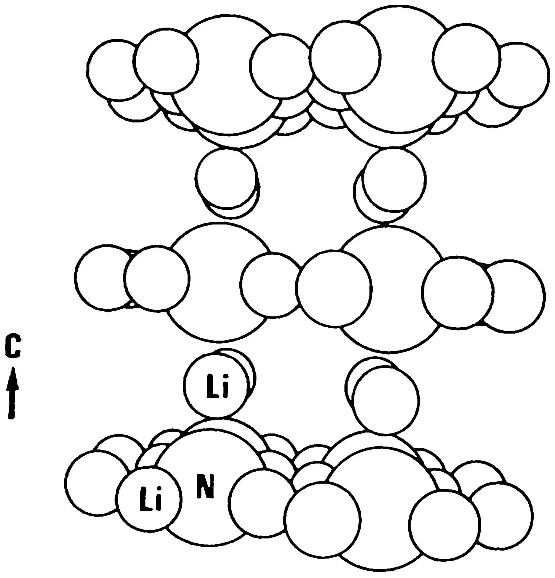

Figure 1.12 Crystal Structure of Li_3N

1.9.3 Polymer Electrolytes

Polymer electrolytes are broadly defined as ionically conducting solid phases formed by the dissolution of salts in ion-coordinating macromolecules.[66] A more precise definition implies that the macromolecules are also free from low molecular-weight additives or contaminants.

The majority of the research on polymer electrolytes has been directed at improving the conductivity, or ion transport properties, and the mechanical properties of these solvent free solid materials, in an attempt to realise their potential in high energy density lithium batteries and other applications. To date the most promising model which describes this ionic motion has been presented in the context of a percolation-type of ion transport mechanism for the amorphous regions of polymer electrolyte materials.[24,67]

1.9.3.1 Polymer Electrolyte Composition

Lithium ion-conducting polymer electrolytes are generally composed of three parts:

- a polymer host (backbone) which promotes lithium ion transport
- counter-ions, these are lithium-solvating groups (polar solvents)
- a lithium ion source, which is usually introduced as a salt (solute) into the polymer matrix. (Polymers can also be fabricated to conduct a wide range of other ions, such as, copper and calcium ions.)[68,69]

In a polymer electrolyte, the motion of the polymer host is responsible for ion mobility; the ions move only if polymer segments also undergo fairly large amplitude excursions.[70] In other words, a flexible polymer can undergo re-orientation of the local co-ordination geometry, to achieve effective solvation. Vincent,[71] has proposed three essential characteristics for a polymer, or the active part of a copolymer, to be a successful host, namely:

- Barriers to bond rotation are low, so that segmental motion of the polymer chain can readily take place
- Atoms or groups which have sufficient electron-donor power to form coordinate bonds with cations
- An acceptable distance between coordinating centres.

Counter-ions are typically introduced into lithium ion-conducting polymer electrolytes, as the anion of the introduced salt. This often forms a bi-ion conductor, where both cation and anion are mobile charge carriers, and where the anion mobility has been shown to be prevalent. This gives rise to unwanted local concentration gradients, with deleterious effects on the power output of the device to which the material is applied. A technically more desirable development for designing electrolyte materials for lithium battery applications has been to bond the counter ion to the polymer backbone, thus immobilising the counter ion and forming a single ion conductor, a polyelectrolyte.

The specific definition of a polyelectrolyte is that the charged groups are chemically bonded to a polymer chain and the counter ions, solvated by water, are free to migrate in the aqueous medium which surrounds the polymer matrix. However, the broader and more commonly used definition, adopted by polymer electrolyte researchers, is that the non-conducting counter ion is bonded to the polymer backbone. Solvent-free polyelectrolytes, in the past, have generally been hard materials with low conductivities, such as sodium poly(styrenesulfonate) and poly(diallyldimethylammonium chloride), as demonstrated by Hardy.[72] These single ion conductors (polyelectrolytes) display increased conductivities when plasticised, and more recently, when fabricated with host polymers that have amorphous properties with low glass transition temperatures (T_g).[73,74]

The solubility of a salt is important if the salt is to be successfully incorporated into a polymer host. The solubility of a salt is determined by the lattice energy, and to a lesser extent, by the solvation of the cations. Some of the desirable properties of salts are:

- large electrochemical window (voltage range),
- formation of eutectic composition with host polymer, resulting in a lower melting point and/or decreasing T_g,
- salts that have non-coordination anions with extensive charge delocalisation (softness), that is, anions which have a low tendency to form tight ion pairs.

Table 1.9 lists some examples of polymer hosts and lithium salts commonly used in polymer electrolyte materials.

Table 1.9 Common Polymer Hosts and Lithium Salts

Host Polymer(Coordinating groups)	**Lithium Salt**
Oxa alkanes	$LiClO_4$
$- CH_2CH_2O -$	
$- CH(CH_3)CH_2O -$	$LiCF_3SO_3$
Aza alkanes	
$- CH_2CH_2NH -$	$LiAsF_6$
$- CH_2CH_2N(CH_3) -$	
Thia alkanes	$LiBF_4$
$- CH_2CH_2S -$	
Siloxane	$LiPF_6$
$- CH_3(H)SiO -$	
Esters	$Li(CF_3SO_2)_2N$
$- OCH_2CH_2OCOCH_2CH_2O -$	

1.9.3.2 Fabrication

Polymer electrolyte materials are formed by dissolving metal salts in ion-coordinating macromolecules. A wide variety of salts are soluble in ion coordinating macromolecules (pure polymers). These include salts based on alkali-metal, alkaline-earth-metal, transition metal and lanthanide ions.[75] However, the solubility of these salts is limited. The process often involves a solid to solid reaction, for the formation of a metal salt complex, (Equation 1.6).[76]

$$m\mathrm{MX} + (-\mathrm{RY}-)_n \rightarrow (\mathrm{MX})_m \cdot (-\mathrm{RY}-)_n \qquad \text{Equation 1.6}$$

Where MX and $(-\mathrm{RY}-)$ denote an alkali metal salt and a polymer repeat unit respectively. For reactions of this type (solid/solid), the kinetics are unfavourable, even when stable complexes are formed. There are two standard methods commonly used for accelerating the formation of metal salt complexes for the fabrication of polymer electrolyte materials.

The most commonly used is a "solvent casting" method. This involves dissolving or suspending known weights of both the salt and the host polymer in a common solvent (usually acetonitrile or methanol). The mixture is then stirred and cast into either a film, or bulk product. Afterwards the solvent is slowly removed by evaporation, vacuum, or heat treatment, to give a solvent-free polymer electrolyte.

The second method is to cryogrind appropriate mixtures of polymer and salt, followed by a modest heat treatment.[75] This is an all solid state method in which no solvent is used, which is an advantage as the purity of the solvent, especially acetonitrile, is critical in controlling the properties of the polymer product.[68] However, the method requires expensive equipment and skilled operators, hence it is not as popular as solvent casting.

Key requirements for polymeric electrolytes:

- Conductivity between 10^{-4} and 10^{-3} Scm^{-1} between -40 and 70 °C.
- Good dimensional and thermal stability in this temperature range
- Electrochemical stability window spanning potentials between 0 and 4.5V vs. Li/Li^+ couple.
- Chemical compatibility with both anode and cathode over entire temperature range.
- Ability to afford recharge at an efficiency of greater than 99%.

1.9.3.3 Classification

Many of the emerging electrolyte materials are either variations of polymer electrolytes or combinations of polymer electrolyte materials with conventional electrolyte materials, such as organic liquids or vitreous and glass electrolytes. Table 1.10 illustrates and summarises the classes of electrolytes. The table details some of the conventional electrolytes, polymer salt complexes and polymer hybrid materials as described in the literature. Examples of the class and the conductivity at 20-30 °C, are also given.

Table 1.10 Classification of Conventional and Polymeric Electrolyte Materials

Classification	**Example (electrolyte-composition)**	**Conductivity mScm^{-1}**	**Ref.**
Conventional Electrolyte Materials			
Liquid	1M $LiCF_3SO_3$/PC	1.75 (20 °C)	77
Ceramic	Li_3N, single crystal	0.30 (25 °C)	78
Vitreous	$0.36B_2S_3$-$0.64Li_2S$	0.11 (25 °C)	79
Polymer-Salt Complexes			
Polymer-salt complex	$(PEO)_6LiClO_4$	1.0×10^{-5} (30 °C)	80
comb-branched CP*	MEEP($LiCF_3SO_3$)	~10^{-1} (25 °C)	81
network structures			
chemical x-link	(PEO-M-iPht)/Styrene7/ 3$LiClO_4$	3.2×10^{-3} (25 °C)	82
radiation x-link	MEEP($LiCF_3SO_3$)	0.5 (20 °C)	83
polymer blends (alloys)	55w/oMEEP 45w/oPEO–Li $(LiCF_3SO_3)_{0.13}$	1×10^{-3} (20 °C)	84
Polymer Hybrids			
Gelled liquid electrolyte	PVC,PC,EC,$LiClO_4$ w/o ratio = 15/40/40/5	1.2 (20 °C)	85
Plasticised polymer electrolyte	PEO/PPO (mw 2000) +10%$LiClO_4$,20% BDDGE,50% PC	2 (25 °C)	86
Ceramic/polymer electrolyte	Li_3N + 8v/o $(PEO)_{12}$ ($LiCF_3SO_3$)	0.12 (30 °C)	87

* = Co-Polymer

1.10 The Anode

The anode in a primary lithium battery is typically lithium metal which has been prepared under very dry conditions (less than 2% humidity). Elemental lithium reacts with the known Li^+-ion electrolytes to form a passivating film on the lithium surface at the lithium-electrolyte interface. This passive layer ensures long shelf life for lithium cells, which is a desirable feature, and permits primary batteries to function adequately (for small power drain applications). The passive film also leads to the formation of dendrites in secondary batteries during discharge/recharge cycles. Eventually the dendrites grow across the gap that separates the two electrodes and make contact with the cathode, hence short-circuiting the cell.[16] A more recent development is to replace the lithium anode with a lithium intercalation electrode,[43] which overcomes many of the drawbacks associated with secondary lithium including dendrite formation.

Carbon intercalation anodes are one of the most extensively researched anode materials for application to lithium batteries.[88] However, transition metal oxides, chalcogenides, lithium alloys and polymers have also been considered. These are summarised in Table 1.11.[44]

Table 1.11 Potential Negative Electrode Material Characteristics

Anode Material	Molecular Weight	Density (kg/L)	Theoretical Specific Charge (Ah/kg)	Theoretical Charge Density (Ah/L)
Li Primary	6.94	0.53	3862	2047
Li_4 Secondary	27.76	0.53	965	511
LiC_6 Graphite	79.00	2.24	339	758
LiAl	33.92	1.75	790	1383
$Li_{21}Sn_5$	739.31	2.55	761	1941
$LiWO_2$	222.79	11.30	120	1356
$LiMoO_2$	134.88	6.06	199	1206
$LiTiS_2$	118.94	3.06	225	689

In practice, some actual capacity values are considerably less than the theoretical values. Metallic lithium has a cycling efficiency of ≤ 99%, so a four-fold excess of lithium, Li_4, is necessary to achieve a sufficient cycle life for use in secondary batteries. This means that its practical charge density is not considerably greater than its alternatives. However, the potential of the electrode materials is important because a higher potential vs. Li/Li^+ of the negative electrode results in a lower cell voltage.

1.10.1 Carbon

Carbon is the most commonly used negative electrode of commercial secondary lithium batteries. This is because it has higher specific charges and more negative redox potentials than most metal oxides, chalcogenides, and polymers. It also has good dimensional stability, which provides better cycling performance than Li alloys.

The insertion of lithium into carbon, known commonly as intercalation, proceeds according to the following equation:

$$Li_xC_n \leftrightarrows Li^+ + xe^+ + C_n \qquad \text{Equation 1.7}$$

As electrochemical reduction of the carbon host proceeds, lithium ions penetrate into the carbon forming the intercalation compound Li_xC. This reaction is reversible.

The quantity of sites capable of lithium accommodation strongly depends on the crystallinity, the microstructure and the morphology of the carbonaceous material.[89,90,91,92]

The electrochemical intercalation reaction current/potential and the risk of solvent co-intercalation are determined by the type of carbon used. There are hundreds of different types of carbons that have been synthesised by pyrolysis of various precursors, with many exotic types tested including fullerenes. Some of these have a relatively high specific charge.

Carbons that can be reversibly intercalated are roughly divided into two groups, graphitic and non-graphitic.

1.10.1.1 Graphitic Carbons

Graphitic carbons are materials with a layered structure, typically with a number of defects. Normally, the term graphite is applied only to carbons that have the layered lattice structure with a perfect stacking order of graphene layers, either the prevalent AB (hexagonal graphite, Figure 1.13)[44] or the less common ABC (rhombohedral graphite). The AB and ABC graphites may transform into each other, making it difficult to achieve a perfect stacking order. Hence the term "graphite" is used regardless.

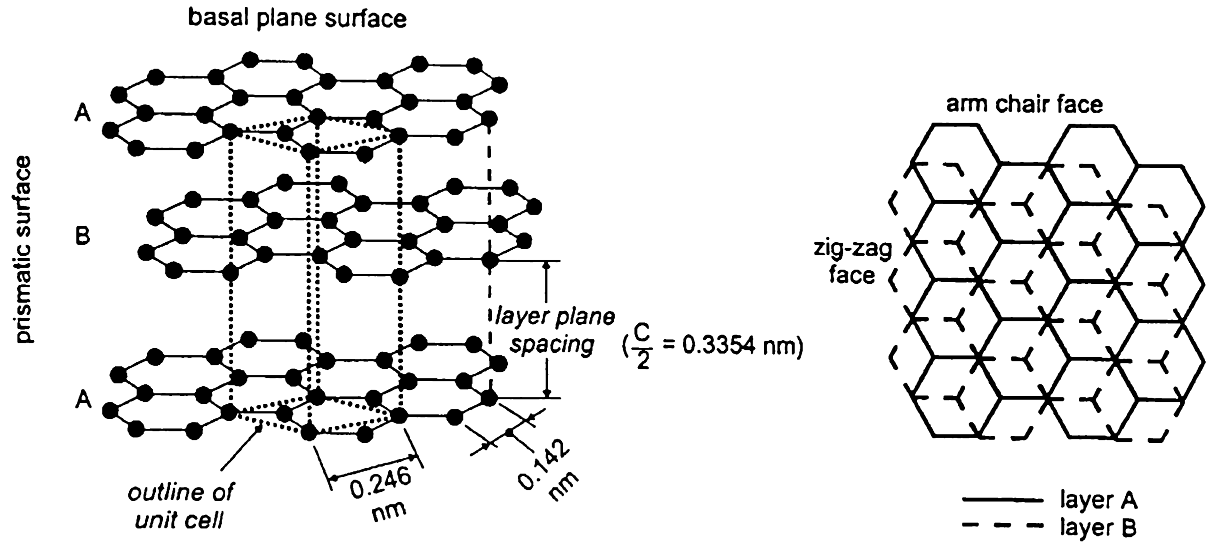

Figure 1.13 Crystal Structure of Hexagonal Graphite

Materials consisting of aggregates of graphite crystallites are also named graphites Some examples include natural graphite, artificial graphite and pyrolitic graphite, which are commonly used even though these materials are polycrystalline.[93]

At ambient temperature and pressure, graphitic carbon can reversibly intercalate a maximum of one lithium guest atom per six carbon host atoms. The intercalation reaction occurs only at prismatic surfaces (arm chair and zig-zag faces) as through the basal planes, intercalation is only possible at defect sites.[94] During intercalation, the graphene layer stacking order shifts to AA, which means that two neighbouring graphene layers in LiC_6 directly face each other. As lithium intercalation proceeds, there is an interlayer expansion of up to 10.3%.[95] The lithium is distributed in-plane in such a manner that it avoids occupation of nearest neighbour sites, (Figure 1.14).

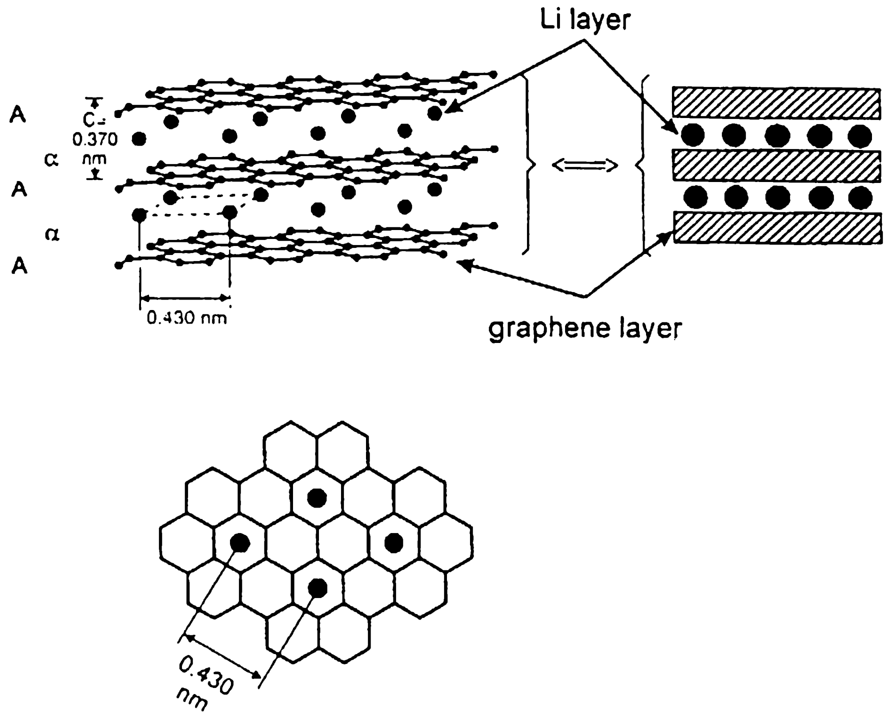

Figure 1.14 Crystal Structure of LiC_6

Theoretically, Li^+ intercalation into carbons is fully reversible. In practice however, the charge consumed in the first cycle notably exceeds the theoretical specific charge for the first stage LiC_6 of 372Ah/kg. The subsequent deintercalation of Li^+ recovers only about 80 – 95% of this charge. In subsequent cycles, charge recovery is closer to 100%. The excess consumed in the first charge is generally ascribed to a solid electrolyte interface (SEI) formation.[96] Similar to metallic lithium and lithium rich alloys, lithium/carbon intercalation alloys are thermodynamically unstable in all known aprotic electrolytes. Therefore, the surfaces exposed to the electrolyte have to be protected kinetically by SEI films.

Unlike the spontaneous film formation on metallic lithium, the film formation on Li_xC_6 surfaces takes place upon contact with the electrolyte as a charge-consuming side reaction in the first few Li^+ intercalation/deintercalation cycles, especially during the first reduction of the carbon host material. Irreversible consumption of both the lithium and electrolyte results in a "irreversible specific charge" loss. This is detrimental to cell performance, especially because the source of lithium in a Li ion cell is from the cathode.

1.10.1.2 Non-graphitic Carbons

These types of materials consist of carbon atoms that are mainly arranged in a planar hexagonal network, but without extensive crystallographic order in the *c*-direction. Amorphous areas embed in and crosslink with more graphitic areas (Figure 1.15). The precursor materials used and the manufacturing temperature determine the number and size of these areas, and therefore material's properties.

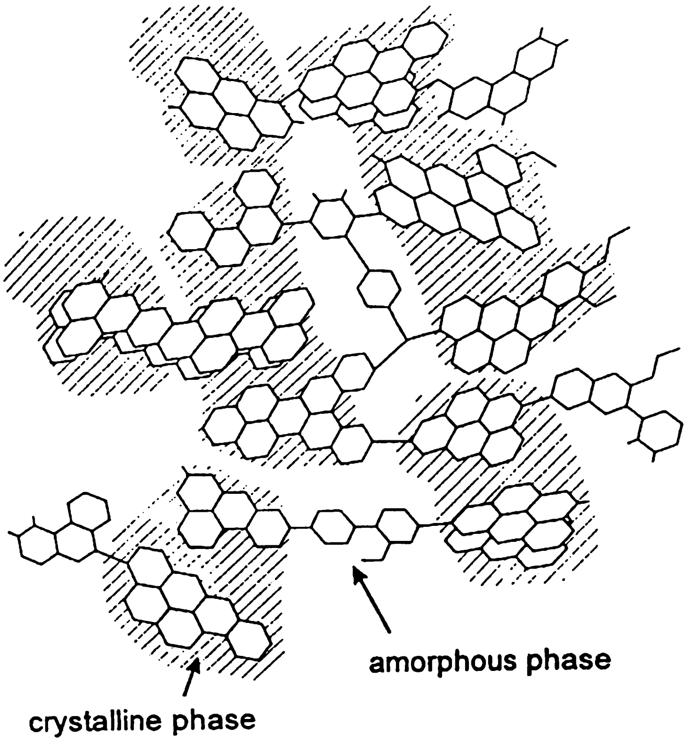

Figure 1.15 Non-graphitic Disordered Carbon

Non-graphitic carbons are mainly prepared by pyrolysis of organic polymer or hydrocarbon precursors at temperatures around 1500 °C. Heat treatments of up to 3000 °C reveal differences between ordered (graphitic) and disordered (non-graphitic) carbons. Graphitising carbons develop the graphite structure continuously during the heating process, as cross-linking between carbon layers is weak, and therefore the layers are mobile. Non-graphitic carbons show no graphitic structure development even at high temperatures, as the carbon layers are immobilised by cross-linking.[97]

For use in lithium intercalation, non-graphitic carbons can be classified by their capability of reversible lithium storage.[44] *High specific charge* carbons can store more lithium than graphite (x >1 in Li_xC_6). *Low specific charge* carbons are carbonaceous materials that can incorporate considerably less lithium than graphite.

Currently, much attention is being paid to the development of high specific charge carbons. These materials are synthesised at relatively low temperatures (500 – 1000 °C) and show a range of reversible charge from 400 to 2000 Ah/kg (with x = 1.2 – 5 in Li_xC_6), depending on heat treatment temperature, organic precursor and electrolyte used. This higher specific charge requires a larger volume of carbon matrix to hold the lithium, which means that although the specific charge in Ah/kg is greater than graphite, the charge density in Ah/L is similar.

1.10.2 Lithium Alloys

Requirements for Li Alloy anodes include:

- Intermetallic phases with high capacity over 0 – 1.2V vs. Li/Li^+ couple for reversible intercalation or insertion/extraction.
- Performance of > 500 mAh/g over 0 – 1.2V vs. Li/Li^+ couple.
- Less than 10% capacity loss of Li ion cells over 200 charge/discharge cycles.

Dey was the first to demonstrate the feasibility of electrochemical formation of lithium alloys in liquid electrolytes.[98] The equation usually proceeds reversibly according to the following equation:

$$Li_xM \leftrightarrows x\text{Li} + xe^- + \text{M} \qquad \text{Equation 1.8}$$

Alloys are formed at ambient temperature by polarising the metal M sufficiently negatively in a Li^+ containing electrolyte. Al, Si, Sn, Pb, In, Bi, Sb and Ag are all matrix metals that form Li alloys electrochemically.[89,99,100] Aluminium is the most frequently studied matrix metal that is alloyed with lithium. In general, the matrix metals undergo major structural changes while alloying with lithium. In the case of aluminium, the alloying occurs with successive phase formations: an α-phase up to about 7% Li in LiAl; a β-phase (non-stoichiometric) between about 47 to 56% Li in LiAl; and several lithium rich phases.[100,101,102] The LiAl frequently used as an insertion electrode is therefore a mixture of α-phase and β-phase. During discharge, some Li remains in the Al (i.e. the α-phase is kept) and only the β-phase is cycled so that the Li_xAl is cycled within the stoichiometric range of $0.1 < x < 1$, or approximately 50% of the Li.

The composite $(Li^+Al^-)_xAl^0$ is formed when the matrix metal accepts negative charges during the insertion of Li^+ cations. The Al^- ions formed by the charge transfer reaction $Al^0 + e^- \Leftrightarrow Al^-$ are significantly larger than neutral Al^0 atoms. Therefore, there is a large volume change associated with the cycling of LiAl and other Li-alloy electrodes.[89]

Lithium alloys Li_xM are highly ionic and therefore usually brittle. Mechanical stresses related to volume changes induce a rapid decay in mechanical properties and degradation of the electrode due to particle cracking. The charge densities of Li alloys are high. In lithium rich phases Li^+ mobility at room temperature with good current densities can be achieved for charging and discharging.[103] There have many attempts to improve the dimensional stability of alloy electrodes during cycling by manipulating grain size, shape, texture and orientation. One method for avoiding mechanical degradation is the use of thin layers of alloys with nano-size particles. In such materials, the volume changes do not cause particle cracking, as the absolute changes in particle dimensions are small.[104,105]

1.10.3 Transition Metal Oxides, Chalcogenides and Polymers

Early Li^+ ion transfer systems used negative electrodes containing transition metal oxides or chalcogenides with low redox potentials, including MoO_2, WO_2 and TiS_2.[106] These materials show comparatively low specific charges (Table 1.11). If combined with an oxidic positive electrode, they result in a low cell voltage of about 1.5 – 2.0 V. This low voltage makes them relatively safe, even for use with aqueous electrolytes. These may provide batteries which are useful in special applications.

Lithium ion-inserting polymers such as polyacetylene, polythiophene or poly(*p*-phenylene) have also been suggested as negative electrodes, but they have moderate specific charge and poor stability.[107]

1.11 The Cathode

Insertion compounds have been successfully and extensively applied as cathodes in many primary and secondary power storage systems.

1.11.1 Design Criteria

Selection of a cathode material is subject to the following engineering constraints:[108]

- Reversible insertion/extraction of Li^+ ions from/into the material over a large solid solution range. Rechargeable batteries require reversibility, and a large capacity requires a large solid solution range. Accommodation of lithium can result in a two (or more) phase compositional range, which is acceptable as long as the insertion/extraction reaction remains topotactic.
- The electrode and electrolyte must remain chemically stable. In order to achieve a long shelf life, thermodynamic stability against oxidation of the electrolyte in the charged state and disproportionation of the host in the discharged state are necessary.
- Large energy storage per gram, and per unit volume. The available energy stored per formula unit in a cathode material is:

$$E_{Store} = e_0 \sum_{x_1}^{x_2} V_{oc}(x) dx \qquad \text{Equation 1.9}$$

- Where $x_2 - x_1$ is the number of lithium atoms that can be inserted per formula unit in a discharge/charge cycle. As well as a minimum weight and volume of the host molecular formula, it is desirable to optimise $V_{oc}(x_1)$ with constraint 2 by placing the Fermi energy of the charged host, $x = x_1$, close to, but above the HOMO of the electrolyte.

- A nearly flat $V_{oc}(x)$ over the solid solution range $x_2 - x_1$. A constant V_{oc} vs. x is desired to obtain a nearly constant power output during discharge.
- A high bulk Li^+ ion conductivity and electronic conductivity. High electrode conductivities lower the internal resistance of the battery, hence the voltage drops with increasing current density, and they also reduce reversible capacity loss at higher current densities. Reversible capacity loss occurs where there is a frontal area between lithium rich and lithium poor regions within the cathode as the lithium ions diffuse from the surface to the centre of a particle.
- Low interfacial resistances for both electronic and ionic transport. Interfacial resistances introduce an initial drop in the voltage-current polarisation curve, and this drop is generally greater when there is a two-phase interface.
- Inexpensive, non-toxic host materials that are easily fabricated.

Structure, chemical stability and the availability of a redox couple at a suitable energy are the primary considerations in the design of a cathode material. Ideally, the host structure provides an interconnected interstitial space, containing as many energetically equivalent interstitial sites of the guest Li^+ ion as there are host transition metal ions to be reduced and a low energy barrier separating these sites.

Three structural classes of cathode materials can be distinguished: tunnel structures, which confine Li^+ ion motion to one dimension; layered structures with two-dimensional Li^+ ion motion; and framework structures with three-dimensional Li^+ ion motion. Both layered and framework structures find applications as cathode materials. However tunnel structures are utilised less often as they are easily blocked and are limited by insufficient interstitial sites.

The simplest structures contain a close packed anion array with a single transition metal atom M occupying half the octahedral sites in am ordered array. They are the layered $Li_{1-x}MO_2$ or Li_xTiS_2 and the spinel framework $Li_x[M_2]X_4$, X = O or S. The layered compounds contain an interstitial array of edge-shared octahedral sites and a degree of freedom along the *c*-axis can allow for a lowering of the potential energy barrier between the sites. The spinel framework also contains an interstitial array of edge shared octahedral sites, but the structure has strong 3D bonding. Two face-sharing tetrahedral sites 8a may compete for the Li^+ ions, and there are only half as many 8a sites as interstitial 16c octahedral sites or 16d M occupied sites. Preferential occupancy of 8a sites in the range of $0.5 < x < 1$ of $Li_x[M_x]O_4$ limits the practical capacity of oxospinel hosts.

More complex layered and framework structures have also been explored; they can offer greater free volume for the Li^+ ions, but at the expense of volumetric energy density. The use of $(XO_4)^{n-}$ polyanions in place of O^{2-} ions has permitted study of the influence of a counter cation as well as structure on a particular transition metal redox energy, but at the expense of some capacity. When X = P is of particular interest to the topic of this thesis.

By far the largest numbers of positive electrode materials being discussed are inorganic transition metal oxides or sulfides. Some of these are listed in Table 1.12. Their specific charges are based on a reversible range Δx of the lithium content during the charging/discharging process shown in Equation 1.10.

Generally, positive electrode materials that contain no lithium after their synthesis are in the charged state, (although this is not always true). They must be combined with negative electrodes that serve as a lithium source in the first discharge cycle. These non-lithiated positive electroactive materials usually electrochemically insert lithium at potentials less than 3 V vs. Li/Li^+. In the lithiated state they are usually not stable to air and moisture. In contrast, there are various lithium containing materials that could serve as a lithium source in electrochemical cells. They must be charged (extraction of lithium) in a first formation cycle. These lithium containing materials are typically stable to air and moisture, and electrochemically de-insert lithium in the 4 V potential region.[44,109]

$$\Delta x\, Li^+ + \Delta x\, e^- + Li_xMX \leftrightarrows Li_{x+\Delta x}MX \qquad \text{Equation 1.10}$$

Table 1.12 Potential Positive Electrode Materials Characteristics

Cathode	Molecular Weight	Density kg/L	Reversible Range Δx	Theoretical Specific Charge Ah/kg	Theoretical Charge Density Ah/L
Charged					
TiS_2	112.01	3.27	1	239	782
MoS_2	160.06	5.06	0.8	134	678
V_2O_5	181.88	5.36	1	147	495
V_6O_{13}	513.64	3.91	3.6	188	734
MnO_2	86.94	5.03	0.5	1[illegible]4	775
$NbSe_3$	329.81	8.7	3	244	2121
Discharged					
$LiCoO_2$	97.87	5.16	0.5	137	706
$LiNiO_2$	97.63	4.78	0.7	192	919
$LiMn_2O_4$	180.82	4.28	1	148	634

1.11.2 One Dimensional Hosts

The two interesting materials in this class are the trichalcogenides TiS_3 and $NbSe_3$. The crystal structures of these materials are quite similar, consisting of chains of face-sharing trigonal prismatic MX_6 units.[109,110,111] Both compounds insert three lithiums per formula unit into their one dimensional structures either electrochemically or chemically (e.g. using butyl-lithium as a lithiation agent).

For TiS_3, the electrochemical insertion of the first two lithium leads to the reduction of the disulfide to isolated sulphide ions. It is not reversible, due to a rearrangement of TiS_6 groups from a trigonal prism to a more favoured octahedron, thereby forming one-dimensional chains for lithium incorporation. Although insertion of the third lithium is reversible, large capacity fading occurs with cycling.

In contrast to TiS_3, the electrochemical lithiation of $NbSe_3$ is reversible and of a topotactic nature. This is because of the trigonal prismatic coordination of niobium is more stable than the octahedral coordination and no conversion is involved.[112] Lithium-free $NbSe_3$ and lithiated $LiNbSe_3$ both show metallic conductivity, allowing fabrication of electrodes without additional carbon additives. The first discharge proceeds in two distinct steps: the flat plateau region at about 1.6V vs. Li/Li$^+$ corresponds to the insertion of two lithium ions per one $NbSe_3$. The third Li$^+$ is inserted down to 1.0V, and with subsequent cycling, structural changes occur so that repeated discharges occur at higher potentials with a average potential of about 1.8V. There is limited interest in $NbSe_3$ due to its toxicity, high cost and relatively low potential.[109,112]

1.11.3 Two Dimensional Hosts

Layered type dichalcogenides of the transition metals Ti, Nb, Ta, Mo, and W, as well as the dioxides of the transition metals V, Cr, Fe, Co, and Ni, are of interest as positive insertion electrode materials.

1.11.3.1 Layered Type Transition Metal Dichalcogenides

The sulphides MS_2 form close-packed S-M-S layers of edge-shared octahedra that are held together by van der Waals forces between the sulphide ions of neighbouring layers. The crystal structures of various polymorphs are shown in Figure 1.16.[113]

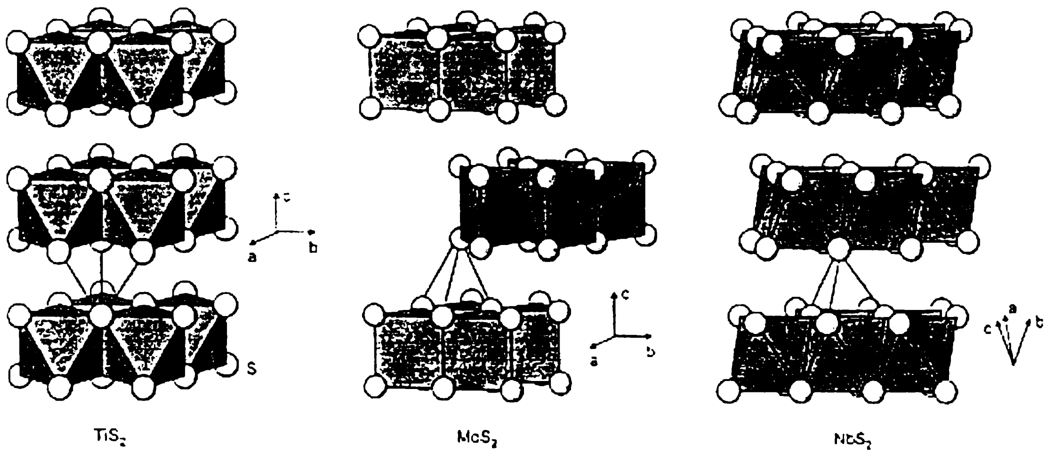

Figure 1.16 Crystal Structure of TiS_2, MoS_2 and NbS_2

During the intercalation of lithium, a complete charge transfer occurs that involves the reduction of M^{4+} to M^{3+} and the diffusion of Li$^+$ into the van der Waals gaps, resulting in the expansion of the host structure along the crystallographic *c*-direction. The van der Waals forces between the layers are thereby replaced by coulombic interactions. In all the polymorphs, octahedral and tetrahedral interstitial sites are available for the intercalation of lithium ions. Generally, the octahedral sites are favoured, resulting in a maximum possible intercalation of one lithium atom per formula unit.

Out of these polymorphs, TiS_2 in particular best satisfies the criteria for an electrode, with an average discharge voltage of 2.1V. Almost 100% TiS_2 utilisation results in a specific energy of about 450Wh/kg in a rechargeable cell with a lithium metal anode. The small energy gap of TiS_2 limits the V_{oc}, which leads to the consideration of oxides.

1.11.3.2 Layered Type Transition Metal Dioxides

The analogous MO_2 oxides crystallise in the rutile or fluorite structure. $LiMO_2$ oxides form layered oxides with Li^+ ions occupying the octahedral sites between close-packed O-M-O layers. The structure of the two dimensional lithium transition-metal oxides is shown in Figure 1.17.[44,114,115]

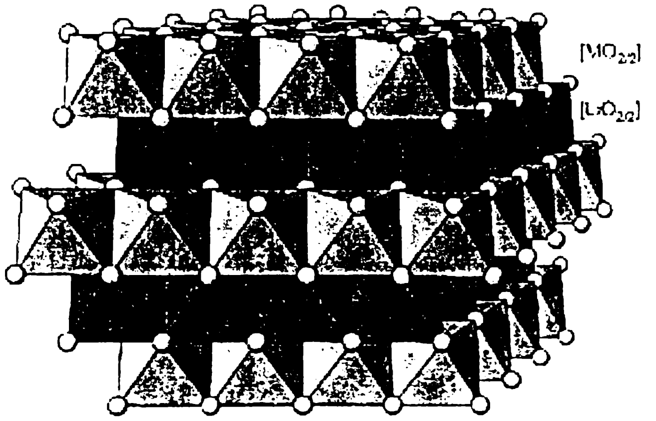

Figure 1.17 Crystal Structure of $LiMO_2$ (M = Ni, Co, V, Cr)

These materials are related to the α-$NaFeO_2$ type structure, and can be regarded as a distorted rock salt superstructure. In a cubic close-packed oxygen array, the lithium and transition-metal atoms are distributed in the octahedral interstitial sites in such a way that MO_2 layers are formed consisting of the edge-sharing MO_6 octahedral. In between these layers, lithium resides in octahedral LiO_6 coordination, leading to alternating (111) planes of the cubic rock salt structure. This ordering induces a slight distortion of the lattice to hexagonal symmetry. Complete extraction of the lithium ions results in the layered $CdCl_2$ structure type.

Out of these materials, $LiCoO_2$ has been researched since 1980[116] and has since been commercialised in a cell first by Sony.[32] The Li/Li_xCoO_2 cells exhibit very high voltages with OCV in the range from 3.9 to 4.7V for stoichiometries of $0.07 < x < 1$. With an average discharge of 3.9V, a high specific energy of 1070 Wh/kg is expected.

The isostructural $LiNiO_2$ is an attractive alternative to $LiCoO_2$ due to its lower cost and its slightly more negative (about 0.25V) redox potential, making it less prone to electrolyte oxidation problems.[117] There is an irreversible capacity in the first cycle, and a material with the composition $Li_{0.85}NiO_2$ is formed at the end of the first discharge. Lithium extraction from this material is reversible during subsequent cycles, with the reversible electrode reaction in the potential range from 2.5 to 4.1V.

$LiMnO_2$ crystallises in the thermodynamically stable orthorhombic space group *Pmmn*. Among layered oxides, this material would be the most attractive in terms of toxicity and cost. Its structure could be described as a modified rock-salt type with a distorted cubic close-packed oxygen anion array. The lithium and manganese cations occupy the octahedral interstitial sites in such a way that alternating zig-zag layers of edge sharing LiO_6 and MnO_6 octahedra are generated, as described in Figure 1.18.[118] The lithiation of δ'-MnO_2 with lithium iodide leads to $Li_{1.09}Mn_{0.91}O_2$ which has an excess of lithium in the manganese layers.[119] A layered $LiMnO_2$ with the α-$NaFeO_2$ structure has been prepared by substitution of Al, Cr or Ga into the lattice, and also a layered monoclinic $LiMnO_2$ has been prepared by an ion exchange process. There are various forms of lithium manganese oxides, but the performance of all of them suffers from limited cycling stability. The best of the various forms is that of monoclinic $LiMnO_2$ prepared by the ion-exchange reaction of $NaMnO_2$ in LiCl/*n*-hexanol. This material can electrochemically de-insert up to 0.95 Li^+ per formula unit, corresponding to 270 Ah/kg. In a potential range between 3.4V and 4.3V vs. Li/Li^+, a specific charge of about 200 Ah/kg is obtained, but only in the first few cycles and at low current rates.[120]

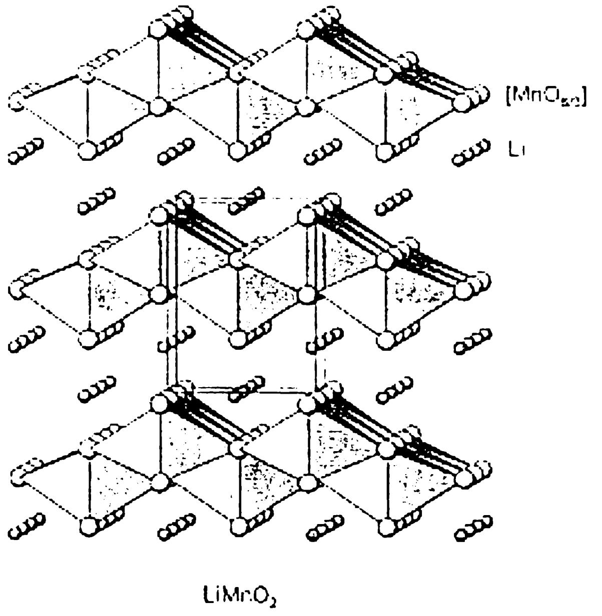

Figure 1.18 Crystal Structure of Orthorhombic LiMnO$_2$

1.11.4 Three Dimensional Hosts

Three dimensional framework structures have cross-linked channels allowing ion insertion. The size of the channels must be sufficiently large to accommodate the ions. They have the advantage of avoiding the co-insertion of bulky solvent molecules, and have a smaller degree of expansion/contraction on the framework upon lithium insertion/extraction.

1.11.4.1 LiMn$_2$O$_4$

Manganese oxides are amongst the most popular positive electrode materials in primary batteries due to their low cost, good charge density, high electronic conductivity and good electrode potential. In an attempt to find an inexpensive, non-toxic cathode, Thackeray et al. inserted lithium into Fe$_3$O$_4$. They realised that the [Fe$_2$]O$_4$ spinel framework of Figure 1.19 must remain intact. The Li$^+$ ions enter the empty 16c octahedral site of the spinel framework and displace the 8a tetrahedral site Fe^{3+} ions to these same 16c sites.[121] This led to the Li$_{1+x}$[Mn$_2$]O$_4$ system, and subsequently to the Li$_{1=x}$[Mn$_2$]O$_4$ system, as only lithium would occupy the interstitial space of the [Mn$_2$]O$_4$ spinel framework.[122,123] Hunter had previously shown that the leaching of Li^+ and Mn^{2+} from $Li_{1-x}[Mn_2]O_4$ in strong acid could be used to prepare a λ-MnO_2 structurally equivalent to $Li_\delta[Mn_2]O_4$ having the spinel framework.[124]

The electrochemical Li^+ extraction from the tetrahedral sites of $LiMn_2O_4$ is reversible and proceeds at about +4V vs. Li/Li^+. This process is represented by the peaks 2 and 3 in the typical cyclic voltammogram of $LiMn_2O_4$ (Figure 1.20).[44] The two-step indicates a phase transition at $Li_{0.5}Mn_2O_4$, which is due to an ordering of lithium on the tetrahedral 8a sites. During cycling in the 4V potential range the cubic symmetry of the structure is maintained. It is not possible, however, to extract all the lithium electrochemically at practical potentials and form λ-MnO_2. The cycling stability of $LiMn_2O_4$ is poor however, and this has limited its commercial application.

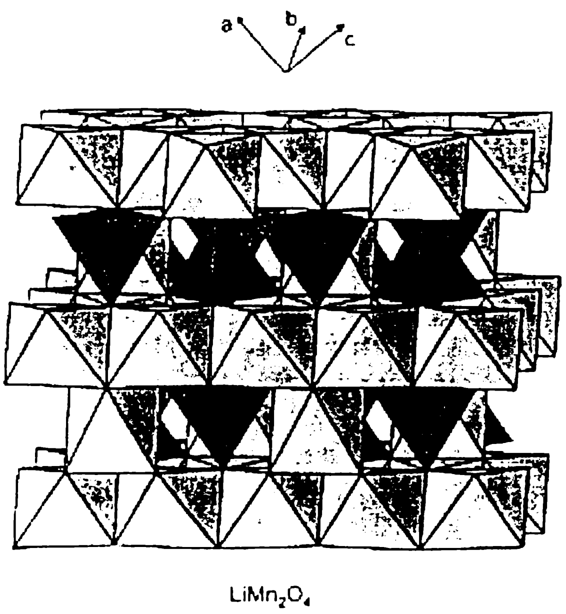

Figure 1.19 Three Dimensional Crystal Structure of $LiMn_2O_4$

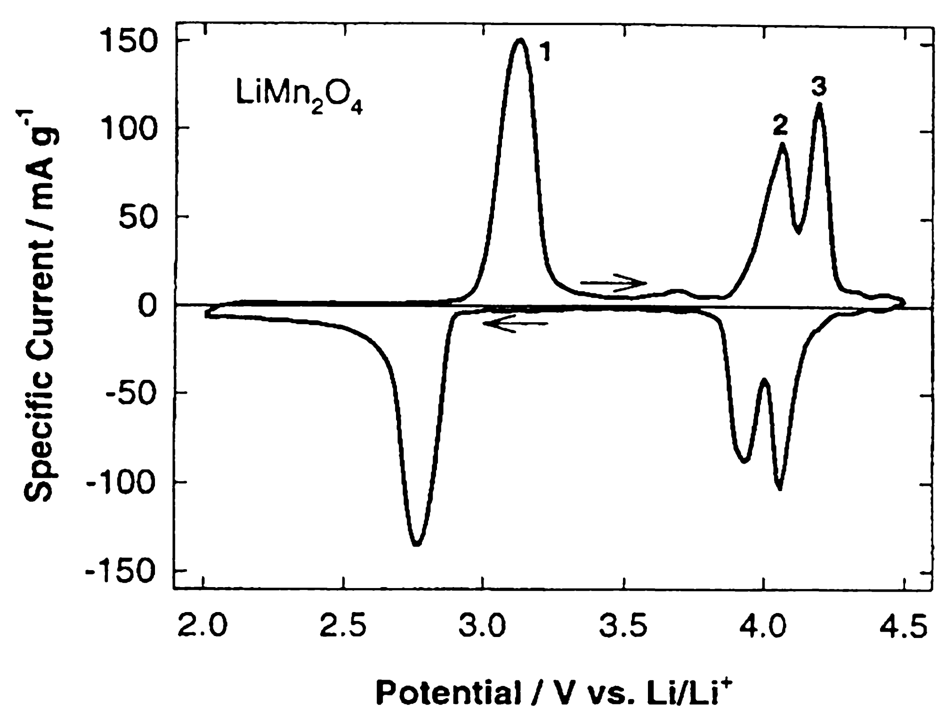

Figure 1.20 Cyclic Voltammogram of $LiMn_2O_4$

Long term cycling performance of the best $LiMn_2O_4$ materials to date, has resulted due to the introduction of a new electrolyte system compatible up to +5V vs. Li/Li$^+$.[125] Even these optimised cells have shown a slight capacity fading, which is attributed to the instability of the organic-based electrolyte at the very high voltages reached when charging the cells, although other fading mechanisms have been identified for cells in both the charge and discharge state. Efforts to address this include: replacing some manganese in $LiMn_2O_4$ with mono or multivalent cations; doping the oxide with additional oxygen; or by substitution of the Jahn-Teller ion Mn^{3+} by other trivalent cations such as Al^{3+}, Fe^{3+}, Ni^{3+}, Co^{3+} or Cr^{3+}.

1.11.4.2 Vanadium Oxides

The vanadium oxides V_2O_5 and V_6O_{13} have gained significance as rechargeable 3 V electrode materials. Their structure is presented in Figure 1.21.[126,127] The best results from a V_2O_5 material are shown by the ω-$Li_xV_2O_5$ phase, which can de-insert almost all of its lithium, obtaining a specific energy of up to 900 Wh/kg. For a ω-$Li_xV_2O_5$/Li cell in a voltage range between 3.4 and 1.9V, 100 cycles with a specific energy of more than 450 Wh/kg have been demonstrated.[128] As well as crystalline V_2O_5, good results have been reported for V_2O_5 glasses with P_2O_5[129] or other network formers, V_2O_5 xerogels[130] and V_2O_5 aerogels.[131] These amorphous or low crystalline materials offer considerable advantages due to their morphology. They have a large electrochemically active surface area, small particle size and low density providing high overall diffusion coefficients and low volume expansion during lithium insertion. However these materials have problems with long term cycling stability.

Stoichiometric V_6O_{13} was first reported as a positive electrode material by Murphy et al.[132] and can chemically insert up to eight Li^+ ions per formula unit using butyl-lithium. Even more lithium can be inserted into non-stoichiometric V_6O_{13+z}. However, only up to six Li^+ ions can be inserted electrochemically into V_6O_{13}. Problems with this material include a relatively high lattice expansion of around 15%, a high electronic resistivity of lithiated V_6O_{13} and a capacity loss during cycling.[133,134]

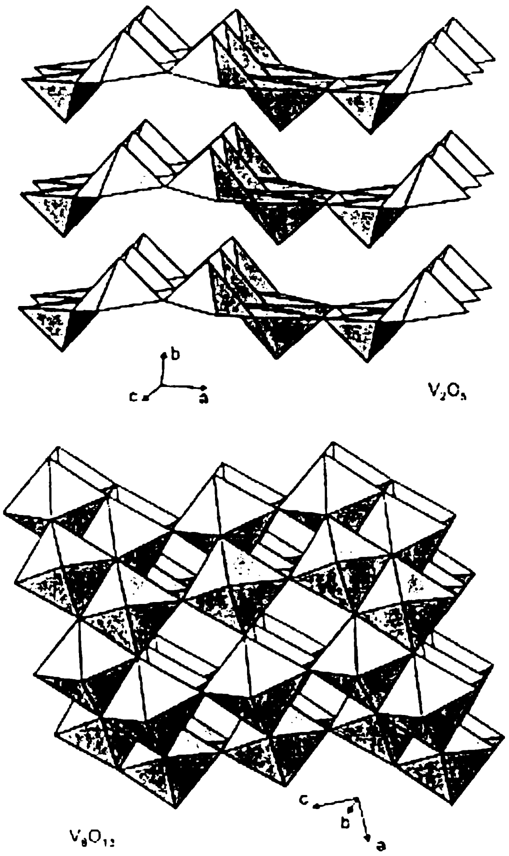

Figure 1.21 The Crystal Structures of V_2O_5 and V_6O_{13}.

1.11.4.3 Polyanions

The NASICON (sodium-super-ion-conductor) family of materials has been shown by Goodenough et al. to be good candidates as solid electrolyte materials in high energy density batteries. Considerable work has been done in improving the ionic conductivity of these materials and to the understanding of the diffusion mechanism.[135]

The NASICON family of materials is a family of compounds with $M_2(XO_4)_3$ frameworks made up of XO_4 tetrahedra sharing corners with MO_6 octahedra and vice versa. The $M_2(XO_4)_3$ framework is chemically versatile; it can be stabilised with a variety of transition metal cations M and XO_4 polyanions. These framework oxides are known to undergo topotactic insertion/extraction of a mobile atom,[136,137,138] and are therefore also potential candidates as electrode materials for lithium secondary batteries. The open structure of $M_2(XO_4)_3$, (Figure 1.22) supports fast Li^+ or Na^+ ion conduction and accepts up to five Li^+ ions per formula unit in the interstitial space.[139]

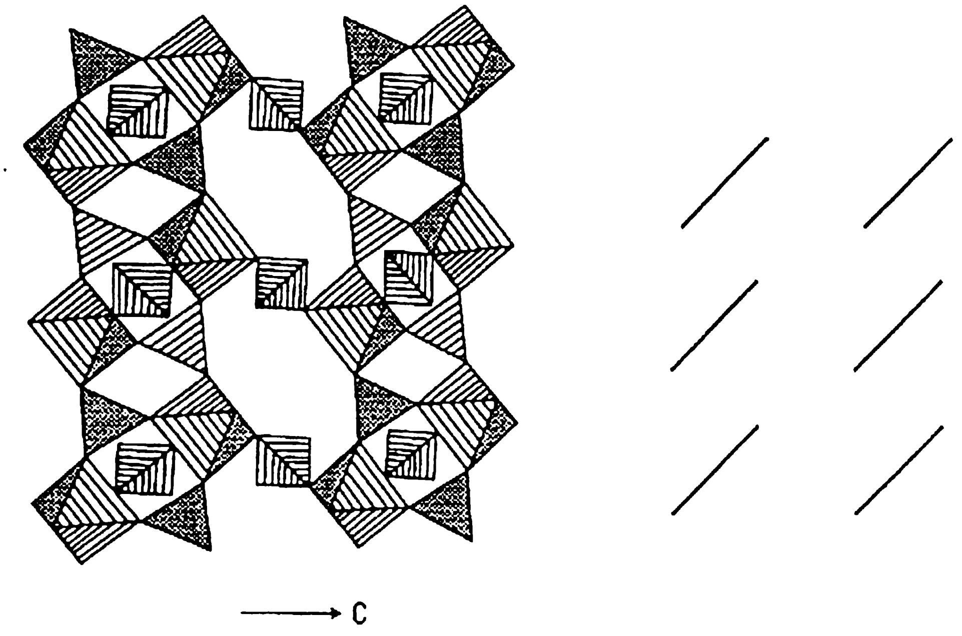

Figure 1.22 Rhombohedral NASICON $M_2(XO_4)_3$ Structure

Lithium can be inserted into the NASICON host either chemically or electrochemically provided the atom present in the structure is reducible by elemental lithium. This becomes attractive if the framework structures are built using polyanions comprising less expensive, and less toxic transition metals. The $M_2(XO_4)_3$ (M = Ti, Fe, Nb, V, and X = P, S, As, Mo, W) compounds having the NASICON framework allow a high mobility for Li^+ ions even with smaller transition metal atoms M.[139] The larger size of the polyanions provides a larger free volume for the three dimensional motion of the guest species Li^+.[140,141]

Initial experiments with $Li_xFe_2(SO_4)_3$ Manthiram et al.[142] showed that the strong polarisation of the oxide ions toward the S atom stabilises the Fe^{3+}/Fe^{2+} couple to 3.6 eV below the Fermi energy of lithium. This prompted a mapping of the redox energies for different first-row transition-metal elements, and also a comparison of these redox energies for $(PO_4)^{3-}$ and $(SO_4)^{2-}$ polyanions in isostructural hosts.[143,140] H_2SO_4 is a stronger acid than H_3PO_4 so a greater stabilisation can be expected with $(SO_4)^{2-}$ as compared with $(PO_4)^{3-}$ ions.

In the hexagonal $M_2(XO_4)_3$ hosts, the redox energies of the various M cations are nearly independent of the Li^+ ion concentration and distribution over the two types of interstitial sites. It was found that the relative positions of the redox potentials remain the same upon exchanging $(PO_4)^{3-}$ for $(SO_4)^{2-}$; however, the V_{oc} of a phosphate is reduced by 0.8 eV relative to its value in a sulphate, which is consistent with the stronger Bronsted acidity of sulphuric vs. phosphoric acid.[141] Furthermore, it was found that by anionic substitution of one $(PO_4)^{3-}$ for a $(SO_4)^{2-}$ per formula unit, the hexagonal structure for all x in $Li_{1+x}Fe(SO_4)_2(PO_4)$ is preserved with a sacrifice of about 0.3 eV in the V_{oc}, or about 1/3 of the 0.8 eV found between $Li_xFe_2(SO_4)_3$ and $Li_{3+x}Fe_2(PO_4)_3$. A summary of the redox couples is found in Figure 1.23.[141]

This difference in the position of the redox couples has been ascribed to the difference in the strength of the covalent bonds of the polyanion. The counter-cation that shares a common oxygen nearest neighbour with Fe in an Fe-O-X linkage determines the strength of the Fe-O co-valency via the inductive effect. The stronger the X-O bonding in the polyanion, the weaker the Fe-O bonding, and hence a higher OCV. [1,144]

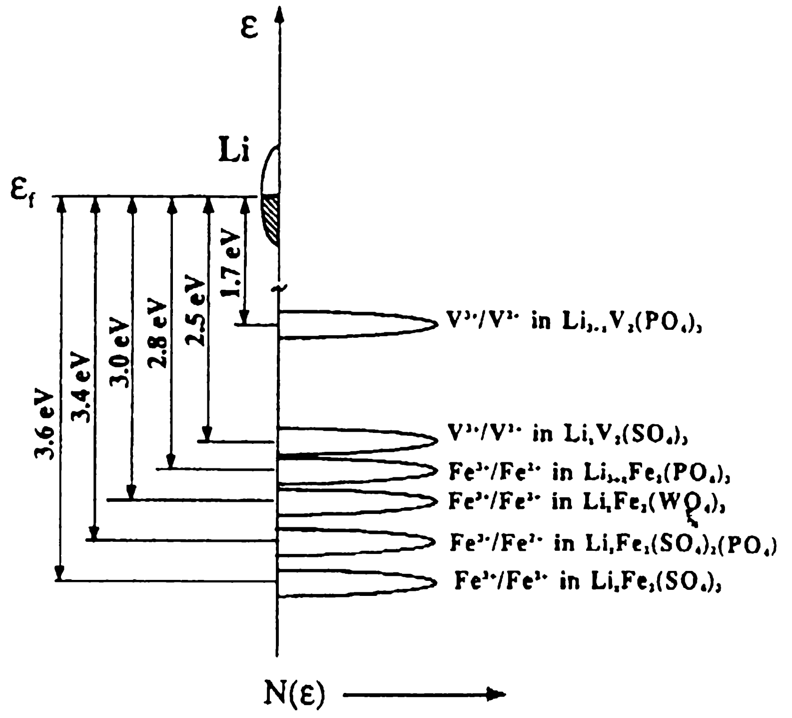

Figure 1.23 Relative Energies of Redox Couples

1.12 Aims

The topic of this thesis is the development of potential cathode materials based on two structures; the NASICON related systems of orthorhombic titanium doped $Li_{3-2x}Fe_{2-2x}Ti_{2x}(PO_4)_3$, and titanium doped $Li_{3-2x}V_{2-2x}Ti_{2x}(PO_4)_3$; and the olivine related structures of doped $LiNiPO_4$ and $LiCoPO_4$

The iron-related compound of the NASICON materials has been extensively evaluated for use as cathodes in lithium batteries previously, as discussed in section 1.11.4.3. At the time of this research, little work had been done on the Raman characterisation of $Li_{3-2x}Fe_{2-2x}Ti_{2x}(PO_4)_3$, and $Li_{3-2x}V_{2-2x}Ti_{2x}(PO_4)_3$ or the ionic conductivity and electrochemical performance of these materials to determine their suitability as either a solid-state electrolyte or a solid-state electrode. There has been considerable research done on related materials where Fe[145] is substituted by Zr,[146] Ge, Sn, Hf,[147] Cr,[148] Sc[149,150] and In.[151,152] These materials are usually either the monoclinic or the stabilised orthorhombic forms. Research on the electrochemical data of the vanadium analogue and a Zr doped orthorhombic form has previously been published.[153,154]

$LiNiPO_4$ and $LiCoPO_4$ are essentially isostructural with $LiMnPO_4$[155] of the type *AB*PO_4 where *A* and *B* are mono and divalent cations respectively. The cations have a hexagonal closed packed oxygen system with *A* and *B* in half the octahedral sites and P in 1/8 of the tetrahedral sites.

Recently, Goodenough[156] suggested that some lithium metal phosphates showed a high cell voltage in lithium metal anode couples by theoretical calculations. $LiNiPO_4$ is an orthorhombic olivine-related material, with P*nma* space group, where a = 10.0317, b = 5.8537, and c = 4.6768 Å at room temperature.[157] $LiCoPO_4$ has the same space group with a = 10.2001, b = 5.9199, and c = 4.690 Å at room temperature.[158] There is no published literature on the Raman spectra of $LiNiPO_4$, Ti-doped $LiNiPO_4$ $LiCoPO_4$ and Ti or V doped $LiCoPO_4$. This research examines the potential of $Li_{1-x}Ni_{1-x}Ti_xPO_4$ with ($0 \leq x \leq 0.2$), $Li_{1-x}Co_{1-x}V_xPO_4$ and solid-state materials as higher voltage cathodes.

Some research has been undertaken at the same time as this study by several researchers on the $LiMPO_4$ systems.[159,160,161,162,163,164] Results of their work are compared in this thesis. There are other structures that are relevant to the course of this work, including the related structure Li-$VOPO_4$ and its analogues.[165,166,167]

1.13 References

---

[1] J. R. MacCallum and C. A. Vincent, eds., *Polymer Electrolyte Reviews*, Parts 1 and 2, Elsevier, London, **1987.**

[2] C. A. Vincent, *Prog. Solid State Chem.*, 17, p145, **1987.**

[3] M. A. Ratner and D. F. Shriver, *Chem. Rev.*, p109, **1988.**

[4] M. Anderman, *Solid State Ionics*, 69, p336, **1994.**

[5] D. Woodruff, *Business Week*, p36, May 30, **1994.**

[6] W. R. Grove, *Philos. Mag.*, 14, pp127-30, **1839.**

[7] W. Nernst, *Z. Elektrochem.*, 6, pp41-43, **1899.**

[8] E. Bauer and H. Preis, *Z. Elektrochem.*, 43, 727-32, **1937.**

[9] M. Armand and M. Gauthier, "High Conductivity Solid Ionic Conductors", ed. T. Takahashi, *World Scientific*, Singapore, p114, **1989.**

[10] N. Q. Minh, "Ceramic Fuel Cells", *J. Am. Ceram. Soc.*, 76, (3), pp563-88, **1993.**

[11] B. B. Owens and P. M. Skarstad, *Solid State Ionics*, 53-56, p665, **1992.**

[12] Advanced Automotive Technologies, *Annual Report to Congress*, **1996.**

[13] R. A. Sutula, K. L. Heitner, S. A. Rogers, T. Q. Duong and P. G. Patil, "Electric and Hybrid Vehicle Storage R&D Programs of the U.S. Department of Energy", *in proceedings of the 15th International Electric Vehicle Symposium*, October, **1998.**

[14] C. A. Vincent, F. Bonino, M. Lazzari and B. Scrosati, "An introduction to electrochemical power sources", *Edward Arnold*, p9, **1984.**

[15] *New Zealand Electric Vehicle Association*, Newsletter, March-April, **1994.**

[16] J.B Goodenough, *Solid State Ionics*, 69, p185, **1994.**

[17] DeLuca et al., "Results of Advanced Battery Technology Evaluations For Electric Vehicle Applications", W. H. *SAE technical Paper Series,* 921572.

[18] T. R. Crompton, "Battery Reference Book", *Butterworth & Co. (Publishers) Ltd*, **1990.**

[19] P. Bruce, "Solid State Electrochemistry", *Cambridge University Press*, **1995.**

[20] M. Faraday. *Phil. Trans. of the R. Soc. Of Lond.*, Richard and John Taylor Eds., London, p90, **1838.**

[21] C. Tubandt, *Z. Anorg. Allg. Chem.*, 115, p105, **1921.**

[22] P.V. Wright, *Br. Polym. J.*, 7, p319, **1975.**

[23] M. B. Armand, J. M. Chabagno and M. Duclot, *Extended Abstracts, Second International Conference on Solid Electrolytes,* St Andrews, Scotland, **1978.**

---

[24] D. F. Shriver and G. C. Farrington, "Solid Ionic, These unusual materials applications in high-energy density", Special Report, *C&EN*, 42, **1985.**

[25] E. Warburg, *Ann. Physik Chem.*, 2, p622, **1884.**

[26] B. Henderson, "The Structures and Properties of Solids 1, Defects in Crystalline Solids", *Edward Arnold,* **1972.**

[27] T. A. Zawodzinki Jr., T. E. Sringer, F. Uribe and S. Gottesfeld, *Solid State Ionics*, 60, p199, **1993.**

[28] L. Boguslavsky, P. D. Hale, L. Gneg, T. A. Skotheim and H. Lee, *Solid State Ionics*, 60, p189, **1993.**

[29] C. B. McArdle, "Applied Photochromic Polymer Systems", *Blackie*, Chapman and Hall, New York, **1992.**

[30] C. G. Granqvist, *Solid State Ionics*, 60, p213, **1993.**

[31] B. Vuillemin and O. Bohnke, *Solid State Ionics*, 68, p257, **1994.**

[32] T. Naugaura, in *Proc. 5th International Seminar on Lithium Battery Technology and Applications*, Deerfield Beach, Fl, March, **1990.**

[33] S.D. Jones, J. R. Akridge and F. K. Shokoohi, *Solid State Ionics*, 69, p357, **1994.**

[34] J. C. Bailar Jr, T. Moeller, J. Kleinbergl, C. O. Guss, M. E. Castellion and C. Metz, "Chemistry", *Academic Press*, p670, **1978.**

[35] R. Jasinki, "High Energy Batteries", *Plenum Press*, New York, **1967.**

[36] A. V. Fraioly, W. A. Barber and A. M. Feldman, U.S. Patent no. 3,551,205, **1970.**

[37] H. Ikeda, T. Saito and H. Tamura *in Proceedings of the Manganese Dioxide Symposium*, Vol. 1, eds. A Kozawa and R. H. Brodd, I.C. Sample Office, Cleveland, OH, **1975.**

[38] M. Fukuda and T. Iijima, in *Power Sources*, Vol. 5, ed D. H. Collins, Academic Press, London, **1975.**

[39] J. Moser, U.S. Patent No. 3,660,163, **1972.**

[40] R. Selim and P. Bro, *J. Electro. Chem. Soc.*, 121, p1421, **1974.**

[41] E. S. Buzzelli, U. S. Patent no. 3,445,288, **1969.**

[42] M. S. Whittingham, *Science*, 192, p1126, **1976.**

[43] K. Brandt, *Solid State Ionics*, 69, p173, **1994.**

[44] M. Winter, J. Besenhard, M. Spahr and P. Novak, *Advanced Materials*, 10, p725, **1998.**

[45] P. Bruce, *Phil. Trans. R. Soc. Lond.*, A, p1577, **1996.**

---

[46] J. R. Dahn, A. K. Sleigh, Shi Hang, B. M. Way, W. J. Weydanz, J. N. Reimers, Q. Zhong, and U. von Sacken, *Lithium Batteries* ed. G. Pistoia, Elselvier, Amsterdam, p1, **1994.**

[47] T. R. Compton, "Battery Reference Book", *Butterworth & Co.Ltd.*, chp. 24, **1990.**

[48] W. Li and J. R. Dahn, *J. Electrochem. Soc.*, 142, p1742, **1995.**

[49] K. Ozawa, *Solid State Ionics*, 69, p212, **1994.**

[50] H. Dai and T. A. Zawodzinski, Jr., *J. Electrochem. Soc.*, 143, pL107, **1996.**

[51] V. R. Koch, *J. Power Sources*, 6, p357, **1981.**

[52] K. M. Abraham, *J. Power Sources*, 9, p239, **1983.**

[53] L. A. Dominey and J. L. Goldman, *Proc. 34th Int. Power Sources Symp.*, IEEE, Piscataway, New Jersey, p84, **1990.**

[54] D. Aurbach, Y. Malik, P. Dan and A. Meitav, *J. Electroanal. Chem.*, 282, p73, **1990.**

[55] G. Pistoia, *J. Electrochem. Soc.*, 118, p153, **1971.**

[56] Y. Matsuda, M. Morita, K. Yamada and K. Hirai, *J. Electrochem. Soc.*, 132, p2538, **1985.**

[57] J. Barthel and F. Feuerlein, *J. Physik. Chem.*, 148, p157, **1986.**

[58] M. Saloman, *Proc. 4th Int. Rechargeable Battery Sem.* eds. S. Wolsky and N. Marincic, Amsum Enterprises, Boca Raton, Florida, **1992.**

[59] L. Bretherick, *Chem. and Eng. News*, 68, p4, **1990.**

[60] L. A. Dominey, C. Nanjundiah, J. L. Goldman and V. R. Koch, *J. Electrochem. Soc.*, 135, p2914, **1988.**

[61] J. T. Dudley et al. *J. Power Sources*, 35, p59, **1991.**

[62] B. M. L. Rao, D. Eustace and D. Farcasiu, U. S. Patent no. 4,284,692, **1981.**

[63] D. Guyomard and J. M. Tarascon, U. S. Patent No. 5,192,269, **1993.**

[64] J. T. S. Irvine and A. R. West, "High Conductivity Solid Ionic Conductors", ed. T. Takahashi, World Scientific, Singapore, p201, **1989.**

[65] T. Lapp, S. Skaarup and A. Hooper, *Solid State Ionics*, 11, p97, **1983.**

[66] P.G. Bruce and C.A. Vincent, *Chem. Soc. Faraday Transactions*, 89, (17), p3187, **1993.**

[67] S. D. Druger, A. Nitzan and M. A. Ratner, *J. Chem. Phys.*, 79, p3133, **1983.**

[68] G. Petersen, L. M. Torell, S. Panero, B. Scrosati, C. J. da Silva and M. Smith, *Solid State Ionics*, 60, p55, **1993.**

[69] R. Frech and W. Huang, *Solid State Ionics*, 66, p103, **1993.**

[70] M.A. Ratner and D.F. Shriver, *Chem. Rev.*, p109, **1988.**

[71] C. A. Vincent, *Chemistry in Britain*, April, p391, **1989.**

---

[72] L. C. Hardy and D. F. Shriver, *Macromolecules*, 17, p975, **1984.**

[73] L. C. Hardy and D. F. Shriver, *J. Am. Chem. Soc.*, 107, p3823, **1985.**

[74] T. F. Yeh, H. Liu, Y. Okamoto, H. S. Lee and T. A. Skotheim, *2nd Int. Symp. on Polm. Elect.*, p83-89, **1990.**

[75] P. G. Bruce and C.A. Vincent, *Chem. Soc. Faraday Transactions*, 89, No 17, p3187, **1993.**

[76] P. Lobitz, H. Fullbier, A. Reiche and K. Ambrahsat, *Solid State Ionics* , 58, p49, **1992.**

[77] I. I. Olsen, Ph.D Thesis, University of Odense, Odense, Denmark, **1993.**

[78] T. Lapp, S. Skaarup and A. Hooper, *Solid State Ionics*, 11, p97, **1983.**

[79] M. Menetrier, A. Hojjaji, C. Estournes and A. Levasscur, *Solid State Ionics*, 48, p325, **1991.**

[80] A. Alamgir, R. D. Moulton and K. M. Abraham, *Electrochim. Acta.*, 36, p773, **1991.**

[81] G. Nazari, D. M. MacArthur and J. F. Ogara, *Chem. of Mater.*, 1, p370, **1989.**

[82] C. P. Hu and P. V. Wright, *Br. Polymer J.*, 21, p421, **1989.**

[83] G. A. Nazari and S. G. Meibuhr, *J. Electrochem. Soc.*, 136, p2450, **1989.**

[84] K. M. Abraham, M. Alamgir and R. K. Reynolds, *J. Electrochem. Soc.,* 136, p3576, **1989.**

[85] M. Alamgir and K. M. Abraham, *J. Electrochem. Soc.*, 140, L96, **1993.**

[86] X. Andrieu, J. P. Boeuve and T. Vicedo, *J. Power Sources*, 43-44, p445, **1993.**

[87] S. Skaarup, K. West and B. Zachau-Christiansen, *Solid State Ionics,* 28, p975, **1988.**

[88] U. V. Sacken, E. Nodwell, A. Sundher and J. R. Dahn, *Solid State Ionics*, 69, p284, **1994.**

[89] D. Fateaux and R. Koksbang, *J. Applied Chem.*, 23, p1, **1993.**

[90] K. Sawai, Y. Iwakoshi and T. Ohzuku, *Solid State Ionics*, 69, p273, **1994.**

[91] A. Satoh, N. Takami and T. Ohsaki, *Solid State Ionics.*, 80, p291, **1995.**

[92] H. Shi, J. Barker, M. Y. Saiidi, R. Koksbang and L. Morris, *J. Power Sources*, 68, p291, **1997.**

[93] H. O. Pierson, "Handbook of Carbon, Graphite, Diamond and Fullerenes", *Noyes*, Park Ridge, NJ, p43, **1993.**

[94] T. D. Tran and K. Kinoshita, *J. Electroanal. Chem.*, 386, p221, **1995.**

[95] X. Y. Song, K. Kinoshita and T. D. Tran, *J. Electrochem. Soc.*, 143, L120, **1996.**

[96] M. Winter, P. Novak and A. Monnier, *J. Electrochem. Soc.*, 145, p428, **1998.**

[97] R. E. Franklin, *Proc. R. Soc. London A*, 209, p196, **1951.**

[98] A. N. Dey, *J. Electrochem. Soc.*, 118, p1547, **1971.**

[99] R. Nesper, *Prog. Solid State Chem.*, 20, p1, **1990.**

[100] A. V. Churikov, E. S. Nimon and A. L. Lov, *Electrochim. Acta*, 42, p179, **1997.**

[101] C. J. Wen, B. A. Boukamp, R. A. Huggins and W. Weppner, *J. Electrochem. Soc.*, 126, p2258, **1979.**

[102] P. Zlatilova, I. Balkanov and Y. Geronov, *J. Power Sources*, 24, p71, **1988.**

[103] R. A. Huggins, *J. Power Sources*, 26, p109, **1989.**

[104] J. O. Besenhard, J. Yang and M. Winter, *J. Power Sources*, 68, p87, **1997.**

[105] J. Yang, M. Winter and O. Besenhard, *Solid State Ionics,* 90, p281, **1996.**

[106] M.S. Whittingham, *Prog. Solid State Chem.*, 12, p41, **1978.**

[107] P. Novak, K. Muller, K. S. V. Santhanam and O. Haas, *Chem. Rev.*, 97, p207, **1997.**

[108] J. B. Goodenough and V. Manivannan, *Denki Kagaku,* 66, p1173, **1998.**

[109] M. S. Whittingham, *J. Electrochem. Soc.*, 123, p315, **1975.**

[110] F. A. Trumbore, *J. Power Sources*, 26, p65, **1989.**

[111] S. Basu and F. A. Trumbore, *J. Electrochem. Soc.*, 139, p3379, **1992.**

[112] G. Pistoia, L. Li and G. Wang, *Electrochim. Acta*, 37, p63, **1992.**

[113] J. A. Wilson and A. D. Yoffe, *Adv. Phys.*, 18, p193, **1969.**

[114] W. D. Johnston, R. R. Heikes and D. Sestrich, *J. Phys. Chem. Solids*, 7, p1, **1958.**

[115] J. B. Goodenough, D. G. Wickham and W. J. Croft, *J. Appl. Phys.*, 29, p382, **1958.**

[116] K. Mizushima, P. C. Jones, P. J. Wiseman and J. B. Goodenough, *Mater. Res. Bull.* 15, p783, **1980.**

[117] S. A. Campbell, C. Bows and R. S. McMillan, *J. Electroanal. Chem.*, 284, p195, **1990.**

[118] R. Hoppe, G. Brachtel and M. Jansen, *Z. Anorg. Allg. Chem.*, 417, p1, **1975.**

[119] M. H. Rossouw, D. C. Liles and M. M. Thackeray, *J. Solid State Chem.*, 104, p464, **1993.**

[120] A. R. Armstrong and P. G. Bruce, *Nature*, 381, p499, **1996.**

[121] M. M. Thackeray, W. I. F. David and J. B. Goodenough, *Mat. Res. Bull.*, 17, p785, **1982.**

[122] M. M. Thackeray, W. I. F. David and J. B. Goodenough, *Mat. Res. Bull.*, 18, p461, **1983.**

[123] M. M. Thackeray, P. J. Johnson, L. A. dePicciotto, P. G. Bruce and J. B. Goodenough, *Mat. Res. Bull.*, 19, p179, **1984.**

[124] J. C. Hunter, *J. Solid State Chem.*, 39, p142, **1981.**

[125] J. M. Tarascon and D. Guyomard, *Solid State Ionics*, 69, p293, **1994.**

[126] A. M. Chippendale, P. G. Dickens and A. V. Powel, *Prog. Solid State Chem.*, 21, p133, **1991.**

[127] J. O. Besenhard and R. Schollhorn, *J. Electrochem. Soc.*, 124, p968, **1977.**

---

[128] C. Delmas, H. Cognac-Auradou, J. M. Cocciantelli, M. Menetrier and J. P. Doumerc, *J. Power Sources*, 69, p257, **1994.**

[129] Y. Sakurai, S. Okada, J. Yamaki and T. Okada, *J. Power Sources*, 20, p173, **1987.**

[130] K. West, B. Zachau-Cristiansen, M. J. L. Ostergard and T. Jacobsen, *J. Power Sources*, 20, p165, **1987.**

[131] K. Salloux, F. Chaput, H. P. Wong, B. Dunn and M. W. Breiter, *J. Electrochem. Soc.*, 142, L191, **1995.**

[132] D. W. Murphy, P. A. Christian, F. J. DiSalvo and J. N. Carides, *J. Electrochem. Soc.*, 126, p497, **1979.**

[133] K. West, B. Zachau-Cristiansen and T. Jacobsen, *Electrochim. Acta.*, 28, p1829, **1983.**

[134] C. Lampe-Onnerud, J. O. Thomas, M. Hardgrave and S. Yds-Andersen, *J. Electrochem. Soc.* 142, p3648, **1995.**

[135] J. B. Goodenough, H. Y. P. Hong and J. A. Kafalas, *Mater. Res. Bull.*, 11, p203, **1976.**

[136] C. C. Toradi and A. Prince, *Mater. Res. Bull.*, 21, p719, **1976.**

[137] A. Nadiri, C. Delmas, R. Salmon and P. Hagenmuller, *Rev. Chim. Miner.*, 21, p537, **1976.**

[138] A. Manthiram and J. B. Goodenough, *J. Solid State Chem.*, 71, p349, **1987.**

[139] A. K. Padhi, K.S. Nanjundaswamy and J.B. Goodenough, *J Electrochem Soc*, 144, (5), p1188-1194. **1997.**

[140] A. K. Padhi, K. S. Nanjundswamy, C. Masquelier and J. B. Goodenough. *J. Electrochem. Soc.* 144, (8), p2581, **1997.**

[141] A. K. Padhi, V. Manivanannan and J. B. Goodenough. *J. Electrochem. Soc.*, 145, (5), p1518 **1998.**

[142] A. Manthiram and J. B. Goodenough, *J. Power Sources*, 26, p403, **1989.**

[143] J. B. Goodenough, A. K. Padhi, C. Masquelier, K. S. Nanjundaswamy and S. Okada, *37th Battery Symposium,* Tokyo Institute of Technology, Tokyo, Japan, September, **1996.**

[144] J. B. Goodenough, A. K. Padhi, K. S. Nanjundaswamy and C. Masquelier, U.S. Patent No. 5,910,382, **1999.**

[145] A. B. Bykov, A. P. Chirkin, L. N. Demyanets, S. N. Doronin, E. A. Genkina, A. K. Ivanov-Shits, I. P. Kondratyuk, B. A. Maksimov, O. K. Mel'nikov, L. N. Muradyan, V. I. Simonov and V. A. Timofeeva, *Solid-State Ionics,* 38, p31, **1990.**

[146] C. M. Mari, R. Ruffo and M. Catti, *in 196th Meeting of the Electrochem. Soc.*, Honolulu, Oct, Abstract no. 195, **1999.**

---

[147] H. Aono, E. Suigmoto, Y. Yoshihiko, N. Imanaka and G. Adachi, *J. Electrochem. Soc.*, 140, (7), p1827, **1993.**

[148] E. Losilla, S. Bruque, M. A. G. Aranda, L. Moreno-Real, E. Morin and M. Quarton, *Solid-State Ionics*, 112, p53, **1998.**

[149] G. G. Amatucci, A. Safari, F. K. Shokoohi and B. J. Wilkens, *Solid-State Ionics*, 60, p357, **1993.**

[150] T. Suzuki, K. Yoshida, K. Uematsu, T. Kodama, K. Toda, A. Ye and M. Sato, *Solid-State Ionics,* 104, p27, **1997.**

[151] I. S. Pronin, S. E. Sigaryov and A. A. Vashman, *Solid-State Ionics*, 38, p9, **1990.**

[152] V. V. Kravchenko and S. E. Sigaryov, *J. Mater. Science*, 29, p6004, **1994.**

[153] J. Barker and S. M. Yazid, US Patent No. 5,871,866, **1999.**

[154] H. Ohkawa, K. Yoshida, M. Saito, K. Uematsu, K. Toda and M. Sato, *Chem. Lett.*, p1017, **1999.**

[155] S. Geller and J. L. Duran, *Acta Cryst.*, 13, p325, **1960.**

[156] J.B.Goodenough, *Personal Communication.* **1997.**

[157] I. Abrahams and K. S. Easson, *Acta. Cryst* C49, p925, **1993.**

[158] F. Kubel, *Zeitschrift fur Kristallographie*, 209, p755, **1994.**

[159] N. Ravet, J. B. Goodenough, S. Besner, M. Simoneau, P. Hovington and M. Armand. *in 196th Meeting of the Electrochem. Soc.*, Honolulu, Oct, Abstract no. 127, **1999.**

[160] S. Besner, Y. Choquette, J. F. Magnan, F. Allaire, A. Vallee, E. Potvin and P. Hovington, *in 196th Meeting of the Electrochem. Soc.*, Honolulu, Oct, Abstract no. 204, **1999.**

[161] S. Okada, S. Sawa, M Egashira and J. Yamaki, *in 196th Meeting of the Electrochem. Soc.*, Honolulu, Oct, Abstract no. 232, **1999.**

[162] K. Amine, H. Yasuda and M. Yamachi, *in 196th Meeting of the Electrochem. Soc.*, Honolulu, Oct, Abstract no. 277, **1999.**

[163] K. Amine, H. Yasuda and M. Yamachi, *Electrochem. and Solid-State. Lett.*, 3, (4), p178, **2000.**

[164] A. S. Andersson, J. O. Thomas, B. Kalska and L. Haggstrom, *Electrochem. And Solid-State. Lett.*, 3, (2), p66, **2000.**

[165] N. Dupre, J. Angenault, G. Wallez and M. Quarton, *196th Meeting of the Electrochem. Soc.*, Honolulu, Oct, Abstract no. 206, **1999.**

---

[166] T. A. Kerr, J. Gaubicher and L. F. Nazar, *Electrochem. and Solid-State Letters*, 3, (10), p460, **2000.**

[167] E. J, Baran and M. B. Vassallo, *J. Raman Spectroscopy*, 25, p199, **1994.**

2 Experimental Method

2 Experimental Method

2.1 Introduction

This chapter details the materials, equipment, procedures and analyses involved in the powder synthesis, fabrication and experimental testing of the materials studied.

2.2 Powder Synthesis

Two methods of powder synthesis were employed: the solid state method and mixing of solutions of transition-metal chlorides, lithium chloride, ammonium phosphate and ammonium sulphate followed by evaporation of the solvent in order to obtain a more homogenous mixture of reactant components.

2.2.1 Milling

Most milling and mixing of powders was carried out using a simple ball mill, polyethylene containers, PSZ balls and either ethanol or acetone as a solvent. All powders were milled for at least 24 hours to ensure homogeneity. After milling, the solvent was evaporated and the powders were dried in an oven then pressed into pellets prior to firing.

2.2.2 Materials Used

Materials used for powder synthesis, and their purities as assayed by the manufacturer are shown in Table 2.1.

Table 2.1 Chemicals used and their Respective Purities and Manufacturers

Chemical	Purity %	Manufacturer
Carbon	99.5+	Chevron
Co_3O_4	99.9	High Purity Chemicals
Cr_2O_3	99.9	High Purity Chemicals
EC-DEC	Selectipur	Merck
Fe_2O_3	99	Nacalai Tesque (Japan)
$FeCl_3$	99	Riedel de Haen
Li_2Co_3	99	Nacalai Tesque/Pacific Lithium
$LiBF_4$	Selectipur	Merck
LiCl	99+	Aldrich
$LiClO_4$	99.9	Merck
$LiPF_6$	Selectipur	Merck
Lithium metal	99.9	Aldrich
$(NH_4)_2PO_4$	99	Aldrich
$NH_4H_2PO_4$	99	Nacalai Tesque (Japan)
NH_4HSO_4	99	Aldrich
NiO	99.9	High Purity Chemicals
NMP	99.5	Aldrich
PC-DME	Selectipur	Merck
PTFE	99	Nacalai Tesque (Japan)
Sc_2O_3	99.9	High Purity Chemicals
SnO	99.9	High Purity Chemicals
Ti_2O_3	99	Aldrich
TiO_2	99.9	High Purity Chemicals
Tetramethylsulfone	99	Aldrich
V_2O_3	99	Aldrich
V_2O_5	99.6	Aldrich
VCl_3	99	Riedel de Haen
Y_2O_3	99	Nakarai
Zr_2O_3	99	Nakarai

All other reagents were analytical grade unless otherwise stated.

2.3 Equipment Used

This section details the equipment used for the experiments following:

2.3.1 X-Ray Diffraction Analysis

Diffraction of X-rays by matter occurs because the wavelength of X-rays is comparable to the interatomic distances found in matter. Most of the analytical work involved X-ray diffractometry, which was performed on one of three automated powder diffractometers. The first is a Rigaku RAD-RC (12KW) using monochromatic CuKα radiation with the CuKα line. The second is a Phillips PW1140 using CoK_α radiation and a graphite diffracted beam monochromator. It consists of a PW1729 generator with a PW1710 microprocessor and has an automatic divergence slit and a 0.2 mm receiving slit. The automatic divergence slit keeps a constant area of illumination, thereby providing good sensitivity over the entire diffraction range. Phases identified from the experimental patterns collected are matched with those in the database maintained by the International Centre for Diffraction Data (ICDD) using the Phillips APD 1700 software.[1] This was used for peak height and position with the latter being corrected according to the most recent external standard run.[2] The third automated powder diffractometer (and that used most often) is a Phillips X'Pert powder diffractometer using monochromatic CuKα radiation with the CuKα line, and Phillips X'Pert data collection and analysis software.

The samples were usually run from 4° to 80° 2θ at 0.025° per second with a measurement interval of 0.030°.

2.3.2 Scanning Electron Microscopes (SEM)

Two scanning electron microscopes were used: the first is a Hitachi S3000 SEM; and the second is a Hitachi S4000 SEM, with a Robinson BSE (Back Scatter Electrons) detector. Samples examined on the Hitachi S4000 were first coated in carbon with a Edwards E12 vacuum coater, or with gold in a Hitachi Magnetron E1030 ion sputter coater.

2.3.3 Energy Dispersive X-Ray Analysis (EDX)

Energy dispersive X-ray analysis was performed using a Kevex Delta IV EDS X-ray microanalyser attached to the Hitachi S4000 SEM. The sintered surfaces of the pellets were prepared for analysis by using a polishing wheel with diamond paste. The appropriate standards were then used for the semi-quantitative analysis.

2.3.4 Raman Spectroscopy

Raman spectroscopy is the measurement of the wavelength and intensity of inelastically scattered light from molecules. The Raman scattering transition moment is:

$$R = < X_i \mid a \mid X_j > \qquad \text{Equation 2.1}$$

Where X_i and X_j are the initial and final states respectively, and a is the polarisability of the molecule:

$$a = a_o + (r-r_e)(da/dr) \qquad \text{Equation 2.2}$$

Where r is the distance between atoms and a_o is the polarisability at the equilibrium bond length r_e. Polarisability in this case can be defined as the ease of which an electron cloud can be distorted by an external electric field. Since a_o is a constant and $< X_i \mid X_j > = 0$, R simplifies to:

$$R = < X_i \mid (r-r_e)(da/dr) \mid X_j > \qquad \text{Equation 2.3}$$

The result is that there must be a change in polarisability during the vibration for that vibration to inelastically scatter radiation.

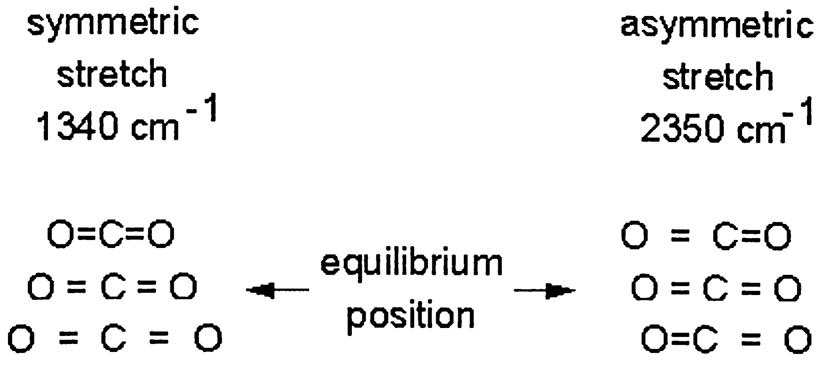

Figure 2.1 Examples of Raman Active and Inactive Vibrations in CO_2

The polarisability depends on how tightly the electrons are bound to the nuclei. In the symmetric stretch, the strength of electron binding is different between the minimum and maximum internuclear distances. Therefore, the polarisability changes during the vibration and this vibrational mode scatters Raman light (the vibration is Raman active). In the asymmetric stretch, the electrons are more easily polarized in the bond that expands but are less easily polarized in the bond that compresses. There is no overall change in polarisability and the asymmetric stretch is Raman inactive. Examples of Raman active and inactive vibrations are shown in Figure 2.1.

Raman line intensities are proportional to:

$v^4\sigma(v)I \exp(-E_i/kT)C$

Where v is the frequency of the incident radiation, $\sigma(v)$ is the Raman cross section (typically 10^{-29} cm^2), I is the radiation intensity, $\exp(-E_i/kT)$ is the Boltzmann factor for state I, and C is the analyte concentration.

Raman spectroscopy was performed on samples of powders at room temperature (23 °C) using a Jobin Yvon U 1000 double beam pass spectrometer equipped with a microscope stage for analysing small samples utilising 180° incident geometry. A Spectra Physics argon-ion laser was employed to excite laser Raman spectra using a 514nm laser line at an incident power of approximately 10 mW, and a water-cooled photomultiplier tube. Spectra were obtained using a x50 objective and 500 μm slit width. The scanning rate used to collect the spectra was kept at 0.5 $cm^{-1}s^{-1}$.

2.3.5 Inductively Coupled Plasma Spectroscopy

In optic emission spectrometry (OES), a sample is subjected to temperatures high enough to cause not only dissociation into atoms but to cause significant amounts of collisional excitation and ionisation of the sample atoms. Once the atoms are in their excited states, they can decay to lower states through thermal or radiative energy transitions. In OES, the intensity of light emitted at specific wavelengths is measured and used to determine the concentration of the analytes.

A Perkin-Elmer Optima 3000 argon supported inductively coupled plasma (ICP) was used as a thermal source in some characterisation. It uses an echelle polychromator with a solid-state detector, which covers the range from 167 to 782 *n*m, and produces a two dimensional spectra that is focused onto the solid-state detector.

2.3.6 Particle Size Analysis

Particle size analysis was undertaken using a Malvern 2000 Mastersizer. The laser diffraction technique is utilised to perform particle analysis on samples. Particles scatter light in all directions with an intensity pattern that is dependent on particle size. A representative sample dispersed in a suitable liquid is passed through a beam of monochromatic light (laser). A multi-element detector measures the light scattered by the particles at various angles and numerical values relating to the scattered pattern are then recorded for analysis. Using an appropriate optical and mathematical model (Mie or Franhofer model), the numerical scattering values are transformed to yield the proportion of total volume to a discrete number of size classes forming a volumetric particle size distribution.

2.3.7 BET Surface Area Analysis

A Tristar 3000 analyser was used to measure the surface area of some materials. Using physical adsorption and capillary condensation principles, it is possible to obtain information about the surface area and porosity of a solid material. A sample contained in an evacuated tube is cooled to cryogenic temperature, then exposed to analysis gas at a series of precisely controlled pressures. With each incremental pressure increase, the number of gas molecules adsorbed on the surface increases. The equilibrium pressure is compared to the saturation pressure, and their relative pressure is recorded along with the quantity of gas adsorbed by the sample at each equilibrated pressure.

2.3.8 Differential Scanning Calorimetry

Differential scanning calorimetry was performed on some materials using a TA Instruments DSC 2920. This instrument employs three thermocouples: a sample, a cell and a reference thermocouple. The cell thermocouple acts as a temperature controller; the other two thermocouples are connected to pans with the sample pan containing the sample to be measured. The sample and reference thermocouple are compared to each other with the difference between the two determining the measure of heat flow from cell to sample and sample to cell. With absorption or phase change, the sample in the sample pan absorbs or desorbs more heat than the reference pan. The sample is allowed to equilibrate at 22 °C, and then measurements are taken between the temperatures of 25 °C and 250 °C with a scanning rate of 20 °C/min.

2.3.9 Furnaces

Several types of furnaces were used, including tube furnaces, and muffle furnaces. The tube furnaces were made by *Ceramic Engineering* using a Eurotherm controller and consisted of a 700 mm long quartz tube, 50 mm in diameter, which is heated by six surrounding silicon carbide resistance elements. These are capable of producing a maximum prolonged temperature of 1200 °C over the middle 100 mm of the tube. The tubes are enclosed by glass fittings through which the required gas can be delivered to give the desired environment for firing. The tube furnaces are controlled by automatic programmers that allow a number of heating steps to be entered in depending on the type of sintering or reaction required.

For solid-state reactions in air, the various materials were heated in a Yamato FP22 muffle furnace at the temperatures required for each reaction.

For AC impedance conductivity measurements and DC four terminal conductivity measurements, McGregor Lab III tubular furnaces were used capable of temperatures up to 1200 °C.

2.4 Density Measurements

Density measurements were performed using Archimedes principle.[3,4] The dry weight of the pellet is recorded and the pellet is then placed in a dessicator. Using an Edward's high vacuum pump, the dessicator is vacuumed for one hour. Distilled water is then sucked into the dessicator until the pellet is covered. The pellet is boiled for 30 minutes and then left to soak under vacuum for several hours. It is then weighed while suspended in distilled water, then blotted dry and weighed again in air. The bulk density (ρ_B) can then be calculated using the following calculation:

$$\rho_B = \frac{W_D}{W_W - W_S} \qquad \text{Equation 2.4}$$

where W_D = dry weight of sample

W_W = wet weight of sample

W_S = suspended weight of sample

Theoretical density (X-ray density, ρ_T) can be calculated from the following equation:

$$\rho_T = \frac{M.z}{V.N} \qquad \text{Equation 2.5}$$

ρ_T = Theoretical density

M = Molecular mass

z = Number of formula units in the cell

V = Cell Volume

N = Avogadros' number

Knowing the theoretical density, the bulk density as a percentage of theoretical density (%ρ) may be calculated:

$$\%\rho = \frac{\rho_B}{\rho_T}.100 \qquad \text{Equation 2.6}$$

2.5 AC Impedance Conductivity Measurements

Electrochemical Impedance Spectroscopy (EIS) is one of the major methods for the characterisation of solid-state ionic conductors.[5] The impedance of the sample is composed of a real and an imaginary part:

$$Z\ \omega = Z_{real} + Z_{im} \qquad \text{Equation 2.7}$$

or

$$Z\ \omega = Z_o\ e^{i\o} = Z_o\cos\o - i\ Z_o\sin\o \qquad \text{Equation 2.8}$$

ω = angular frequency

Zo = amplitude

ø = phase angle

The conductivity is measured by a combination of simple parallel electronic elements such as capacitors and resistors. The reciprocal values of the impedances of these elements are added. In general three major contributors to the total cell impedance must be taken into account:

- The impedance of the bulk material.
- The impedance of the interface electrode–ionic conductor.
- The transport of ions at low frequencies (i.e. < 100 mHz).

A Constant Phase Element (CPE) represents this last impedance component's behaviour. This yields a straight line in the plot of -Zim against Z real (a Nyquist-plot). The impedance of this element is given by:

$$Z\omega = 1/Y_o i\omega\text{-}n \qquad \text{Equation 2.9}$$

Where Y_o is the admittance, the factor n varies between 0.5 and 1 where the under limit represents the Warburg impedance (W), and the upper represents an ideal capacitor.

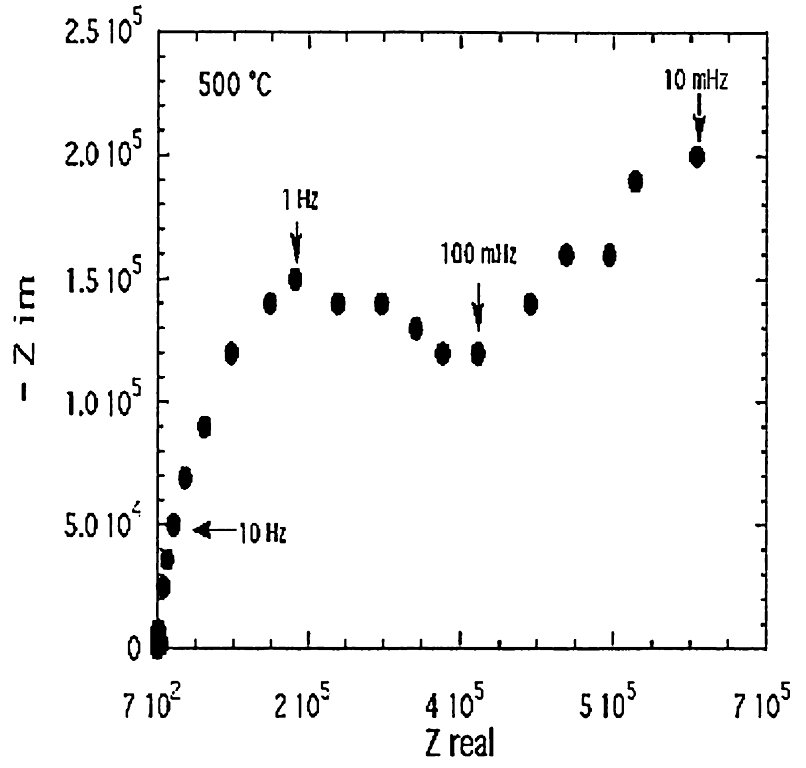

Figure 2.2 Impedance Response of the Electrochemical Chain Au/NASICON/Au

Figure 2.2 shows the impedance behaviour of a NASICON sample in the range from 1 kHz to 10 mHz in the Nyquist-plot. The bulk resistivity is estimated to be 700 from the x-axis intersection of the dispersion curve (Z real) at the frequency of 1 kHz. The second part is a semicircle built up by a parallel RC circuit, charge transfer resistance and double layer capacitance respectively. This leads to a semicircle in the Nyquist-plot. The third part is a linear response transient at the angle of 45° resulting from the low frequency (< 100 mHz) enhanced diffusion of the sodium ions. Figure 2.3 shows the equivalent circuit representation of the frequency dispersion given in Figure 2.2.

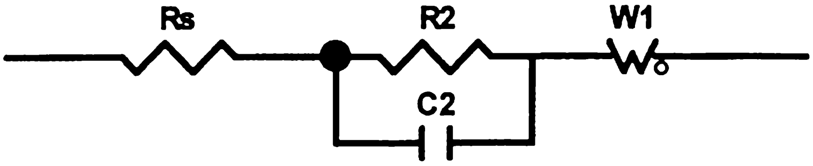

Rs = 700Ω, R2 = 450kΩ and C2 = 353nF

Figure 2.3 Equivalent Circuit of Frequency Dispersion in Figure 2.2

Round pellets 10 mm in diameter were made by cold uniaxially pressing the material in powder form at 20MPa, and then sintering at appropriate temperatures for each material. The pellets' surface area, thickness, and density were measured prior to being coated with electrodes of silver paste. The pellet was then placed between platinum foil electrodes in a silica-quartz tube, and this apparatus was fixed vertically inside a tubular McGregor Lab III furnace. Impedance spectra of the materials were determined in air at temperatures of 25 °C, 50 °C, and then every 50 °C up to 500 °C.

The controller on the furnace raised the temperature at 2 °C per minute until the set temperature was reached. This was held for 1 hour to equilibrate before any readings were taken.

AC impedance readings were performed using a Hewlett-Packard 4192A LF impedance analyser interfaced with an IBM personal computer. An alternating current was applied to the sample via platinum wires connected to the electrodes inside the silica-quartz tube, and to the LF impedance analyser, shown in Figure 2.4 and Figure 2.5. The current ranged in frequency from 1 Hz to 10 MHz. The resulting impedance spectra were recorded and plotted on the IBM PC using Zplot software.

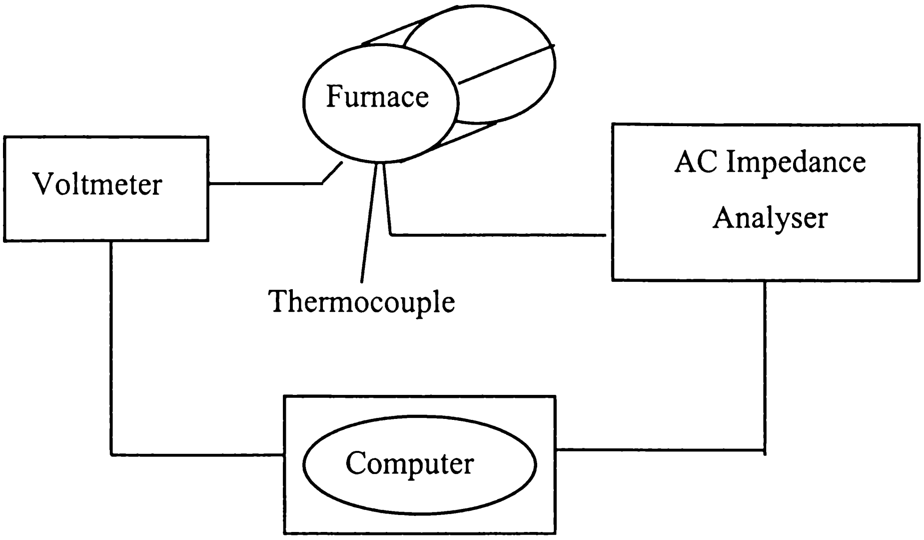

Figure 2.4 AC Equipment Schematic

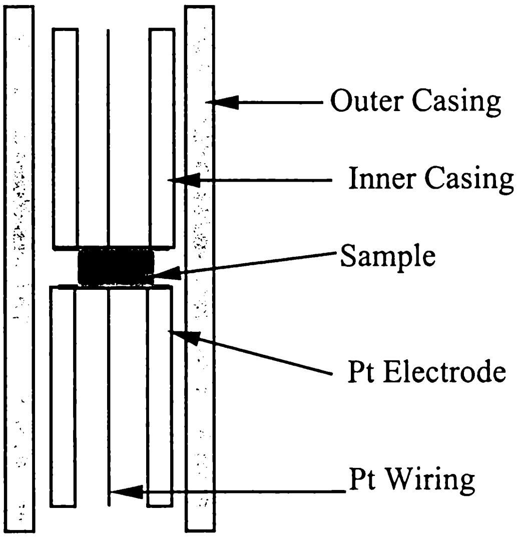

Figure 2.5 Schematic of Silica/Quartz Tube with Sample

2.6 Procedure for Coin Cell Assembly

A drybox (or glovebox) under argon gas is used for all steps in the process except the initial cathode powder preparation stage.

The battery is built from the anode cap up. A stainless steel spring is placed inside the anode cap, and then a stainless steel disc is placed on top. The lithium metal anode is cut into round sheets, which are then pressed onto the stainless steel disc.

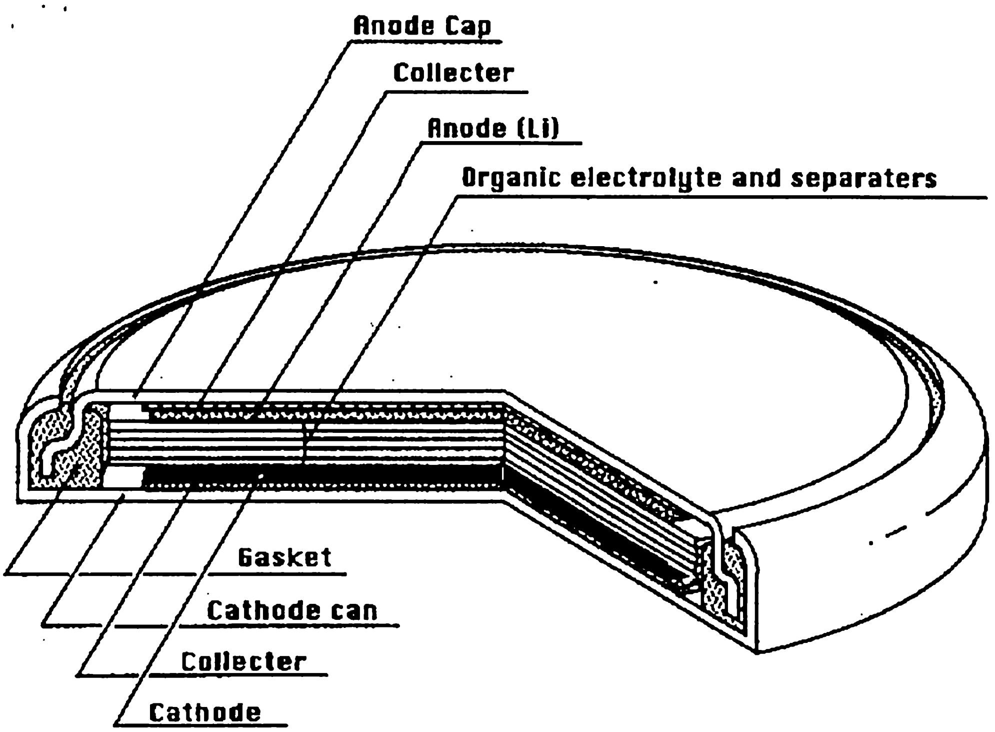

Figure 2.6 Components of Coin Cell

The coin cell and its components are shown in Figure 2.6. A separator is placed onto the anode, and the electrolyte is then soaked into this. In initial experiments, two separators were used. However, this was unnecessary in later experiments due to a change in the types of cathode used from pressed pellets to cathode slurries. The first separator used in all experiments is a 10 layer un-woven polypropylene (Sanyo) separator. 60 μL of the aqueous organic electrolyte is then soaked into this separator via a pipette. Several electrolytes were used throughout the course of this work. A lithium salt, $LiClO_4$, $LiPF_6$ or $LiBF_4$, was dissolved in a two solvent organic electrolyte. The organic materials used included PC + DME, EC + EMC, EC + DMC, EC +

DME and also a higher voltage stability sulfone, tetramethylsulfone. More detailed information on electrolytes is contained in Chapter 1.

The second of the two separators is a thin single layer material called "polyplastic" by its manufacturers. It is placed on top of the polypropylene-soaked electrolyte. The cathode pellet is then placed on top of this separator, and the cathode can is deposited carefully over the top of the whole construction. The cell is then turned upside down and moved either with plastic tweezers (to avoid a short) or by hand, into a press, where the anode cap is pressed into the cathode can to seal the battery.

2.6.1 Production of Cathode Pellet

The method of cathode production involved the preparation of a cathode slurry. Usually 2g of cathode material and 0.3g of carbon were intimately ground together (and sometimes milled for 24 hours in acetone using PSZ media, then dried to obtain a mixed powder). The mixed powders then had 2g of 1-methyl-2-pyrolidine (NMP), and 2g of 5% kynar (PVDF binder material) in NMP added and stirred magnetically for 12 hours to ensure homogenation. The resulting slurry was poured onto an aluminium substrate, and then rolled with a wound wire rod, or a doctor blade that provides a thickness of 20 – 40μm of cathode material coated onto the substrate.

The substrate is dried at 60 °C for 2 hours before being cut into rectangular sections 2.4cm x 6cm. The rectangles are pressed between two stainless steel plates at 60 MPa, before being cut into discs 12mm in diameter. Four discs at a time are then repressed at 60 MPa, and are weighed before being annealed at 160 °C under vacuum in a furnace adjoined to the glovebox.

2.7 Battery Testing

Once a battery is made, it is removed from the glovebox, and the open circuit voltage is tested to ensure the battery has not shorted out. The battery is then left for at least 2 hours to equilibrate, whereupon the voltage is measured again before testing. The battery is then placed in a testing rig which is connected to a data collecting PC.

Two types of instruments were used to collect and analyse battery characteristics. The first involved the use of an NEC PC-9800 computer with CDS 2.65 (in-house) software. Later experiments used one of three Arbin BT2043 testing systems with Mits 97® software.

In the first system, upper limit cut off voltages and lower limit cut off voltages are set, as well as charge and discharge rest time, before testing begins. The battery is charged and discharged at a set current for at least 20 cycles. The voltage and capacity are recorded on the PC as the battery is charged and discharged. In the second system, various charge/discharge schedules are possible, including cyclic voltammetry and a dQ/dV schedule, which enables comparison of the capacity and voltage profiles with varying currents. This last schedule was used predominantly in cathode performance analysis for the materials studied. The cycling conditions for this schedule are shown in the following table.

Table 2.2 Parameters of dQ/dV Schedule

Cycle No	Cycling Conditions
1, 2, 102, 202	Differential capacity 7.5 mA/g
3 - 5	30 mA/g
16-19, 96-99, 196-199	Rate capability 300 mA/g
10, 20, 60, 100, 150, 200	Resistance 400ms
11, 101, 201	Impulse 60s
All others	75 mA/g

2.8 Lithium Cobalt Phosphate

$Li_{1-x}Co_{1-x}M_xPO_4$ was prepared using conventional solid-state reaction techniques. The starting materials were Li_2CO_3, Co_3O_4 and $NH_4H_2PO_4$. The dopant starting materials used were TiO_2, and V_2O_3. The mixtures with stoichiometric amounts of these materials were firstly ground in an agate mortar, although milling for 24 hours using PSZ media in acetone was employed later as conductivity comparisons of the LiNiPO4 materials showed that this process obtained a slightly higher ionically conductive material. The ground powders were then preheated at 300 °C for 3 hours, 650 °C for 2 hours, then 750 °C for 36 hours in air with intermediate regrinding followed by air quenching. The final temperature varied from 675 °C to 900 °C depending on the dopant, as the density varied with dopant and dopant content. Heating rates were around 1 °C/min to avoid Li_2O volatisation.

The samples were then scanned on an automatic powder X-ray diffractometer from 4° to 80° 2θ at 0.025° per second with a sample interval of 0.030°.

Raman spectroscopy was performed on samples of powders as described in section 2.3.4.

Particle size analysis and surface area analysis of raw cathode materials (and also of the cathode and carbon mixture that had been milled in acetone with PSZ media) were undertaken.

Measurement of the bulk density of the pellets for AC impedance was performed, before AC impedance measurements of the undoped and doped materials were carried out using the methods described in section 2.5.

An ultrafine colloidal carbon solution was also used in order to try to improve the carbon to cathode contact. Cathode slurries using this material were prepared simply by mixing the same ratio of cathode material to carbon (1:0.15) as with other cathode pellets. The resulting mixture was milled for 24 hours using PSZ media before the slurry was rolled and the organic components of the colloidal solution dried. SEM analysis was undertaken to show the difference in contact between the two types of carbon used and EDX analysis was used to confirm characterisation.

Cathode performance was determined by constructing button-type cells in a glovebox, before testing using the equipment described in section 2.7. The electrolyte used was 1M $LiPF_6$ in EC:DEC in a 1:1 w/w ratio. A dQ/dV schedule as well as cyclic voltammetry was used to determine the potential of this material as a lithium battery cathode. The initial voltage limits were set at 5.3V upper and 2.7V lower. After it was determined that full performance was not being achieved, a higher voltage electrolyte tetramethylsulfone with either $LiBF_4$ or $LiN(SO_2C_2F_5)_2$ (3M Flourad lithium bisperflouroethanesulfonimide) as a salt was introduced and the upper limit was increased to 5.5V.

2.9 Lithium Nickel Phosphate

$Li_{1-x}Ni_{1-x}M_xPO_4$ (M = Ti, Y, Fe, Cr, Co and Sc) was prepared using conventional solid-state reaction techniques.[6] The starting materials were Li_2CO_3, NiO and $NH_4H_2PO_4$. The dopants' starting materials used were TiO_2, Y_2O_3, Sc_2O_3, Fe_2O_3, Cr_2O_3 and Co_3O_4. The mixtures with stoichiometric amounts of these materials were firstly ground in an agate mortar, although milling for 24 hours using PSZ media in acetone was employed later for conductivity comparisons. The ground powders were then preheated at 300 °C for 3 hours, 650 °C for 2 hours, then 750 °C for 36 hours in air with intermediate regrinding followed by air quenching. The final temperature varied from 750 to 900 °C depending on the dopant cation as the bulk density of the material varied with dopant and dopant content. Heating rates were around 1 °C/min in attempts to avoid Li_2O volatisation.

The samples were then scanned on an automatic powder X-ray diffractometer from 4° to 80° 2θ at 0.025° per second with a sample interval of 0.030°.

Raman spectroscopy was performed on samples of powders as described in section 2.3.4.

Particle size analysis and surface area analysis of raw cathode materials (and also of the cathode and carbon mixture that had been milled in acetone with PSZ media) were undertaken.

Measurement of the bulk density of the pellets for AC impedance was performed, before AC impedance measurements of the undoped and doped materials were carried out using the methods described in section 2.5.

After AC impedance results confirmed poor total conductivity of the cathode materials, a new ultra fine carbon (UFC) material was used in order to try and improve carbon to cathode contact. SEM analysis was done to show the difference in contact between the two types of carbon used and EDX analysis was used to confirm characterisation.

Cathode performance was then determined by constructing button-type cells in a glovebox, before testing using the equipment described in section 2.7. The electrolyte used was firstly 1M $LiClO_4$ in PC:DME in a 1:1 w/w ratio. Later as voltages were increased 1M $LiPF_6$ in EC:DEC in a 1:1 w/w ratio was used. A dQ/dV schedule was used to determine the potential of this material as a lithium battery cathode. The voltage limits were set at 5.0V upper and 1.0V lower.

2.10 Lithium Iron Phosphate

$Li_{3-2x}Fe_{2-2x}Ti_{2x}(PO_4)_3$ was prepared by direct solid-state reaction of stoichiometric amounts of Fe_2O_3, $NH_4H_2PO_4$, Li_2CO_3 and TiO_2.[7,8] The mixtures with stoichiometric amounts of these materials were firstly ground in an agate mortar, then milled for 24 hours using PSZ media in acetone. The ground powders were then preheated in air at 300 °C for 3 hours to drive off ammonia, water and other gases, annealed at 850 °C for 48 hours with intermittent regrinding, and then at 930 °C for a further 24 hours. Heating rates were around 1 °C/min to avoid Li_2O volatisation.

$LiFe_2PO_4(SO_4)_2$, a structurally related material, was prepared by mixing solutions of LiCl, $FeCl_3$, $NH_4H_2PO_4$ and NH_4HSO_4 and stirring magnetically for 1 hour.[9] Some HCl was added before the solutions were mixed in order to avoid Li_3PO_4 precipitation. The solution was then heated to boiling and allowed to dry to powder. The resulting powder was cold uniaxially pressed into pellets at 20Mpa, and then fired in air at 475 °C for 12 hours, with a 1 °C ramp up. It was important not to let the temperature rise above 500 °C in order to avoid SO_2 volatisation.

The samples were then scanned on an automatic powder X-ray diffractometer from 4° to 80° 2θ at 0.025° per second with a sample interval of 0.030°.

Raman spectroscopy was performed on samples of powders as described in section 2.3.4.

Particle size analysis and surface area analysis of raw cathode materials (and also of the cathode and carbon mixture that had been milled in acetone with PSZ media) were undertaken.

Measurement of the bulk density of the pellets for AC impedance was performed, before AC impedance measurements of the undoped and doped materials were carried out using the methods described in section 2.5.

Differential scanning calorimetry was performed in order to determine possible phase changes with temperature or a function of dopant content.

Cathode performance was then determined by constructing button-type cells in a glovebox, before testing using the equipment described in section 2.7. The electrolyte used was 1M $LiPF_6$ in EC:DEC in a 1:1 w/w ratio. A dQ/dV schedule was used to determine the potential of these materials as a lithium battery cathode. The voltage limits were set at 4.5V upper and 2.7V lower.

2.11 Lithium Vanadium Phosphate

$Li_{3-2x}(V_{1-x}Ti_x)_2(PO_4)_3$ was prepared by direct solid-state reaction of stoichiometric amounts of V_2O_3, $NH_4H_2PO_4$, Li_2CO_3 and TiO_2.[10] The mixtures with stoichiometric amounts of these materials were firstly ground in an agate mortar, then milled for 24 hours using PSZ media in acetone. The ground powders were preheated in a pure H_2 atmosphere at 300 °C for 3 hours to drive off ammonia, water and other gases, annealed at 750 °C for 12 hours then sintered at 875 °C for 24 hours. $2\%H_2/98\%N_2$ was later used as it was discovered that it was not necessary to use pure H_2. Heating rates were approximately 1 °C/min in order to avoid Li_2O volatisation.

An attempt was made to synthesise $LiV_2PO_4(SO_4)_2$ by mixing LiCl, VCl_3, $NH_4H_2PO_4$ and NH_4HSO_4, by the same method by which $LiFe_2PO_4(SO_4)_2$ was made in Section 2.09. The results are discussed in Chapter 6.

The samples were then scanned on an automatic powder X-ray diffractometer from 4° to 80° 2θ at 0.025° per second with a sample interval of 0.030°.

ICPS was undertaken on initial materials synthesised to determine chemical composition.

Particle size analysis and surface area analysis of raw cathode materials (and also of the cathode and carbon mixture that had been milled in acetone with PSZ media) were undertaken.

The bulk density of the pellets used for AC impedance was measured, before AC impedance measurements of the undoped and doped materials were carried out using the methods described in section 2.5.

Cathode performance was then determined by constructing button type cells in a glovebox, before testing using the equipment described in section 2.7. The electrolyte used was 1M $LiPF_6$ in EC:DEC in a 1:1 w/w ratio. A dQ/dV schedules was used to determine the potential of these materials as a lithium battery cathode. The voltage limits were set at 5.0V upper and 2.7V lower.

2.12 References

---

[1] N. V. Philips, *Software Automated Powder Diffraction APD1700*, Operations Manual, Fourth Edition, Gloeilampenfabrieken, Einhoven, the Netherlands, **1989.**

[2] National Bureau of Standards, *Standard Reference Material 640b*, NIST Gaithersburg, MD 20899, USA.

[3] *CRC Handbook of Chem. & Physics*, 51st Ed., pub. by Chemical Rubber Co., Cleveland, Ohio, pF4, **1970-71.**

[4] *BS1902*: part 1A: 1966 methods of testing refracting materials, sampling and physical testing p19.

[5] T. Lang, D. Ivanov, J. F. Currie and A. Yelon, http://lisa.polymtl.ca/LISA-Brochure/CIS-Thomas.html

[6] I. Abrahams and K. S. Easson, *Acta Cryst*, C49, p. 925, **1993.**

[7] A. K Padhi, K. S. Nanjundaswamy and J. B. Goodenough, *J. Electrochem. Soc.*, 144-5 p.1188-1194, **1997.**

[8] A. B. Bykov, A. P. Chirkin, L. N. Demyanets, S. N. Doronin, E. A. Genkina, A. K. Ivanov-Shits, I. P. Kondratyuk, B. A. Maksimov, O. K. Mel'nikov, L. N. Muradyan, V. I. Simonov and V. A. Timofeeva, *Solid State Ionics*, 38,1-2, p.31-52. **1990.**

[9] A. K. Padhi, V. Manivannan and J. B. Goodenough, *J. Electrochem. Soc.* 145, p1518, **1998.**

[10] J. Barker and S. M. Yazid, U.S. Patent No. 5871866, **1999.**

3 Lithium Cobalt Phosphate - $LiCoPO_4$

---

3 Lithium Cobalt Phosphate - $LiCoPO_4$

3.1 Characterisation

Firing $LiCoPO_4$ in air showed via X-ray diffraction and Raman spectroscopy that a single solid phase was formed according to the following reaction:

$$3Li_2CO_3 + 6NH_4H_2PO_4 + 2Co_3O_4 \xrightarrow{O_2} 6LiCoPO_4 + 6NH_3 + 9H_2O + 3CO_2 \qquad \text{Equation 3.1}$$

3.1.1 X-Ray Diffraction

XRD results show that an orthorhombic phase formed (space group: 62, *Pnma*) for all of the $Li_{1-x}Co_{1-x}M_xPO_4$ materials. The partial substitution of Ti^{3+} and V^{3+} for Co^{2+} was attempted. Only results for V^{3+} will be discussed in detail.

Results of the Rietveld refinement of the XRD data for pure $LiCoPO_4$ are shown in Figure 3.1 and Table 3.1. The Rietveld analysis was performed using Fullprof 98® software. Initial structural and thermal parameters were taken from the data for $LiNiPO_4$ from Abrahams and Easson[1] as a starting model for the refinement. Scale and background parameters were refined initially, followed in subsequent iterations by cell, zero point and peak shape parameters. The atomic positions were fixed while the cell parameters and then the occupancy factors the cobalt atom were refined. Once the cell parameters and the occupancy factors were established, the refinement of the atomic positions for all atoms was performed. The phosphorus and then the transition metal cobalt atomic positions having the larger scattering factors were refined first followed by the oxygen.

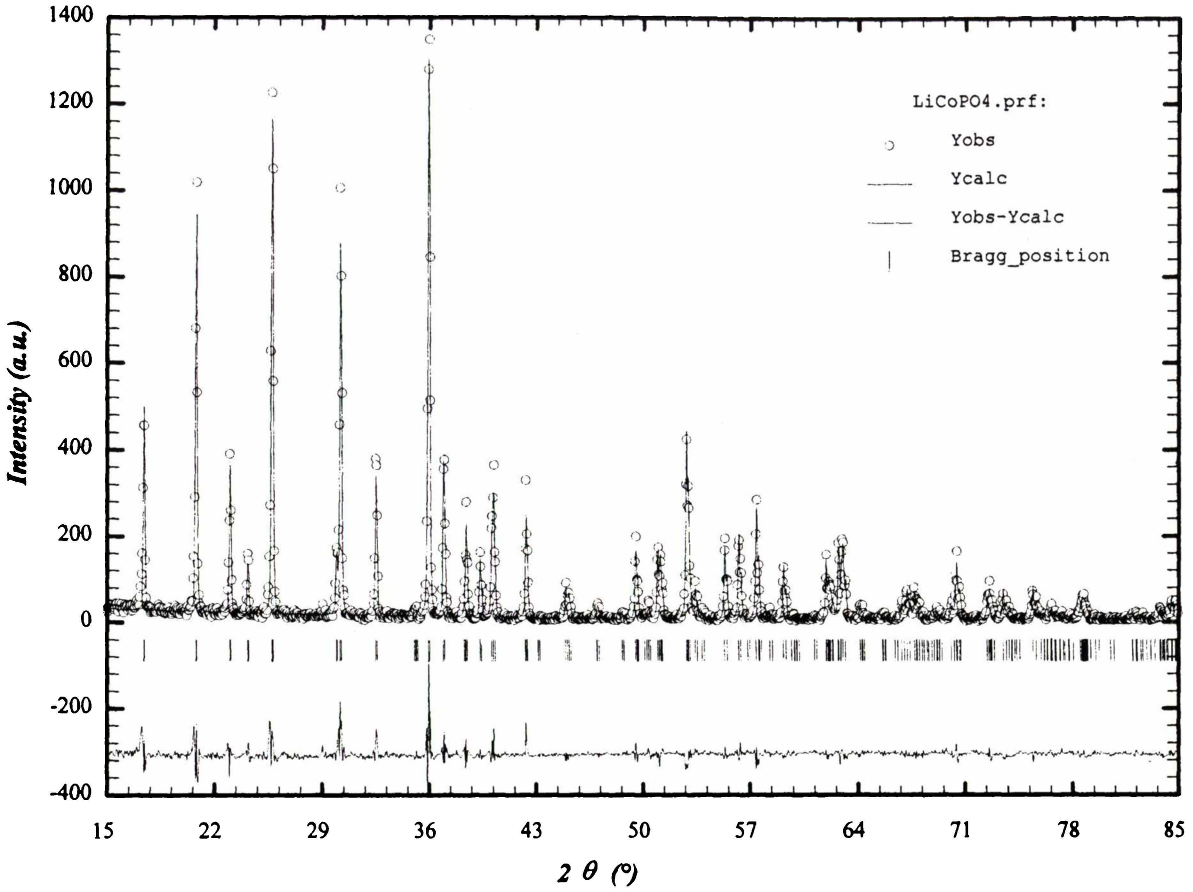

Figure 3.1 Structure Refinement of $LiCoPO_4$

Vanadium doped $LiCoPO_4$ were also indexed in the *Pnma* space group and the diffraction patterns for these set out in Appendix II. The data for the V^{3+} doped materials are summarised in Table 3.2.

Doping of the material was attempted in order to improve the ionic conduction and to determine if any increase in conductivity is beneficial to the materials' electrochemical performance as a cathode in a lithium secondary battery. When partial replacement of ions of one type of formal charge by ions of a different formal charge occurs, interstitial ions, vacancies or charge compensations by a change in electronic state of one or more of the other ions must be generated at the same time in order to maintain charge balance. If the interstitials or vacancies are able to migrate, dramatic increases in conductivity can occur.[2]

For the substitution of V^{3+} for Co^{2+} in $Li_{1-x}Co_{1-x}V_xPO_4$ a secondary phase is clearly evident when x = 0.10 or more as shown in the figures in Appendix II. Two peaks distinguish this best where the peak position 2θ is approximately 29° and 30°. Attempts to identify this phase revealed that it is most likely $LiVOPO_4$. It is very difficult to identify a second phase when x = 0.05, however, the presence of a second phase cannot be ruled out. As the intention was to substitute V^{3+} for Co^{2+} a decreased amount of lithium was used to maintain charge balance. Rather than giving a single phase $Li_{1-x}Co_{1-x}V_xPO_4$ product, the reaction appears to have produced a two-phase mixture with $Li_{1-x}Co_{1-x}M_xPO_4$ and $x$$LiVOPO_4$. There is a small expansion in the cell parameters of the $LiCoPO_4$ but with the cation radius of V^{3+} and Co^{2+} being 0.64 and 0.65 Å respectively, it is difficult to use cell parameters to determine the solubility of vanadium in the system. The scattering factor of V^{3+} is approximately 20 in comparison to Co^{2+} with a scattering factor of 25. These values are probably too close to each other to determine if any decrease in cobalt site occupancy is due to successful doping, and when combined with the relatively high Rp values obtained there is no conclusive evidence that the doping is successful even at smaller dopant quantities, however, doping of the material provides interesting conductivity properties as will be shown.

Table 3.1 Refined Crystallographic Parameters for $LiCoPO_4$ (P*nma*) - X-ray diffraction data for 258 reflections and 24 variables

Atom	*x*	*y*	*z*	Occupancy	B_{iso} (Å^2)
Co	0.2792 (4)	0.25 *	0.9762 (10)	1.083 (12)	0.96 *
P	0.0952 (8)	0.25 *	0.4198 (16)	1.000 *	0.81 *
O	0.0976 (17)	0.25 *	0.7355 (35)	1.000 *	0.3 *
O	0.4570 (19)	0.25 *	0.2046 (32)	1.000 *	0.4 *
O	0.1665 (15)	0.0462 (20)	0.2805 (21)	2.000 *	0.8 *
Li	0.0000 *	0.0000 *	0.0000 *	1.000 *	2.8 *
a = 10.2004, b = 5.9190, c = 4.6982, * = Fixed Parameters V = 283.661 Å^3, wRp = 20.7, Rp =14.7 , $\chi 2$ =2.01					

Table 3.2 V^{3+} doped $LiCoPO_4$ Refinement Summary

Parameters	LiCoPO4	V = 0.05	V = 0.10	V = 0.15	V = 0.20
a	10.2004 (6)	10.2004 (7)	10.2028 (8)	10.2012 (12)	10.2010 (19)
b	5.9190 (4)	5.9197 (4)	5.9199 (5)	5.9195 (7)	5.9182 (11)
c	4.6982 (3)	4.6981 (3)	4.6988 (4)	4.6991 (6)	4.6992 (10)
Volume ($Å^3$)	283.661 (27)	283.688 (30)	283.804 (37)	283.761 (56)	283.695 (92)
Co Site Occupancy	1.083 (12)	1.058 (15)	1.033 (20)	1.088 (25)	1.045 (33)

3.1.2 Raman Spectroscopy

Raman spectroscopy was used simultaneously with XRD to determine characterisation and identification of second phases present in the compounds with substitution of the Co^{2+} cation in $LiCoPO_4$. The number and type of vibrational modes can be calculated for a compound with a known space group and atom position using factor group analysis and this can be used to determine information about the spectra obtained for the specific materials. Factor group analysis was used to determine the following irreducible representations for the orthorhombic $LiCoPO_4$ structure with Z = 4, where Γ_{op} are the optical vibrational modes and Γ_{ac} are the acoustic modes, R = Raman active, ir = infrared active and i = inactive.

Orthorhombic $LiCoPO_4$

Space Group: P*nma* (No. 62)

$$\Gamma_{op} = \underset{(R)}{13A_g} + \underset{(R)}{8B_{1g}} + \underset{(R)}{13B_{2g}} + \underset{(R)}{8B_{3g}} + \underset{(i)}{8A_u} + \underset{(ir)}{12B_{1u}} + \underset{(ir)}{7B_{2u}} + \underset{(ir)}{12B_{3u}}$$

$$\Gamma_{ac} = B_{1u} + B_{2u} + B_{3u}$$

A total of 42 Raman active, 31 infrared active and 8 inactive modes.

The Raman spectra of substituted V^{3+} for Co^{2+} in $Li_{1-x}Co_{1-x}V_xPO_4$, $0 \leq x \leq 0.2$, are shown in Figure 3.2. Band positions and relative intensities of the observed spectra are listed in Table 3.3. For the Raman spectrum of $LiCoPO_4$, there are a total of 15 bands observed at room temperature of the 42 predicted Raman active modes from factor group analysis. The bands are assigned with reference to the relative wavenumber positions and compared to the assignments of the spectra of $LiNiPO_4$ and $LiVOPO_4$. The Raman spectra of vanadium doped $LiCoPO_4$ show the presence of a secondary phase with dopant quantities of 10 or more mol% characterised by strong bands at 875 cm^{-1} (V=O stretching) and 1044 cm^{-1} (PO_4 stretching) for higher dopant quantities. Baran et al. report the major peak for β-$LiVOPO_4$ at 884 cm^{-1} and these peaks are compared in the table following.[3]

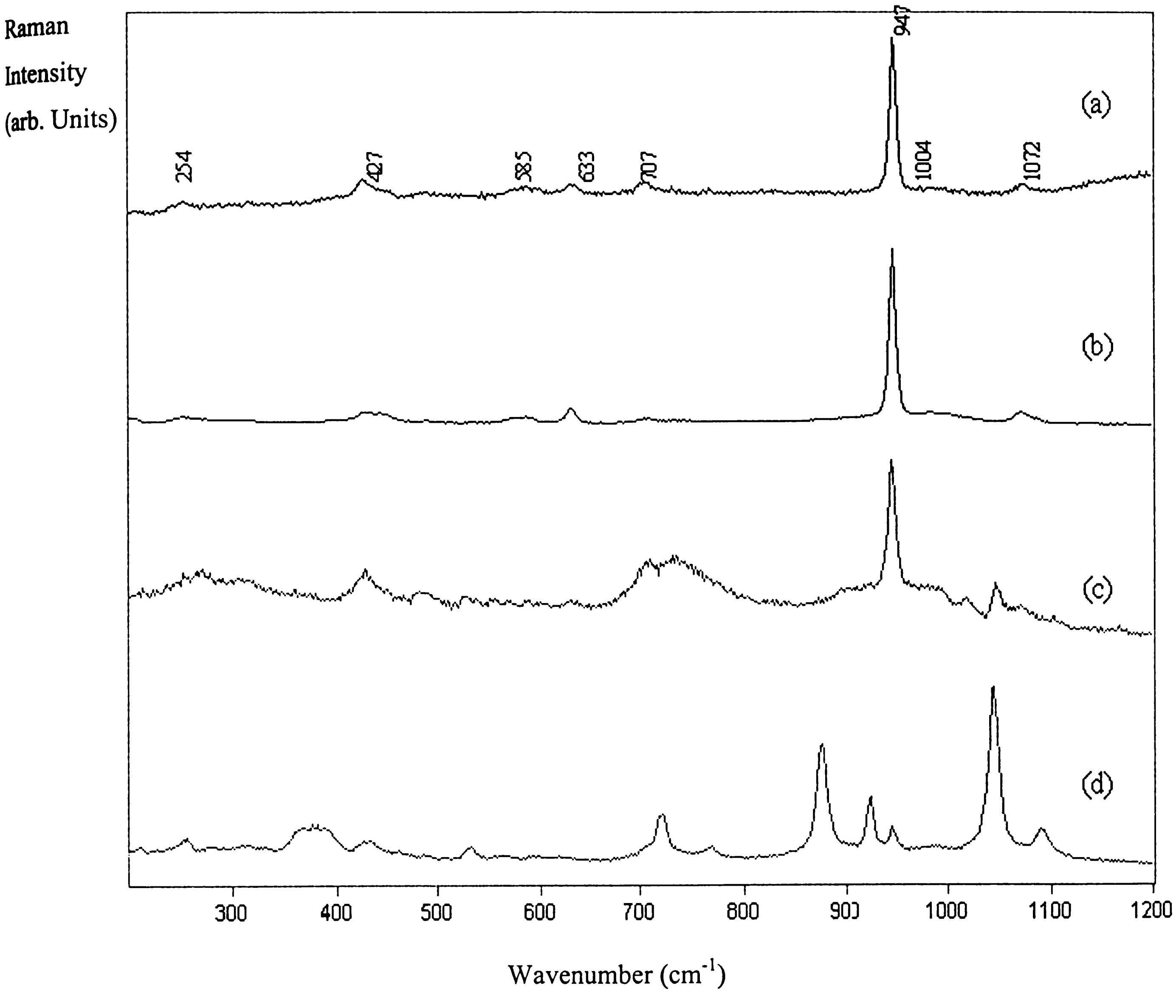

Figure 3.2 Raman Spectra of $Li_{1-x}Co_{1-x}V_xPO_4$, $0 \leq x \leq 0.2$, where x = 0(a), 0.05(b), 0.10(c), 0.20(d)

With x = 0.05 in $Li_{1-x}Co_{1-x}V_xPO_4$ it is unclear whether or not there is a secondary phase present , although with such a small dopant quantity it cannot be ruled out. With x ≥ 0.10 the secondary phase becomes clearly visible. With increasing vanadium dopant concentration after this there is an increase in the relative proportion of the secondary phase. Figure 3.3 shows the comparison of the Raman spectra of $LiCoPO_4$, $Li_{0.80}Co_{0.80}V_{0.20}PO_4$ and the subtraction spectrum of the two. It can be seen that at 20 mol% V, the secondary phase is predominant in the spectrum.

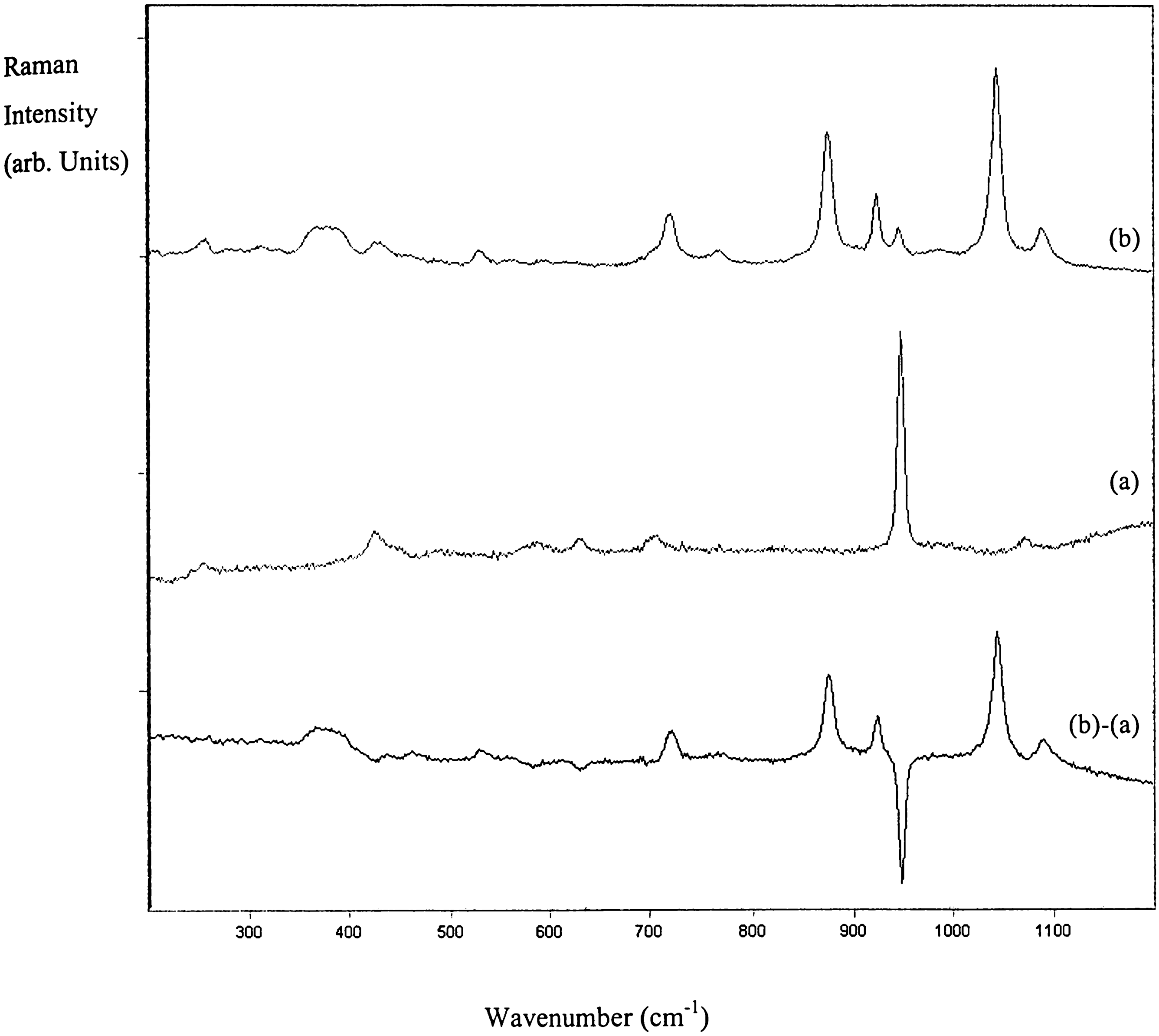

Figure 3.3 Raman Spectra of $LiCoPO_4$ (a), $Li_{0.80}Co_{0.80}V_{0.20}PO_4$ (b) and Subtraction Spectrum of (b) - (a)

Table 3.3 Raman Band Positions of $Li_{1-x}Co_{1-x}V_xPO_4$, $0 \leq x \leq 0.2$

0.00	0.05	0.10	0.15	0.20	$LiNiPO_4$	β-$LiVOPO_4$[3]	Assignment
210 vw	210 vw	211 vw	210 vw	210 vw			LCP (lattice)
254 w	253 w	257 vw	253 w	255 w	270	250	LCP (lattice)
		272 m	297 sh	281 vw		266	*
315 vw	311 vw	314 vw	314 m	311 w	305	310	LCP (lattice)
				330 vw		332	*
362 vw		362vw	362 m		365	363	LCP (CoO_6)
		380vw		375 m,b			*
409vw	408 sh	412 sh	400 w		413		LCP (CoO_6 and PO_4 bending)
427 m	426 w	429 m	430 s	427w		429	LCP (CoO_6 and PO_4 bending)
457 sh	443 sh	450 sh		459 w	461		LCP (CoO_6 and PO_4 bending)
		468 vw				468	
		474 vw					
490 vw	489 vw	486 w					LCP (CoO_6 and PO_4 bending)
		525 w	533 w	530 w			*
		557 w		560 w			*
		572 w					
585 w,b	585 w	587 w			585		LCP (LiO_6 and PO_4 bending)
		602 w	596 w	595 vw			*
633 w	632 w	630 w	631 sh	628 vw	635	629	LCP (LiO_6 and PO_4 bending)
			648 w				
707 w	708w	710 m	705 vw	705 sh			LCP (LiO_6 and PO_4 bending)
		735 m	721 w	721 m			*
				768 w			
843 vw	844vw	843 vw		847 vw	844		LCP (PO_4 stretching)
		872 vw	882 s	875 s		884	*
		904 w,b					
		924 w	925 m	924 m			*
947 s	947 s	947 s	947 m	946 w	943	936	LCP (PO_4 stretching)
		983 w,b	983 s	987 w		979	*
1004 w,b	999 sh	1000 sh	1004 sh			1005	LCP (PO_4 stretching)
		1019 w				1025	
		1047 m	1044 w	1044 s		1062	*
1072 w	1070 w	1070 w	1067 m	1089 w	1074	1077	LCP (PO_4 stretching)
		1101 vw					
		1166 vw	1171 w			1104	*

vw = very weak, w = weak, m = medium, s = strong, b = broad, sh = shoulder, relative intensity

* = secondary phase, LCP = orthorhombic $LiCoPO_4$

The Raman and XRD results do not conclusively show that vanadium is soluble in the $LiCoPO_4$ structure under these synthesis conditions, however, the following AC impedance results point to the possibility that vanadium may be soluble in small quantities.

3.2 AC Impedance

3.2.1 Bulk Density Measurements

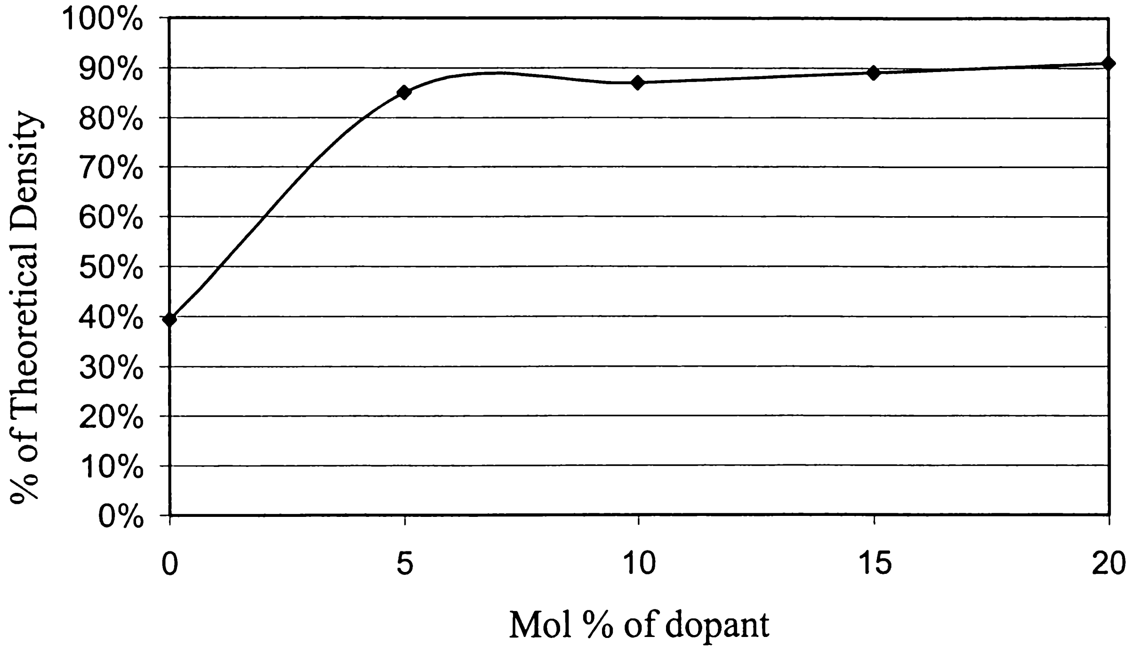

Figure 3.4 Bulk Density of $Li_{1-x}Co_{1-x}V_xPO_4$, $0 \leq x \leq 0.2$

The bulk density of the pellets sintered for AC Impedance measurement was undertaken as per the method described in Section 2.4. The addition of a dopant material changed the sintering temperature with dopant content. With titanium, sintering temperature increased with dopant content. On the other hand, with vanadium, the sintering temperature decreased with dopant content, therefore the bulk density increased with increasing dopant content (Figure 3.4). This resulted in lowering the pellet sintering temperature from 750 °C to 650 °C to avoid a partial melt of the materials with higher dopant quantities, which means that pure $LiCoPO_4$ was only 40% dense. Dividing by the actual density, and multiplying by the theoretical density corrected the conductivity measured. Pellets made from $LiCoPO_4$ were bright purple and darkened with increasing levels of dopant content.

3.2.2 Circuit Modelling

Doped $LiCoPO_4$ has an increasing secondary phase with increasing dopant content as determined by XRD and Raman. Potentially the ionic conduction may be affected depending primarily upon whether or not the vanadium dopant is partially soluble in the $LiCoPO_4$ structure, but also the second phase and how the second phase, the primary phase, and the grain boundary interfaces interact. Initial AC impedance measurements showed that $LiCoPO_4$ had a very poor conductivity. Therefore, the vanadium doped samples were also measured to determine how the doped phase and differing amounts of a secondary phase enhanced or impeded conductivity at various temperatures.

For a pure ionic conductor an expected equivalent circuit is shown below:

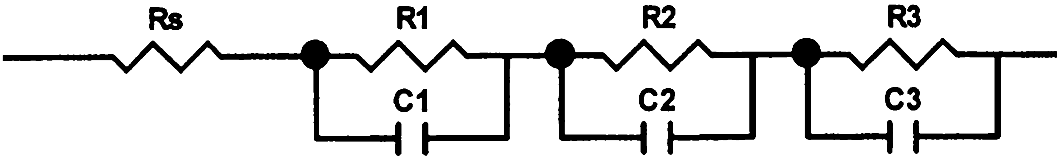

Figure 3.5 Rs3RC Equivalent Circuit

The R1/C1 parallel resistor capacitor represents the resistance of the grains and the associated capacitance; R2/C2 represents the grain boundary resistance; and R3/C3 represents resistance and capacitance associated with the electrodes. Rs, represents the residual resistance of the leads and equipment in general, is usually very small compared to the other factors. Throughout the experiments, conductivity of the leads and set-up were measured to ensure no unexpected resistances existed. These readings showed an average resistance of 3.6 Ω.

Differentiating between different components in the impedance spectra obtained is extremely difficult, so total conductivities were measured. Equivalent circuit fitting was done using a simple Rs1RC circuit (Figure 3.6). At room temperature, $LiCoPO_4$ had conductivity almost two orders of magnitude lower than isostructural $LiNiPO_4$ (see Chapter 4). If a Warburg impedance was present it was too difficult to identify.

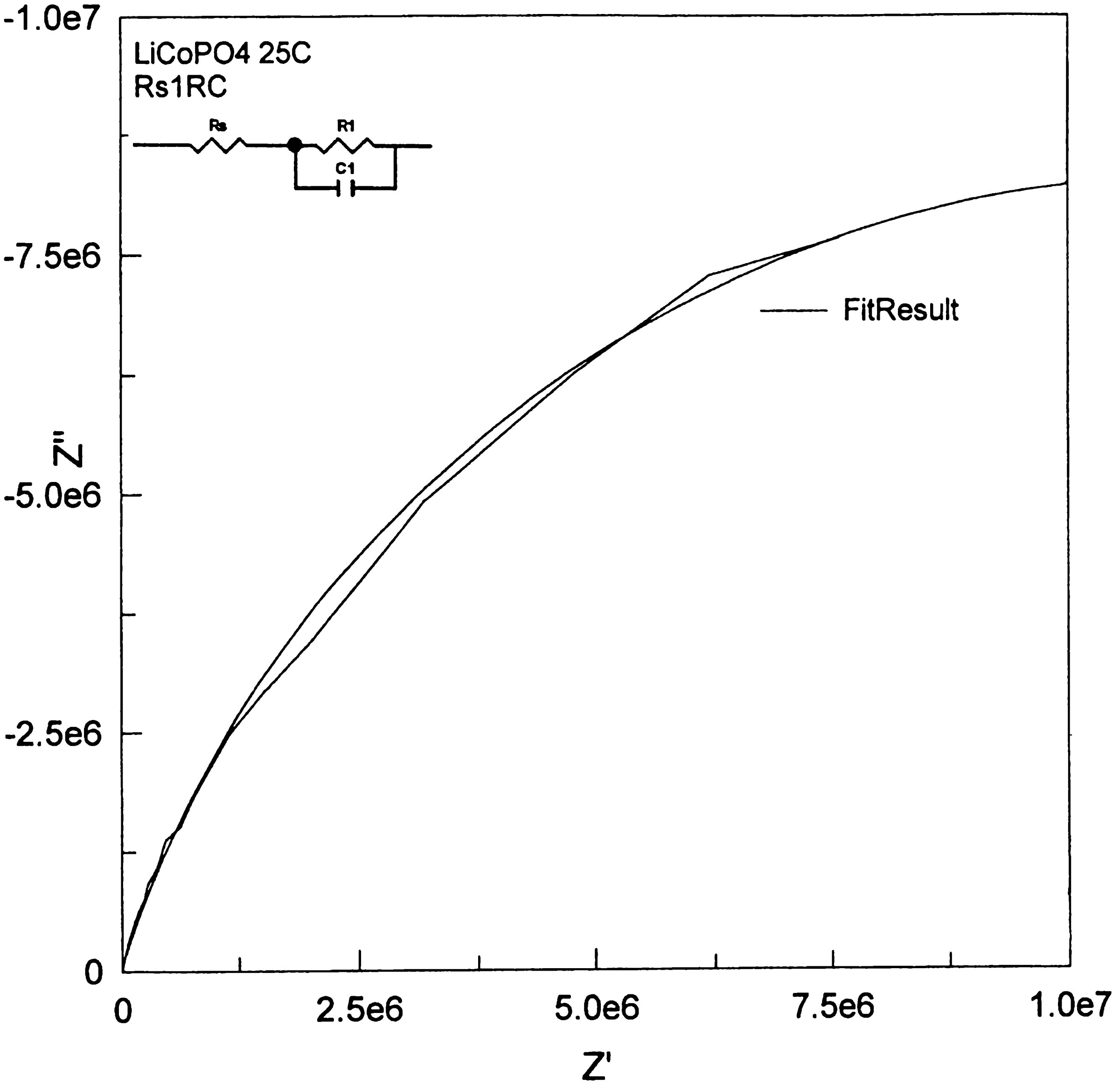

Figure 3.6 Impedance Spectra of $LiCoPO_4$ at 25 °C

At higher temperatures it becomes easier to distinguish the separate components that make up the impedance spectra. Figure 3.7 shows $LiCoPO_4$ at 500 °C. As with higher temperature $LiNiPO_4$, the performance is best fitted with an Rs2RCWo equivalent circuit, where the separate grain, grain boundary and diffusion components are more visible. What is interesting to note is that the bulk impedance of the material appears to be larger than that of the grain boundary as shown by the relatively poor fit. The spectra are suppressed below the x-axis and do not have a constant phase element visible unlike the doped materials shown later.

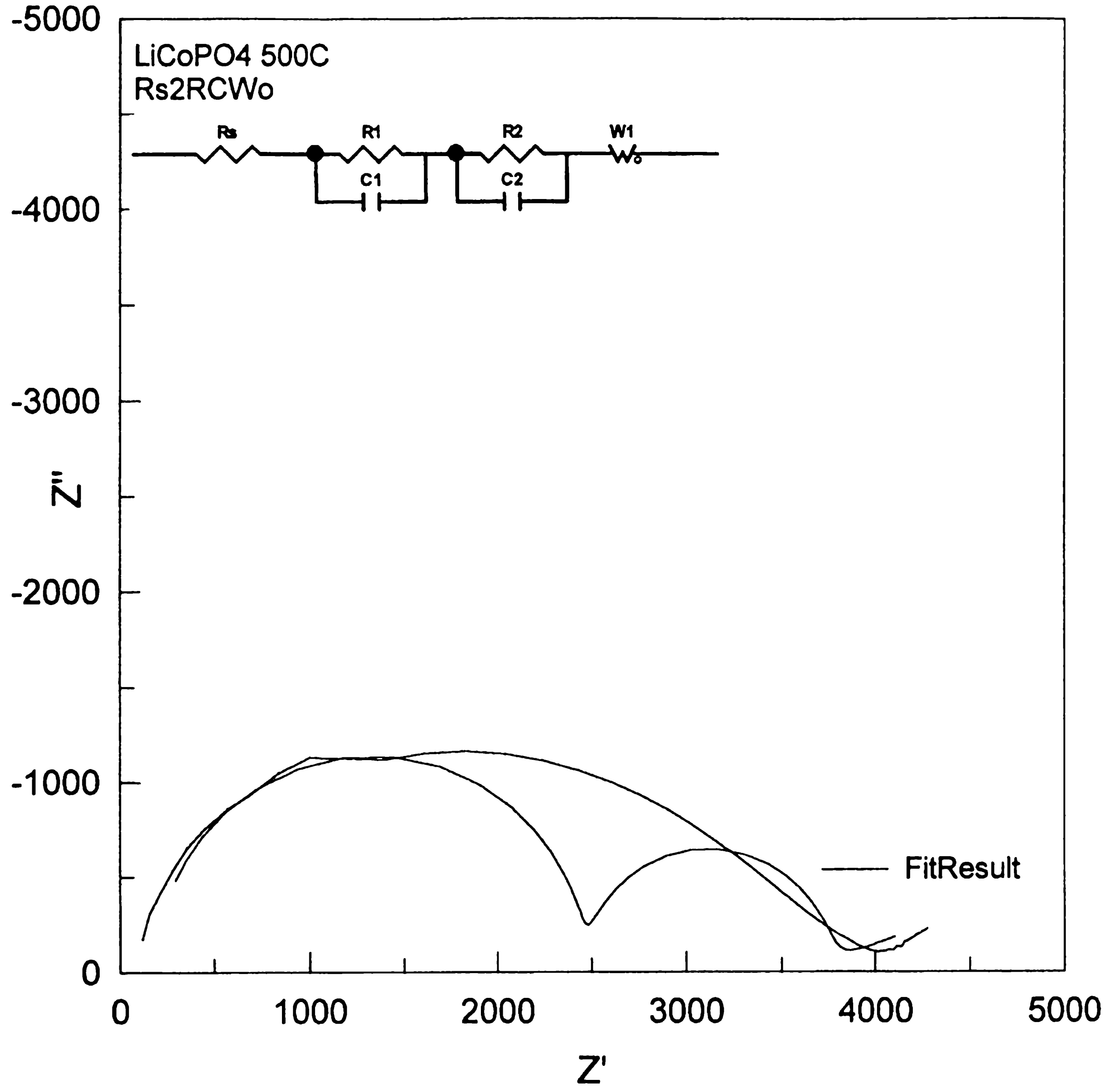

Figure 3.7 Impedance Spectra of $LiCoPO_4$ at 500 °C

The doped materials were much better conductors than pure $LiCoPO_4$. This indicates that either there is a successful substitution of vanadium, potentially saturating between 5 and 10 mol% or the secondary $LiVOPO_4$ phase may significantly enhance grain boundary conduction. The relative increase in conductivity with the secondary phase is quite dramatic. It is possible that the secondary phase is the α-$LiVOPO_4$ polymorph as this is reported to have good Li^+ ion transport due to two crystallographically distinct loosely bound five-coordinate Li ions which lie opposite the phosphate tetrahedra in the interstitial positions.[4,8] Figure 3.8 shows the impedance spectra of all the materials at 400 °C. The spectra reveal decreasing impedance with increasing vanadium. Again there is a suppression of the grain boundary impedance below the x-axis. This is probably related to the heterogeneities in the sample, which cause a dispersion of the time-constants.[5] There is also a CPE component that is visible after the grain boundary semi-circle. This is best represented by a Warburg impedance, which corresponds to diffusion in all materials. Although there has been some electrochemical data published on $LiVOPO_4$ and related materials,[6,7,8] little has been reported on the ionic conductivity of this material.

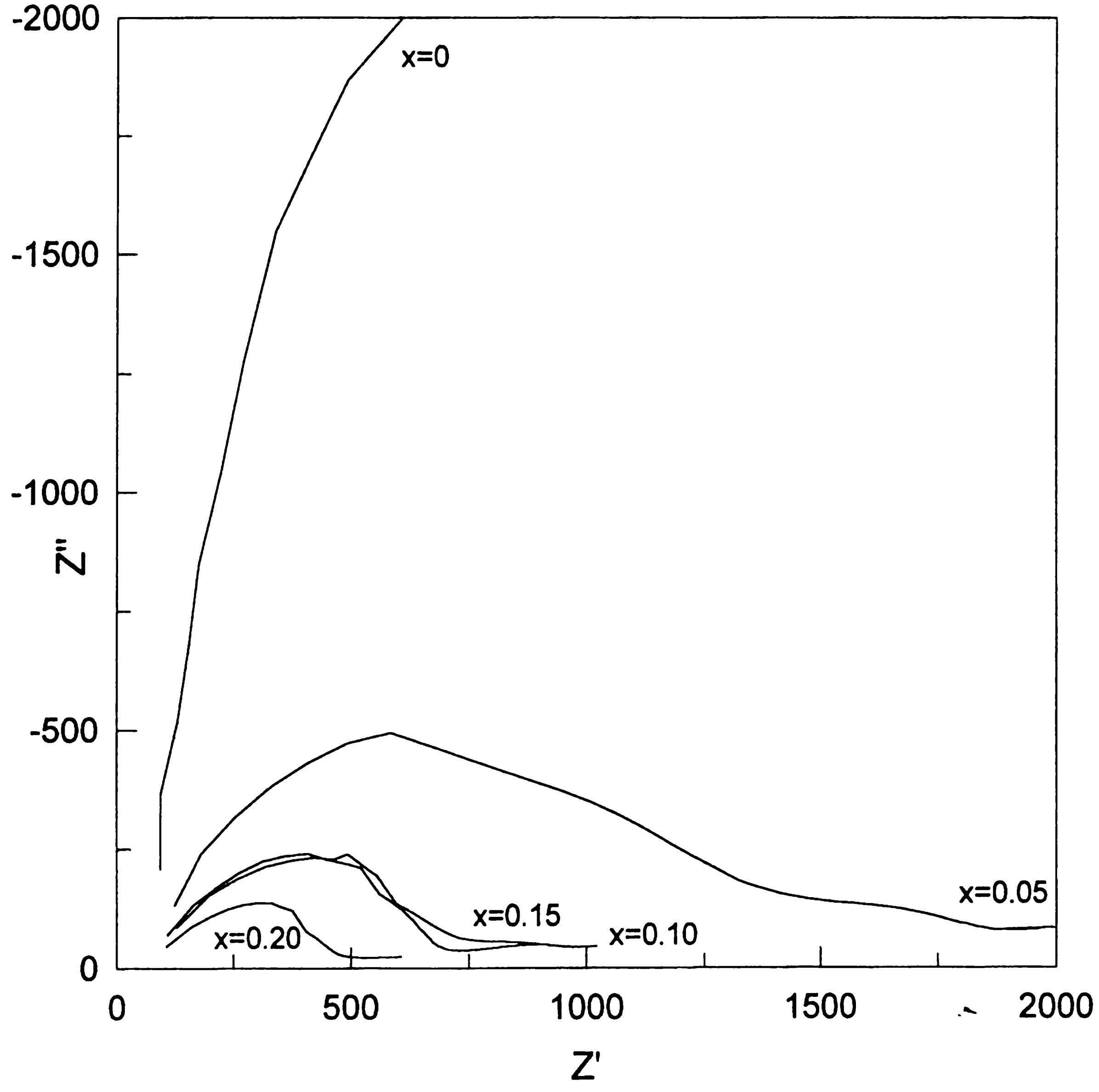

Figure 3.8 Impedance Spectra of $Li_{1-x}Co_{1-x}V_xPO_4$, $0 \leq x \leq 0.2$ at 400 °C

The total conductivity data of $Li_{1-x}Co_{1-x}V_xPO_4$, $0 \leq x \leq 0.2$ is presented in Figure 3.9. Total conductivity (grain and grain boundary) is presented due to the difficulty in determining different components with many of the impedance spectra.

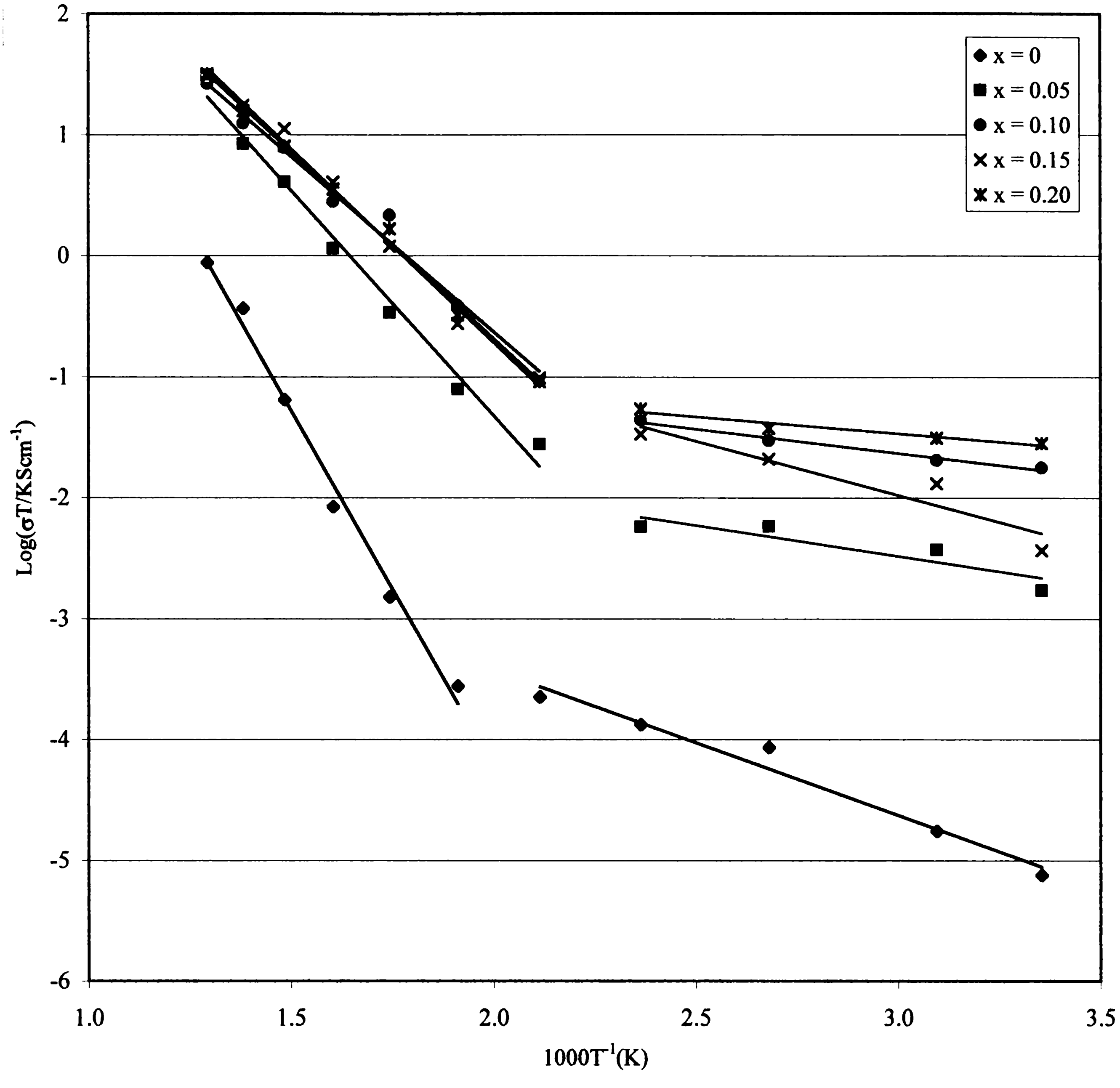

Figure 3.9 Total Conductivity of $Li_{1-x}Co_{1-x}V_xPO_4$, $0 \le x \le 0.2$

Ionic conductivity is predominant in the system and for all the materials there is a change in slope that indicates a transformation into a better ionic conducting phase. This occurs at between 150 and 200 °C for the doped materials, and between 200 and 250 °C for $LiCoPO_4$. It is unknown at this stage what this phase is as no high temperature X-ray diffraction has been attempted. It is also interesting that the temperature at which the change occurs is different for the doped and for single phase $LiCoPO_4$. This may be due to the impedance measurements for $LiCoPO_4$ being inaccurate. If the possible error values for these measurements are taken into account, it brings the reading closer to the temperature observed for the doped materials. Although it was not proven that the substitution was successful using XRD or Raman techniques, overall, the small quantity of vanadium substituted for cobalt acts as a dramatic conduction enhancer. This is more likely to be the result of a successful substitution than enhanced grain boundary performance as the conductivity is improved by almost 3 orders of magnitude even with only 5 mol% vanadium. Percolation theory would hold that normally in a two phase system with phase *a* being a significantly better ionic or electronic conductor than the phase *b*, phase *a* would need to exist in amounts of approximately 30 vol% in order to improve the total conductivity of the two phase system.

The best room temperature conductivity shown by these materials was $Li_{0.80}Co_{0.80}V_{0.20}PO_4$, with a value of 9.48 x 10^{-5} Scm^{-1} in comparison to $LiCoPO_4$ at 2.52 x 10^{-8}.

The activation energy for a material can be calculated given the Arrhenius expression:

$$\sigma_T = A_T \exp(-E_a / kT) \qquad \text{Equation 3.2}$$

Thus:

$$\ln \sigma = A_T - (E_a / kT) \qquad \text{Equation 3.3}$$

There were two activation energies for $LiCoPO_4$ as the slope changed somewhere between 200 and 250 °C. These were calculated using equations 3.3 and 3.4, and Figure 3.9. Between 25 and 200 °C the activation energy is 0.10 eV. Between 250 and 500 °C the slope of the graph is much steeper and the activation energy is 0.53. The general trend for the secondary phase of vanadium oxide phosphate in $LiCoPO_4$ that exists above 5 mol% vanadium doping, is for the slope to decrease and hence the overall activation energy also decreases.

3.3 Electrochemical Data

The theoretical reversible capacity of $LiCoPO_4$ is 167 mAh/g based on the following reaction:

$$LiCo^{II}PO_4 \rightleftharpoons Co^{III}PO_4 + Li^+ + e^- \qquad \text{Equation 3.4}$$

During the course of this work, other investigators examining the potential of this material reported varying results. Amine et al.[9,10] reported a discharge capacity of 80 mAh/g at 4.8V while Okada et al.[11] reported a discharge capacity of 100 mAh/g at 4.8V.

Data from initial experiments on the electrochemical performance of this material were very poor. This was due primarily to the use of EC/DEC/$LiPF_6$ as an electrolyte, which underwent oxidation at higher voltages (5V upper cut off). In order to be able to charge above 4.8V, experiments were undertaken using tetramethylene sulfone (TMS), an unsymmetrical non-cyclic aliphatic sulfone.[12] This material has a very wide stability window of approximately 6V. However it has disadvantage of having a very high viscosity (10.3 cP). Several cells with different salts in combination with TMS were prepared and tested using cyclic voltammetry. These results are in Appendix III. The two salts originally tested were $LiBF_4$ and Flourad™ lithium bisperfluoroethanesulfonimide $LiN(SO_2C_2F_5)_2$ by 3M (hereafter referred to as 3M), which has been specifically designed to operate at higher voltages without decomposition or corrosion of the aluminium current collector.

Figure 3.10 shows the first two discharge curves of a cell using $LiCoPO_4$ as an electrode and $LiBF_4$/TMS as an electrolyte, and also another cell using $LiCoPO_4$ with 3M/TMS as an electrolyte. During testing, the cells were charged at a current of 7.5mA/g to extract lithium from the cathode material, and then discharged at the same current rate to insert lithium ions. Both cell potentials show a discharge plateau at 4.6V. The $LiBF_4$/TMS cell shows the highest discharge capacity of 130 mAh/g, which is the highest value for this material published to date. The charge curves for the two cells are not shown on this graph. The cell with $LiBF_4$/TMS showed a high charge capacity of 350mAh/g, which is almost three times its discharge capacity. The high charge capacity is probably due to electrolyte decomposition at higher voltages, which would contribute to poor cycling performance. The 3M/TMS cell behaves similarly with a charge capacity of 280mAh/g. The second charge was significantly lower for both cells, with a value of 220 mAh/g for the $LiBF_4$ cell in comparison to 120 mAh/g to 3M/TMS.

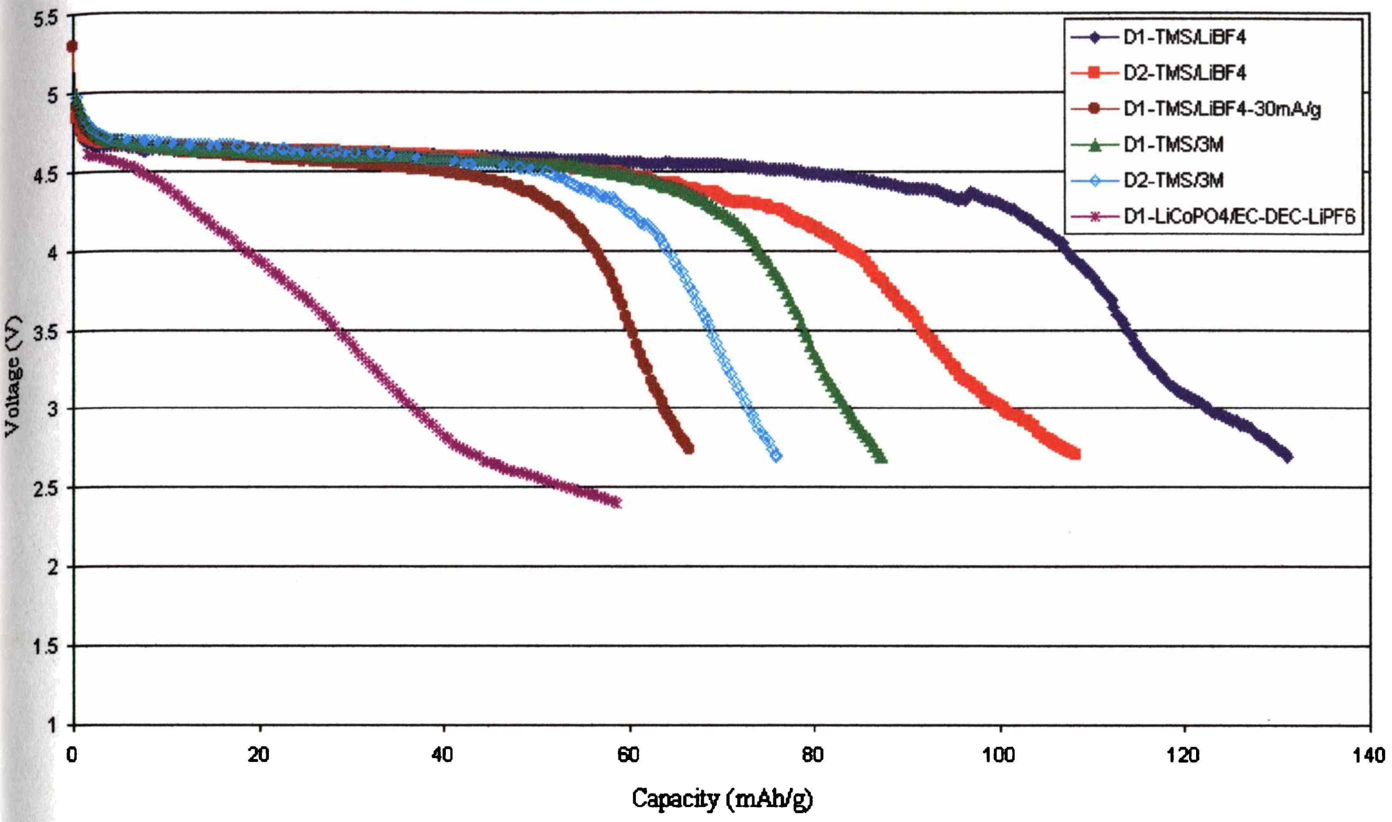

Figure 3.10 Discharge Curves for $LiCoPO_4$ Using Different Electrolyte Formulations

The cycling schedule varied the currents to see if the capacity of the cell was rate dependent. When the current was increased to 30 mA/g for the first cycle, the first discharge capacity was considerably lower for both cells, which would indicate kinetic limitations at the cathode. During cycling, the cells had a steady decrease in capacity to eventually cycle at 20 mAh/g by the 20th cycle. This coincided with increases in current densities every few cycles. When the discharge current was dropped back to 7.5 mA/g, however, there was little recovery in discharge capacity, which indicates that the kinetics are not the factor limiting performance. This indicates that electrolyte breakdown, cathode decomposition or disconnection had occurred, leading to poor capacity even at low current rates.

Figure 3.10 also shows the first discharge curve for a cell with a $LiCoPO_4$ electrode and $EC/DEC/LiPF_6$ as an electrolyte. This cell was one of the first constructed and again had a first discharge capacity approximately one third the first charge. This cell was charged with a constant current to 5.2V and then held with a constant voltage while the current tapered off to maximise charge without dramatically decomposing the electrolyte. This method can be useful but was inadequate for the high voltages required to fully charge this material. It is likely that there was severe oxidation of the electrolyte during cycling. The discharge capacity is considerably less. This can be seen by the slope of the discharge curve, which also shows the insertion of lithium at lower voltages than that of cells using TMS as an electrolyte solvent. Solvent decomposition is believed to be the major component responsible for the catalytic decomposition on the porous surface of composite cathodes.[13]

3.4 Particle Size Analysis and BET Surface Area

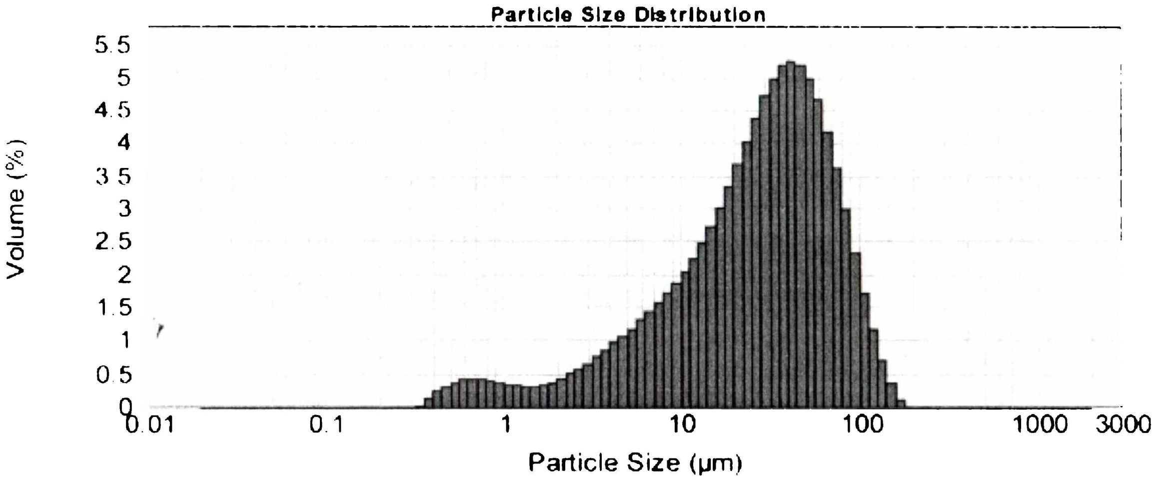

Figure 3.11 Particle Size Distribution of $LiCoPO_4$

$LiCoPO_4$ has a broad distribution of particle size ranging from small to very large particles (Figure 3.11) and a relatively low surface area by BET of $0.35m^2g^{-1}$. The particle size and the surface area can dramatically affect the electrochemical performance of a material, particularly when the bulk phase has an inherently low conductivity. With finer particle size and larger surface area the cathode material would have better overall contact of active surface with electrolyte and also with the network of fine carbon particles added as an electronic conductivity enhancer. It also reduces the length of the diffusion pathways for lithium ions and electrons from the surface into the bulk. A broad distribution of particles can lead to non-equilibrium effects during charge and discharge because of the lower bulk diffusion pathway in larger particles compared with smaller particles. This could result in overall less cell resistance and better cell performance. The SEM pictures in section 3.4.1

show the particle size at the 4 μm level. Resolution at 75μm shows the larger size particles although this is not shown here.

3.4.1 SEM and EDX Analysis

Although the capacity of $LiCoPO_4$ is considerably better than $LiNiPO_4$ (Chapter 4), and the discharge voltage is very attractive, its cycling performance is still relatively poor. $LiCoPO_4$ has the worst room temperature conductivity measured for all the materials. In an attempt to improve the cathode performance of $LiCoPO_4$, UFC-3N, an ultra fine colloidal carbon, was used as the electronic conductivity enhancer in the electrode. The UFC is made from carbon black and organic polymer such as polyvinylalcohol, polyvinylpyrolidone, and sodium polyacrylate. The average particle size of this material is 0.15μm and it gives a far better overall inter-particle contact. [14] This can be seen in the SEM micrographs; Figure 3.12 shows a milled $LiCoPO_4$/carbon cathode slurry deposited onto an aluminium substrate and Figure 3.13 shows the $LiCoPO_4$/UFC material. It is clear that the UFC material covers the cathode material better. The darker patches in both figures is the carbon. In Figure 3.12 carbon and $LiCoPO_4$ are mainly separate particles in comparison to Figure 3.13 where the $LiCoPO_4$ particles are mostly covered by a thin carbon layer.

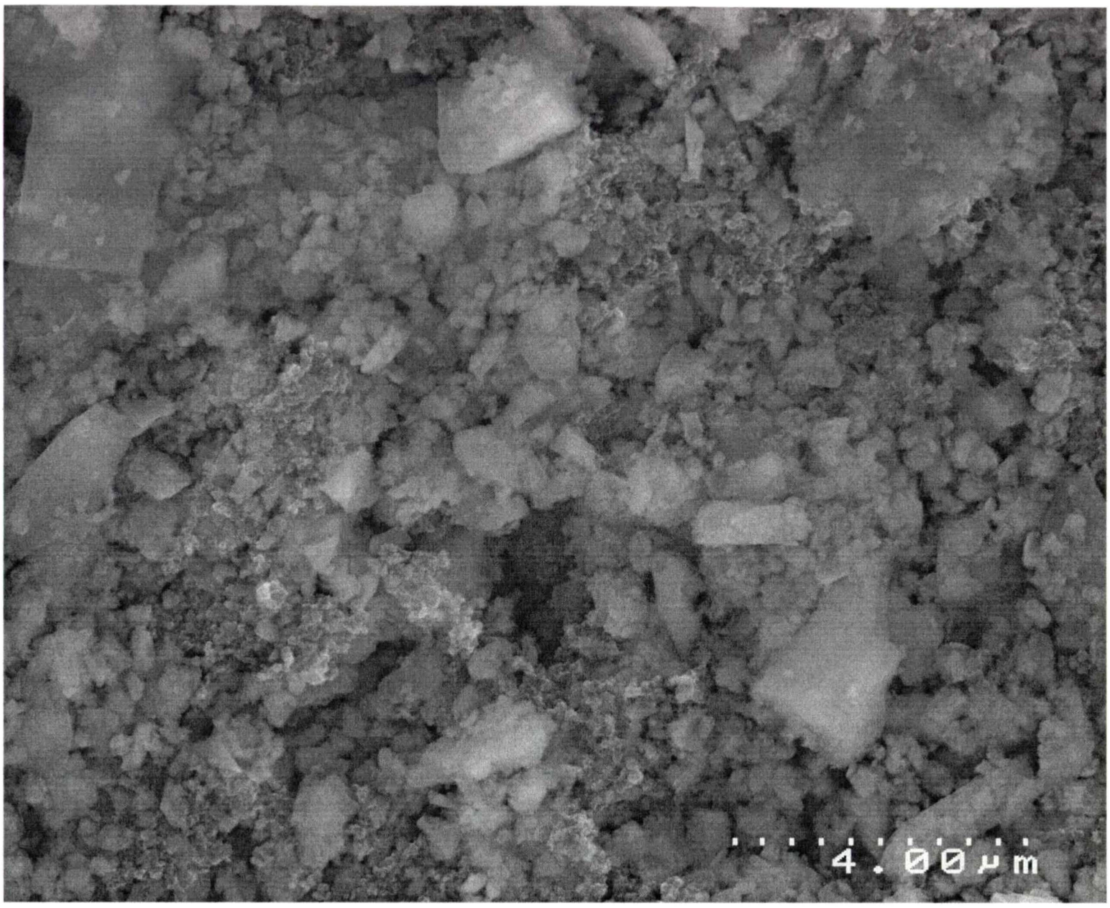

Figure 3.12 SEM Micrograph of $LiCoPO_4$/Carbon

Extensive research on $LiFePO_4$ has found that limitations in the practical capacity of this material are in part due to poor electronic conductivity.[15,16] $LiFePO_4$ was limited to a practical capacity of 110 mAh/g as only 0.6 Li per unit formula could be reversibly inserted and extracted, rather than its theoretical capacity of 170 mAh/g. New synthesis routes, and also the addition of a carbon/polymer mixture, an electronically conductive substance that is added during the synthesis before the crystallisation of $LiFePO_4$ have addressed this.[17] This enables close to 100% of the theoretical capacity to be reached.

However, the results of the cells constructed using UFC-3N are not shown here as the discharge capacity and the cell cycling performance was extremely poor.

EDX analysis was performed and the results confirmed the chemical composition. The analysis was performed on the particles in the area shown in Figure 3.12. Analysis of the particles in Figure 3.13 showed little difference.

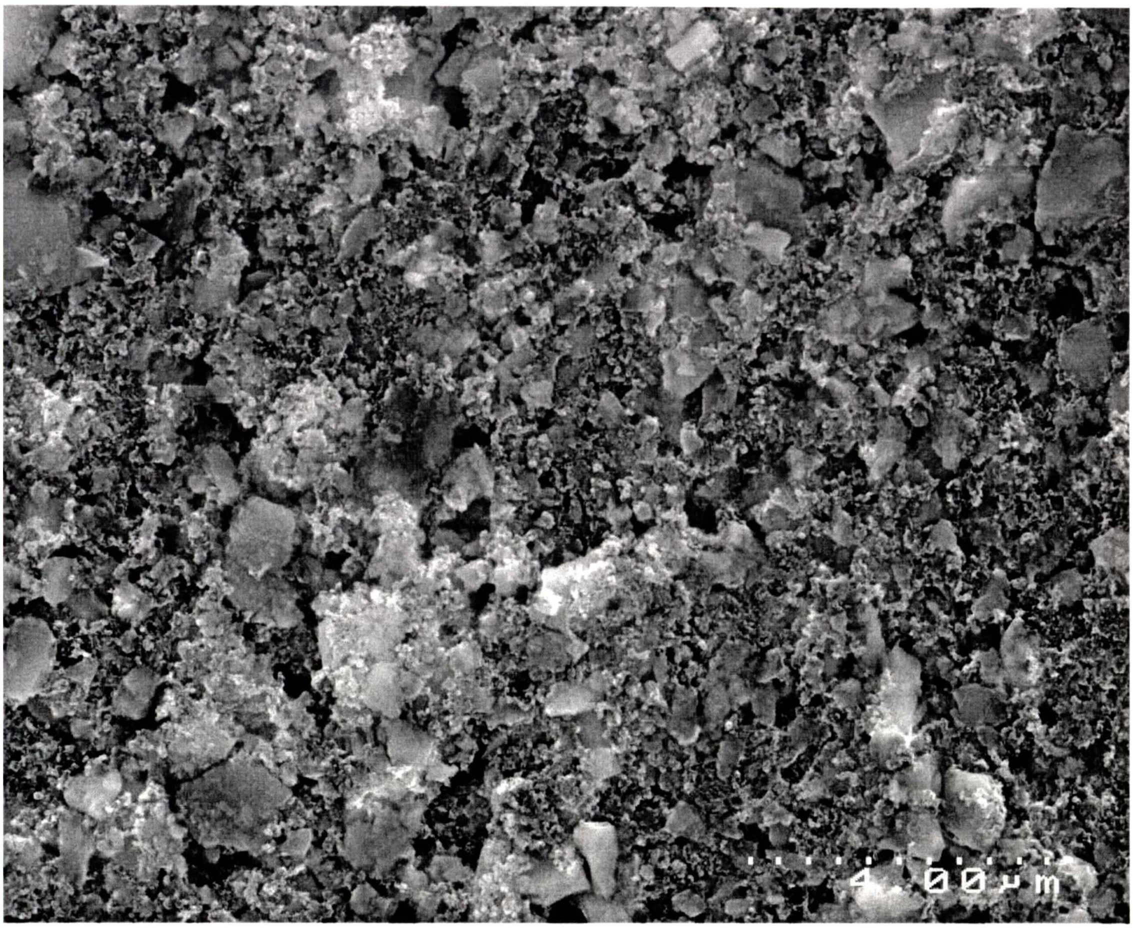

Figure 3.13 SEM Micrograph of $LiCoPO_4$/UFC

The main limiting factor for this material in application as a cathode would appear to be the stability of the high redox potential of the Co^{3+}/Co^{2+} couple in the presence of the polyanion $(PO_4)^{3-}$. As has been shown for $LiFePO_4$, [18,19] the relatively strong covalence of the PO_4 tetrahedron of the olivine compounds stabilise the transition metal redox couples at the octahedral sites i.e the potentials are made more positive by the presence of the PO_4 tetrahedron in the structure due to the strong polarisation of the oxygen atoms towards the P cation and subsequent lowering of the covalent component in the M-O bond by the inductive effect. This produces the high voltages required to effectively delithiate this material. The stronger the π-bond M-O covalence, the higher the energy of the M^{3+}/M^{2+} couple and hence, the lower the OCV. The cation which shares a common oxygen nearest neighbour with M in an M-O-P linkage determines the strength of the M-O covalency via the inductive effect. The stronger the P-O bonding, the weaker the M-O bonding, and hence the larger the OCV.

3.5 References

[1] I. Abrahams and K. S. Easson. *Acta Cryst.*, C49, p925, **1993.**

[2] A. R. West, in "Solid State Electrochemistry" ed. P. G. Bruce, *Cambridge University Press*, Cambridge, p7, **1995.**

[3] E. J. Baran, M. B. Vassallo and K-H. Lii, *J. Raman Spec.*, 25, p199, **1994.**

[4] K. H. Lii, C. H. Li, C. Y. Cheng and S. L. Wang, *J. Solid State Chem.*, 95, (2), p352, **1991.**

[5] J. Hwang, K. S. Kirkpatrick, T. O. Mason and E. J. Garboczi, *Solid State Ionics*, 98, p93, **1997.**

[6] N. Dupre, J. Angenault, G. Wallez and M. Quarton, *in 196th Meeting of the Electrochem. Soc.*, Honolulu, Oct, Abstract no. 206, **1999.**

[7] T. A. Kerr, J. Gaubicher and L. F. Nazar, *in 196th Meeting of the Electrochem. Soc.*, Honolulu, Oct, Abstract no. 249, **1999.**

[8] T. A. Kerr, J. Gaubicher and L. F. Nazar, *Electrochem. and Solid-State Letters*, 3, (10), p460, **2000.**

[9] K. Amine, H. Yasuda and M. Yamachi, *in 196th Meeting of the Electrochem. Soc.*, Honolulu, Oct, Abstract no. 277, **1999.**

[10] K. Amine, H. Yasuda and M. Yamachi, *Electrochem. and Solid-State. Lett.*, 3, (4), p178, **2000.**

[11] S. Okada, S. Sawa, M Egashira and J. Yamaki, *in 196th Meeting of the Electrochem. Soc.*, Honolulu, Oct, Abstract no. 232, **1999.**

[12] K. Xu and C. A. Agnell, *J. Electrochem. Soc.*, 145 (4)L70, **1998.**

[13] J. M. Tarascon and D. Guyomard, *J. Electrochem. Soc.*, 140, p3071, **1993.**

[14] T. Takei, A. Kozawa and R. V. Mostev, *ITE Battery Newsletter*, 4, p55, **1997.**

[15] N. Ravet, J. B. Goodenough, S. Besner, M. Simoneau, P. Hovington and M. Armand, *in 196th Meeting of the Electrochem. Soc.*, Honolulu, Oct, Abstract no. 127, **1999.**

[16] S. Besner, Y. Choquette, J. F. Magnan, F. Allaire, A. Vallee, E. Potvin and P. Hovington, *in 196th Meeting of the Electrochem. Soc.*, Honolulu, Oct, Abstract no. 204, **1999.**

[17] N. Ravet, Y. Chouinard, J. F. Magnan, S. Besner, M. Gauthier, and M. Armand, *IMLB X Meeting,* Lake Como, Italy, Abstract no 166, **2000.**

[18] A. K. Padhi, K.S. Nanjundaswamy and J.B. Goodenough, *J. Electrochem. Soc.*, 144, 5, p1188-1194. **1997.**

---

[19] J. B. Goodenough, A. K. Padhi, K. S. Nanjundaswamy and C. Masquelier, U.S. Patent No. 5,910,382, **1999.**

4 Lithium Nickel Phosphate - $LiNiPO_4$

4 Lithium Nickel Phosphate - $LiNiPO_4$

4.1 Characterisation

Firing $LiNiPO_4$ in air showed via X-ray diffraction and Raman spectroscopy that a single solid phase was formed according to the following reaction:

$$Li_2CO_3 + 2NH_4H_2PO_4 + 2NiO \xrightarrow{O_2} 2LiNiPO_4 + 2NH_3 + 3H_2O + CO_2 \qquad \text{Equation 4.1}$$

4.1.1 X-Ray Diffraction

XRD results show that an orthorhombic phase formed (space group: 62, *Pnma*) for all of the $Li_{1-x}Ni_{1-x}M_xPO_4$ materials. The partial substitution of Ti^{3+}, Fe^{3+}, Cr^{3+}, Co^{3+}, Y^{3+} and Sc^{3+} for Ni^{2+} was attempted. Results for Sc^{3+} and Ti^{3+} will be discussed in detail.

Results of the Rietveld refinement of the XRD data for pure $LiNiPO_4$ are shown in Figure 4.1 and Table 4.1. The Rietveld analysis was performed using Fullprof 98® software. Initial structural and thermal parameters were taken from the data from Abrahams and Easson as a starting model for the refinement.[1] Scale and background parameters were refined initially followed in subsequent iterations by cell, zero point and peak shape parameters. The atomic positions were fixed while the cell parameters and then the occupancy factors for the nickel atom were refined. Once the cell parameters and the occupancy factors were established, the refinement of the atomic positions for all atoms was performed. The phosphorus and then the transition metal nickel atomic positions having the larger scattering factors were refined first followed by the oxygen.

Titanium doped $LiNiPO_4$ were also indexed in the *Pnma* space group, and the diffraction patterns for these set out in Appendix II. The data for the substituted Ti^{3+} and Sc^{3+} are summarised in Table 4.2 and Table 4.3 respectively. When titanium is used as a substitute, a secondary phase is evident with increasing dopant content (see the figures in Appendix II). This is most obvious when the peak position 2θ is approximately 27°. It is also evident that from the lack of change in the cell parameters of $LiNiPO_4$ that titanium was probably not dissolved in the system. As Ti^{3+} was substituted for Ni^{2+}, a decreasing amount of lithium was used to maintain charge balance.

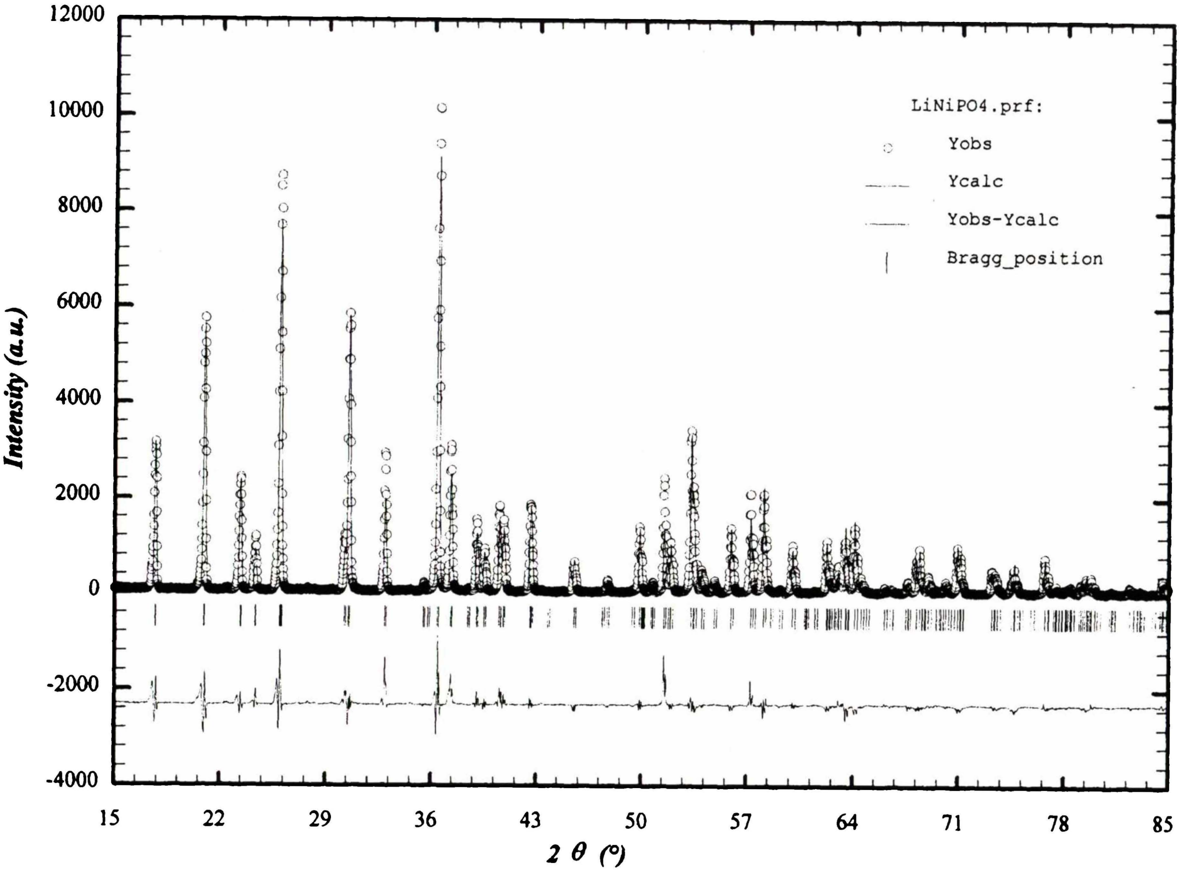

Figure 4.1 Structure Refinement of $LiNiPO_4$

Substituting Ni^{2+} with higher valency cations will induce either cation vacancies or anion interstitials, while doping with lower valency cations induces either cation interstitials or anion vacancies assuming there is no other charge compensating mechanism. Due to the size of the polyanion in this case and because Ni^{2+} is unlikely to be reduced creating holes, it was assumed any successful substitution with higher valency cations would induce cation vacancies. Different cations were also tried to determine if success depended on the ionic radius of the dopant ion. Due to the failure of doping with Ti^{3+}, Fe^{3+}, Cr^{3+}, Co^{3+} with ionic radii ranging from 0.55 to 1.02 Å compared with Ni^{2+} at 0.69 Å, it was postulated that what might be occurring during the reaction is reduction of the 3+ dopant to a 2+ state, so the cations Sc^{3+} and Y^{3+} which can only exist in the 3+ state were substituted for Ni^{2+}. However, this also proved unsuccessful.

Table 4.1 Refined Crystallographic Parameters for LiNiPO$_4$ (P*nma*) - X-ray diffraction data for 252 reflections and 25 variables.

Atom	*x*	*y*	*z*	Occupancy	B$_{iso}$ (Å^2)
Ni	0.2761 (2)	0.25 *	0.9813 (4)	1.065 (4)	0.96 *
P	0.0946 (4)	0.25 *	0.4173 (7)	1.000 *	0.81 *
O	0.1022 (7)	0.25 *	0.7435 (13)	1.000 *	0.3 *
O	0.4524 (7)	0.25 *	0.1966 (13)	1.000 *	0.4 *
O	0.1649 (5)	0.0434 (8)	0.2802 (9)	2.000 *	0.8 *
Li	0.0000 *	0.0000 *	0.0000 *	1.000 *	2.8 *

a = 10.0317, b = 5.8579, c = 4.6782, * = Fixed Parameters

V = 274.912 Å^3 , wRp = 17.3, Rp =12.7 , χ2 =9.13

Table 4.2 Ti^{3+} doped LiNiPO$_4$ Refinement Summary

Parameter	LiNiPO$_4$	Ti = 0.05	Ti = 0.10	Ti = 0.15	Ti = 0.20
a	10.0317 (3)	10.0318 (4)	10.0309 (4)	10.0290 (5)	10.0321 (6)
b	5.8579 (2)	5.8572 (2)	5.8581 (3)	5.8575 (3)	5.8604 (4)
c	4.6782 (2)	4.6776 (2)	4.6782 (2)	4.6771 (3)	4.6792 (3)
Volume (Å^3)	274.912 (11)	274.845 (16)	274.899 (17)	274.755 (22)	275.098 (26)
Ni Site Occupancy	1.065 (4)	1.054 (6)	1.060 (7)	1.051 (8)	1.056 (9)

The lack of change in cell parameters in LiNiPO$_4$, (Table 4.3), indicate that the substituting Sc^{3+} results in the formation of a secondary phase. The refined structures of the scandium materials are shown in Appendix II. Similar to the titanium dopant a scandium phosphate phase $ScPO_4$ formed, which increases with increasing levels of substitution. This is most obvious when 2θ is approximately 27°.

Table 4.3 Sc^{3+} doped $LiNiPO_4$ Refinement Summary

Parameter	$LiNiPO_4$	Sc = 0.05	Sc = 0.10	Sc = 0.15	Sc = 0.20
a	10.0317 (3)	10.0355 (4)	10.0370 (5)	10.0419 (6)	10.0404 (7)
b	5.8579 (2)	5.8580 (2)	5.8588 (3)	5.8574 (4)	5.8570 (4)
c	4.6782 (2)	4.6799 (2)	4.6812 (3)	4.6819 (3)	4.6822 (4)
Volume (Å^3)	274.912 (11)	275.122 (15)	275.276 (22)	275.387 (28)	275.345 (33)
Ni Site Occupancy	1.065 (4)	1.052 (5)	1.071 (7)	1.051 (9)	1.064 (10)

The scandium data shown is for non-balanced, non-stoichiometric dopant quantities to maintain the lithium amounts to determine their effects on dopant success. In this case, a scandium phosphate phase forms at low dopant quantities. Due to the excess lithium, a lithium scandium phosphate forms at higher dopant quantities and also an unreacted nickel oxide phase that increases with dopant content.

4.1.2 Raman Spectroscopy

Raman spectroscopy was used as well XRD to characterise and identify any second phases with substitution of the Ni^{2+} cation in $LiNiPO_4$. Factor group analysis was used to determine the following irreducible representations for the orthorhombic $LiNiPO_4$ structure with Z = 4, where Γ_{op} are the optical vibrational modes and Γ_{ac} are the acoustic modes, R = Raman active, ir = infrared active and i = inactive.

Orthorhombic $LiNiPO_4$

Space Group: P*nma* (No. 62)

$$\begin{array}{lcccccccc} \Gamma_{op} = & 13A_g & + 8B_{1g} & + 13B_{2g} & + 8B_{3g} & + 8A_u & + 12B_{1u} & + 7B_{2u} & + 12B_{3u} \\ & (R) & (R) & (R) & (R) & (i) & (ir) & (ir) & (ir) \end{array}$$

$$\Gamma_{ac} = B_{1u} + B_{2u} + B_{3u}$$

A total of 42 Raman active, 31 infrared active and 8 inactive modes.

The Raman spectra of substituted Ti^{3+} for Ni^{2+} in $LiNiPO_4$ are shown in Figure 4.2. Band positions and relative intensities of the observed spectra are listed in Table 4.4. For the Raman spectrum of $LiNiPO_4$, there are a total of 15 bands observed at room temperature (of the 42 predicted Raman active modes from factor group analysis). The bands are assigned with reference to the relative wavenumber positions and are compared to the reported assignments of the spectra of $Li_3Fe_2(PO_4)_3$ and $LiTi_2(PO_4)_3$ and NiO.[2,3,4] The Raman spectra of Ti-doped $LiNiPO_4$ (Figure 4.2) show the presence of a secondary phase, characterised by a strong band at 784 cm^{-1}.

With increasing Ti-dopant concentration there is an increase in the relative proportion of the secondary phase. Figure 4.3 shows the comparison of the Raman spectra of $LiNiPO_4$, $Li_{0.80}Ni_{0.80}Ti_{0.20}PO_4$ and the subtraction spectrum of the two. It can be seen that at 20 mol% Ti, the secondary phase is predominant in the spectrum. The spectrum of the secondary phase matches that of the secondary phase reported by Cretin et al.[2] for the system $Li_{1.3}Al_{0.3}Ti_{1.7}(PO_4)_3$ prepared by sol gel method and sintered at 950°C. Cretin et al. did not assign this secondary phase and report that it was unobserved by X-ray diffraction. It is likely this secondary phase is a titanium phosphate phase as it increases with increase in Ti-dopant concentration and the major band at 784 cm^{-1} is within the range for PO_4 stretching vibrations.

The Raman results agree with the XRD results and reveal that any dopants are most likely insoluble in the $LiNiPO_4$ structure under the synthesis conditions used.

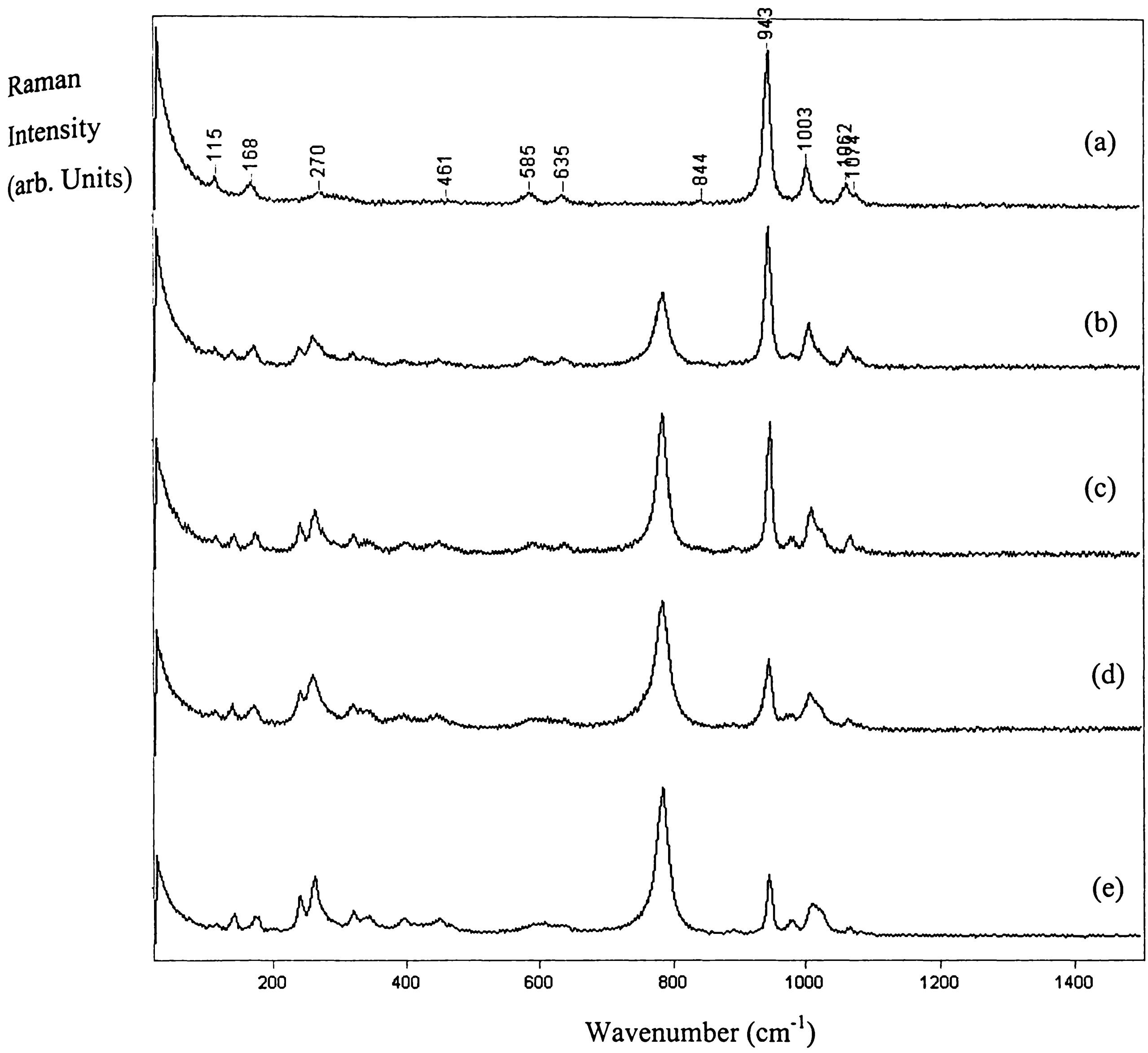

Figure 4.2 Raman Spectra of $Li_{1-x}Ni_{1-x}Ti_xPO_4$, $0 \leq x \leq 0.2$, where x = 0(a), 0.05(b), 0.10(c), 0.15(d), 0.20(e)

Table 4.4 Raman Band Positions of $Li_{1-x}Ni_{1-x}Ti_xPO_4$, $0 \leq x \leq 0.2$

0	0.05	0.10	0.15	0.20	$LiTi_2(PO_4)_3$ Ref.3	Assignment Ref.2,3,4
			107 vw	108 vw		
115 w	113 w	117 w	115 w	116 w		LNP (lattice)
	139 w	142 w	139 w	141 w	139	*
168 w	163 sh	165 sh				LNP (lattice)
	171 w	175 w	172 w	175 w	177	*
		199 vw	198 vw	201 vw	195	*
	239 w	241 m	242 m	241 m	240	*
270 w	260 m	263 m	260 m	262 m		LNP (lattice)
	273 sh	275 sh	277 sh	276 sh	274	*
		293 vw		291 w		
305 sh						LNP (lattice)
	320 w	322 w	319 w	320 w	310	*
365 vw	342 w,b	345 w,b	343 w	343 w	352	LNP (NiO_6)
		369 vw				
413 w,b	396 w	400 w,b	395 w,b	397 w,b	431	LNP (NiO_6 and PO_4 bending)
461 vw	449 w	450 w,b	447 w,b	450 w,b	448	LNP (NiO_6 and PO_4 bending)
		469 sh		469 sh		
	497 vw					
		534 vw			548	*
585 w	588 w	589 w,b	590 w,b	590 w,b	589	LNP (LiO_6 and PO_4 bending)
				608 w,b		
635 w	636 w	639 w	636 w,b	638 w,b	657	LNP (LiO_6 and PO_4 bending)
	785 m	785 s	784 s	785 s	784*	*
844 vw	861 vw	842 vw	853 vw	846 vw		LNP (PO_4 stretching)
		892 vw	891 vw	893 vw		*
943 s	945 s	947 s	947 m	946 m	968	LNP (PO_4 stretching)
	980 w	981 w	978 vw	980 w	987	*
1003 m	1006 m	1009 m	1008 m	1011 m	1006	LNP (PO_4 stretching)
	1023 sh	1014 sh			1016	*
		1027 sh	1025 sh	1025 w		*
1062 m	1063 w	1069 w	1066 w	1067 w	1065	LNP (PO_4 stretching)
1074 w	1081 sh	1084 vw	1084 vw	1082 vw	1093	LNP (PO_4 stretching)
1289 vw	1294 vw	1295 vw				LNP (PO_4 stretching)

vw = very weak, w = weak, m = medium, s = strong, b = broad, sh = shoulder, relative intensity.

* = secondary phase, LNP = orthorhombic $LiNiPO_4$.

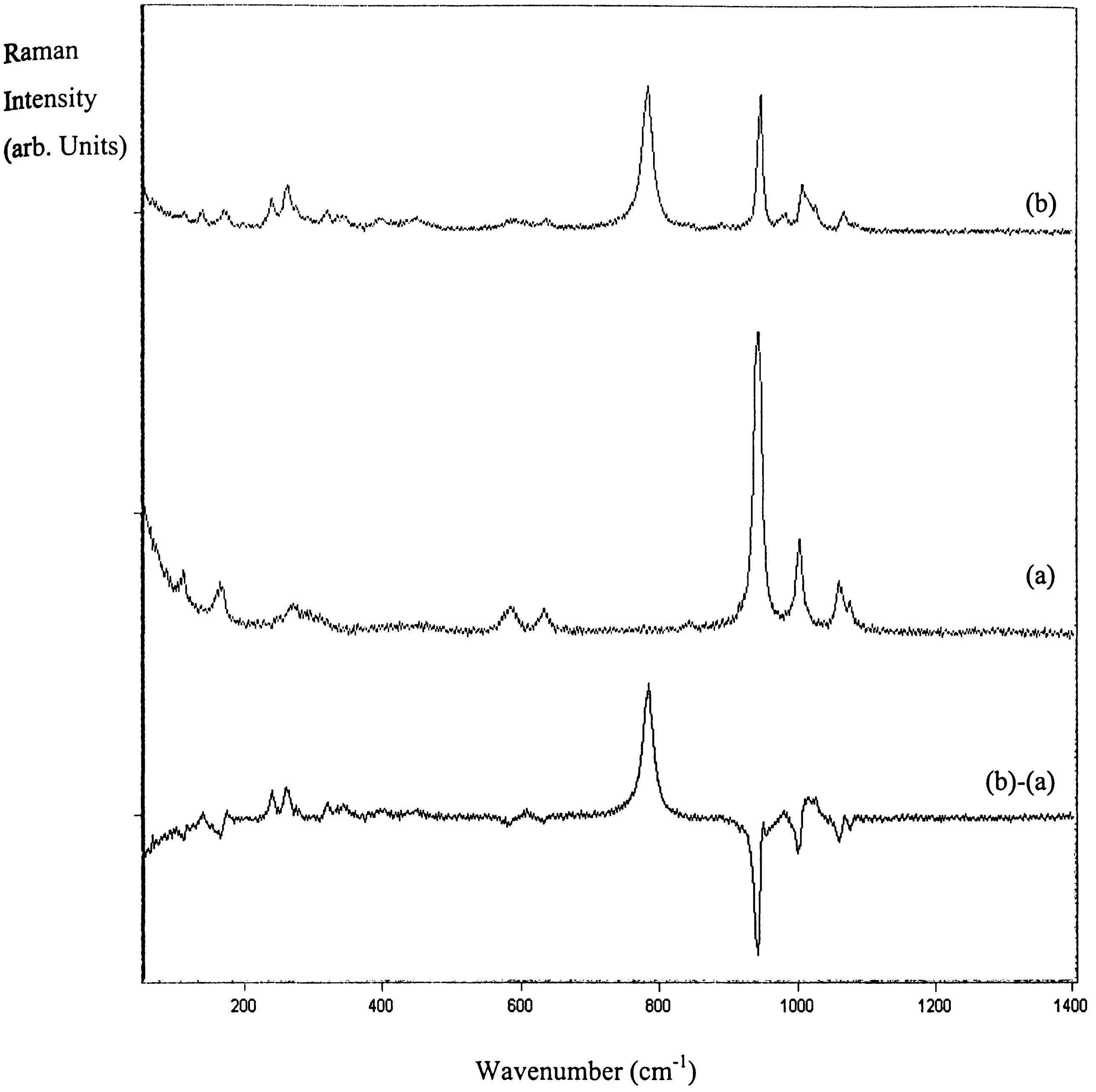

Figure 4.3 Raman Spectra of $LiNiPO_4$ (a), $Li_{0.90}Ni_{0.90}Ti_{0.10}PO_4$ (b) and Subtraction Spectrum of (b) - (a)

4.2 AC Impedance

4.2.1 Bulk Density Measurements

The bulk density of the pellets sintered for AC Impedance measurement was undertaken as per the method described in Section 2.4. During the various firing regimes for different dopants, it had been suspected that the density changed with dopant and dopant content. Using titanium as an example, the bulk density of the sample decreased with increasing dopant content (Figure 4.4). AC impedance measurements were performed only on the titanium doped $LiNiPO_4$. Because the bulk density decreased with dopant content, the sintering temperature was raised to 900 °C for all samples. Bulk density measurements were taken and for all results dividing by the actual density and multiplying by the theoretical density corrected the conductivity measured. Pellets made from this material were bright yellow in colour for $LiNiPO_4$, and this lightened with increasing Ti dopant content.

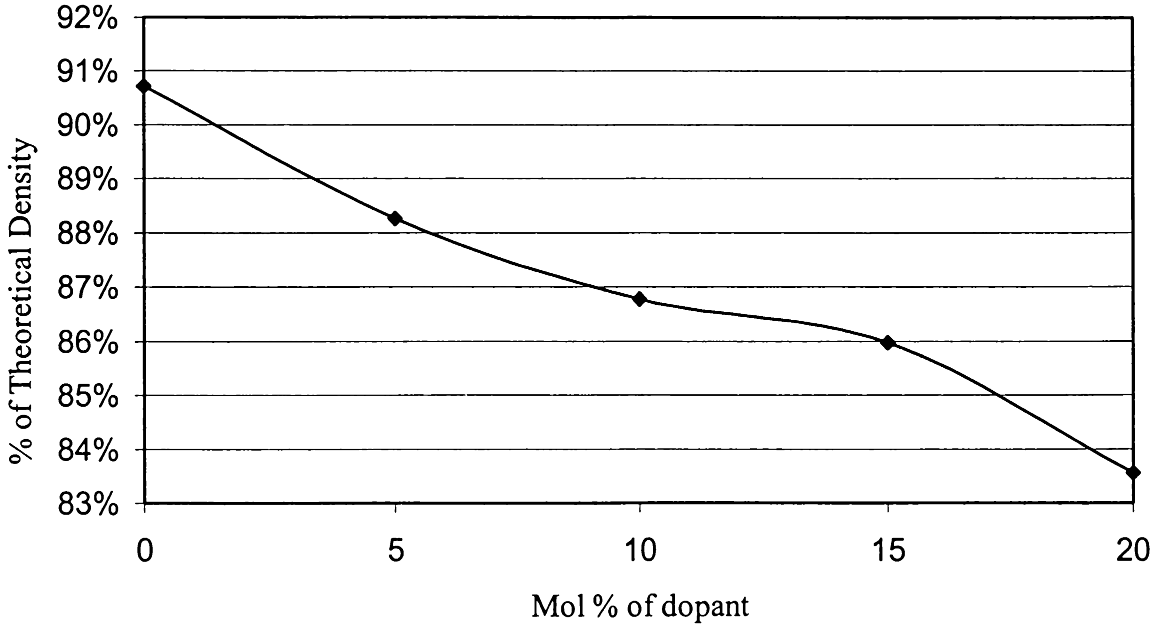

Figure 4.4 Bulk Density of $Li_{1-x}Ni_{1-x}Ti_xPO_4$, $0 \leq x \leq 0.2$

4.2.2 Circuit Modelling

Doped LiNiPO4 has an increasing secondary phase with increasing dopant content as determined by XRD and Raman. This means that potentially the ionic conduction may be different depending upon the performance of the second phase, and how it, the primary phase, and the grain boundary interfaces interact. Initial AC impedance measurements of LiNiPO4 revealed a very poor conductivity, so the titanium doped samples were measured as well to determine if differing amounts of a secondary phase would perhaps enhance or impede conductivity at various temperatures.

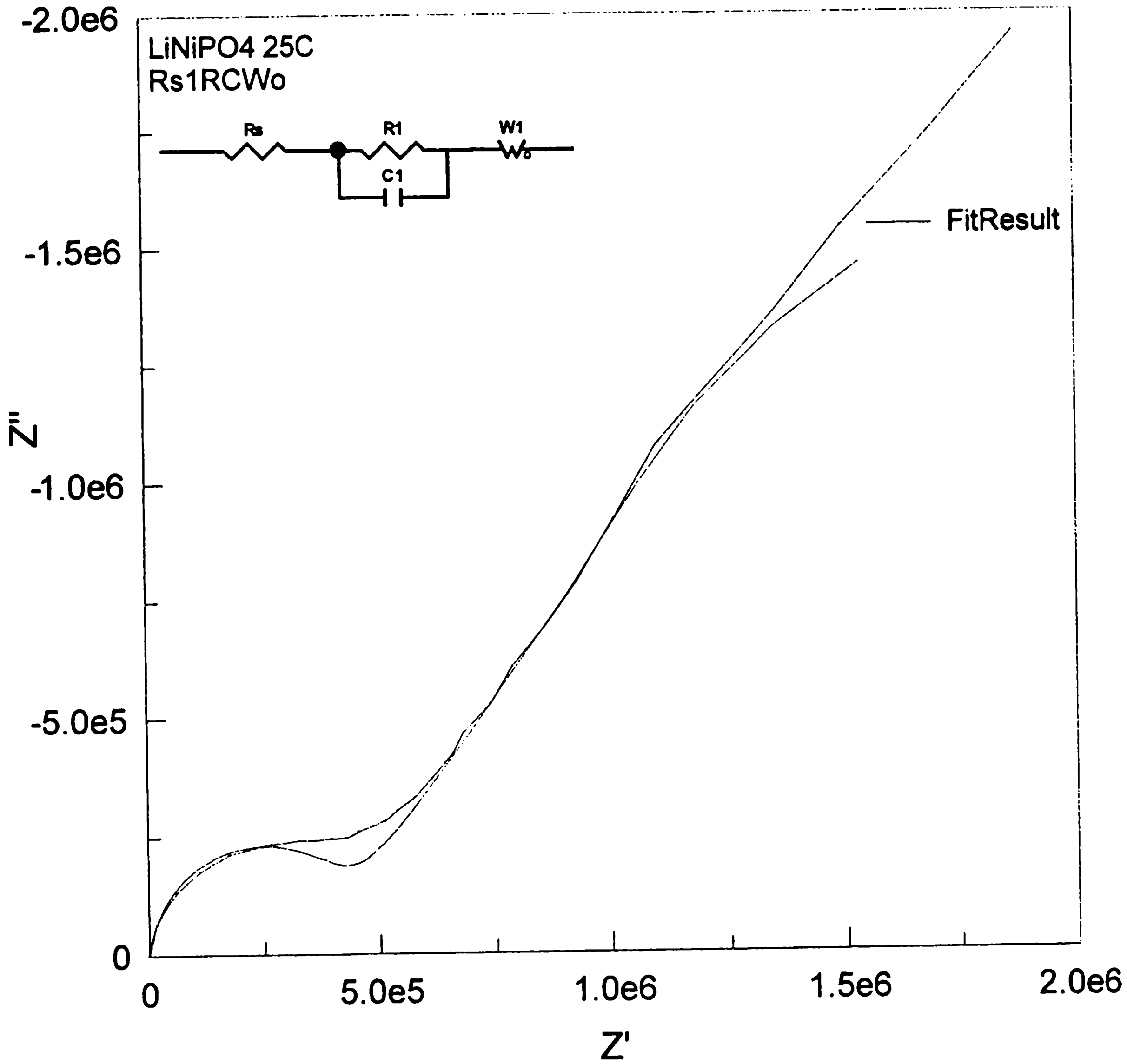

Figure 4.5 Impedance Spectra of LiNiPO4 at 25 °C

Similar to $LiCoPO_4$, pure $LiNiPO_4$ was difficult to separate into grains and grain boundary components at low temperatures, and was therefore measured using total conductivities. For example, at low temperatures, $LiNiPO_4$ actually shows only one large semi-circle and a diffusion component, represented as an open Warburg component (Figure 4.5). This is probably due to very high grain boundary impedances being measured, which tends to overshadow anything else. In this situation, an Rs1RCWo equivalent circuit only is used, which gives a good fitting for a total impedance value.

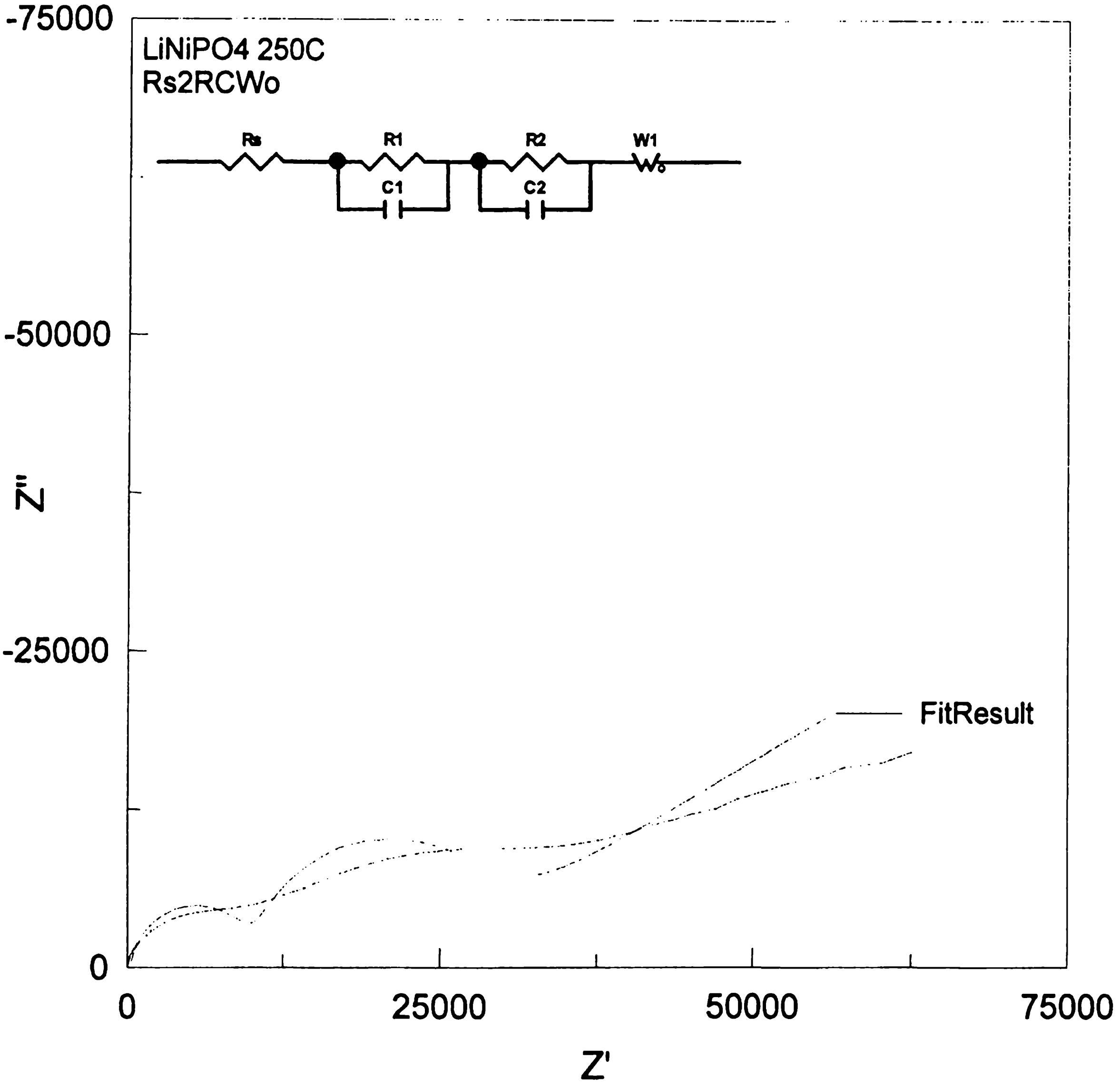

Figure 4.6 Impedance Spectra of $LiNiPO_4$ at 250 °C

At higher temperatures, the different components of the total impedance are more easily distinguished as shown for $LiNiPO_4$ at 200 °C. The data represented in Figure 4.6 is fitted with an Rs2RCWo equivalent circuit.

The second phase in the materials show poorer conductivity than pure $LiNiPO_4$ at lower temperatures, but improve and are better at higher temperatures (Figure 4.8). Many phosphates form amorphous glasses at higher temperatures that reduce grain boundary resistances. The titanium phosphate phase definitely improves conduction at higher temperatures and may be more glass-like than pure $LiNiPO_4$. This is also shown by the spectra for all materials at 400 °C (Figure 4.7).

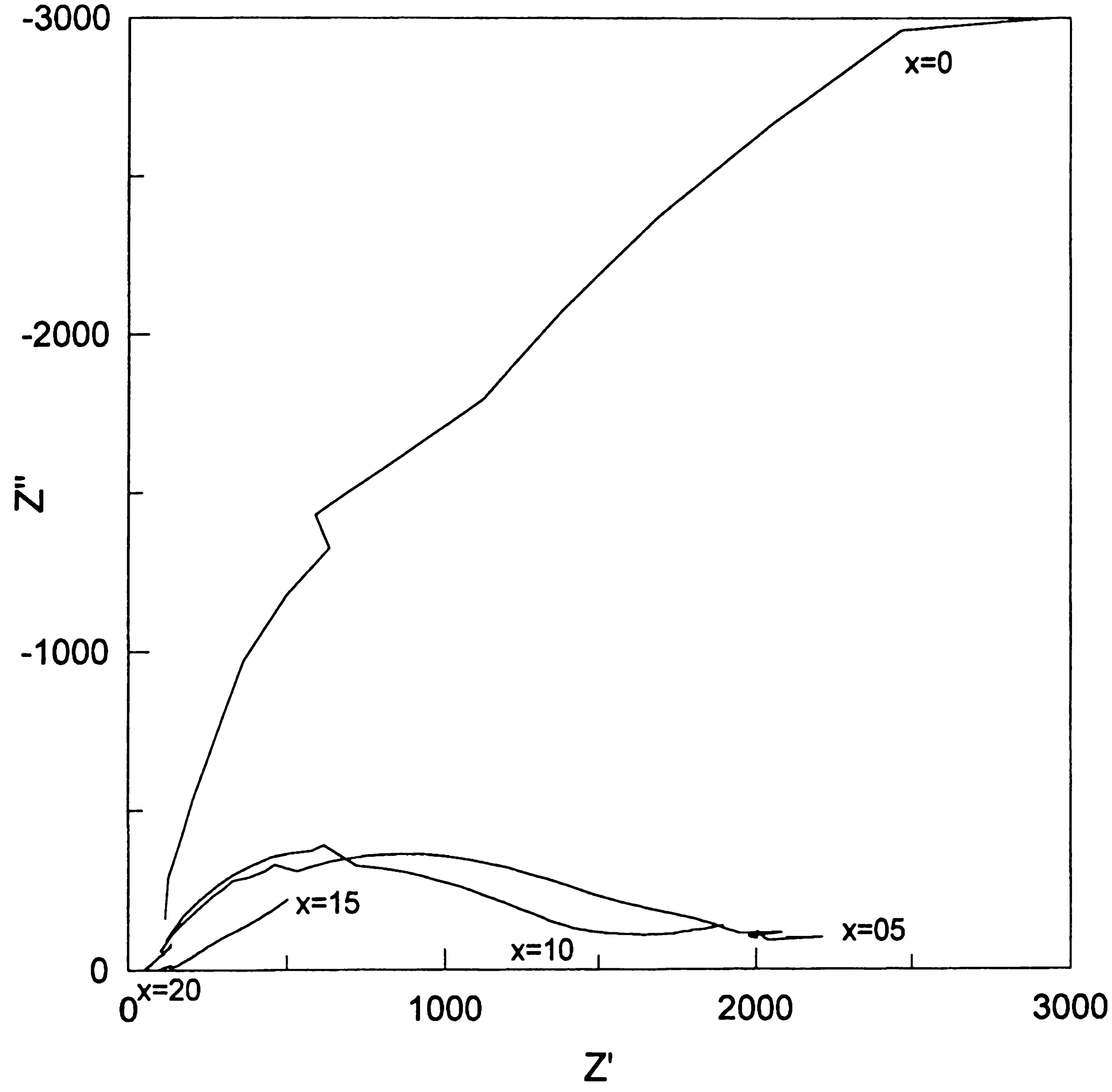

Figure 4.7 Impedance Spectra of $Li_{1-x}Ni_{1-x}Ti_xPO_4$, $0 \leq x \leq 0.2$ at 400 °C

Also visible are the semicircles which are now suppressed below the x-axis. This is probably related to the heterogeneities in the sample, which cause a dispersion of the time-constants.[5] When a given time constant associated with interface or bulk processes is thermally activated with a distribution of activation energies (as shown by the slopes in Figure 4.8), a simple resistor and capacitor in parallel or series is no longer a feasible representation, and a distributed impedance element, for example, a constant phase element (CPE) is more likely.[6]

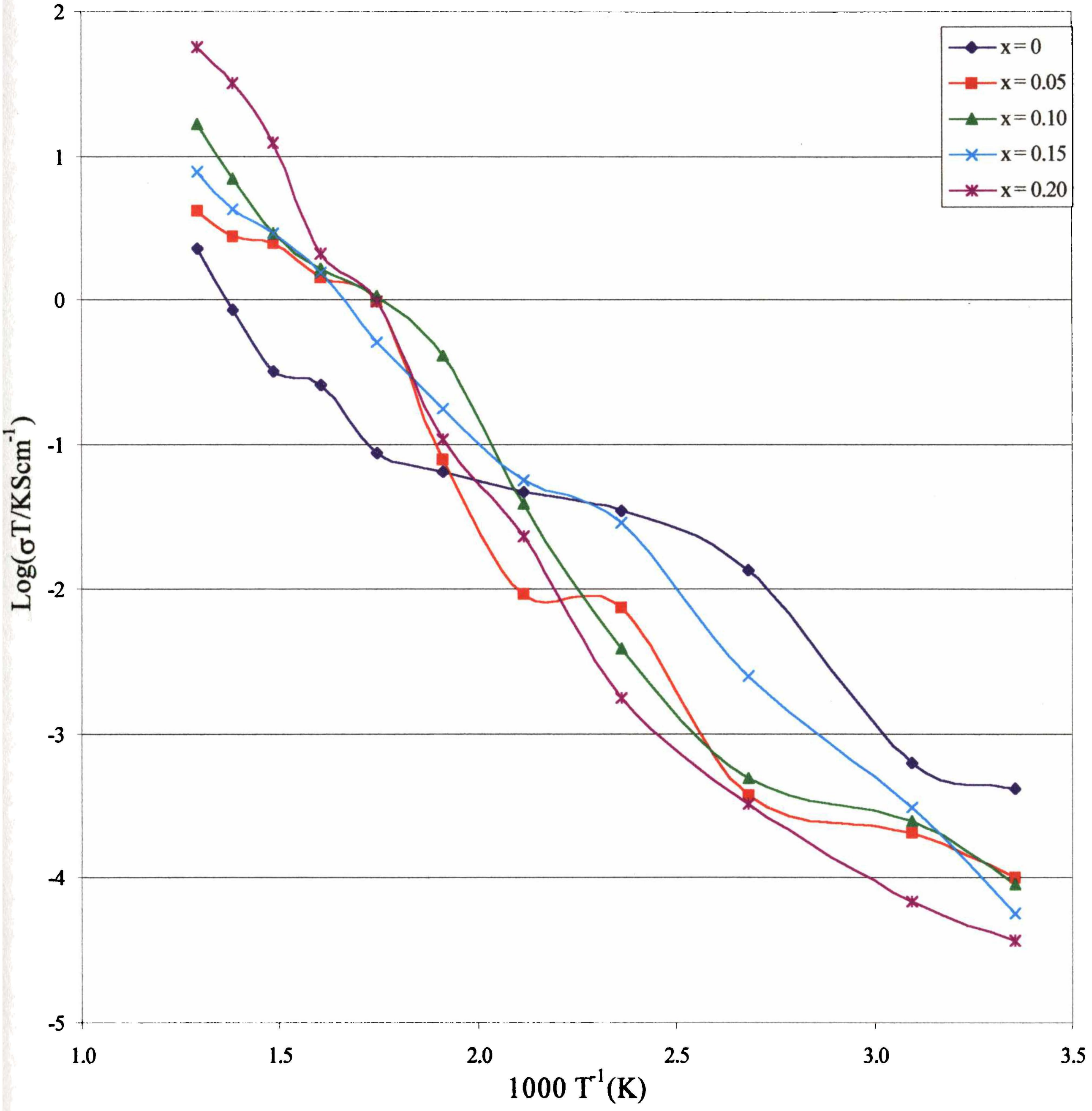

Figure 4.8 Total Conductivity of $Li_{1-x}Ni_{1-x}Ti_xPO_4$, $0 \leq x \leq 0.2$

The total conductivity data of $Li_{1-x}Ni_{1-x}Ti_xPO_4$, $0 \leq x \leq 0.2$ is presented in Figure 4.8. Total conductivity (grain and grain boundary) is presented due to the difficulty with many of the spectra in determining different components. Ionic conductivity is predominant in the system, as confirmed by some preliminary DC experiments. However, for all the dopants, the conductivity is extremely low for a cathode material. The best room temperature conductivity shown by these materials was $LiNiPO_4$ with a value of 1.38×10^{-6} Scm^{-1}.

The slope calculated for $LiNiPO_4$ using Equations 3.2, 3.3 and Figure 4.8 reveals an activation energy of 0.14 eV. Of course the activation energy of the materials with a second phase were not calculated to compare. However, they do have a steeper slope with increasing dopant content so it would seem reasonable to assume the titanium phosphate second phase almost certainly has a higher activation energy than $LiNiPO_4$, in contrast to the secondary phase of vanadium oxide phosphate in $LiCoPO_4$, which decreases the slope and lowers the activation energy.

4.3 Electrochemical Data

Figure 4.9 shows the first two charge and discharge curves for $LiNiPO_4$ using a current of 7.5mA/g. It has a theoretical capacity of 161 mAh/g based on the reaction:

$$LiNi^{II}PO_4 \rightleftharpoons Ni^{III}PO_4 + Li^+ + e^- \qquad \text{Equation 4.2}$$

During the course of this work, other investigators have examined the potential of $LiNiPO_4$ and concluded it had no voltage plateaus at all.[7] Most likely, they did not discharge down to the low voltages that are presented here. The first charge curve shows a capacity of approximately 30 mAh/g up to the upper voltage limit of 5V. Electrolyte decomposition is almost certainly occurring with the electrolyte employed. A first discharge of approximately 300 mAh/g was achieved with a voltage plateau of 1.4V. The large capacity is most probably due to the decomposition reaction and formation of lithium-rich Li_3PO_4 and metallic Ni. This was difficult to determine by X-ray diffraction due to the amorphous shape of the curve obtained from the cathode pellet after cycling. However, similar behaviour for $LiCuPO_4$ has been reported, with Li_3PO_4 and metallic Cu being formed.[8] The second charge curve shows a capacity of approximately 70 mAh/g and the insertion of lithium into the cathode during the second discharge is considerably less than the first with a value of approximately 70 mAh/g.

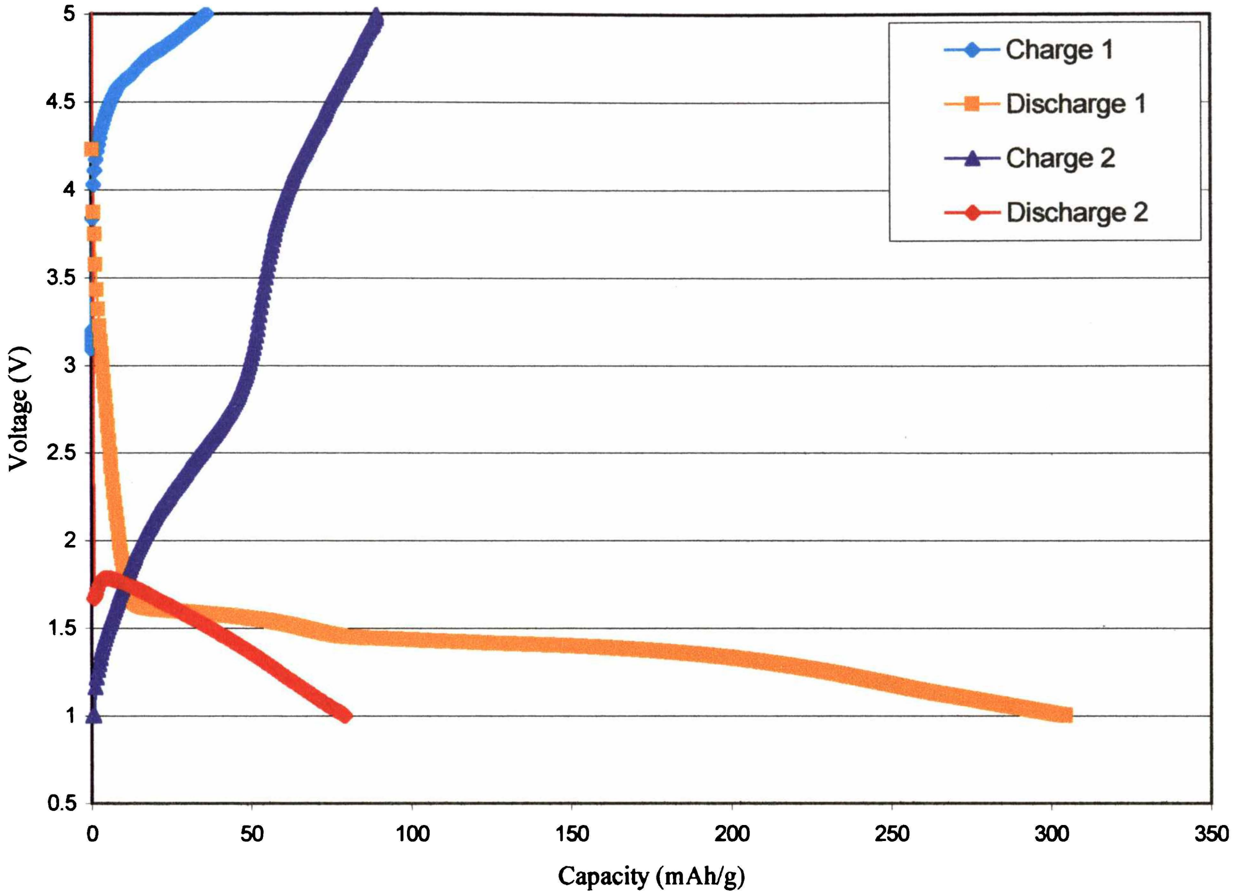

Figure 4.9 Cycling Behaviour of $LiNiPO_4$

$LiNiPO_4$ has a relatively low conductive nature and probably some excessive kinetic limitations. Out of the Olivine family of materials low conductivity is not however limited to only $LiNiPO_4$. As seen in Chapter 3, the conductivity of $LiCoPO_4$ is not as good as that of $LiNiPO_4$.

4.4 Particle Size Analysis and BET Surface Area

The following figure shows the results of a mastersize analysis of $LiNiPO_4$. Similar to its cobalt analogue, the particles are very large and have a large distribution. BET results reveal a very low surface area of $0.33m^2g^{-1}$. The SEM pictures in section 4.4.1 show the particle size at the 4μm level. With the resolution at 75 μm the larger size particles can also be seen although this is not shown here.

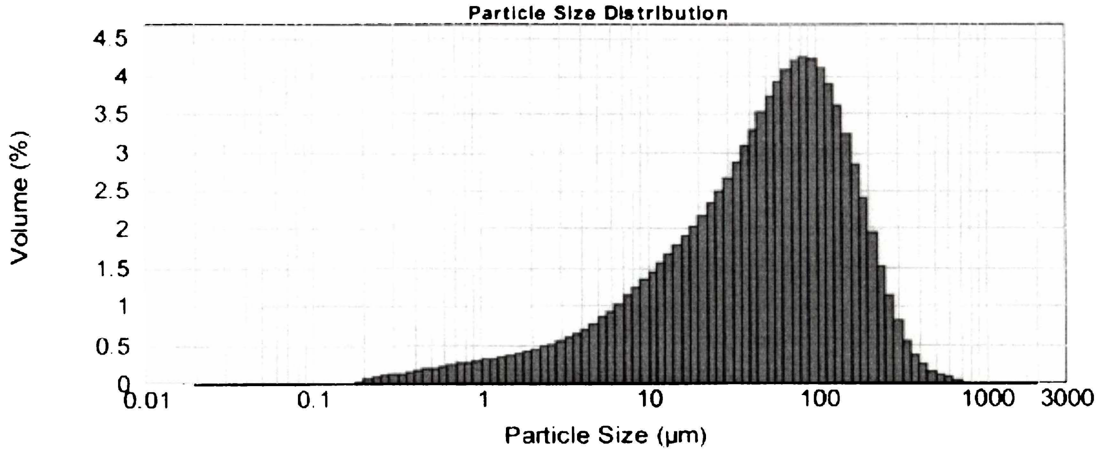

Figure 4.10 Particle Size Distribution of $LiNiPO_4$

4.4.1 SEM and EDX Analysis

UFC-3N was again used in an attempt to improve the electronic conductivity of the cathode.[9] The SEM micrographs (Figure 4.11 and Figure 4.12) show that the UFC material covers the larger $LiNiPO_4$ particles very well, improving the potential for interparticle contact. The darker patches in both figures is the carbon. In Figure 4.11, carbon and $LiNiPO_4$ are mainly separate particles compared to Figure 4.12, where the $LiNiPO_4$ particles are mostly covered by a thin carbon layer.

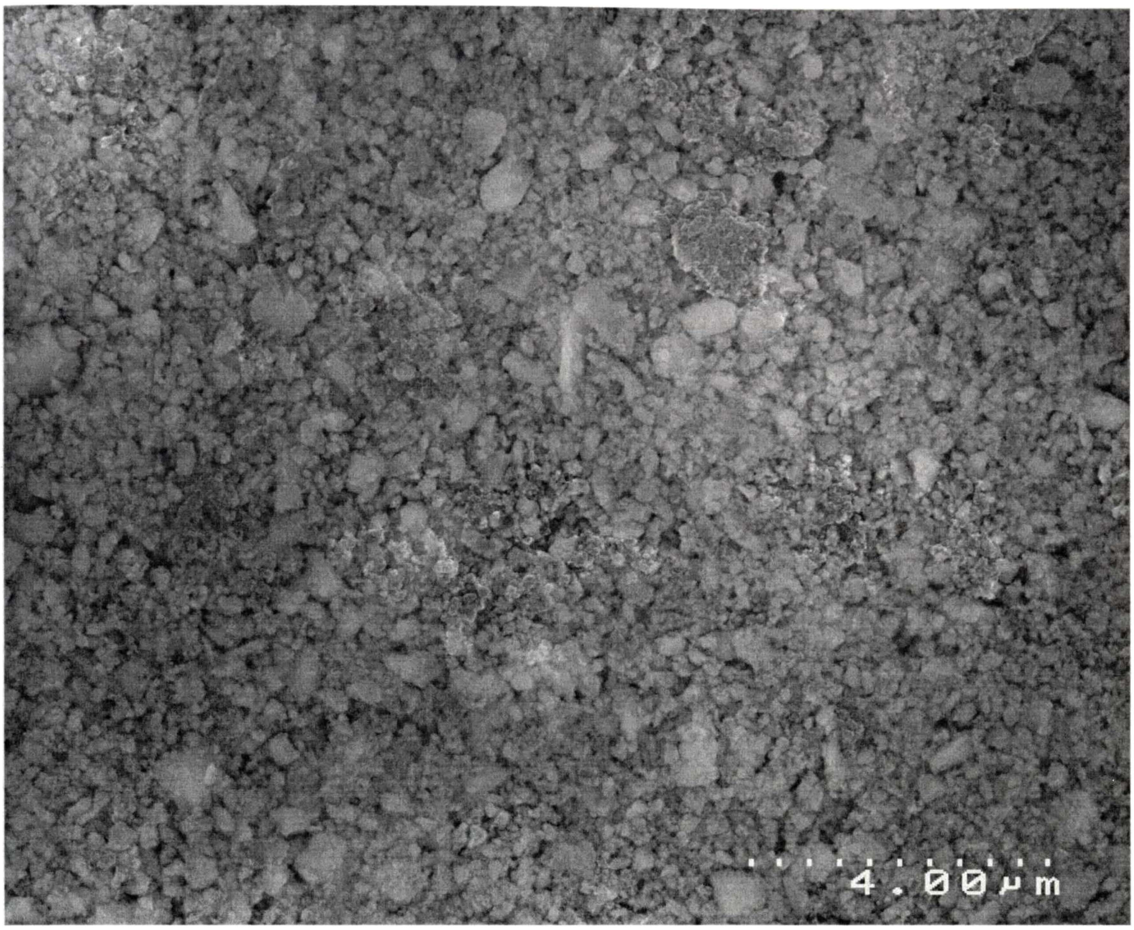

Figure 4.11 SEM Micrograph of $LiNiPO_4$/Carbon

Even though the interparticle contact had improved with the addition of this material the performance did not improve. EDX analysis was performed and the results confirmed the chemical composition. The analysis was performed on the particles in the area shown in Figure 4.11. Analysis of the particles in Figure 4.12 showed little difference.

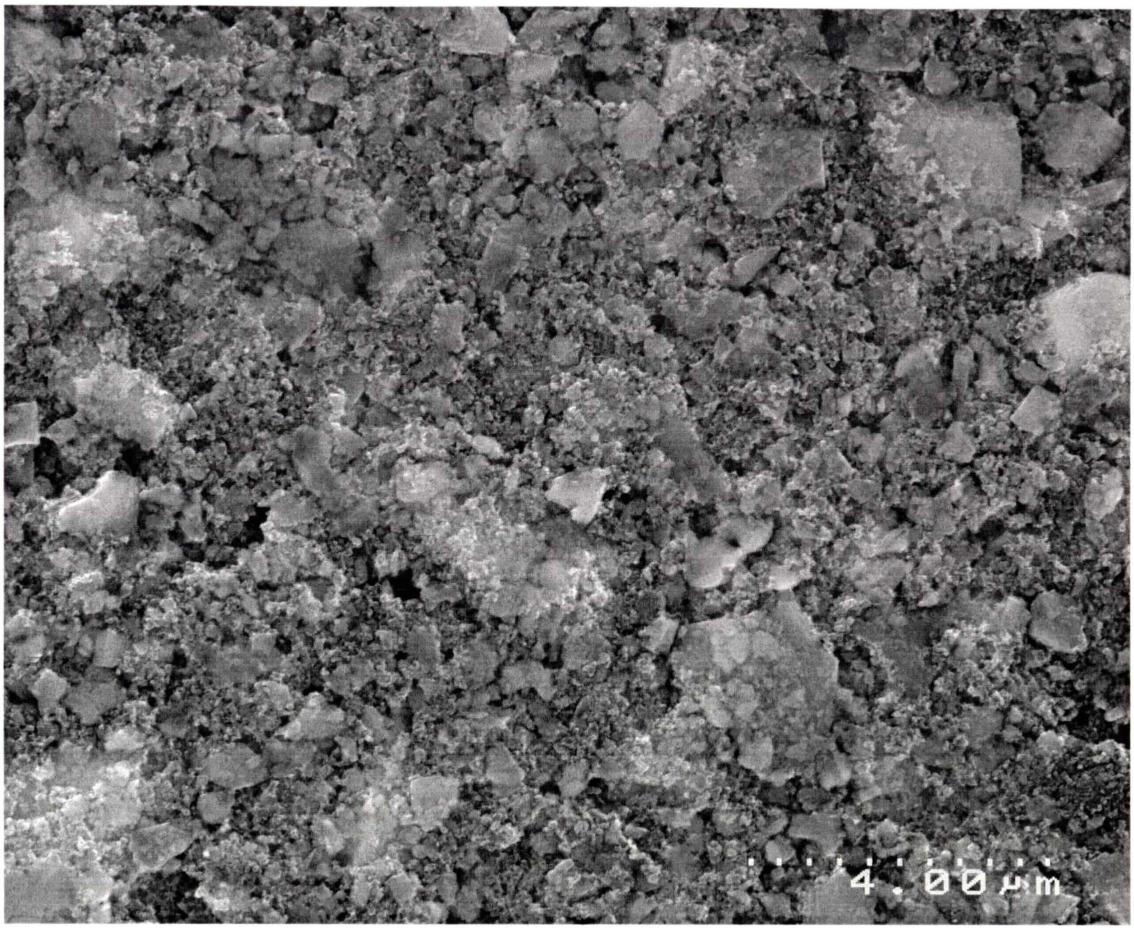

Figure 4.12 SEM Micrograph of $LiNiPO_4$/UFC

With similarly large particle size to $LiCoPO_4$, this material does however have higher ionic conductivity. The application of $LiNiPO_4$ as a cathode material is limited due to the oxidative stability of current electrolytes at high voltages during charging of the cell to the voltages required accessing the Ni^{3+}/Ni^{2+}couple in the presence of the PO_4 tetrahedra. Steps to improve electronic conduction of the cathode have not significantly improved performance. The main factor limiting the performance of $LiNiPO_4$ is most likely because the binding potential for lithium in this material is higher than the oxidative stability of the electrolyte. Padhi et al.[10] report the Ni^{3+}/Ni^{2+} redox couple should lie approximately 0.6 eV below the Co^{3+}/Co^{2+} redox couple as in the case of the inverse spinels $V[LiM]O_4$ with M = Co or Ni. The results from Chapter 3 shows the Co^{3+}/Co^{2+} redox couple lies at approximately 4.8V vs. lithium, indicating that the Ni^{3+}/Ni^{2+} redox couple should lie at approximately 5.4V. Discharging at low voltages vs. lithium decomposes the $LiNiPO_4$ cathode material and charging at high voltages decomposes the electrolyte.

4.5 References

---

[1] I. Abrahams and K. S. Easson. *Acta Cryst.*, C49, p925, **1993.**

[2] M. Cretin, P. Fabry and L. Abello, *J. European Ceram. Soc.*, Study of $Li_{1+x}Al_xTi_{2-x}(PO_4)_3$ for Li^+ Potentiometric Sensors, 15, p1149-56, **1995.**

[3] R.E. Dietz, G.I. Parisot and A.E. Meixner, *Phys. Rev. B*, 4, pp2302-2310, **1971.**

[4] V.V. Kravchenko, V.I. Michailov and S.E. Sigaryov, *Solid State Ionics*, 50, p19-30, **1992.**

[5] J. Hwang, K. S. Kirkpatrick, T. O. Mason and E. J. Garboczi, *Solid State Ionics*, 98, p93, **1997.**

[6] J. R. MacDonald, "Impedance Spectroscopy-Emphasising Solid Materials and Systems", John Wiley & Sons, **1987.**

[7] S. Okada, S. Sawa, M Egashira and J. Yamaki, *in 196th Meeting of the Electrochem. Soc.*, Honolulu, Oct, Abstract no. 232, **1999.**

[8] K. Amine, H. Yasuda and M. Yamachi, *in 196th Meeting of the Electrochem. Soc.*, Honolulu, Oct, Abstract no. 277, **1999.**

[9] T. Takei, A. Kozawa and R. V. Mostev, *ITE Battery Newsletter*, 4, p55, **1997.**

[10] A. K. Padhi, K. S. Nanjundaswamy and J. B. Goodenough, *J. Electrochem. Soc.*, 144, 4, p1188, **1997.**

5 Lithium Iron Phosphate – $Li_3Fe_2(PO_4)_3$

5 Lithium Iron Phosphate – $Li_3Fe_2(PO_4)_3$

5.1 Characterisation

Firing $Li_3Fe_2(PO_4)_3$ in air showed via X-ray diffraction and Raman spectroscopy that a single solid phase was formed according to the following reaction:

$$3Li_2CO_3 + 6NH_4H_2PO_4 + 2Fe_2O_3 \xrightarrow{O_2} 2Li_3Fe_2(PO_4)_3 + 6NH_3 + 9H_2O + 3CO_2 \quad \text{Equation 5.1}$$

5.1.1 X-Ray Diffraction

The materials under investigation here, namely $Li_{3-2x}(Fe_{1-x}Ti_x)_2(PO_4)_3$ belong to the $Fe_3(SO_4)_3$ -type structures which are related to the NASICON (Na Super Ionic Conductors) family of structures. The structure is based on a three dimensional network of $[Fe_2(PO_4)_3]_x$ of FeO_6-octahedra and PO_4-tetrahedra sharing oxygen vertices. The lithium ions are situated in interstitial voids in the framework.[1]

For the $Na_3Fe_2(PO_4)_3$ structure, the space group has been reported as monoclinic *C2/c* (No. 15) with 2 formula units, ie Z = 2 at room temperature, at 368 K the monoclinic β–phase is formed (space group, C*2/c*) and above 418 K the rhombohedral γ–phase exists (R$\bar{3}c$). [11,15] Similarly, $Li_3Fe_2(PO_4)_3$ has three phases reported all with the same basic framework structure but differing slightly in the orientation of the FeO_6 octahedra, PO_4 tetrahedra and position of the Li^+ ions. These three phases are monoclinic ($P2_1/n$) α, monoclinic ($P2_1/n$) β and orthorhombic (P*can*) γ.[2]

Suzuki et al.[3] and Losilla et al.[4] have reported the stabilisation with various dopants of the high temperature γ–phase to room temperature of $Li_3Sc_2(PO_4)_3$ and $Li_{1+x}Hf_{2-x}M_x(PO_4)_3$ respectively. In this research, a titanium dopant was used to attempt to introduce vacancies on the Li^+ sites and the stabilisation of the high temperature orthorhombic γ–phase (P*can*) of $Li_3Fe_2(PO_4)_3$ at room temperature by doping Fe^{3+} with Ti^{4+}.

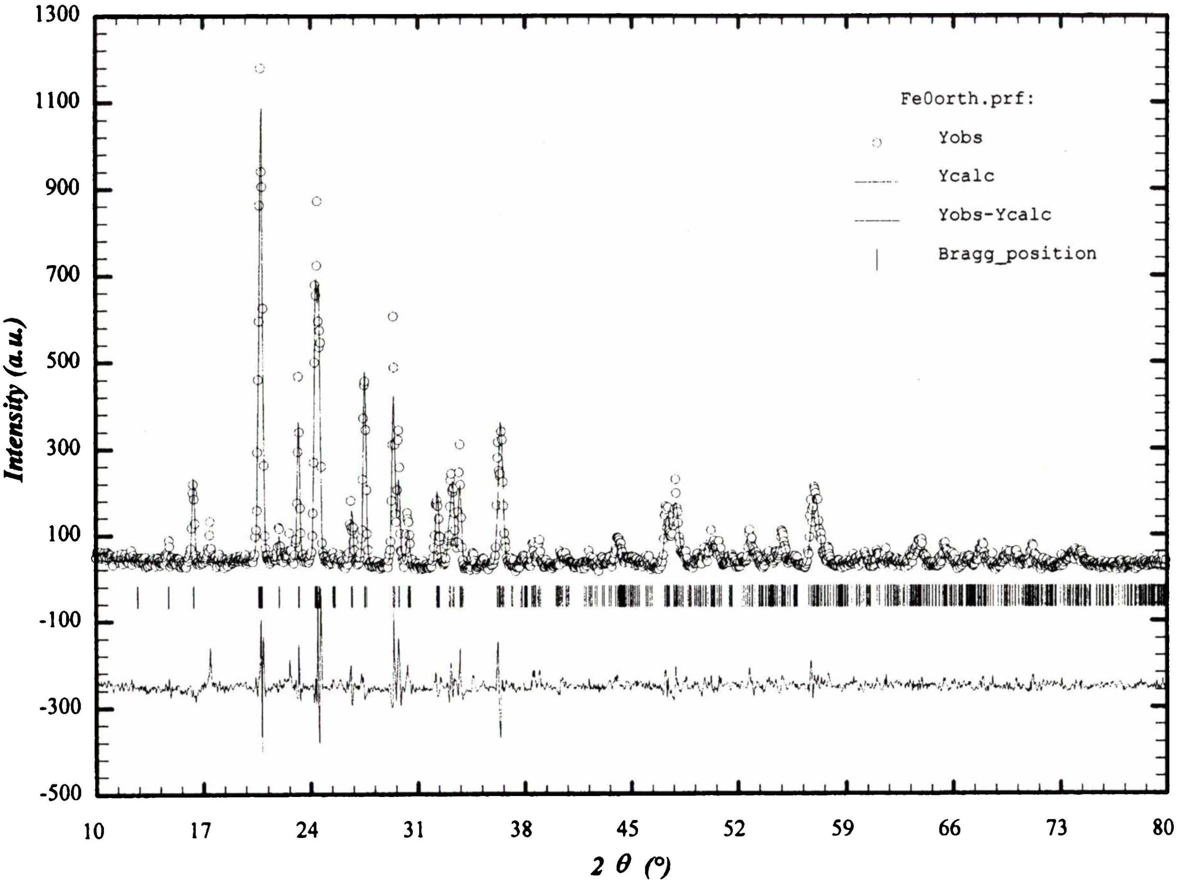

Figure 5.1 Structure Refinement of $Li_3Fe_2(PO_4)_3$

Bykov et al. report that the XRD data for single crystal $Li_3Fe_2(PO_4)_3$ could be indexed in a slightly distorted $P2_1/n$ monoclinic cell.[2] Orthorhombic symmetry is obtained at temperatures above 260 °C. The monoclinic cell results from a small distortion of the framework from orthorhombic symmetry due to lithium ordering. [5,6,7] Our refinements of the powder X-ray diffraction data showed no significant difference using $P2_1/n$ monoclinic or P*can* orthorhombic symmetry. The value obtained for alpha in the monoclinic refinement presents an angle of 90.2°, i.e. a minimal distortion from the orthorhombic cell. The single crystal data obtained by Bykov et al. better distinguish between these two symmetries, owing to the higher resolution of single crystal vs. powder diffraction. The differences between the atomic coordinates of the monoclinic and orthorhombic unit cells reported by Bykov et al. are less than 2%. Our powder X-ray diffraction data is unable to distinguish a significant difference between the two symmetries, so the orthorhombic refinement having higher symmetry is presented here. The results of the Rietveld refinement of the XRD data of $Li_3Fe_2(PO_4)_3$ are shown in Figure 5.1 and Table 5.1.

Table 5.1 Refined Crystallographic Parameters for $Li_3Fe_2(PO_4)_3$ (P*can*) - X-ray diffraction data for 711 reflections and 38 variables.

Atom	*x*	*y*	*z*	Occupancy	B_{iso} (Å^2)
Fe	0.2416 (16)	0.1072 (6)	0.4661 (9)	1.922 (28)	0.61 *
P	0.1067 (23)	0.1488 (15)	0.1040 (22)	2.000 *	0.58 *
P	0.0381 (31)	0.5000 *	0.2500 *	1.000 *	0.62 *
O	0.4287 (45)	0.3435 (35)	0.0975 (39)	2.000 *	1.10 *
O	0.3271 (43)	0.2758 (28)	0.4731 (42)	2.000 *	1.29 *
O	0.1542 (43)	0.0327 (30)	0.0680 (38)	2.000 *	1.63 *
O	0.4309 (34)	0.0921 (24)	0.3603 (36)	2.000 *	1.17 *
O	0.1482 (43)	0.4199 (26)	0.1417 (38)	2.000 *	1.32 *
O	0.1500 (39)	0.1818 (34)	0.2500 (41)	2.000 *	1.03 *
Li	0.2950 *	0.3220 *	0.2760 *	1.000 *	1.50 *
Li	0.5770 *	0.1930 *	0.4210 *	1.000 *	2.40 *
Li	0.9120 *	0.2410 *	0.2970 *	1.000 *	4.10 *
a = 8.5601, b = 12.0084, c = 8.6154, * = Fixed Parameters V = 885.597 Å^3 , wRp = 20.8, Rp =16.7, $\chi 2$ =2.57					

The Rietveld analysis was performed using Fullprof 98® software. Initial structural and thermal parameters were taken from the data for γ-phase $Li_3Fe_2(PO_4)_3$ from Bykov et al.[2] as a starting model for the refinement. Scale and background parameters were refined initially, followed in subsequent iterations by cell, zero point and peak shape parameters. The atomic positions, phosphorus and oxygen occupancies were fixed while the cell parameters and then the occupancy factors for the iron atoms were refined. Once the cell parameters and the occupancy factors were established the atomic positions of the iron, the phosphorus and then the oxygen atoms were refined.

$Li_{3-2x}(Fe_{1-x}Ti_x)_2(PO_4)_3$ $0 \le x \le 0.20$ can also be indexed using orthorhombic symmetry. The Rietveld refinements of the XRD data for these materials are shown in Appendix II. Initial structural and thermal parameters were also taken from the data for γ-phase $Li_3Fe_2(PO_4)_3$ from Bykov et al.[2] as a starting model for the refinement. Scale and background parameters were refined initially, followed in subsequent iterations by cell, zero point and peak shape parameters. The atomic positions, phosphorus and oxygen occupancies were fixed while the cell parameters and then the occupancy factors for the iron atoms were refined. Once the cell parameters and the occupancy factors were established, the atomic positions of the iron, the phosphorus and then the oxygen atoms were refined.

The data for $Li_{3-2x}(Fe_{1-x}Ti_x)_2(PO_4)_3$ $0 \le x \le 0.20$ based on the orthorhombic unit cell is summarised in Table 5.2. There appears to be a contraction in the lattice parameters with even the lowest amount of titanium dopant. The cell volume is significantly less for x = 0.05 and for all dopant quantities in the system. The lack of any visible secondary phase and the change in the lattice parameters suggests the titanium is soluble in the system.

Table 5.2 Ti^{4+} doped $Li_3Fe_2(PO_4)_3$ Refinement Summary

Parameter	$Li_3Fe_2(PO_4)_3$	Ti = 0.05	Ti = 0.10	Ti = 0.15	Ti = 0.20
a	8.5601 (21)	8.5591 (14)	8.5536 (14)	8.5508 (13)	8.5508 (11)
b	12.0084 (26)	11.9928 (17)	11.9889 (17)	11.9905 (16)	11.9955 (14)
c	8.6154 (19)	8.6008 (13)	8.6017 (13)	8.6047 (11)	8.6108 (10)
Volume ($Å^3$)	885.597 (344)	882.851 (222)	882.086 (225)	881.234 (203)	883.423 (162)
Fe Site Occupancy	1.922 (28)	1.913 (21)	1.956 (22)	1.876 (19)	1.824 (16)

The Rietveld fit to the experimental data for the $Li_3V_2(PO_4)_3$ material is adequate in so far that it fits the peak portions but does not fully reproduce the relative intensities of several of the major peaks. A particular problem was in reproducing intensities for peaks such as those at 21, 24, and 30° 2θ, which are actually envelopes of two or more closely positioned peaks. This problem in the refinements could not be solved by adjusting peak shape parameters.

Padhi et al. [1,8] have reported the mapping of transition metal redox energies in phosphates with the NASICON structure by lithium intercalation, revealing that the Fe^{3+}/Fe^{2+} redox couple is 2.8 eV with respect to the Fermi energy of lithium. Results were also reported for anionic substitution of MoO_4, WO_4, and SO_4 for PO_4 and the effect this had on the position of the redox couples of transition metals. It was found was that in $Li_xFe_2(XO_4)_3$ with X = Mo, W, S or P, the Fe^{3+}/Fe^{2+} redox couple lies at 3.0, 3.0, 3.6 and 2.8 eV respectively, below the Fermi level of lithium. [5,9,10]

With a complete substitution of SO_4 for PO_4 in the $Li_3Fe_2(PO_4)_3$ NASICON structure, the redox position moves 0.8 eV from 2.8 eV to 3.6 eV with respect to lithium. Changing from sulphate to phosphate ions for all transition metal NASICON analogues lowers the open circuit voltage by 0.8 eV. The sulphate analogue, however, is of a monoclinic symmetry that has less free volume of interstitial space available for lithium ion mobility. Each structure contains units of two FeO_6 octahedra bridged by three corner-sharing SO_4 tetrahedra. These units form 3D frameworks by the bridging SO_4 tetrahedra of one unit sharing corners with FeO_6 octahedra of neighbouring $Fe_2(SO_4)_3$ elementary building blocks so that each tetrahedra shares corners with one only one octahedra, and each octahedra with only one tetrahedra.

As shown in Figure 5.2, the rhombohedral phase building blocks are aligned parallel. However, they are aligned nearly perpendicular in the monoclinic phase, which decreases the free space available for lithium ion motion. Partial substitution of one $(PO_4)^{3-}$ polyanion for one $(SO_4)^{2-}$ per formula unit preserves the hexagonal structure for all x in $Li_{1+x}Fe(PO_4)(SO_4)_2$ with a sacrifice of 0.3 eV or about one third of the 0.8 eV found between $Li_xFe_2(SO_4)_3$ and $Li_{3+x}Fe_2(PO_4)_3$.[8]

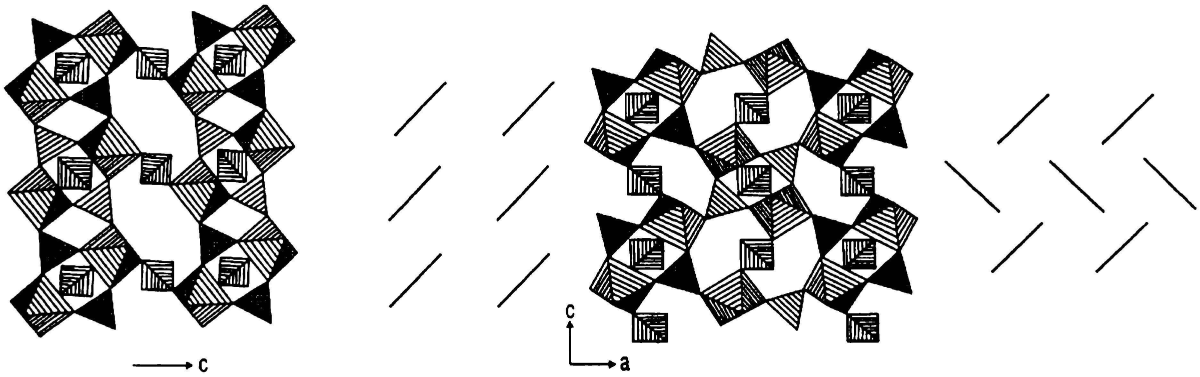

Figure 5.2 Rhombohedral vs Monoclinic Symmetry

$LiFe_2PO_4(SO_4)_2$ was prepared using the method of Goodenough et al.[144] and analysed by X-ray diffraction and Rietveld analysis. It was difficult to precisely index the data in any specific space group. Using full pattern matches, the best fitting pattern, which matched the literature, was the $R\bar{3}c$ space group shown in Figure 5.3. This corresponds to the structure on the left in Figure 5.2.

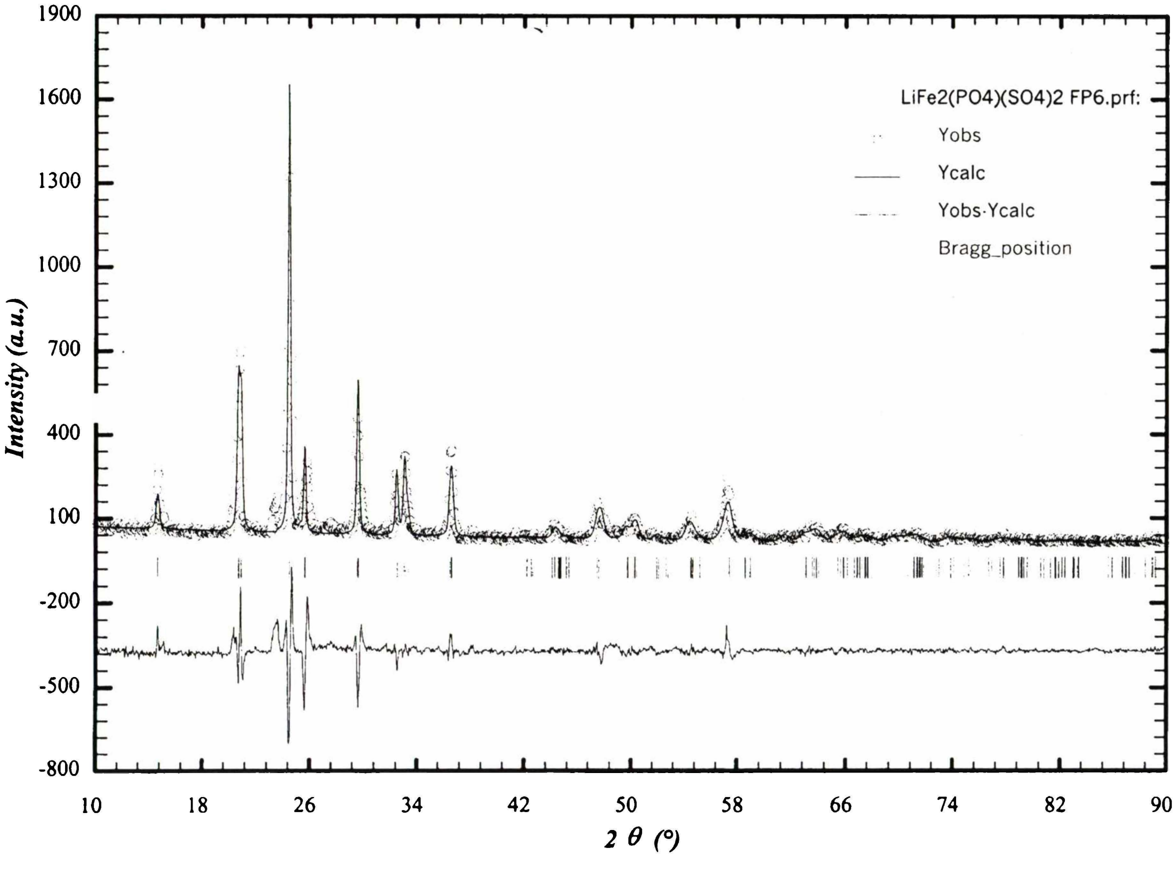

Figure 5.3 Full Pattern Match of $LiFe_2PO_4(SO_4)_2$

5.1.2 Raman Spectroscopy

Several workers have utilised Raman and infrared spectroscopy to characterise the structure of the monoclinic $A_3M_2(PO_4)_3$ where A = Li and Na, and M = Fe, Sc, In, Zr and Cr. [11,12,13,14,15,16]

Kravchenko et al.[11] have reported the Raman spectrum of $Li_3Fe_2(PO_4)_3$ and $Li_3Sc_2(PO_4)_3$, however, only the bands due to Li vibrations were assessed in any detail and the full assignment of the Raman modes has not been reported to date. Barj et al.[13] report the factor group analysis and spectra of compounds belonging to the NASICON family of structures, and characterised the short-range disorder occurring in these systems. Table 5.3 shows the Raman and infrared modes predicted for these compounds and structures.

Table 5.3. Raman and Infrared Modes for the Compounds $Na_3Fe_2(PO_4)_3$ and $Li_3Fe_2(PO_4)_3$

Compound	Structure	Space Group	Raman Active Modes (No.)	Infrared Active Modes (No.)	Acoustic Modes	Reference
$Na_3Fe_2(PO_4)_3$	Monoclinic	$C2/c$ (No. 15) (at 293 K)	$29A_g + 31B_g$ (60)	$32A_u + 34B_u$ (63)	$A_u + 2B_u$	5
$Na_3Fe_2(PO_4)_3$	Rhombohedral	$R\bar{3}c$ (No.167) (at ? K)	$9A_{1g} + 20E_g$ (29)	$11A_{2u} + 21E_u$ (32)	$A_{2u} + E_u$	5
α-$Li_3Fe_2(PO_4)_3$	Monoclinic	$P2_1/n$ (No. 14) (at 293 K)	$60A_g + 60B_g$ (120)	$59A_u + 58B_u$ (117)	$A_u + 2B_u$	3
γ-$Li_3Fe_2(PO_4)_3$	Orthorhombic	$Pcan$ (No.61) (at 573 K)	$36A_{1g} + 36B_{1g} + 36B_{2g} + 36B_{3g}$ (144)	$35B_{1u} + 35B_{2u} + 35B_{3u}$ (105)	$B_{1u} + B_{2u} + B_{3u}$	3, This work

A total of 60 Raman active, 117 infrared active and no coincident or inactive modes are predicted for the low temperature α-phase of $Li_3Fe_2(PO_4)_3$, while for the high temperature γ-phase there are 144 Raman and 105 infrared modes predicted for the orthorhombic structure.

The factor group analysis of the $Na_3Fe_2(PO_4)_3$ phases is included here as this is a closely related compound. This shows the change in the number of active modes with change in symmetry.

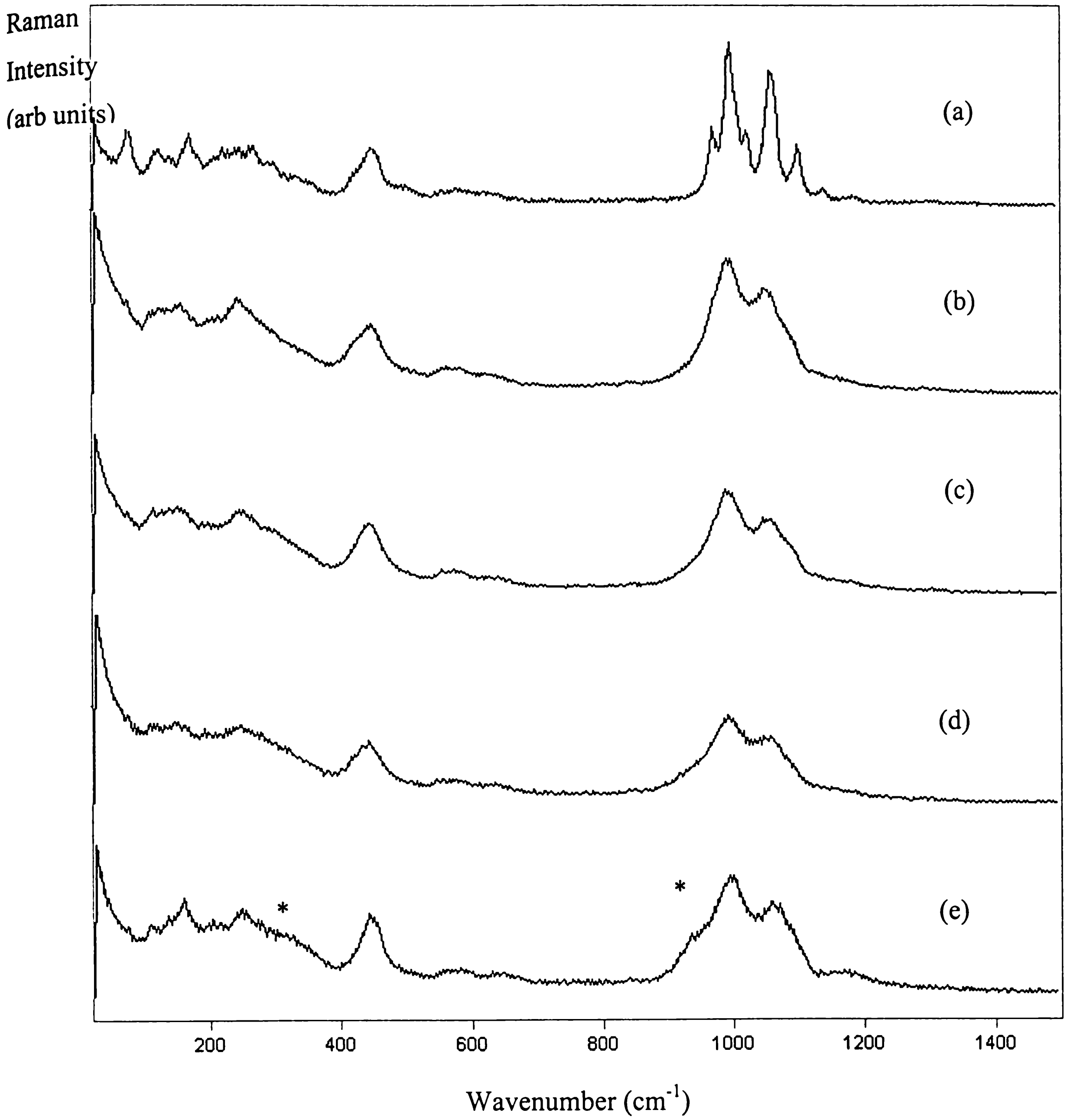

* indicates possible secondary phase.

Figure 5.4 Raman Spectra of $Li_{3-2x}(Fe_{1-x}Ti_x)_2(PO_4)_3$ where x = 0 (a), 0.0.5 (b), 0.10 (c), 0.15 (d) and 0.20 (e).

Table 5.4 Raman Band Positions and Assignments of $Li_3Fe_2(PO_4)_3$ - Compared to those observed for isostructural and NASICON–type structure compounds.

$Li_3Fe_2(PO_4)_3$ This work	$Li_3Fe_2(PO_4)_3$ Ref.3 Approx.	$Li_3In_2(PO_4)_3$ Ref.3 Approx.	$Na_3Fe_2(PO_4)_3$ Ref.5	Assignment Ref.3
			49 w	Lattice modes
			60 w	“
			72 w	“
79 m			82 w	“
124 w	120		131 m	“
141 vw	140	150 vw	147 m	“
171 m	160	160 vw	172 m	“
186 sh	180		195 m	“
207 vw	210	200 m	204 sh	“
228 w	220	215 s		“
248 w	250	230 s	237 m	“
272 w	270	250 s	290 w	“
301 w,b	290	300 s		LiO_4, FeO_6 octahedra modes
336 w,b	330	340 s	320 m	“
357 w,b	370		330 w	“
420 sh	400	410 sh		PO_4 deformations,
		425 s		“
		440 s	445 m	“
451 m,b	450	450 s		“
		475 s	480 vw	“
497 w,b	490	493 sh		“
		497 m		“
		500 sh		“
556 w	530	540 w	543 w	“
			560 w	“
580 w,b	590		586 w	“
			597 w	“
627 w,b	600		624 w	“
			642 vw	“
846 vw				
972 m			963 m	PO_4 Stretching
996 s	990		973 s	“
1004 sh	1010		1015 vs	“
			1019 sh,s	“
1025 m	1020		1025 sh,s	“
			1034 sh,s	“
1059 s	1050		1045 vs	“
1100 m	1090		1060 m	“
1139 w	1130		1130 vw	“
1187 vw	1180		1180	“
	1210			“
	1240		1215 m	“
1302 vw				

Table 5.5 Raman Band Positions of $Li_{3-2x}(Fe_{1-x}Ti_x)_2(PO_4)_3$, $0 \leq x \leq 0.20$

0	0.05	0.10	0.15	0.20	$Li_3Fe_2(PO_4)_3$ Ref.3 Approx.	$Na_3Fe_2(PO_4)_3$ Ref.5 At 670 K
						34
						50
79 m				76 vw		70
124 w	130 m,b	117 m	115 w	112 w	120	122
141 vw	158 m	138 m		138 sh	140	140
171 m		154 m	151 m	161 m	160	
186 sh					180	182
207 vw	213 w	199 vw	194 w	205 w,b	210	
228 w					220	223
248 w	246 m	246 m	247 m,b	245 m,b	250	235
272 w					270	
301 w,b	292 sh	293 sh	281 sh	274 sh	290	
				317 sh		316
336 w,b	345 sh	357 sh			330	
357 w,b					370	
420 sh	427 sh				400	
451 m,b	446 m	444 m	444 m,b	446 m,b	450	446
497 w,b		493 sh		506 vw	490	
556 w	565 w	570 w,b	568 w,b	576 w,b	530	550
580 w,b					590	584
627 w,b	623 w,b	634 w,b	629 w,b	643 w,b	600	616
		788 vw				
846 vw	846 vw	846 vw	845 vw	847 vw		
972 m			938 sh	942 sh		
996 s	994 s	990 s	993 s	996 s	990	
1004 sh		1000 sh			1010	
1025 m					1020	
1059 s	1049 s	1054 s	1054 s	1059 s	1050	1020
1100 m	1083 sh	1081 sh	1084 sh	1082 sh	1090	
1139 w	1124 sh	1128 sh			1130	
1187 vw	1160 vw	1184 vw	1153 vw	1177 w,b	1180	
					1210	
					1240	
1302 vw	1293 vw	1302 vw	1301 vw	1300 vw		

The Raman spectra of $Li_{3-2x}(Fe_{1-x}Ti_x)_2(PO_4)_3$ $0 \leq x \leq 0.20$ are shown in Figure 5.4. The Raman spectrum of $Li_3Fe_2(PO_4)_3$ agrees well with that reported in the literature[2] for the monoclinic α-phase. The band positions are compared in Table 5.4 with that observed by Kravchenko et al.[11] for $Li_3Fe_2(PO_4)_3$ and other compounds with similar structures, to characterise the spectrum. It can be seen that the bands' positions match those reported for $Li_3Fe_2(PO_4)_3$, and the spectra of monoclinic $Li_3In_2(PO_4)_3$ and $Na_3Fe_2(PO_4)_3$ show very similar band positions. The bands are assigned to vibrations of lattice modes (0-400 cm^{-1}), FeO_6 octahedra (300-400 cm^{-1}), PO_4 deformations (400-700 cm^{-1}) and vibrations of the valency bonds of PO_4, with respect to Kravchenko et al.[11] Of the 120 Raman modes predicted for the $P2_1/n$ space group a total of 28 bands are observed at room temperature.

Unlike the X-ray diffraction patterns, the spectra of titanium doped lithium iron phosphate, $Li_{3-2x}(Fe_{1-x}Ti_x)_2(PO_4)_3$ $0 \leq x \leq 0.20$, show a Raman profile that is significantly different to that for undoped $Li_3Fe_2(PO_4)_3$. A total of 15 bands are observed, almost half that of the undoped compound, and the bands are broader, particularly in the range 900-1200 cm^{-1}. The band positions of $Li_{3-2x}(Fe_{1-x}Ti_x)_2(PO_4)_3$, $0 \leq x \leq 0.20$, are compared to those of monoclinic $Li_3Fe_2(PO_4)_3$ and rhombohedral $Na_3Fe_2(PO_4)_3$ (Table 5.5). The Raman profiles of the Ti-doped $Li_3Fe_2(PO_4)_3$ more closely resemble that of the rhombohedral $Na_3Fe_2(PO_4)_3$ compound rather than the monoclinic. Doping $Li_3Fe_2(PO_4)_3$ with titanium appears to significantly increase the symmetry of the local structure.

With Ti dopant quantities of 5 and 10 mol%, there are no observable additional bands that could be ascribed to an impurity phase. Doping of $LiNiPO_4$ with titanium in Chapter 4 resulted in an obvious $TiPO_4$ secondary phase. None of the bands from the spectra of $TiPO_4$ are visible here with these dopant quantities.

Only for 15 and 20 mol% Ti dopant are several extra bands observed at 161 and 942 cm^{-1}. These bands most likely indicate the formation of a small amount of secondary phase at the high Ti-dopant level or the formation of a new phase which has not been identified.

5.2 Differential Scanning Calorimetry

The DSC results shown in Figure 5.5 reveal a broad endotherm between 90 and 140 °C for all samples that most likely corresponds to evolution of water. The DSC results for undoped $Li_3Fe_2(PO_4)_3$ differ from those of the doped materials in having an endothermic peak at 230 °C. Previous literature reports that there is a phase change from the monoclinic α-phase to the monoclinic β-phase at this temperature, and then to the orthorhombic γ-phase at approximately 270 °C, giving rise to measurable changes in the DSC.[2,5] The second phase change is not particularly well defined for $Li_3Fe_2(PO_4)_3$. However, what is more important is that no endotherm is observed for any of the doped samples, indicating that the high temperature orthorhombic phase of $Li_3Fe_2(PO_4)_3$ may be stabilised to room temperature for the doped materials.

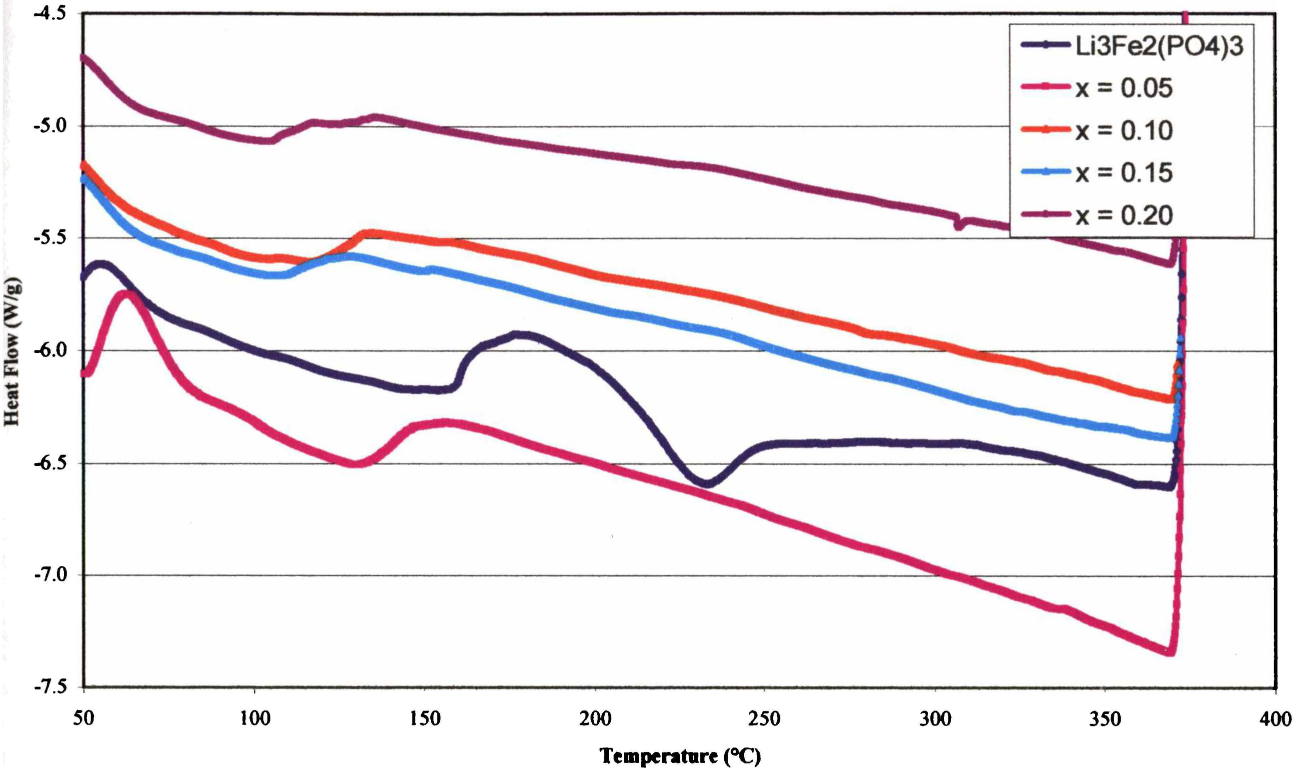

Figure 5.5 DSC of $Li_{3-2x}(Fe_{1-x}Ti_x)_2(PO_4)_3$, $0 \leq x \leq 0.20$

5.3 Particle Size Analysis and BET Surface Area

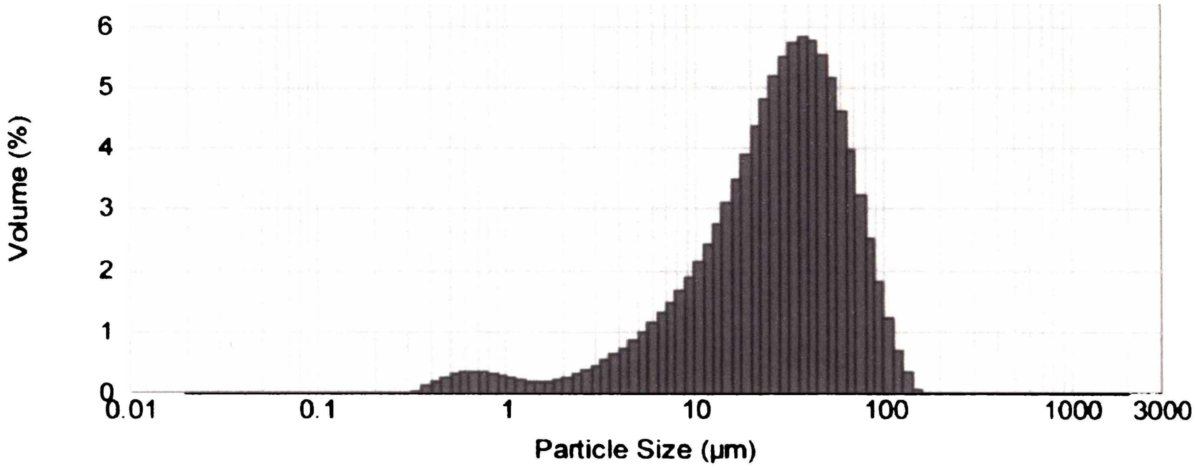

Figure 5.6 Particle Size Distribution of $Li_3Fe_2(PO_4)_3$

Figure 5.6 shows the results of a mastersize analysis. It is obvious that the particles are large and have a large distribution. BET results revealed a very low surface area of 0.27 m^2g^{-1}.

5.4 AC Impedance

5.4.1 Bulk Density Measurements

The bulk density of the pellets sintered for AC Impedance measurement was measured as per the method described in Section 2.4. The results are shown in Figure 5.7.

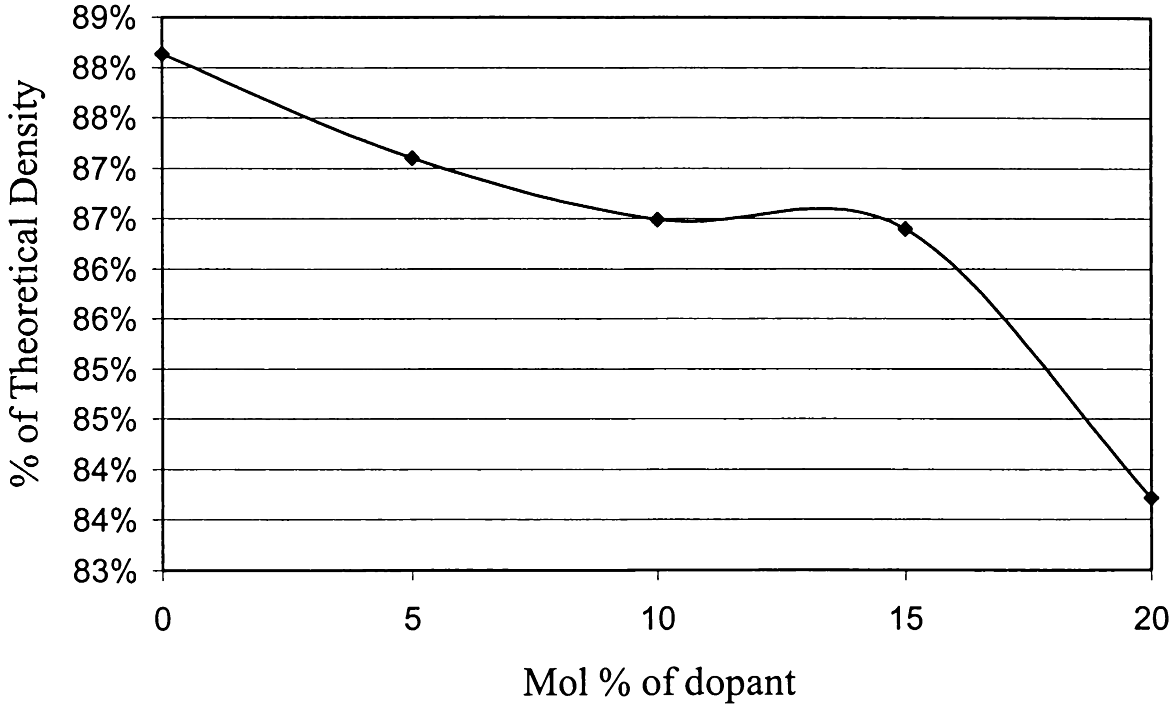

Figure 5.7 Bulk Density of $Li_{3-2x}(Fe_{1-x}Ti_x)_2(PO_4)_3$, $0 \leq x \leq 0.2$

The sintering temperature for $Li_{3-2x}(Fe_{1-x}Ti_x)_2(PO_4)_3$ is relatively high at 930 °C. Therefore, although sintering temperature increases with dopant content, and hence bulk density was expected to decrease with titanium as a dopant, the differences in density were not dramatic. Pellets made from these materials were dark brown and not the brilliant colours shown by the olivine structures.

AC impedance measurements were performed on $Li_{3-2x}(Fe_{1-x}Ti_x)_2(PO_4)_3$ $0 \le x \le 0.2$. Dividing by the actual density and multiplying by the theoretical density corrected the conductivity measured.

5.4.2 Circuit Modelling

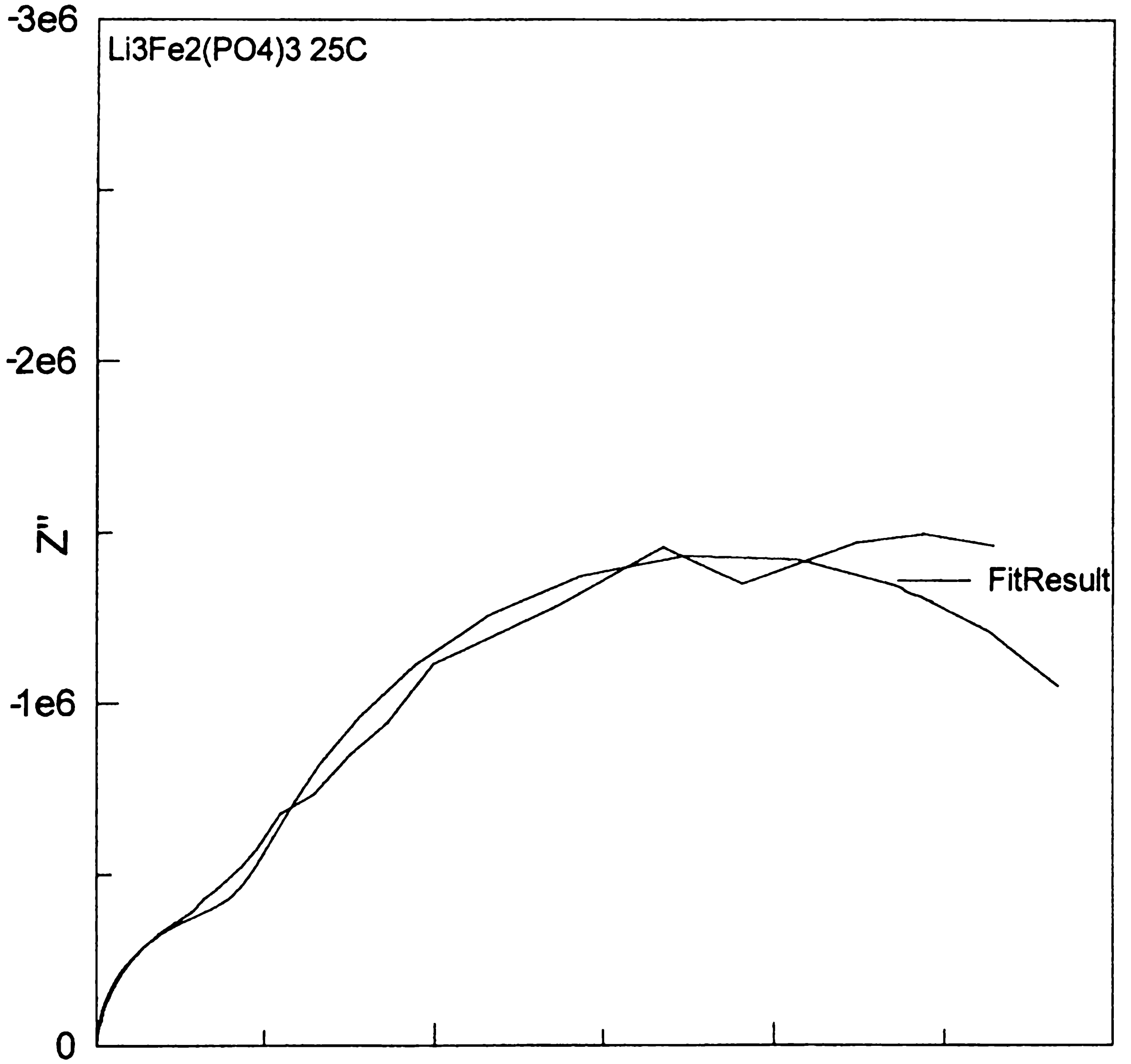

Figure 5.8 Impedance Spectra of $Li_3Fe_2(PO_4)_3$ at 25 °C

The Wagner polarisation technique using Ag blocking electrodes shows no electronic conduction for all samples. For $Li_3Fe_2(PO_4)_3$ at 25 °C (Figure 5.8), the complex impedance plane representation reveals a distorted high frequency semicircle of capacitance 20 pF, which is a typical value for grain boundary phenomena, and a smaller semicircle at high frequency, which is most likely representative of the bulk impedance. This is best represented by a Rs2RC equivalent circuit, and the fitting for this circuit is superimposed on the spectra in Figure 5.8.

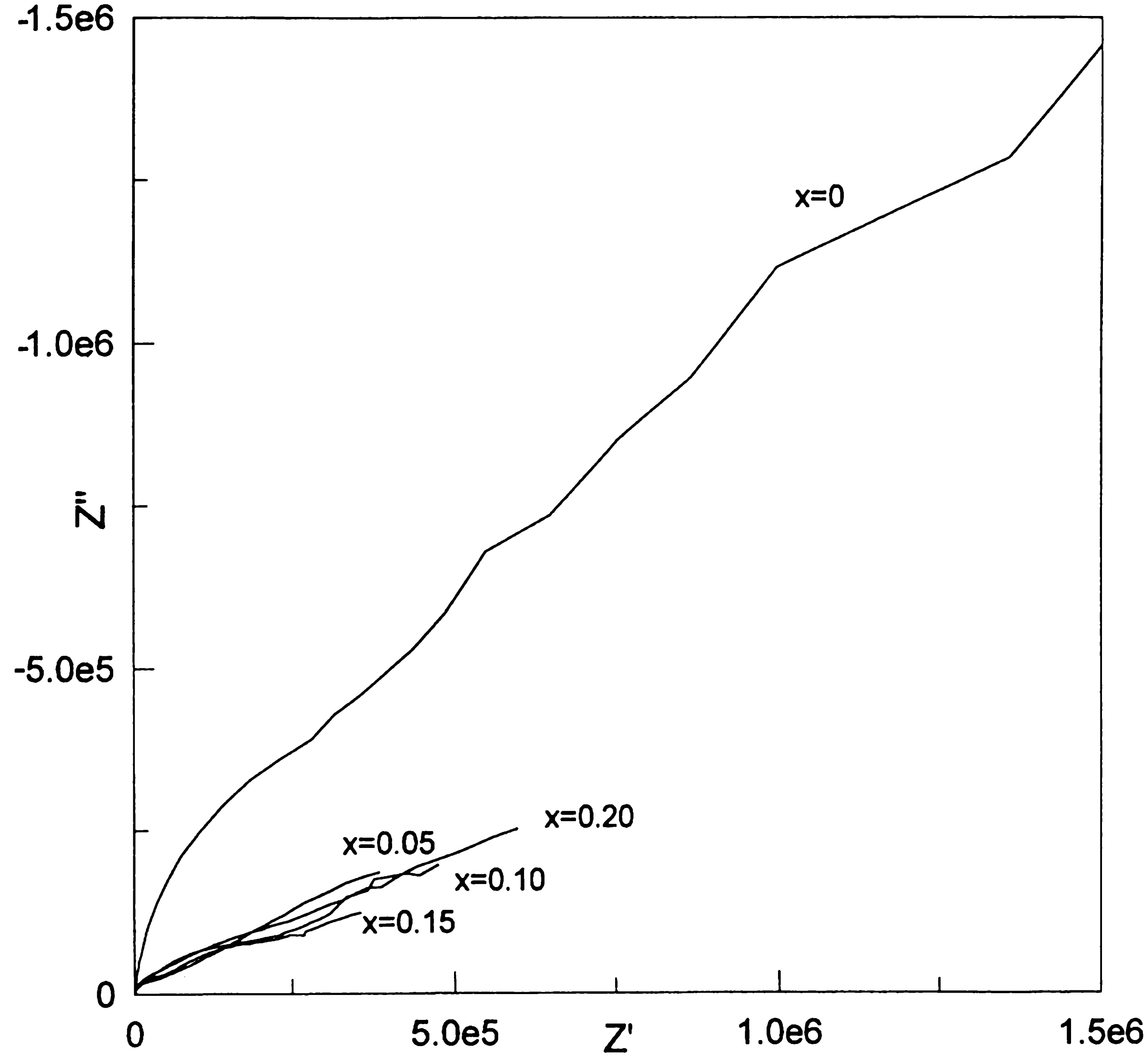

Figure 5.9 Impedance Spectra of $Li_{3-2x}(Fe_{1-x}Ti_x)_2(PO_4)_3$, $0 \leq x \leq 0.20$ at 25 °C

As has been determined by Rietveld analysis of the XRD data, there is no real difference in the refinement of $Li_3Fe_2(PO_4)_3$ using both monoclinic and orthorhombic symmetries at room temperature, although previous literature using single crystal X-ray diffraction data presents a slight difference between the two symmetries. However, Raman spectroscopy and DSC clearly reveals that the titanium doped samples have been stabilised in the orthorhombic γ-phase which is typical for $Li_3Fe_2(PO_4)_3$ at temperatures above 270 °C. The Impedance spectra for $Li_3Fe_2(PO_4)_3$ and the doped samples at room temperature are shown in Figure 5.9. It is obvious from the spectra and also from the Arrhenius plot in Figure 5.12, that the conductivity of the doped samples are considerably greater than the low temperature $Li_3Fe_2(PO_4)_3$.

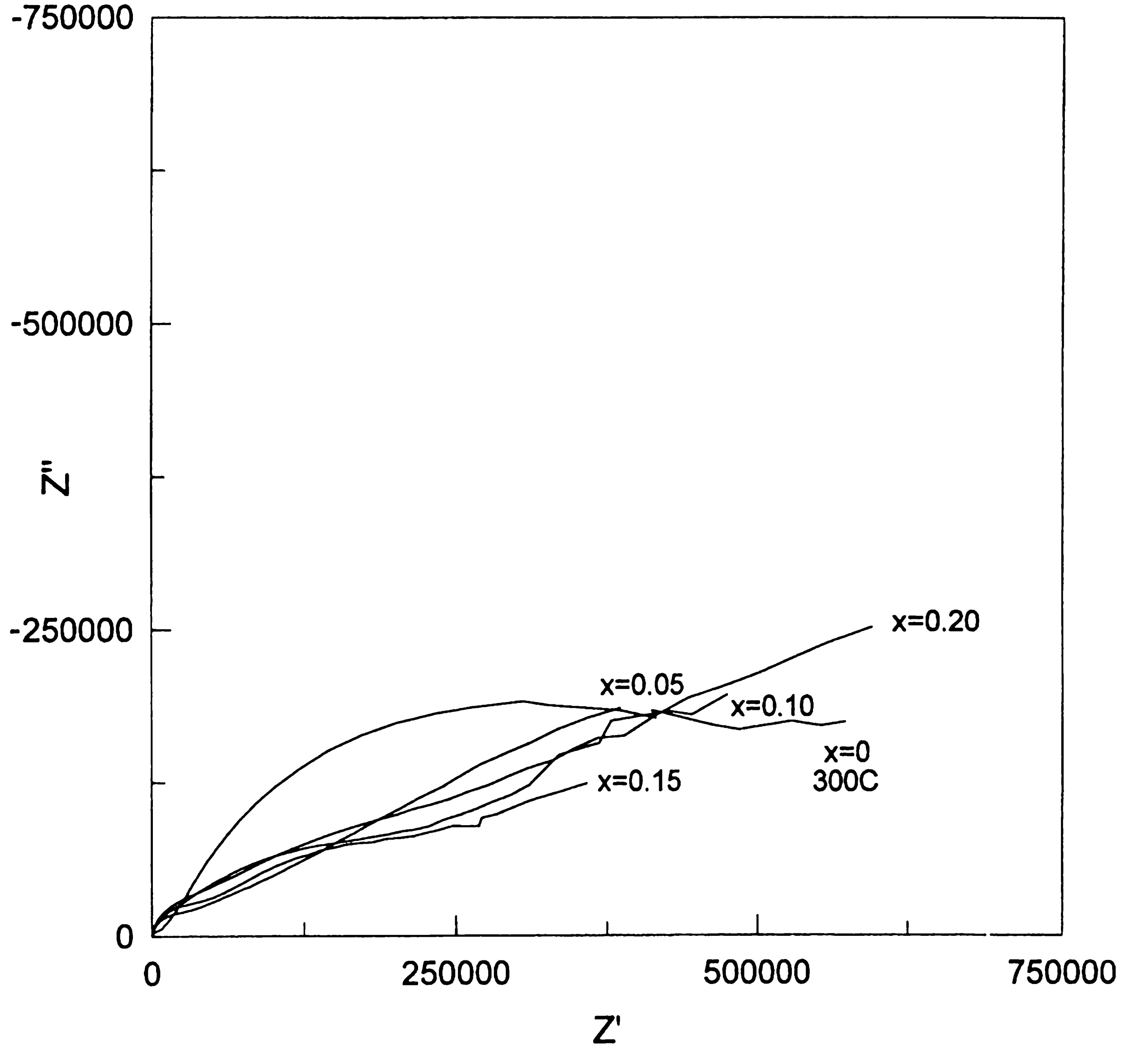

Figure 5.10 Impedance Spectra of $Li_3Fe_2(PO_4)_3$ at 300 °C and $Li_{3-2x}(Fe_{1-x}Ti_x)_2(PO_4)_3$, $0 \leq x \leq 0.20$ at 25 °C

It can be seen that the high temperature spectra for $Li_3Fe_2(PO_4)_3$ which should be in a high ionic conducting orthorhombic γ-phase, looks very similar to the doped samples at room temperature (Figure 5.10).

With increasing temperature the pellet conductivity rises and the features of the AC response are displaced to higher frequencies. With all of the complex impedance plots, there is difficulty in separating the semicircles into their separate components due to severe overlap, hence only total conductivities are reported.

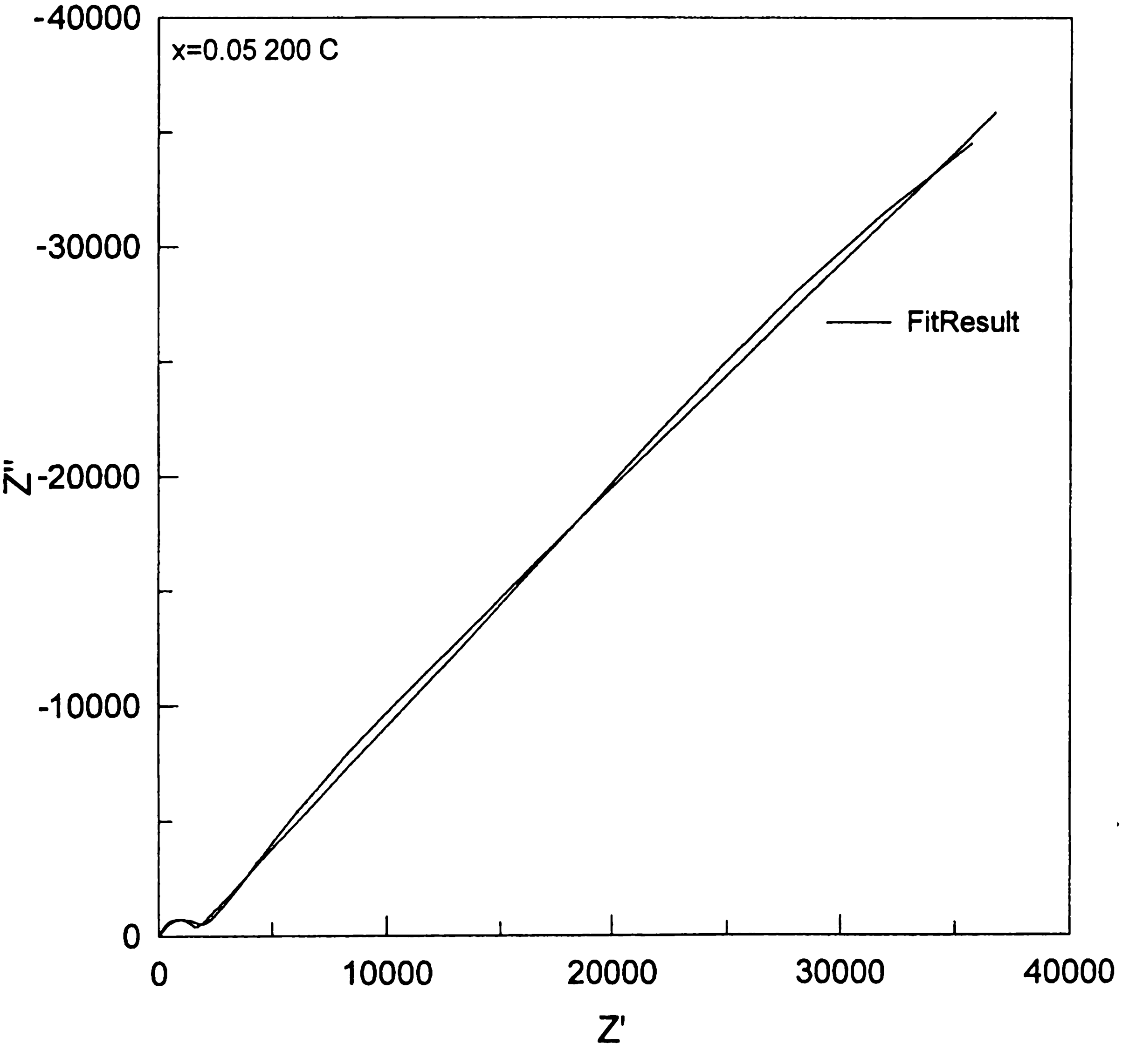

Figure 5.11 Impedance Spectra of $Li_{3-2x}(Fe_{1-x}Ti_x)_2(PO_4)_3$, x = 0.05 at 200 °C

The complex impedance spectra for the doped samples, and for the high temperature γ-phase $Li_3Fe_2(PO_4)_3$, consist of part of a semicircle terminated with a sloping line (Figure 5.11). The conductivity was determined by the low frequency intercept of the semicircle. The results for all the spectra are shown in Figure 5.12

The best room temperature results for all samples is from $Li_{2.70}Fe_{1.70}Ti_{0.30}(PO_4)_3$ with a value of 4.72 x 10^{-6} Scm^{-1} in comparison to $Li_3Fe_2(PO_4)_3$ with a value of 8.54 x 10^{-8} Scm^{-1}.

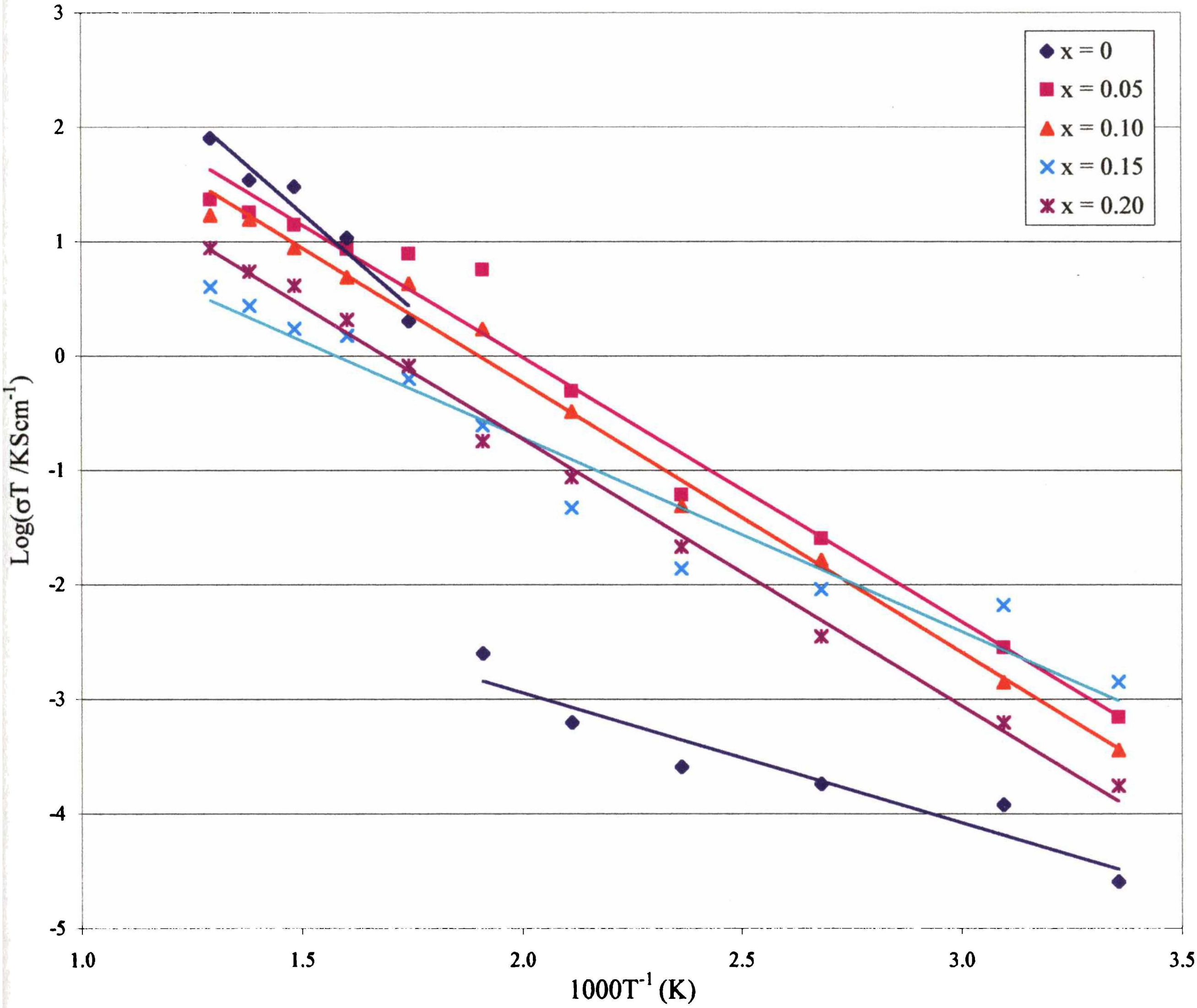

Figure 5.12 Total Conductivity of $Li_{3-2x}(Fe_{1-x}Ti_x)_2(PO_4)_3$, $0 \leq x \leq 0.2$

It can be seen from Figure 5.12 that the doped materials exhibit one slope only, while $Li_3Fe_2(PO_4)_3$ reveals two slopes, which is consistent with a phase change from monoclinic to orthorhombic. The activation energy was calculated from the slopes in this graph and is presented in Figure 5.13. The slope of $Li_3Fe_2(PO_4)_3$ is steeper in the orthorhombic phase with an activation energy value of 0.29 eV compared to the monoclinic phase with 0.10 eV. The doped materials should be performing similarly to the orthorhombic high temperature phase of $Li_3Fe_2(PO_4)_3$. However, their slopes are less steep, giving a lower activation energy than orthorhombic $Li_3Fe_2(PO_4)_3$ but higher than monoclinic. Higher temperatures and more frequent measurement intervals would provide more data points and would make these measurements more accurate. Other methods for improving the quality of the AC impedance data are discussed in Chapter 7.

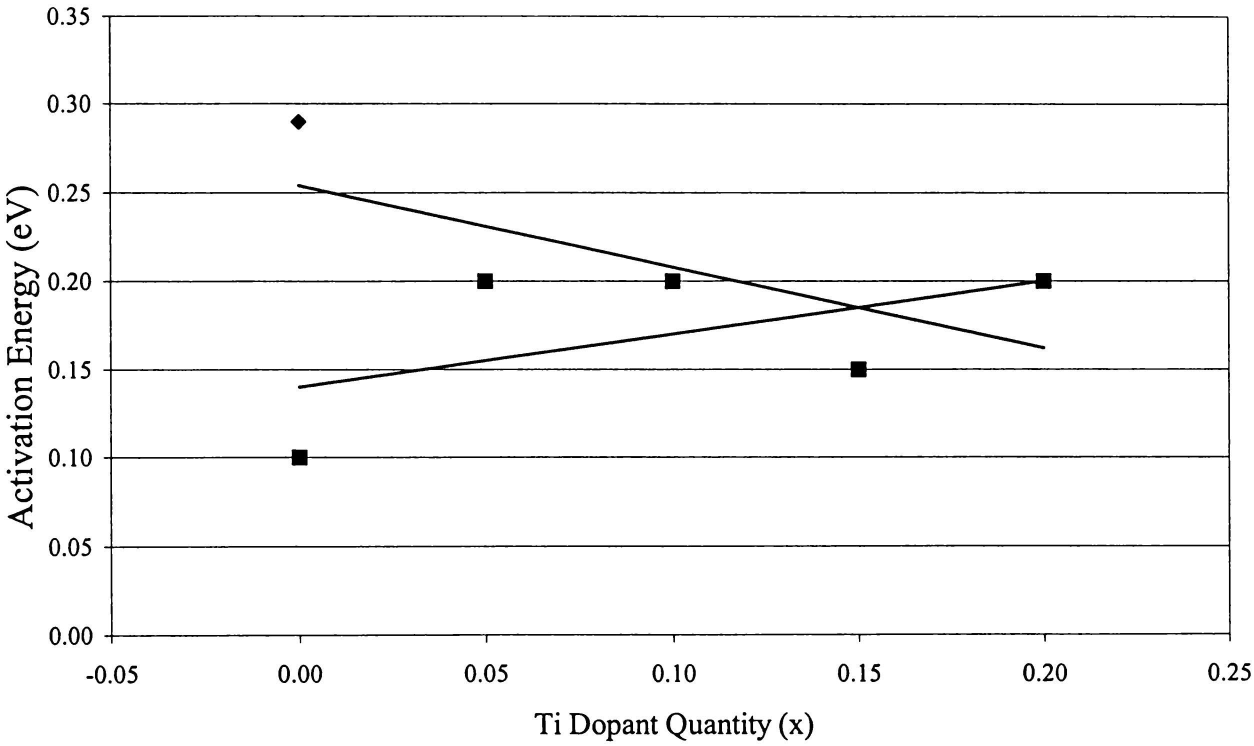

Figure 5.13 Activation Energy for $Li_{3-2x}(Fe_{1-x}Ti_x)_2(PO_4)_3$, $0 \leq x \leq 0.2$

5.5 Electrochemical Data

$Li_{3-2x}(Fe_{1-x}Ti_x)_2(PO_4)_3$, $0 \leq x \leq 0.2$ was initially examined as a prospective solid state electrolyte, due to the potential to stabilise the higher ionic conducting orthorhombic phase. There has been research on similar analogues for this purpose. Yadachi et al.[17,18] examined $Li_{1.3}Al_{0.3}Ti_{1.7}(PO_4)_{3-x}(ZO_4)_x$ (Z = V, Nb) (LATP). In LATP, lithium ions move through tunnels in a NASICON type structure, and efforts concentrated on increasing conductivity by enlarging the tunnel size again via anionic substitution and also by cationic substitution to stabilise a high temperature phase. Lithium scandium phosphate has been studied due to its advantage of having a single valence state, and the expectation this brings of improving the dielectric stability in comparison to LATP.[19,3] Studies involving the conductivity enhancement of the Fe analogue, include Losilla et al.,[4] Mari et al.[20] and this work.

The electrochemical performances of $Li_3Fe_3(PO_4)_3$, and $LiFe_2PO_4(SO_4)_2$ have been studied extensively.[1,5,8,10,144] Some of this work was repeated here, and then extended by utilising $Li_{2.70}Fe_{1.70}Ti_{0.30}(PO_4)_3$ as a cathode material in a lithium rechargeable battery. $Li_{2.70}Fe_{1.70}Ti_{0.30}(PO_4)_3$ was chosen as it had the best ionic conduction at room temperature out of the materials described in this chapter.

Solid-state reaction techniques were the only methods of synthesis available throughout this work, which limits the materials to the monoclinic and orthorhombic phases as the preferred rhombohedral form is generally synthesised via an ion-exchange process. The exception to this is rhombohedral $LiFe_2PO_4(SO_4)_2$, which makes it very attractive.

The advantage of the rhombohedral phase NASICON structure is that it has higher lithium ion mobility compared with the monoclinic phase, due to a larger free volume for Li^+ ion motion which results in higher lithium ion conduction. This provides better stability at higher current densities and therefore better cycling performance. It was hoped that the stabilised orthorhombic phase, having considerably higher room temperature conductivity than that of the monoclinic phase, would also behave better electrochemically at higher current densities.

Up to 2 lithiums per unit formula can be inserted into $Li_3Fe_2(PO_4)_3$ leading to $Li_5Fe_2(PO_4)_3$.[144] This corresponds to a theoretical capacity of approximately 130 mAh/g. In practice about 1.8 lithiums per unit formula can be reversibly inserted and extracted. The rhombohedral form displays a relatively flat discharge curve that averages 2.8V. The monoclinic $Li_3Fe_2(PO_4)_3$ discharge curve is distinguished by two plateaus at 2.85 and 2.70V, which correspond to the reduction of the two crystallographically distinct Fe^{3+} ions to Fe^{2+}. A reversible capacity loss for both structures occurs upon increasing the current density. The decrease in capacity is much less for the rhombohedral form than the monoclinic, which is ascribed to the differences in the free volume for Li^+ ion motion.

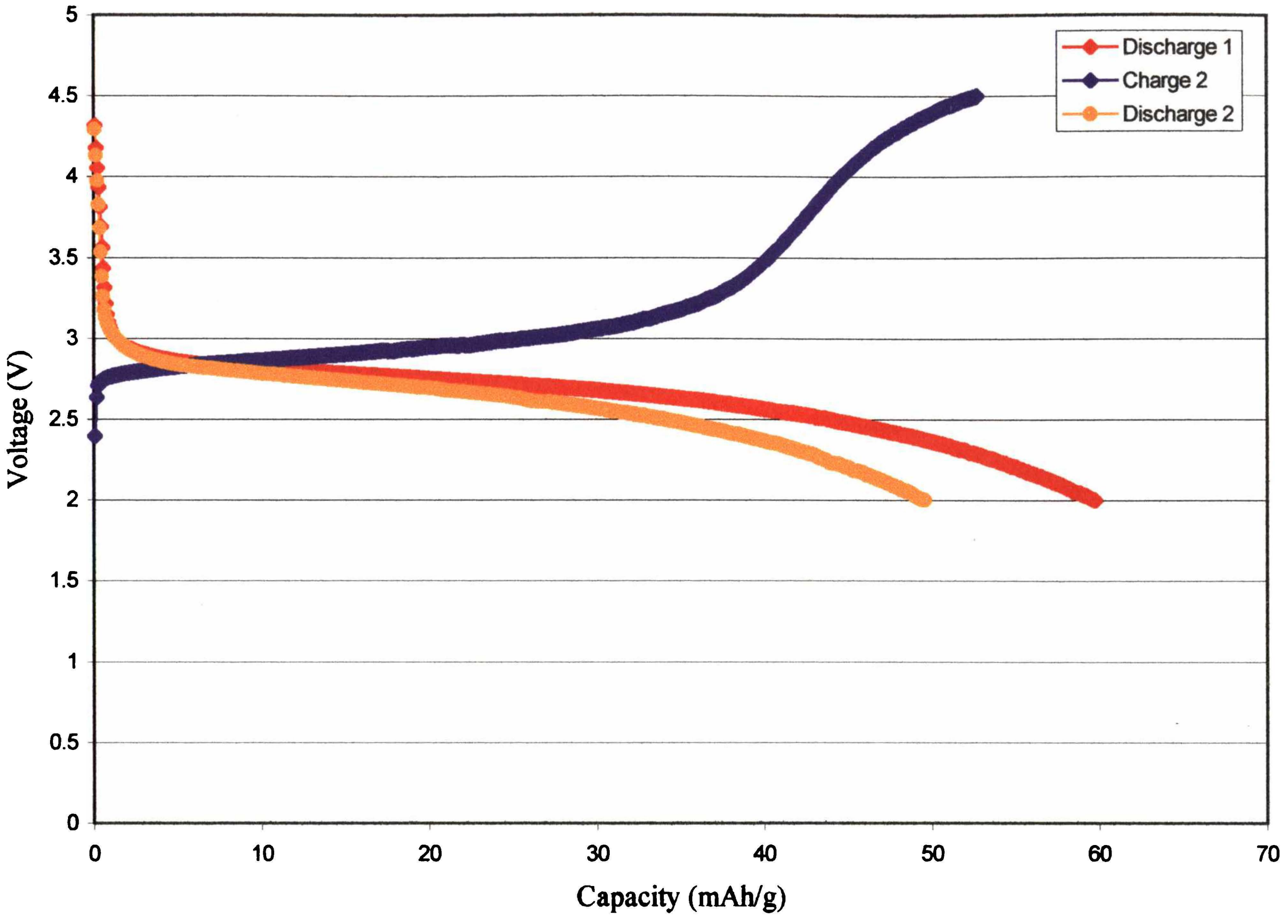

Figure 5.14 Cycling Behaviour of $Li_{2.70}Fe_{1.70}Ti_{0.30}(PO_4)_3$

Figure 5.14 shows the first two discharges and the second charge curves for $Li_{2.70}Fe_{1.70}Ti_{0.30}(PO_4)_3$. The maximum lithium that may practically be reversibly inserted into this structure is less than for $Li_3Fe_2(PO_4)_3$. The cell was first charged at a current density of 7.5 mA/g to extract lithium from the cathode, and then discharged at 7.5 mAh/g to insert lithium ions. $Li_{2.70}Fe_{1.70}Ti_{0.30}(PO_4)_3$ is already in the charged state so the first charge should be minimal, which is indeed the case. The first discharge of 60 mAh/g corresponds to the insertion of approximately 1 lithium per unit formula, the capacity could be improved if a lower cut off voltage was employed. Full extraction of the lithium inserted during the first discharge is not achieved during the next charge phase, and the second discharge inserts less lithium again.

The shape of the discharge curve for this material displays similar behaviour to the rhombohedral rather than the monoclinic $Li_3Fe_2(PO_4)_3$. There are no distinct plateaus in the shape of the curve as is shown by monoclinic $Li_3Fe_2(PO_4)_3$[1,144] and also by monoclinic $Li_3V_2(PO_4)_3$ in Chapter 6. Typically there is a downwards sloping curve right at the end of discharge for cathode materials but this material behaves differently. For the first half of the discharge, the curve is relatively flat at approximately 2.7V but towards the second half it curves downwards between 2.5 and 2.0V. One reason for this behaviour may be due to the titanium dopant. The first half of the discharge curve may correspond to the reduction of some of the Fe^{3+} to Fe^{2+}, and the second half may incorporate the reduction of some of the Ti^{4+} to Ti^{3+}. The Fe^{3+}/Fe^{2+} and the Ti^{4+}/Ti^{3+} redox couples lie at 2.8V and 2.4V respectively in the NASICON structure.[21]

The shape of the curve, its lack of plateaus and the polarisation observed between charge and discharge indicate that the kinetic behaviour of this material may be relatively poor, even though there is a significant improvement in conductivity in comparison to undoped $Li_3Fe_2(PO_4)_3$. Capacity fading, especially at faster rates, may be due to the trapping of lithium ions within the structure, possibly at grain boundary interfaces generated during the extraction and insertion of lithium. Increasing the current density decreases the discharge capacity achieved. When the current density is decreased again, there is some recovery of the discharge capacity, indicating that the cell performance is diffusion limited. A cell becomes diffusion limited when the total rate of lithium transported per unit area across a two-phase interface is no longer able to sustain a current. This occurs with shrinking surface area of the interface as lithiation proceeds.

The shape of the discharge curves of $Li_{2.70}Fe_{1.70}Ti_{0.30}(PO_4)_3$ are actually quite similar to $LiFe_2PO_4(SO_4)_2$ (Figure 5.15). In $LiFe_2PO_4(SO_4)_2$ insertion and extraction of lithium proceeds via a solid solution type behaviour and $Li_{2.70}Fe_{1.70}Ti_{0.30}(PO_4)_3$ may be performing in a similar fashion. $Li_{2.70}Fe_{1.70}Ti_{0.30}(PO_4)_3$ has a significantly increased symmetry in comparison to $Li_3Fe_2(PO_4)_3$ as shown by its similarity to the Raman results of the rhombohedral bands observed for $Na_3Fe_2(PO_4)_3$.

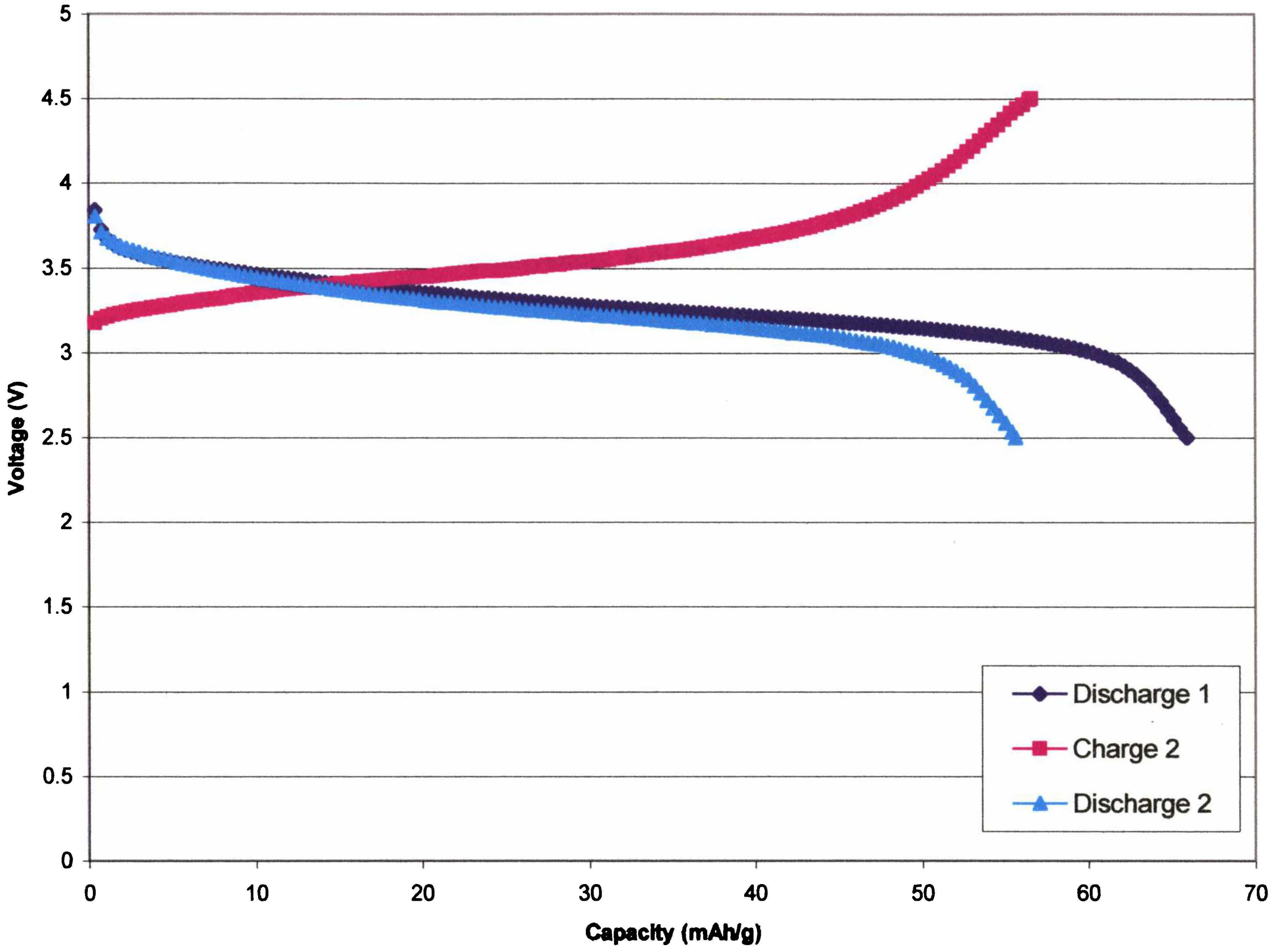

Figure 5.15 Cycling Behaviour of $LiFe_2PO_4(SO_4)_2$

Figure 5.15 shows the first two discharges and second charge curves for rhombohedral $LiFe_2PO_4(SO_4)_2$. The discharge curves demonstrate the 0.5 eV difference in the redox potentials of $LiFe_2PO_4(SO_4)_2$ and $Li_3Fe_2(PO_4)_3$ due to the partial substitution of $(SO_4)^{2-}$ for $(PO_4)^{3-}$. The discharge capacity of 65 mAh/g obtained for $LiFe_2PO_4(SO_4)_2$ corresponds to the insertion of 1 lithium per unit formula. This is actually less than previously published material with a capacity of 100mAh/g.[144] It can be seen that there are no distinct plateaus on the charge and discharge curves indicating the insertion and extraction of lithium proceeds with a solid solution type behaviour.

5.6 References

---

[1] A.K. Padhi, K.S. Nanjundaswamy, C. Masquelier, S. Okada and J.B. Goodenough, *J. Electrochem. Soc.*, 144, pp1609-1613, **1997.**

[2] A.B. Bykov, A.P. Chirkin, L.N. Demyanets, S.N. Doronin, E.A. Genkina, A.K. Ivanov-shits, I.P. Kondratyuk, B.A. Maksimov, O.K. Mel'nokov, L.N. Muradyan, V.I. Simonov and V.A. Timofeeva, *Solid State Ionics*, 38, pp31-50, **1990.**

[3] T.Suzuki, K. Yoshida, K. Uematsu, T. Kodama, K. Toda, Z. Guang Ye and M. Sato, *Solid State Ionics*, 104 (1-2), p27-33, **1997.**

[4] E.R. Losilla, S. Bruque, M. A. G. Aranda, L. Moreno-Real, E. Morin and M. Quarton, *Solid State Ionics*, 112, pp53-62, **1998.**

[5] F. d'Yvoire, M. Pintard-Screpel, E. Bretey and M. de la Rochere, *Solid State Ionics*, 9&10, p851, **1983.**

[6] J. M. Winand, A. Rulmont and P. Tarte, *Solid State Chem.*, 87, p83, **1990.**

[7] C. Masquelier, A. K. Padhi, K. S. Nanjundaswamy and J. B. Goodenough., *J. Solid State Chem.*, 135, pp228-234, **1998.**

[8] A. K. Padhi, V. Manivannan and J. B. Goodenough, *J. Electrochem. Soc.*, 145, (5), p1518, **1998.**

[9] A. Manthiram and J. B. Goodenough, *J. Solid State Chem.*, 71, p349, **1987.**

[10] S. Okada, K. S. Najundaswamy, A. Manthiram and J. B. Goodenough, *in Proceedings of the 36th Power Sources Conference,* Cherry Hill, NJ, June, **1994.**

[11] V.V. Kravchenko, V.I. Michailov and S.E. Sigaryov, *Solid State Ionics*, 50, pp19-30, **1992.**

[12] V.V. Kravchenko and S.E. Sigaryov, *J. Mater. Sci.*, 29 (22), pp6004-10, **1994.**

[13] M. Barj, G. Lucazeau and C. Delmas, *J. Solid State Chem.*, 100, pp141-150, **1992.**

[14] S.E. Sigaryov, *Mater. Sci. Eng.*, B13, pp121-123, **1992.**

[15] V.V. Kravchenko and S.E. Sigaryov, *Solid State Commun.*, 83, pp149-152, **1992.**

[16] M.Barj, H. Perthuis and Ph. Colomban, *Solid State Ionics*, 9&10, pp845-850, **1983.**

[17] H. Aono, E. Sugimoto, Y. Sadaoka, N. Imanaka and G. Adachi, *J. Electrochem. Soc.*, 140, (7), p1827, **1993.**

[18] G. Yadachi, N. Imanaka and H. Aono, *Adv. Mater.*, 8, p127, **1996.**

---

[19] G. G. Amatucci and A. Safari, *Solid State Ionics*, 60, p357, **1993.**

[20] C. M. Mari, R. Ruffo and M. Catti, *in 196th Meeting of the Electrochem. Soc.*, Honolulu, Oct, Abstract no. 195, **1999.**

[21] A.K. Padhi, K.S. Nanjundaswamy, C. Masquelier and J.B. Goodenough, *J. Electrochem. Soc.*, 144, pp2581-2586, **1997.**

6 Lithium Vanadium Phosphate – $Li_3V_2(PO_4)_3$

6 Lithium Vanadium Phosphate – $Li_3V_2(PO_4)_3$

6.1 Characterisation

Firing $Li_3V_2(PO_4)_3$ in 2%H_2/98%N_2 showed via X-ray diffraction and Raman spectroscopy that a single solid phase was formed according to the following reaction:

$$3Li_2CO_3 + 6NH_4H_2PO_4 + 2V_2O_3 \xrightarrow{reducing} 2Li_3V_2(PO_4)_3 + 6NH_3 + 9H_2O + 3CO_2 \qquad \text{Equation 6.1}$$

6.1.1 X-Ray Diffraction

The materials under investigation here, namely $Li_3V_2(PO_4)_3$ along with its iron analogue from Chapter 5, belong to the $Fe_2(SO_4)_3$ –type structure which are related to the NASICON (Na Super Ionic Conductors) family of structures. $Li_3V_2(PO_4)_3$ also crystallises in two modifications of the β-$Fe_2(SO_4)_3$ -type compound: the first is synthesised by conventional solid state reactions resulting in a monoclinic ($P2_1/n$) α,β-phase or orthorhombic (P*can*) symmetry, and the second is via a soft chemistry reaction like an ion exchange process, resulting in the rhombohedral symmetry.[1] Again, like its iron analogue, $V_2(PO_4)_3$ frameworks are built up of PO_4 tetrahedra sharing corners with VO_6 octahedra.

As in Chapter 5, a titanium dopant was used to attempt to introduce vacancies on the Li^+ sites and the stabilisation of the high temperature orthorhombic γ–phase (P*can*) of $Li_3V_2(PO_4)_3$ by doping V^{3+} with Ti^{4+} ions.

Initial firing experiments were done in pure hydrogen at 875 °C via the method proposed by Barker et al.[2] This revealed a single phase of monoclinic or orthorhombic symmetry, however efforts were made to simplify this process. Ohkawa et al.[3] synthesised this material at 1100 °C under an argon atmosphere, which is a relatively limiting temperature. Synthesis was attempted at 875 °C under a nitrogen atmosphere. However, it was revealed via X-ray diffraction and ICPS analysis that although the starting elements for the compound were in the right ratio, there were secondary phases of unreacted starting components. A compromise was found by using V_2O_3 instead of V_2O_5, which lowered the reducing strength needed of the sintering atmosphere. 2% H_2 in 98% N_2 was used as a sintering atmosphere, with a sintering temperature of 875 °C producing a single phase material.

Similar to the iron analogue from Chapter 5, analysis of the powder X-ray diffraction results show that $Li_3V_2(PO_4)_3$ can be refined using both $P2_1/n$ monoclinic and P*can* orthorhombic symmetry. The refinement of both symmetries reveals there is little difference between the monoclinic and orthorhombic symmetry. Like the iron analogue, the value obtained for alpha in the monoclinic refinement presents an angle of 90.3°, a minimal distortion from orthorhombic symmetry, hence the orthorhombic refinement is presented here.

Differential scanning calorimetry experiments and X-ray diffraction analysis from the literature show that for $Li_3V_2(PO_4)_3$, there is a change from a monoclinic α-phase to a monoclinic β-phase at approximately 120 °C, and from a monoclinic β-phase to the orthorhombic γ–phase at approximately 170 °C.[1,4] Ohkawa et al. demonstrated that doping $Li_3V_2(PO_4)_3$ with zirconia stabilises the orthorhombic γ–phase at room temperature. Their DSC results for their doped samples reveal a flat line with no phase changes.[3]

The results of the Rietveld refinement of the XRD data of $Li_3V_2(PO_4)_3$ are shown in Figure 6.1 and Table 6.1. The Rietveld analysis was performed using Fullprof 98® software. Initial structural and thermal parameters were taken from the data for α-phase $Li_3Fe_2(PO_4)_3$ from Bykov et al.[5] as a starting model for the refinement. Scale and background parameters were refined initially followed in subsequent iterations by cell, zero point and peak shape parameters. The atomic positions and oxygen occupancies were fixed while the cell parameters and then the occupancy factors for the phosphorus and then the vanadium atoms were refined. Once the cell parameters and the occupancy factors were established, the atomic positions of the vanadium, the phosphorus and then the oxygen atoms were refined.

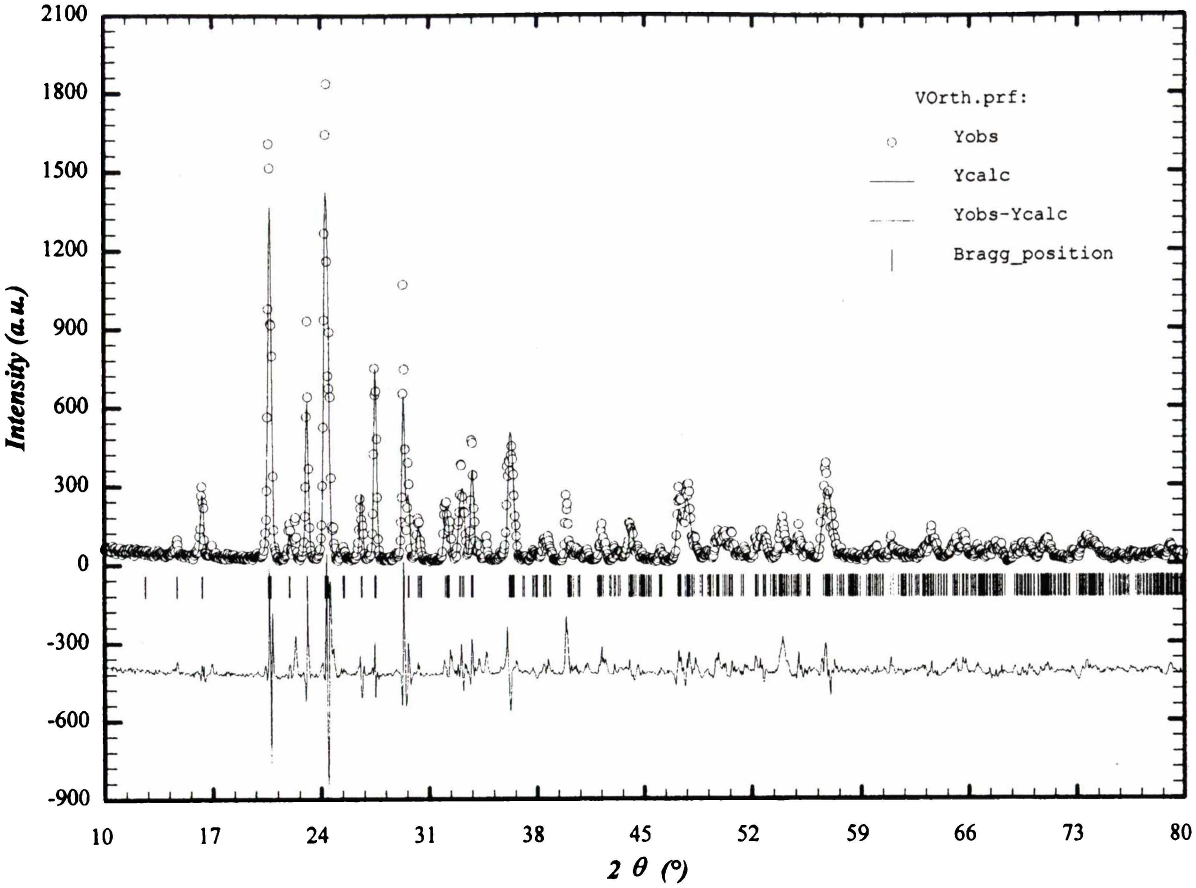

Figure 6.1 Structure Refinement of $Li_3V_2(PO_4)_3$

Similar to its iron analogue, $Li_{3-2x}(V_{1-x}Ti_x)_2(PO_4)_3$ $0 \leq x \leq 0.20$ can also be indexed in the orthorhombic symmetry. The Rietveld refinement results of these materials are shown in Appendix II. The data for $Li_{3-2x}(V_{1-x}Ti_x)_2(PO_4)_3$ $0 \leq x \leq 0.20$ are summarised in Table 6.2. There is an expansion in the volume of the crystal lattice with increasing dopant content. The increase is in all directions but notably in the *c*-axis. Titanium 4+ has a scattering factor of 18 in comparison to vanadium 3+ with a scattering factor of 20 so a decrease in the occupancy of the vanadium site would be expected. The data in Table 6.2 confirms there is a general trend showing a small decrease in vanadium site occupancy with increasing titanium content.

The Rietveld fit to the experimental data for the $Li_3V_2(PO_4)_3$ material is adequate in so far that it fits the peak portions but does not fully reproduce the relative intensities of several of the major peaks. A particular problem was in reproducing intensities for peaks such as those at 21, 24, and 30° 2θ, which are actually envelopes of two or more closely positioned peaks. This problem in the refinements could not be solved by adjusting peak shape parameters. It is interesting to note, however, that with increasing Ti dopant the peaks in these positions become more separated and better defined, and the corresponding Rietveld fits are improved (Appendix II).

Table 6.1 Refined Crystallographic Parameters for $Li_3V_2(PO_4)_3$ (P*can*) - X-ray diffraction data for 639 reflections and 38 variables.

Atom	*x*	*y*	*z*	Occupancy	B_{iso} (Å^2)
V	0.2438 (18)	0.1081 (7)	0.4671 (11)	2.014 (33)	0.61 *
P	0.1078 (30)	0.1460 (16)	0.1094 (26)	2.000 *	0.58 *
P	0.0446 (32)	0.5000 *	0.2500 *	1.000 *	0.62 *
O	0.4347 (52)	0.3357 (33)	0.0787 (45)	2.000 *	1.10 *
O	0.3194 (48)	0.2808 (33)	0.4758 (48)	2.000 *	1.29 *
O	0.1694 (47)	0.0399 (32)	0.0713 (46)	2.000 *	1.53 *
O	0.4326 (41)	0.0959 (29)	0.3402 (48)	2.000 *	1.17 *
O	0.1434 (50)	0.4274 (27)	0.1554 (45)	2.000 *	1.32 *
O	0.1600 (48)	0.2013 (34)	0.2564 (47)	2.000 *	1.03 *
Li	0.2950 *	0.3220 *	0.2760 *	1.000 *	1.50 *
Li	0.5770 *	0.1930 *	0.4210 *	1.000 *	2.40 *
Li	0.9120 *	0.2410 *	0.2970 *	1.000 *	4.10 *
a = 8.6093, b = 12.0401, c = 8.5916, * = Fixed Parameters V =890.575 (422) Å^3 , wRp = 31.8, Rp =24.9 , $\chi 2$ =7.73					

Table 6.2 Ti^{4+} doped $Li_3V_2(PO_4)_3$ Refinement Summary

Parameter	$Li_3V_2(PO_4)_3$	Ti = 0.05	Ti = 0.10	Ti = 0.15	Ti = 0.20
a	8.6093 (26)	8.6082 (19)	8.6142 (19)	8.6217 (16)	8.6265 (15)
b	12.0401 (32)	12.0326 (25)	12.0368 (23)	12.0368 (19)	12.0432 (18)
c	8.5916 (23)	8.5981 (18)	8.6085 (17)	8.6177 (15)	8.6273 (14)
Volume ($Å^3$)	890.575 (421)	890.588 (323)	892.590 (309)	894.325 (257)	896.292 (244)
V Site Occupancy	2.014 (33)	1.984 (28)	1.908 (30)	1.883 (23)	1.845 (23)

As had been shown in the iron analogue, partial substitution of one $(PO_4)^{3-}$ polyanion for one $(SO_4)^{2-}$ per formula unit preserves the hexagonal structure for all *x* in $Li_{1+x}Fe(PO_4)(SO_4)_2$ with a sacrifice of 0.3 eV or about one third of the 0.8 eV found between $Li_xFe_2(SO_4)_3$ and $Li_{3+x}Fe_2(PO_4)_3$.[6] It was hoped that the same polyanion substitution that was successful for $Li_{1+x}Fe(PO_4)(SO_4)_2$, which resulted in a higher voltage, could be performed with a vanadium analogue. The synthesis of the vanadium analogue of $Li_{1+x}Fe(PO_4)(SO_4)_2$ was attempted using the same process as the iron analogue. A limiting step in this process is the maximum sintering temperature of approximately 475 °C due to the formation of gaseous SO_2. If the substitution of V^{3+} for Fe^{3+} was successful, the open circuit voltage (vs. lithium) of a battery would be 3.8V, in comparison to 3.3V for a cell made with $Li_3V_2(PO_4)_3$.

As will be shown later in section 6.4, an attractive open circuit voltage was obtained with a value of 3.89V. However, the material obtained from this synthesis was not an analogue of $Li_{1+x}Fe(PO_4)(SO_4)_2$ but a mixture of various phases. Figure 6.2 shows the X-ray diffraction patterns of the $Li_{1+x}Fe(PO_4)(SO_4)_2$ and the attempted vanadium analogue. It is obvious that the desired rhombohedral structure was not obtained, and that several phases consisting mainly of lithium vanadium phosphorus oxide $LiVOPO_4$, vanadium pentoxide V_2O_5, and possibly lithium sulphate Li_2SO_4 resulted instead. The main interest in this material was the potential increase in voltage, so a cell was therefore constructed to determine cell voltage. The cell voltage of 3.89V obtained was due to the V^{5+}/V^{3+} redox couple in the presence of the

$(PO_4)^{3-}$ polyanion, rather than the desired V^{4+}/V^{3+} redox couple in the presence of the $(PO_4)^{3-}$ polyanion partially substituted with the $(SO_4)^{2}$.

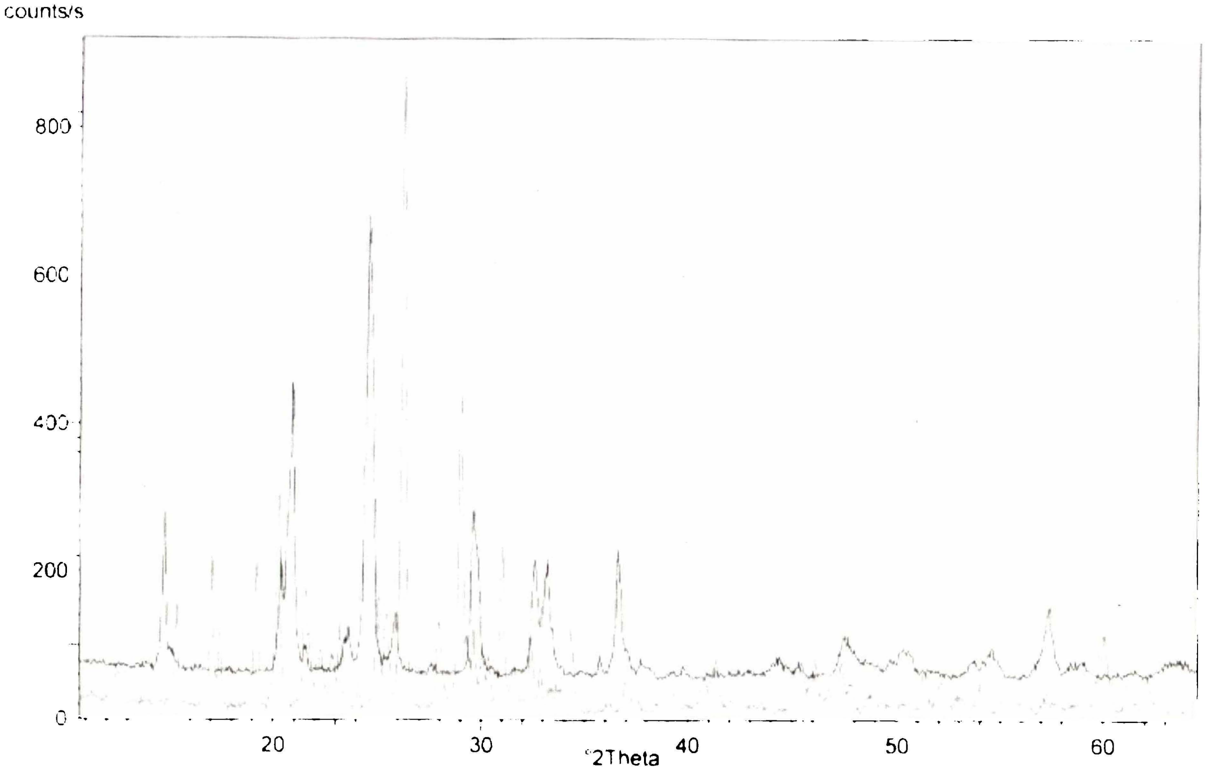

Figure 6.2 X-ray Diffraction Patterns of $Li_{1+x}Fe(PO_4)(SO_4)_2$ (top) and V^{3+} Substitution (bottom)

6.2 Particle Size Analysis and BET Surface Area

The following figure shows the results of a mastersize analysis. Again, it is obvious that the particles are relatively large, although not as large as the iron analogue, and have a large distribution. In contrast, BET results revealed a high surface area of 6.82 m^2g^{-1}. This is the highest by far out of the four materials studied and may be due to the different sintering conditions.

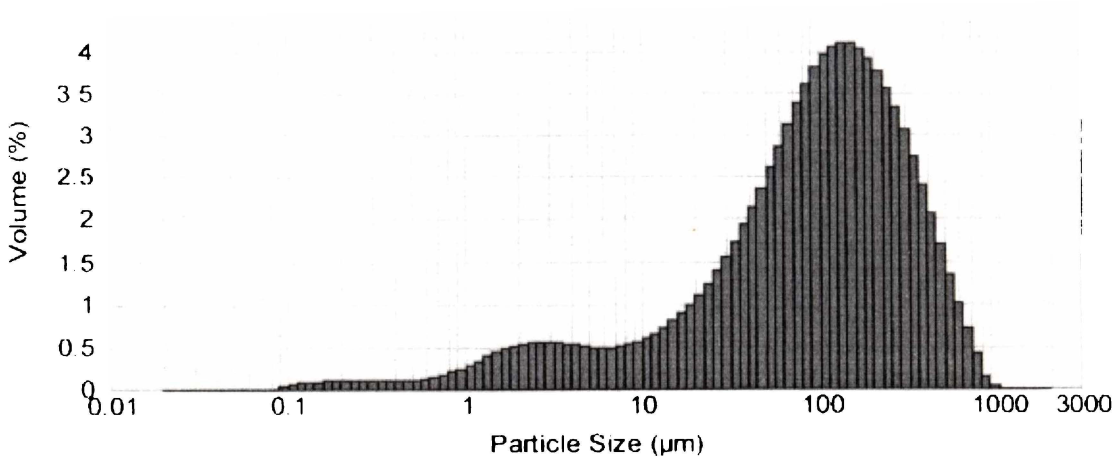

Figure 6.3 Particle Size Distribution of $Li_3V_2(PO_4)_3$

6.3 AC Impedance

6.3.1 Bulk Density Measurements

The sintering temperature for $Li_{3-2x}(V_{1-x}Ti_x)_2(PO_4)_3$ is 875 °C with a reducing atmosphere of $2\%H_2/98\%N_2$. This temperature was increased to 925 °C for the AC impedance pellets in order to maximise the bulk density. Although an increase in sintering temperature with dopant content and hence a decrease in bulk density was expected with titanium as a dopant, the differences in density were not dramatic. The overall densities of these materials in comparison to the other phosphates studied are much lower, and this is most likely due to the reducing atmosphere employed. The pellets made for AC impedance measurements were very brittle, and were of a uniform grey/green colour.

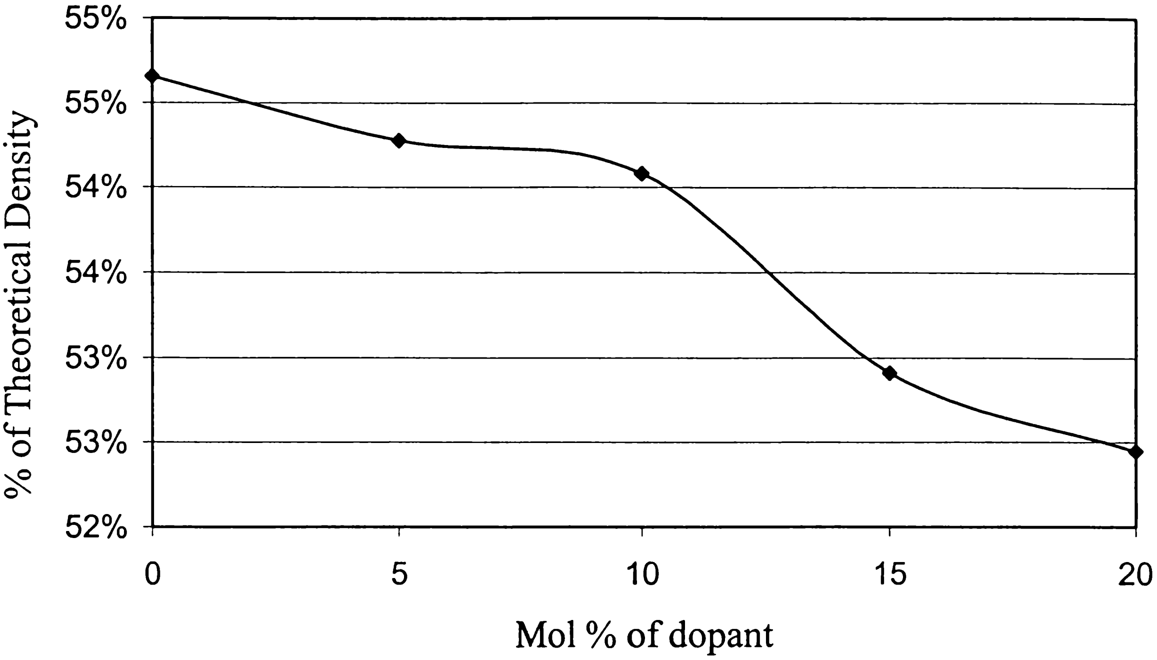

Figure 6.4 Bulk Density of $Li_{3-2x}(V_{1-x}Ti_x)_2(PO_4)_3$, $0 \leq x \leq 0.2$

AC impedance measurements were performed on $Li_{3-2x}(V_{1-x}Ti_x)_2(PO_4)_3$ $0 \leq x \leq 0.2$. Dividing by the actual density and multiplying by the theoretical density corrected the conductivity measured. The materials measured here were considerably different to their iron analogue in terms of the components that make up the total impedance. Warburg impedances representative of lithium ion diffusion were prevalent and were easily distinguished at high temperatures. However, the general trends in terms of total conductivity were similar.

6.3.2 Circuit Modelling

For $Li_3V_2(PO_4)_3$ at 25 °C (Figure 6.5), the grain and grain boundary impedances are again very hard to distinguish, so a simple RsRC equivalent circuit was used for fitting. This circuit is superimposed on the spectra. The spectra does not match the fit that well and this is probably due to a suppression of the spectra below the x axis.

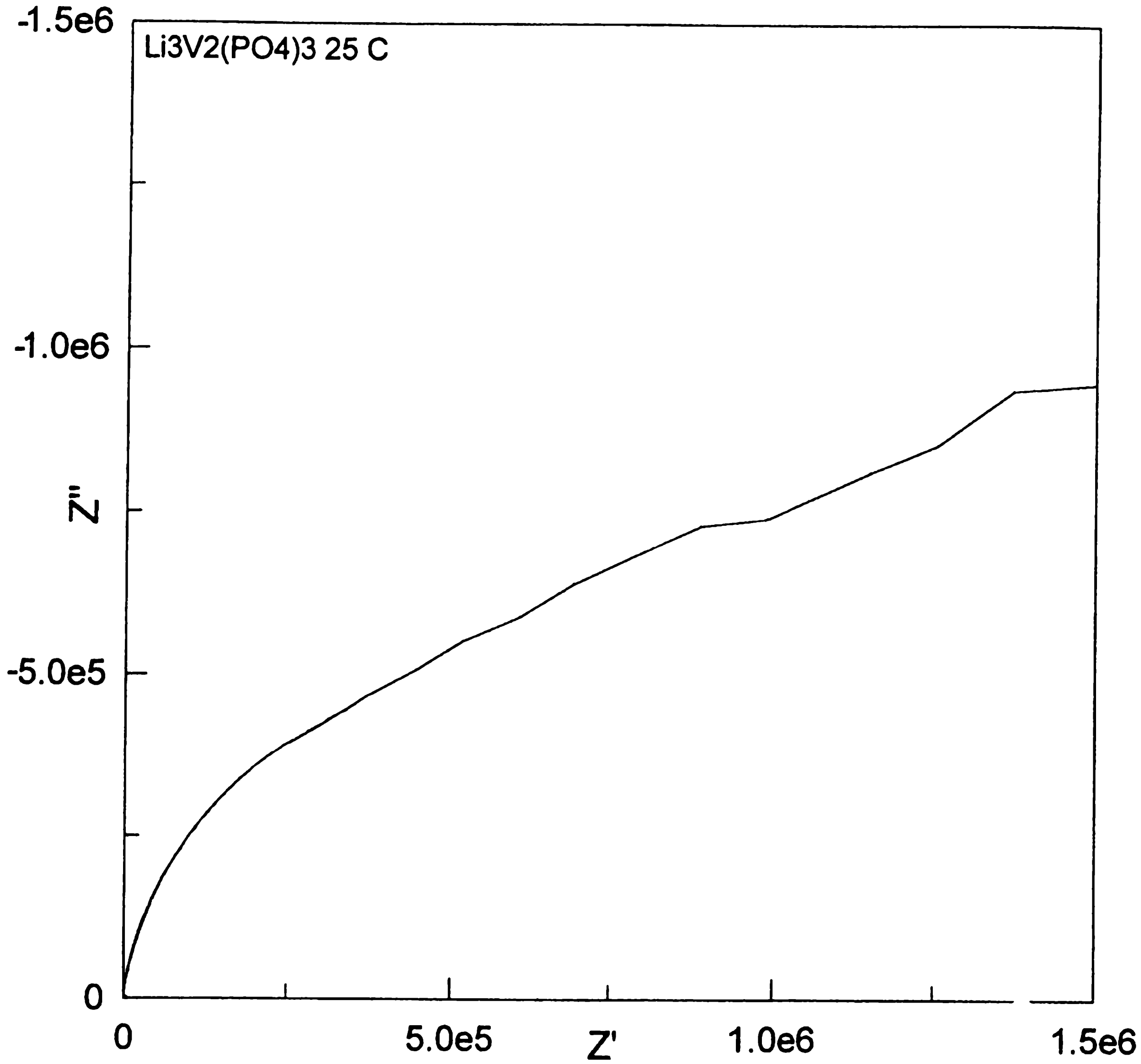

Figure 6.5 Impedance Spectra of $Li_3V_2(PO_4)_3$ at 25 °C

According to published literature, $Li_3V_2(PO_4)_3$ is a monoclinic α-phase at room temperature.[2,3] The powder X-ray diffraction data obtained for $Li_3V_2(PO_4)_3$ showed little or no difference between the monoclinic and orthorhombic refinements, so the higher symmetry data is presented. The titanium doped $Li_3V_2(PO_4)_3$ fit only as the orthorhombic γ-phase, which is typical for $Li_3V_2(PO_4)_3$ at temperatures above 170 °C. The impedance spectra for $Li_3V_2(PO_4)_3$ and the doped samples at room temperature are shown in Figure 6.6. It is obvious from the spectra and also from the Arrhenius plot in Figure 6.9 that the conductivity values for the doped samples are considerably enhanced in comparison to low temperature $Li_3V_2(PO_4)_3$.

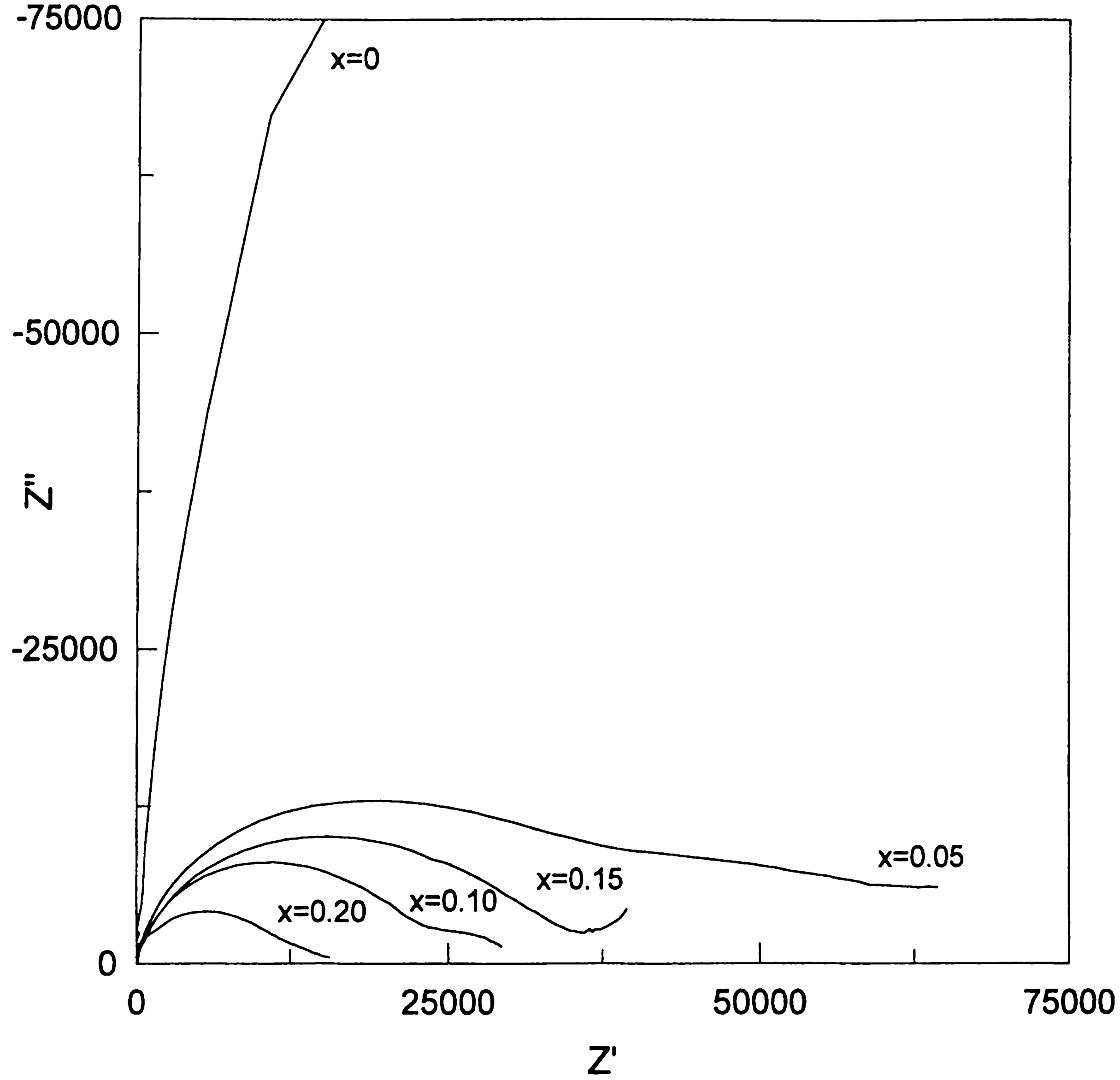

Figure 6.6 Impedance Spectra of $Li_{3-2x}(V_{1-x}Ti_x)_2(PO_4)_3$, $0 \leq x \leq 0.20$ at 25 °C

It can be seen that the high temperature spectra for $Li_3V_2(PO_4)_3$, which should be in its high ionic conducting orthorhombic γ-phase, looks very similar to the doped samples at room temperature (Figure 6.7).

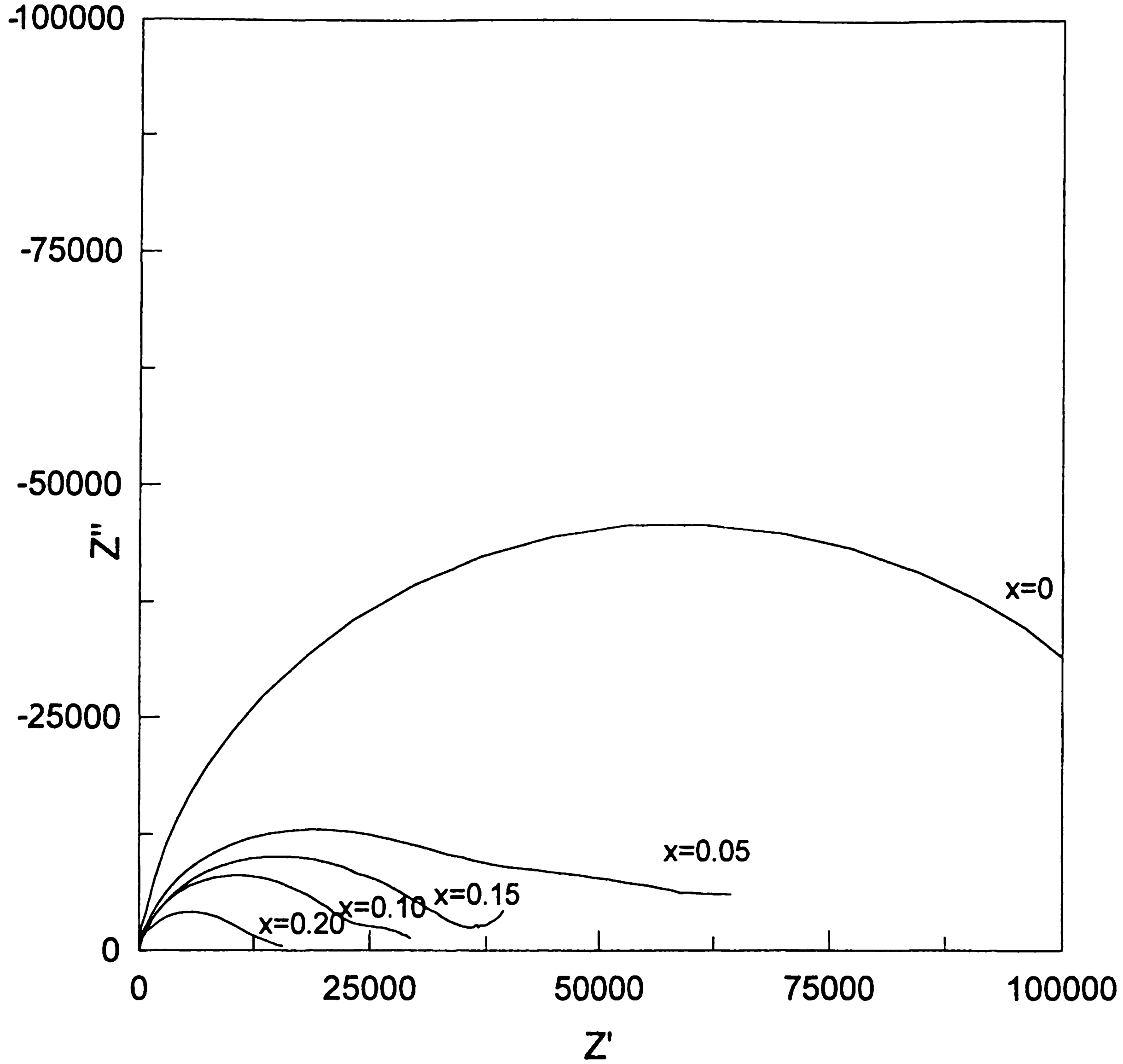

Figure 6.7 Impedance Spectra of $Li_3V_2(PO_4)_3$ at 150 °C and $Li_{3-2x}(V_{1-x}Ti_x)_2(PO_4)_3$, $0 \leq x \leq 0.20$ at 25 °C

With increasing temperature, the pellet conductivity rises and the features of the AC response are displaced to higher frequencies. With all of the complex impedance plots, there is difficulty in separating the semicircles into their separate components due to overlap; hence only total conductivities are reported.

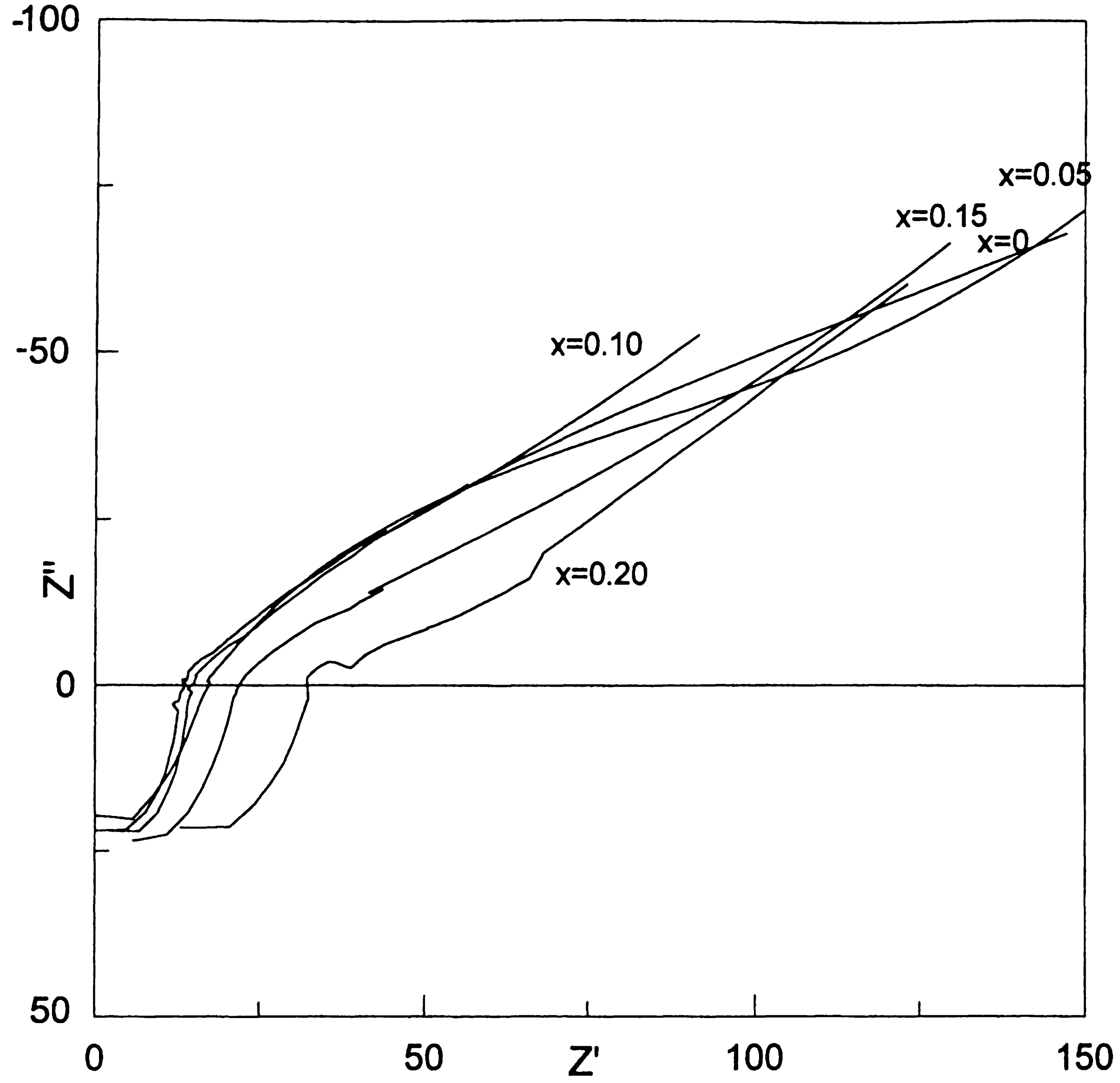

Figure 6.8 Impedance Spectra of $Li_{3-2x}(V_{1-x}Ti_x)_2(PO_4)_3$, $0 \leq x \leq 0.20$ at 300 °C

At 300 °C for all $Li_{3-2x}(V_{1-x}Ti_x)_2(PO_4)_3$ $0 \leq x \leq 0.20$, the diffusion of the lithium ions is prevalent (Figure 6.8). The bulk resistance and the grain boundary resistance are barely visible and are dramatically suppressed below the x-axis.

The best room temperature conductivity of these materials was from $Li_{2.60}V_{1.60}Ti_{0.40}(PO_4)_3$ with a value of 5.77×10^{-4} Scm^{-1} in comparison to $Li_3V_2(PO_4)_3$ with a value of 6.06×10^{-6} Scm^{-1}, which is an improvement of approximately orders of magnitude. Unfortunately, Raman characterisation was not possible with these materials, however, this material behaves similarly to $Li_3Fe_2(PO_4)_3$. The Raman spectra of Ti doped $Li_3Fe_2(PO_4)_3$ more closely resembled that of the rhombohedral $Na_3Fe_2(PO_4)_3$ rather than monoclinic $Li_3Fe_2(PO_4)_3$. With both Ti doped $Li_3Fe_2(PO_4)_3$ and $Li_3V_2(PO_4)_3$, the increase in conductivity is likely due to increased symmetry in the structure likely via the Li ion positions. The materials display behaviour which is more representative of the open framework NASICON structure allowing better Li ion mobility and therefore higher ionic conduction at room temperature.

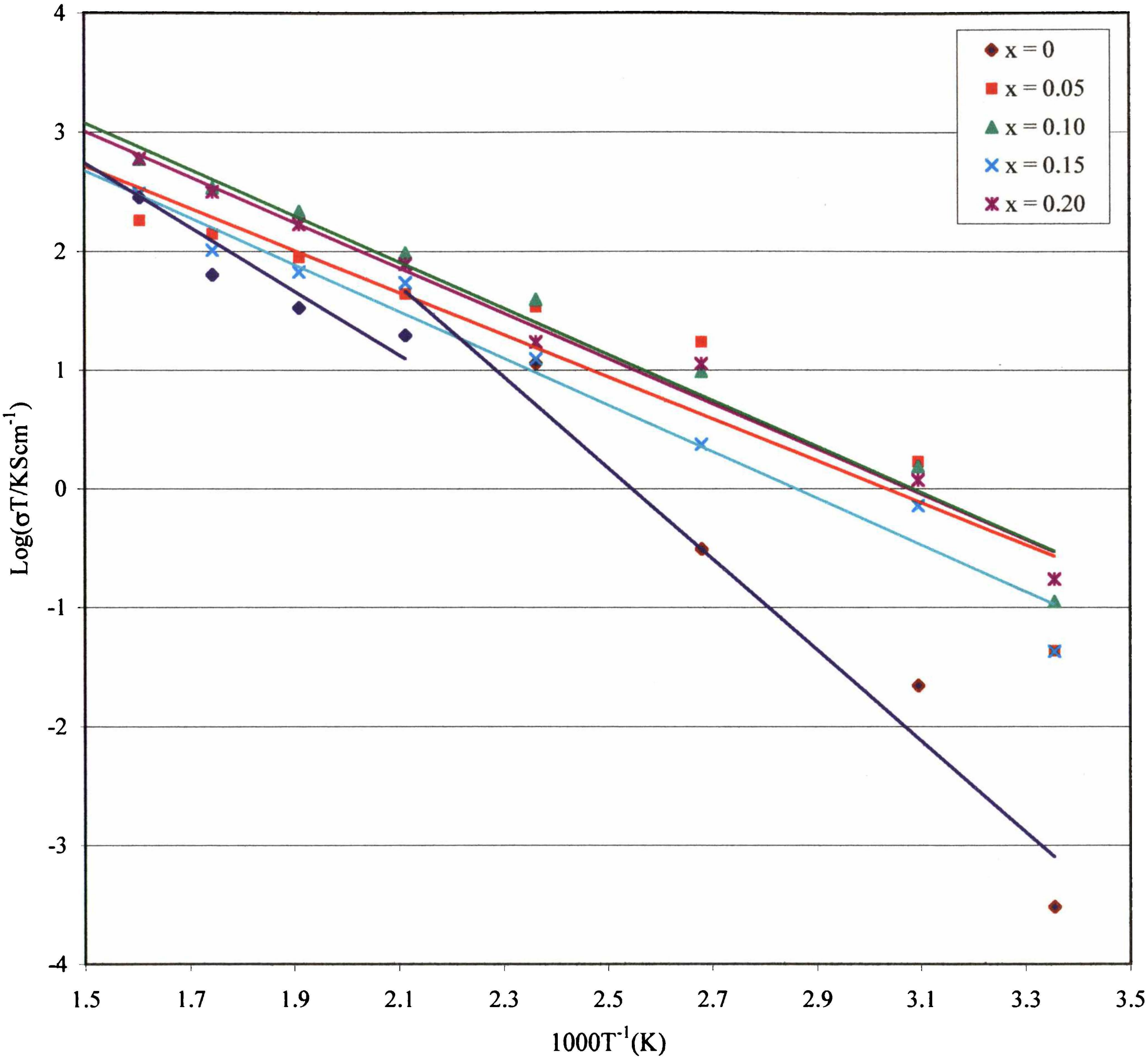

Figure 6.9 Total Conductivity of $Li_{3-2x}(V_{1-x}Ti_x)_2(PO_4)_3$, $0 \leq x \leq 0.2$

It can be seen from Figure 6.9 that the doped materials exhibit one slope only, while $Li_3V_2(PO_4)_3$ reveals two slopes, which is consistent with a phase change from monoclinic to orthorhombic between 150 and 200 °C. The activation energies were calculated from the slopes in this graph and are presented in Figure 6.10. The slope of $Li_3V_2(PO_4)_3$ is steeper in the monoclinic phase with an activation energy value of 0.33 eV compared to the high temperature orthorhombic phase with a value of 0.23 eV. The doped materials perform similarly to the orthorhombic high temperature phase of $Li_3V_2(PO_4)_3$ with similar activation energies.

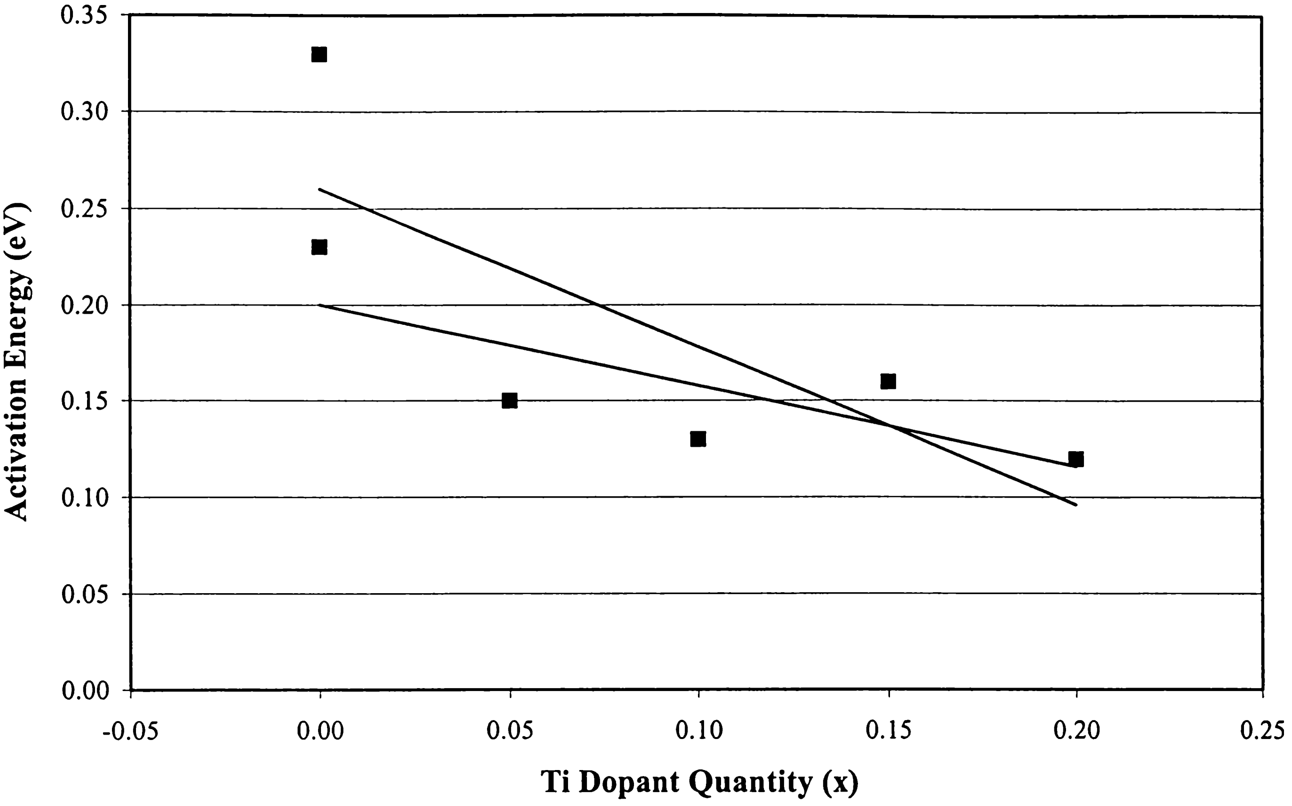

Figure 6.10 Activation Energy for $Li_{3-2x}(V_{1-x}Ti_x)_2(PO_4)_3$, $0 \le x \le 0.2$

6.4 Electrochemical Data

The electrochemical performance of $Li_3V_2(PO_4)_3$ has been studied previously.[1] The results of Ohkawa et al.[3] demonstrate a discharge capacity of approximately 90 mAh/g, and with an improvement via stabilisation of the orthorhombic phase by Zr^{4+} doping this increases to approximately 105 mAh/g between a 3 and 4.3V window. Barker et al.[2] have demonstrated a discharge capacity of 131 mAh/g within the same window. Figure 6.11 shows the first charge and first two discharge curves for $Li_3V_2(PO_4)_3$ synthesised under $2\%H_2/98\%N_2$. The cell was charged at a current of 7.5mA/g to extract lithium from the cathode material, and then discharged at the same to rate to insert lithium ions. The first charge of approximately 135 mAh/g corresponds to the extraction of 2 lithiums per unit formula from $Li_3V_2(PO_4)_3$ oxidising the two V^{3+} ions to V^{4+}. The first discharge with a capacity of 130 mAh/g inserts most of the lithium back into the structure and reduces both vanadiums back to the 3+ state. The second discharge shows a slight loss in capacity. The second charge is not shown but is similar to the first. It is not shown in order to reveal the plateaus of the first charge more clearly.

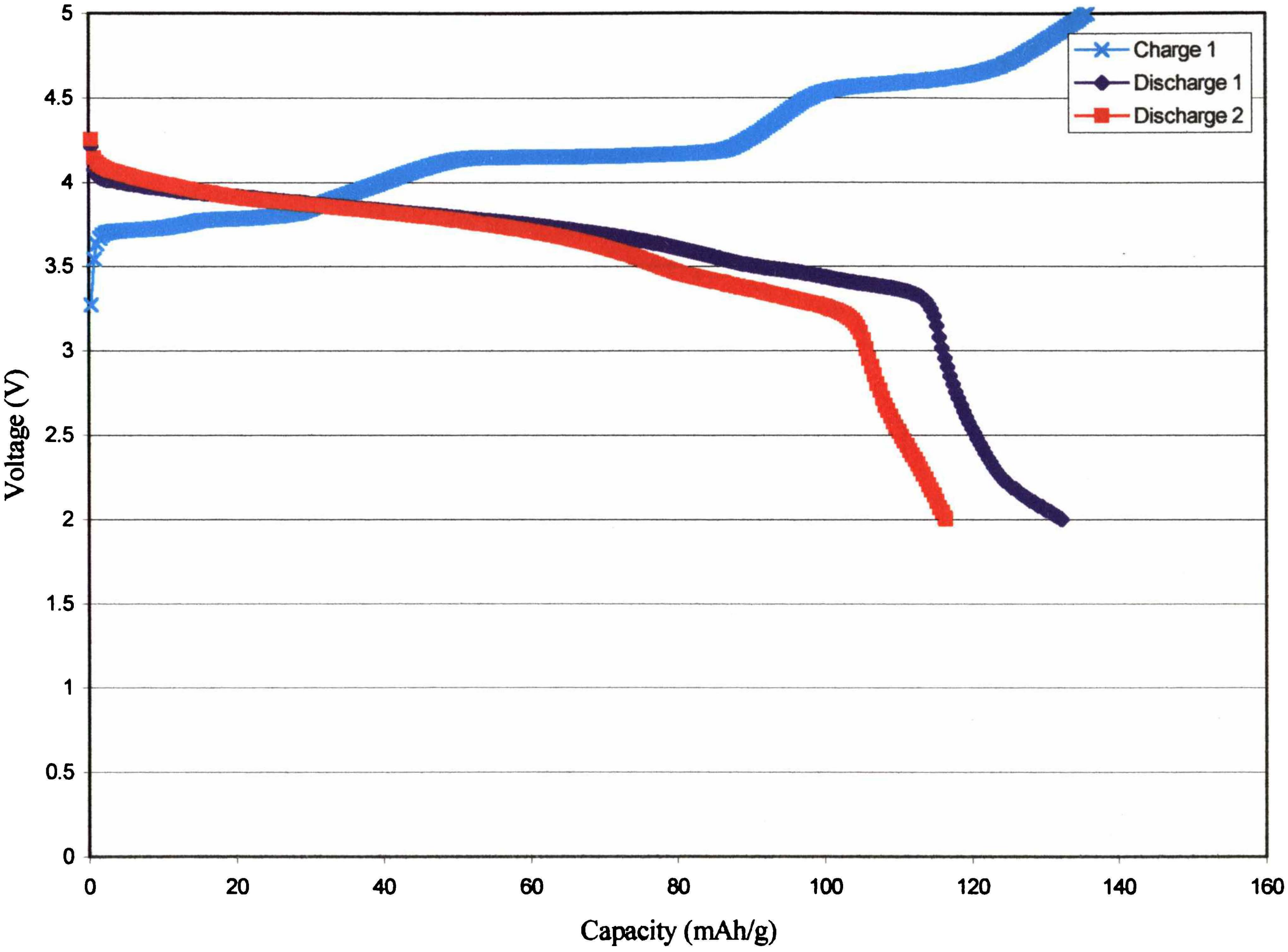

Figure 6.11 Cycling Behaviour of $Li_3V_2(PO_4)_3$

The extraction of the two lithiums per unit formula in the first charge from $Li_3V_2(PO_4)_3$ has several defined plateaus. Barker et al. report the extraction of approximately 2 lithiums per unit formula obtaining a capacity of 136 mAh/g but charged only to 4.2V. Their charge curve corresponds to only the first two plateaus on the charge curve presented here, which was charged to 5V. The charge curve to 5V shows an extra plateau that corresponds to the third lithium available for extraction from the $Li_3V_2(PO_4)_3$ structure. The main difference between the results of Barker et al. and the data presented here is this extra plateau utilised by cycling to higher voltages. However, there is less capacity obtained at each plateau indicating that the active material is not fully utilised in the cathode. The theoretical capacity of this material is 197 mAh/g. This corresponds to approximately 66 mAh/g per lithium in the structure. Each plateau in the charge curve represents the extraction of 1 lithium per unit formula, so from the data presented, approximately 45 mAh/g per plateau is achieved, which corresponds to approximately 70% maximum extraction of each lithium. Each plateau also represents the reduction of three crystallographically distinct vanadiums from V^{3+} to V^{2+}. The doped samples do not display these distinct plateaus.

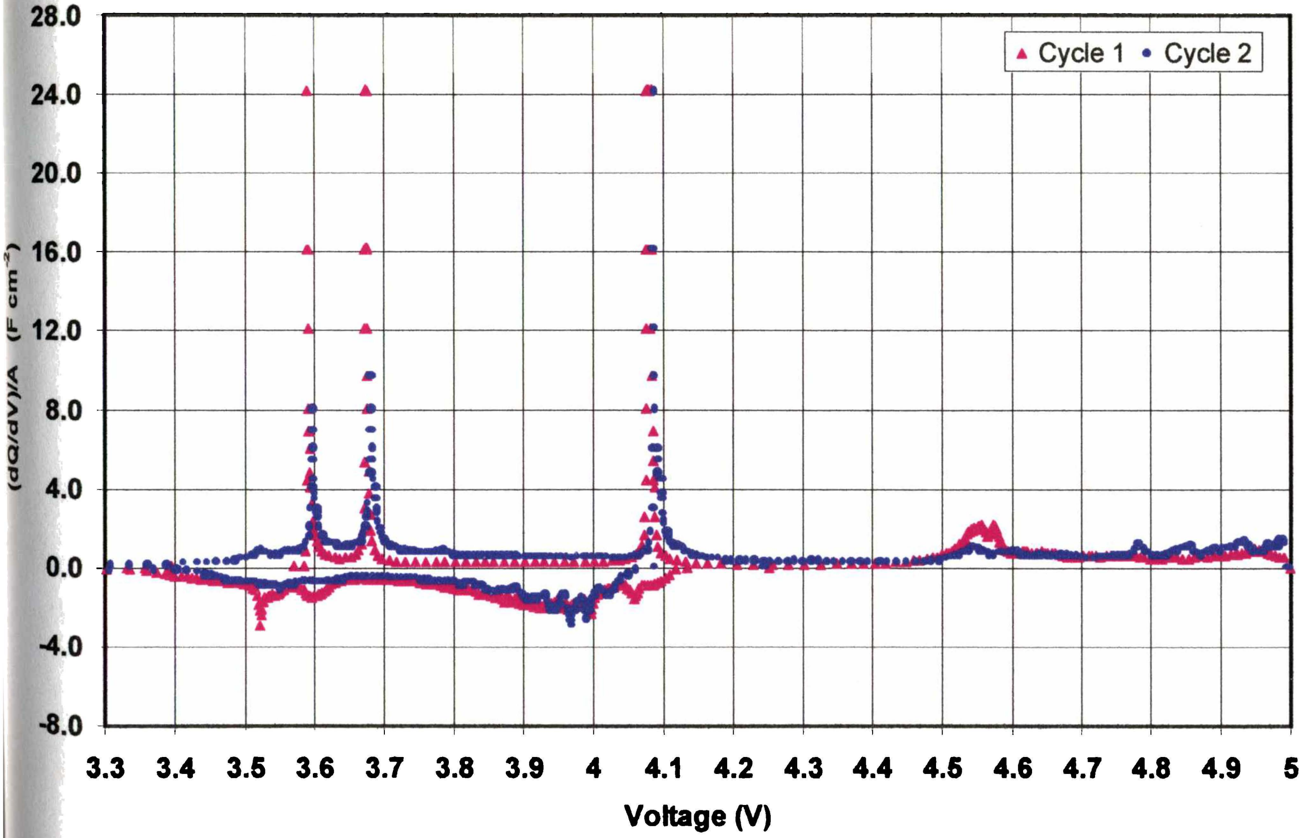

Figure 6.12 dQ/dV of the First Two Cycles of $Li_3V_2(PO_4)_3$

The oxidation and reduction peaks in the differential capacity curves in Figure 6.12 correspond well to the plateaus in both the charge and discharge curves. There are three sharp and one broad oxidation peaks in the first charge at approximately 3.6, 3.7, 4.1 and 4.6V. The discharge curve similarly has three plateaus although these are not nearly as well defined. No high voltage reduction peak is observed corresponding to the 4.6V oxidation peak and the 4.0V reduction peak corresponding to the 4.1V oxidation peak is not distinct but rather broad. This broad peak continues to the lower reduction peaks that correspond to the 3.6 and 3.7V oxidation peaks. It seems that the lithium extracted at 4.6V maybe reinserted between 4.1V and 3.7V, giving rise to the broad feature on the reduction cycle.

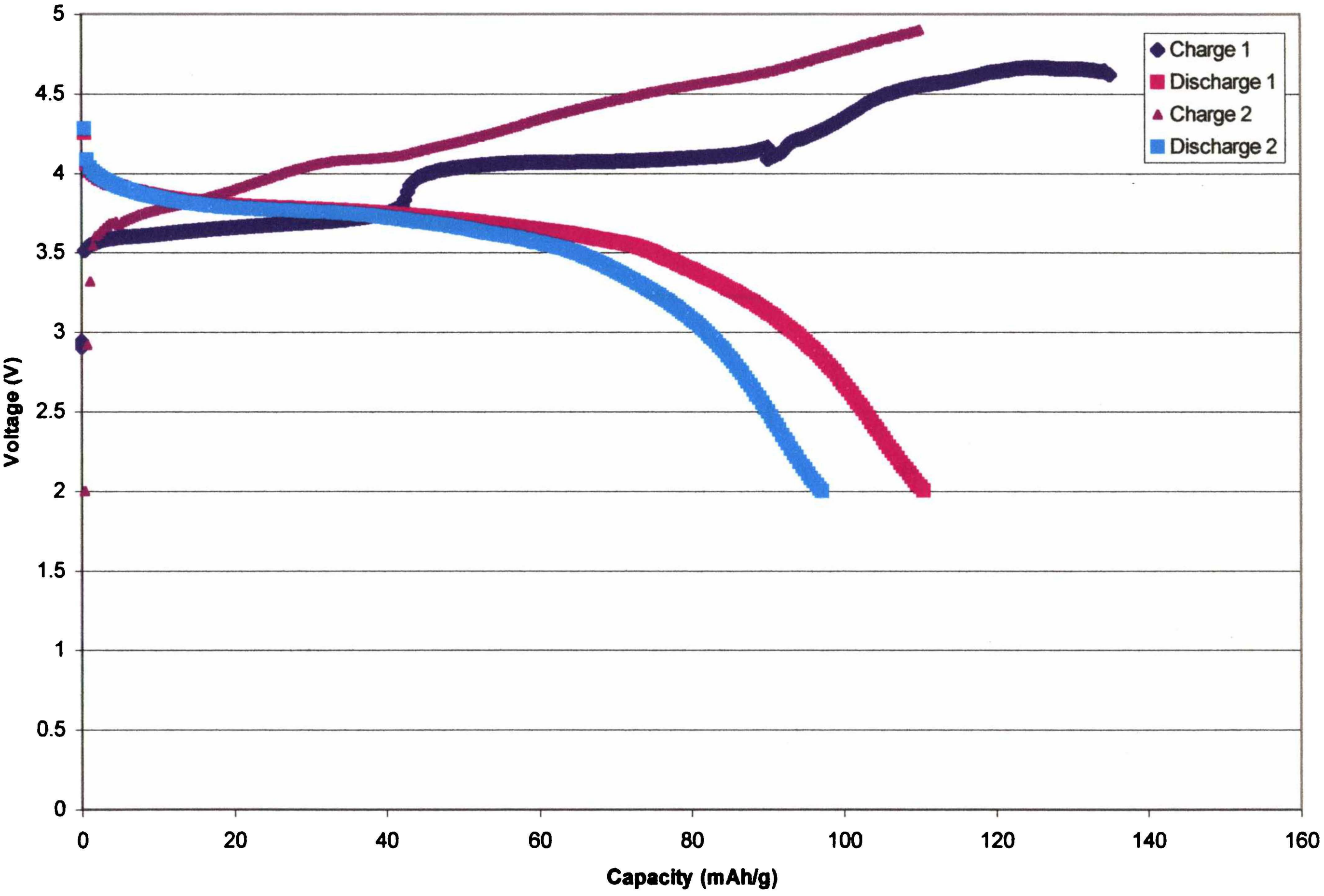

Figure 6.13 Cycling Behaviour of $Li_{2.60}V_{1.60}Ti_{0.40}(PO_4)_3$

With an increase in the current densities, the performance of this material also decreases. Increasing the current density to 30 mAh/g on the third cycle decreases the capacity to only 40 mAh/g. This is not recovered if the current density is decreased again, indicating that the problem is not purely kinetic but probably due to the breakdown of electrical contact between particles in the cathode.

Cells were constructed using orthorhombic $Li_{2.60}V_{1.60}Ti_{0.40}(PO_4)_3$, which had the best ionic conduction of these materials as determined by AC impedance experiments. The cycling behaviour of $Li_{2.60}V_{1.60}Ti_{0.40}(PO_4)_3$ is shown in Figure 6.13.

The first charge cycle of $Li_{2.60}V_{1.60}Ti_{0.40}(PO_4)_3$ is very similar to the first charge cycle for $Li_3V_2(PO_4)_3$. There are also three plateaus on the charge curve as lithium is extracted from the structure. The charge capacity of 130 mAh/g corresponds to the extraction of approximately 1.7 lithiums per unit formula. The first discharge of 110 mAh/g corresponds to the insertion of 1.5 lithiums per unit formula. This shape of the discharge curve is somewhat different to the discharge curve of $Li_3V_2(PO_4)_3$. It is very similar to the shape of $Li_{2.70}Fe_{1.70}Ti_{0.30}(PO_4)_3$. The first half is relatively flat at 3.7V but the second half of the discharge curve slopes downwards dramatically.

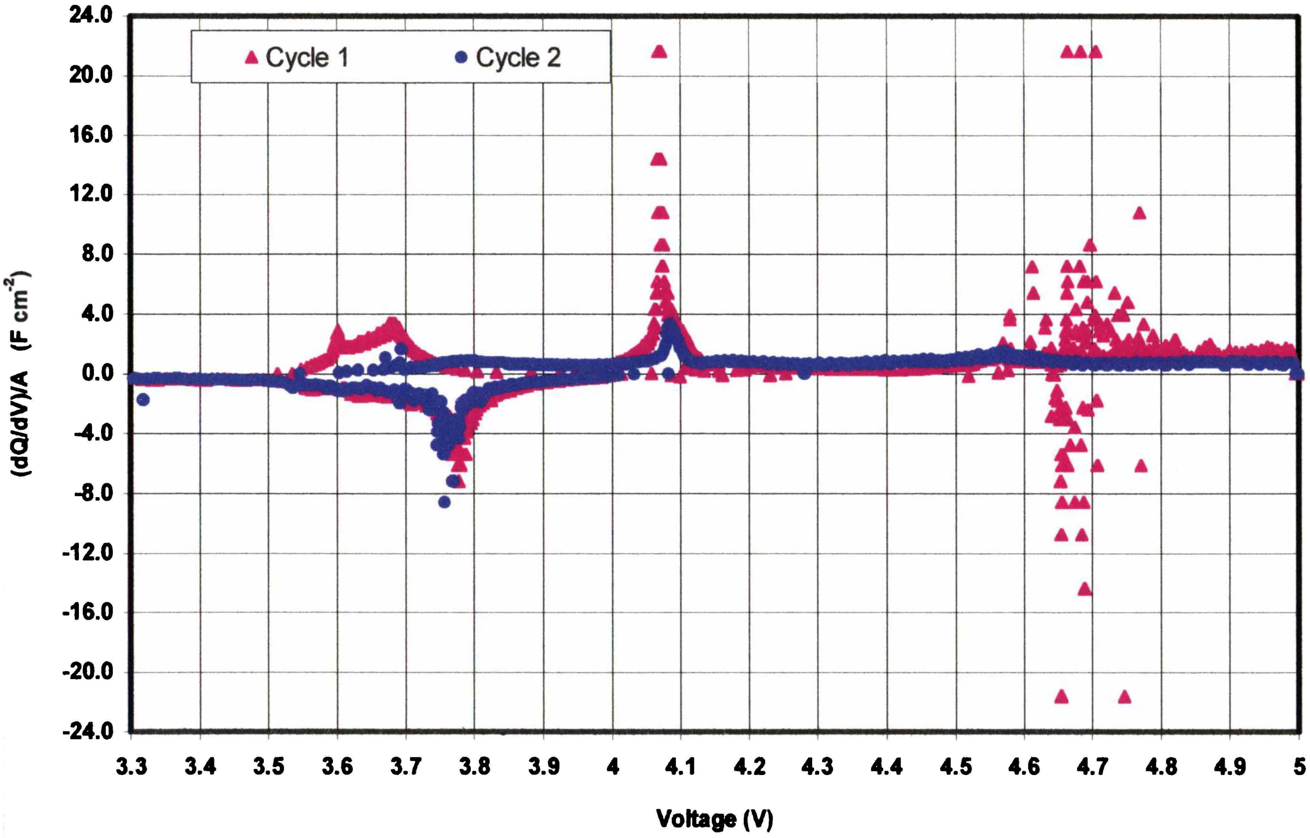

Figure 6.14 dQ/dV of the First Two Cycles of $Li_{2.60}V_{1.60}Ti_{0.40}(PO_4)_3$

The differential capacity curves of the first two cycles $Li_{2.60}V_{1.60}Ti_{0.40}(PO_4)_3$ are shown in Figure 6.14. The oxidation peaks corresponding to the extraction of lithium are very similar to those for $Li_3V_2(PO_4)_3$, with values of approximately 3.6, 3.7, 4.1 and 4.7V. The area under the graphs for these distinct peaks and for $Li_3V_2(PO_4)_3$ are very similar, although the 4.6V peak is relatively broad. In contrast, the oxidation peaks for $Li_{2.60}V_{1.60}Ti_{0.40}(PO_4)_3$ are not nearly as distinct. There is no 4.7V reduction peak for $Li_3V_2(PO_4)_3$ and the three reduction peaks of $Li_{2.60}V_{1.60}Ti_{0.40}(PO_4)_3$ have merged into one broad peak. The second half of the discharge curve is not represented by any reduction peaks. The titanium dopant may be lowering the redox potential of $Li_3V_2(PO_4)_3$ which utilises the V^{4+}/V^{3+} redox couple. A discharge curve for a NASICON structure operating with only the Ti^{4+}/Ti^{3+} redox couple would range between 2.4 and 2.7V with an average of 2.5V.[7] However, what is more likely is that although the material has higher lithium ion conduction as determined by AC impedance measurements, there is a problem with lithium transport when attempting to insert or extract lithium into the structure.

The capacity of $Li_{2.60}V_{1.60}Ti_{0.40}(PO_4)_3$ decreases in subsequent cycles, especially when the current density is increased. With current densities of 30 mA/g and 75mA/g, the capacity decreases to 50 mAh/g and 35 mAh/g respectively. If the current density is dropped again to 7.5 mA/g after approximately 200 cycles, there is a recovery in the discharge capacity to 80 mAh/g. This is not the case for $Li_3V_2(PO_4)_3$ which will not recover any capacity on decreasing the current densities, indicating that $Li_{2.60}V_{1.60}Ti_{0.40}(PO_4)_3$ is diffusion limited and that $Li_3V_2(PO_4)_3$ has problems associated with irreversible capacity loss. The breaking down of electrical contact between particles as a result of volume changes during lithium insertion and extraction commonly causes irreversible capacity loss. The diffusion limitation is caused by the shrinking interface of $Li_xV_2(PO_4)_3/Li_{3-x}V_2(PO_4)_3$ as lithiation occurs. For a constant rate of lithium transport per unit area across the interface, a critical surface area is reached where the rate of total lithium transported across the interface is no longer able to sustain the current.[8] The higher the current, the greater the total critical surface area and hence the smaller the concentration x of inserted lithium before the cell performance becomes diffusion limited. On extraction of lithium, the parent phase at the core of the particle grows back towards the particle surface and is retained on repeated cycling. The loss in capacity is reversed by decreasing the current density.

The attempted substitution of vanadium for iron in $Li_{1+x}Fe_2(PO_4)(SO_4)_2$, as determined by X-ray diffraction, resulted in a mixed phase material consisting of $LiVOPO_4$, V_2O_5 and possibly $Li_2(SO_4)$. The starting materials for this reaction were LiH_2PO_4, $2(NH_4)_2SO_4$ and $2VCl_3$ all dissolved in water. The desired reaction if successful would have obtained $LiV_2PO_4(SO_4)_2$ with ammonia, water and HCl driven off at temperature. Figure 6.15 shows the cycling behaviour between 5 and 2V of the mixed phase that was obtained instead. The OCV was very attractive at 3.9V and the discharge capacity at 7.5 mA/g was reversible at 157 mAh/g. X-ray diffraction revealed the material was not the desired rhombohedral analogue and revealed the possible phases that had formed.

During the attempted synthesis of V^{3+} doped $LiCoPO_4$, it was observed that the sintering temperature decreased considerably with dopant content. A sintering temperature of 750 °C had to be decreased to 675 °C with 20mol% vanadium dopant. What may possibly have occurred is that the vanadium lowered the sintering temperature of the reaction allowing the free formation of SO_2. The reaction is performed at 475 °C and SO_2 formation occurs close to 500 °C. The reaction may have occurred as follows:

$$LiH_2PO_4 + 2(NH_4)_2SO_4 + 2VCl_3 \xrightarrow{Air} 0.5V_2O_5 + LiVOPO_4 + 2SO_2 + 4NH_3 + 6HCl \quad \text{Equation 6.2}$$

This would account for the exceptionally high capacity that would have resulted if data were adjusted for the weight difference of a Li_2SO_4 inactive secondary phase. Considerable research has been done on the electrochemical data for V_2O_5[9,10,11,12,13] and more recently on $LiVOPO_4$.[14,15]

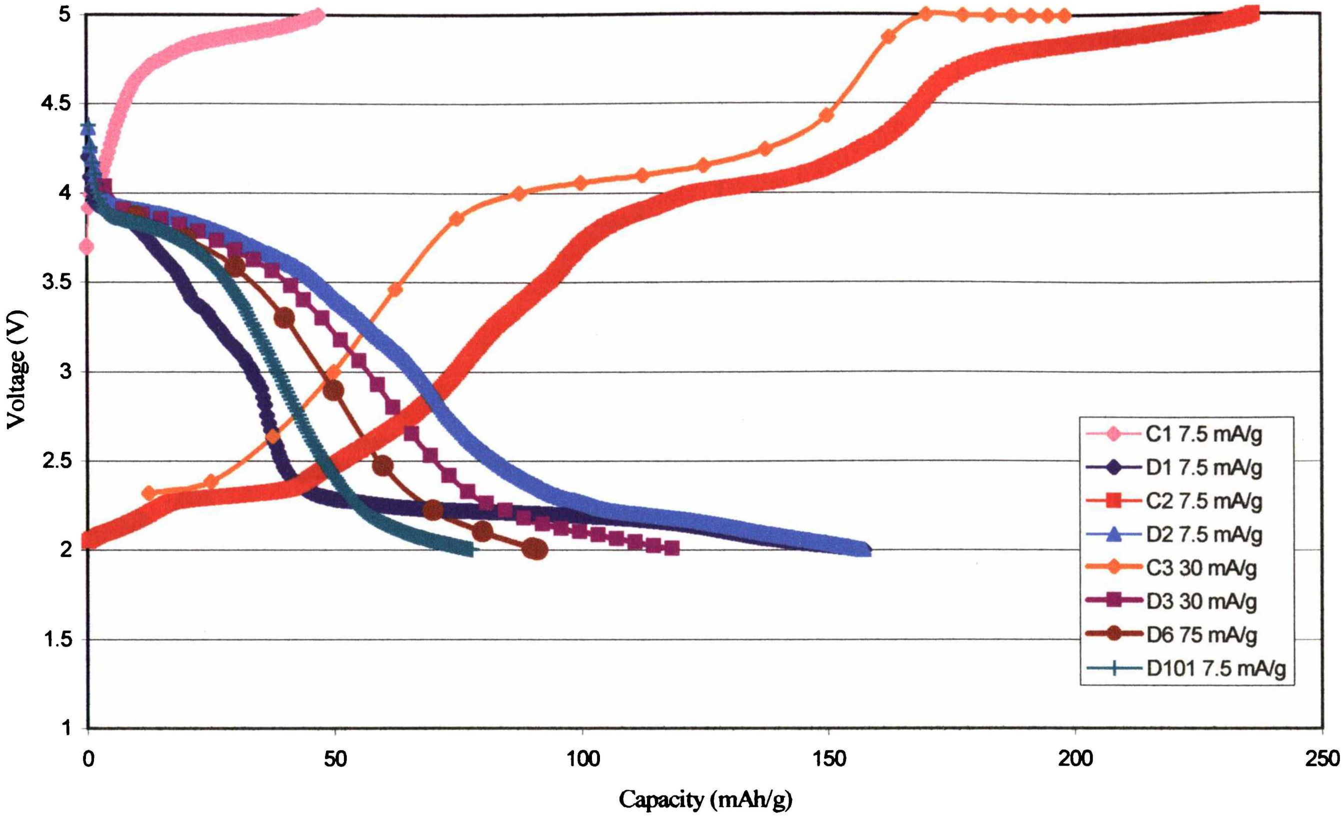

Figure 6.15 Cycling Behaviour of Mixed $LiVOPO_4$ and V_2O_5

If Equation 6.2 is correct, then there is 1 mol of $LiVOPO_4$ to 0.5 mol of V_2O_5 in the cathode material which would correspond to approximately 65% $LiVOPO_4$ and 35% V_2O_5 by weight. Lithium insertion and extraction into and from this mixed valence material is relatively good. The first charge of approximately 45mAh/g extracts approximately 0.4 Li per unit formula from the $LiVOPO_4$, assuming there are no other active lithium containing phases. The first discharge of 157 mAh/g inserts the 0.4 Li extracted back into the $LiVOPO_4$ and also inserts 0.7 Li into the V_2O_5 structure. Addition of the charge and discharge capacities for the first three cycles leave the material with the same amount of lithium it started with. Upon increasing the charge current density to 30 and 75mA/g in the third and sixth cycles, the capacity decreases slightly to approximately 120 and 90 mAh/g respectively. There is a steady decrease in capacity with cycling. After approximately 100 cycles with a charge rate of 75mA/g, the discharge capacity decreased to 55 mAh/g. After this, the current density is decreased again to 7.5 mA/g the discharge capacity improved to 80 mAh/g, indicating the materials experience some rate limitations.

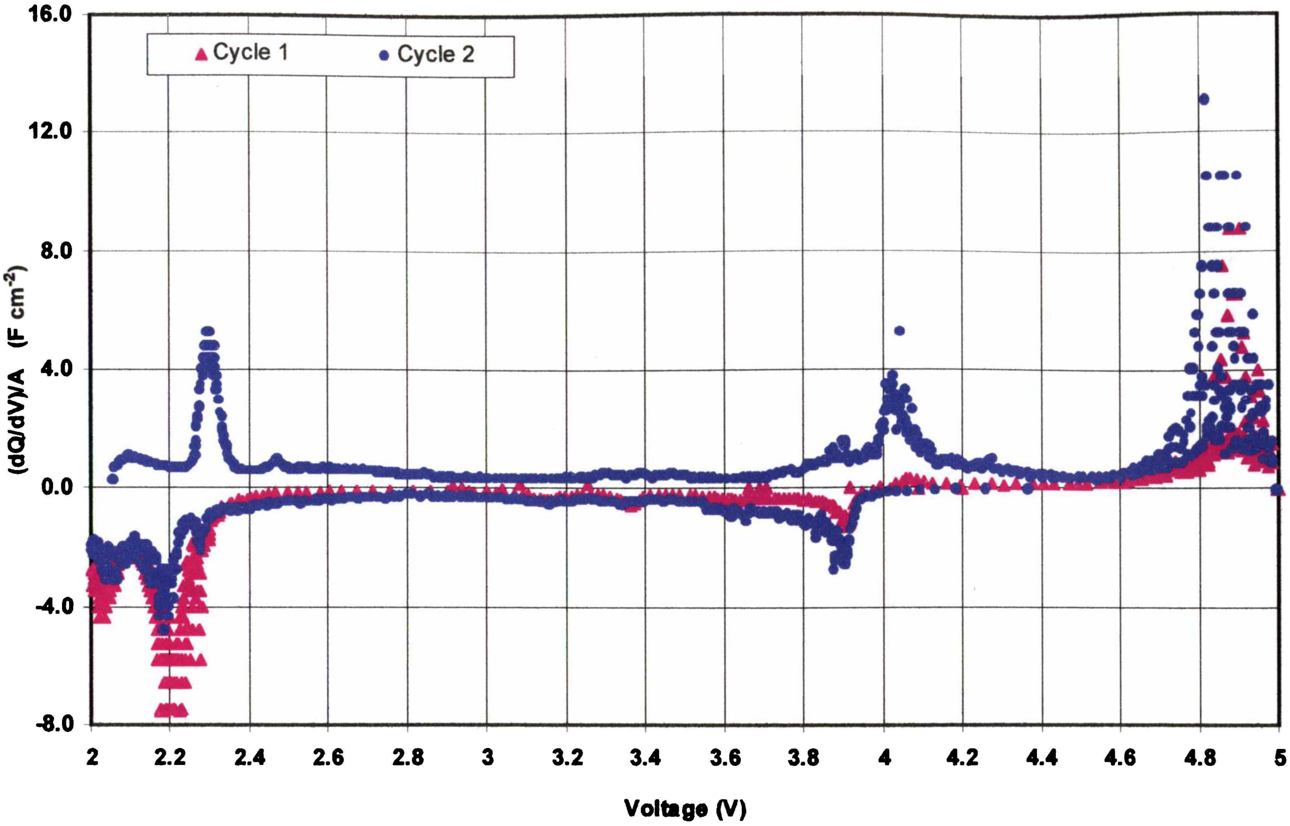

Figure 6.16 dQ/dV of the First Two Cycles of Mixed $LiVOPO_4$ and V_2O_5

Good cycling performance has been shown for a ω-$Li_xV_2O_5$/Li cell in a voltage range between 3.4 and 1.9V[11] which may correspond to the lower voltage region of the differential capacity curve shown in Figure 6.16. The incremental capacity voltammogram published by Kerr et al[14] shows an oxidation peak at just over 4V and a reduction peak at 3.8V for ε-$LiVOPO_4$, which correspond to the middle voltage region of Figure 6.16. The upper voltage region oxidation peaks most likely correspond to some electrolyte decomposition above 4.6V.

6.5 References

---

[1] A. Manthiram and J. B. Goodenough, *J. Power Sources*, 26, p403, **1989.**

[2] J. Barker and S. M. Yazid, U. S. Patent No. 5,871,866, **1999.**

[3] H. Ohkawa, K. Yoshida, M. Saito, K. Uematsu, K. Toda and M. Sato, *Chem. Letters*, **1999.**

[4] K. Yoshida, K. Toda, K. Uematsu and M. Sato, *Electroceramics in Japan I*, 157, p289, **1999.**

[5] A.B. Bykov, A.P. Chirkin, L.N. Demyanets, S.N. Doronin, E.A. Genkina, A.K. Ivanov-shits, I.P. Kondratyuk, B.A. Maksimov, O.K. Mel'nokov, L.N. Muradyan, V.I. Simonov and V.A. Timofeeva, *Solid State Ionics*, 38, pp31-50, **1990.**

[6] A. K. Padhi, V. Manivannan and J. B. Goodenough, *J. Electrochem. Soc.*, 145, (5), p1518, **1998.**

[7] A.K. Padhi, K.S. Nanjundaswamy, C. Masquelier and J.B. Goodenough, *J. Electrochem. Soc.*, 144, pp2581-2586, **1997.**

[8] J. B. Goodenough, A. K. Padhi, K. S. Nanjundaswamy and C. Masquelier, U.S. Patent No. 5,910,382, **1999.**

[9] A. M. Chippendale, P. G. Dickens and A. V. Powel, *Prog. Solid State Chem.*, 21, p133, **1991.**

[10] J. O. Besenhard and R. Schollhorn, *J. Electrochem. Soc.*, 124, p968, **1977.**

[11] C. Delmas, H. Cognac-Auradou, J. M. Cocciantelli, M. Menetrier and J. P. Doumerc, *J. Power Sources*, 69, p257, **1994.**

[12] Y. Sakurai, S. Okada, J. Yamaki and T. Okada, *J. Power Sources*, 20, p173, **1987.**

[13] K. West, B. Zachau-Cristiansen, M. J. L. Ostergard and T. Jacobsen, *J. Power Sources*, 20, p165, **1987.**

[14] T. A. Kerr, J. Gaubicher and L. F. Nazar, *Electrochem. and Solid-State Letters*, 3, (10), p460, **2000.**

[15] N. Dupre, J. Angenault, G. Wallez and M. Quarton, *in 196th Meeting of the Electrochem. Soc.*, Honolulu, Oct, Abstract no. 206, **1999.**

7 Conclusions and Recommendations

7 Conclusions and Recommendations

7.1 Characterisation

The olivine structures $LiCoPO_4$ and $LiNiPO_4$ are both readily prepared via solid-state methods. X-ray diffraction, Rietveld refinement of the X-ray diffraction data and Raman results showed that both materials can be indexed in the orthorhombic space group *Pnma*. Cell parameters are a = 10.2006, b = 5.9193, c = 4.6983 Å for $LiCoPO_4$, and a = 10.0327, b = 5.8582, c = 4.6785 Å for $LiNiPO_4$ at room temperature.

Doping of the $LiCoPO_4$ structure with vanadium may be successful up to 5 mol%. Saturation of the dopant definitely occurred by adding between 5 and 10 mol% vanadium, after which the increasing secondary phase, which is most likely α-$LiVOPO_4$, formed. Doping the $LiNiPO_4$ structure was unsuccessful using the solid-state synthesis methods, regardless of the dopant.

The NASICON related structures $Li_3Fe_2(PO_4)_3$ and $Li_3V_2(PO_4)_3$ were synthesised via solid-state methods in atmospheres of air and $2\%H_2/98\%N_2$ respectively. Rietveld refinement of the X-ray diffraction data showed that both materials can be indexed in the orthorhombic space group P*can*, although literature indicates that the true symmetry is monoclinic in space group $P2_1/n$. Orthorhombic cell parameters are a = 8.5585, b = 12.0175, c = 8.6179 Å for $Li_3Fe_2(PO_4)_3$, and a = 8.6021, b = 12.0294, c = 8.5804Å for $Li_3V_2(PO_4)_3$ at room temperature.

Doping of both the $Li_3Fe_2(PO_4)_3$ and $Li_3V_2(PO_4)_3$ structures with titanium was successful up to 20 mol%. The refinement of the XRD data for the doped materials was again carried out as an orthorhombic symmetry P*can* phase. In the case of the doped materials, DSC and Raman data indicated that the structure may be characteristic of that of the undoped phases at elevated temperatures.

$LiFe_2PO_4(SO_4)_2$ is easily synthesised at low temperatures. Using full pattern matches, the best fitting pattern and that which matched the literature was the $R\bar{3}c$ space group. A vanadium substitution into the $LiFe_2PO_4(SO_4)_2$ structure was unsuccessful and resulted in a two phase mixture of $LiVOPO_4$ and V_2O_5.

Particle size results for $LiCoPO_4$, $LiNiPO_4$, $Li_3Fe_2(PO_4)_3$ and $Li_3V_2(PO_4)_3$ shows large average particle size and a broad distribution. $LiCoPO_4$, $LiNiPO_4$ and $Li_3Fe_2(PO_4)_3$ synthesised in air had relatively small surface areas of 0.35, 0.33 and 0.27 m^2g^{-1} respectively. $Li_3V_2(PO_4)_3$ synthesised in $2\%H_2/98\%N_2$ had a much higher surface area than the other phosphates, with a value of 6.82 m^2g^{-1}.

Bulk density measurements showed that the sintering temperature increases for $LiNiPO_4$, $LiCoPO_4$, $Li_3Fe_2(PO_4)_3$ and $Li_3V_2(PO_4)_3$ with increasing titanium dopant content. In contrast, the sintering temperature decreases for $LiCoPO_4$ with increasing vanadium dopant content.

There was a significant conduction enhancement of approximately two orders of magnitude when $LiCoPO_4$ was doped with vanadium. The highest conductivity for these materials was from $Li_{0.80}Co_{0.80}V_{0.20}PO_4$ with a value of 9.48×10^{-5} Scm^{-1} compared to $LiCoPO_4$ at 2.52×10^{-8} Scm^{-1}. At low temperatures, $LiNiPO_4$ had a conductivity of 1.38×10^{-6} Scm^{-1}. Adding a second phase via the attempted Ti dopant lowered conductivity at low temperatures, but enhanced it at higher temperatures. Titanium doping of $Li_3Fe_2(PO_4)_3$ alters the structure to a higher symmetry as shown by the Raman data. DSC and AC impedance measurements further confirmed the stabilisation of the monoclinic α-phase to orthorhombic γ-phase at room temperature. $Li_3Fe_2(PO_4)_3$ had a room temperature conductivity of 8.54×10^{-8} Scm^{-1} compared with the best doped material $Li_{2.70}Fe_{1.70}Ti_{0.30}(PO_4)_3$, with a value of 4.72×10^{-6} Scm^{-1}. The AC impedance results for titanium doped $Li_3V_2(PO_4)_3$ showed it behaves in a similar fashion to its iron analogue. The room temperature conductivity of $Li_3V_2(PO_4)_3$ was 6.06×10^{-6} Scm^{-1} in comparison to the best doped material $Li_{2.60}V_{1.60}Ti_{0.40}(PO_4)_3$ with a value of 5.77×10^{-4} Scm^{-1}.

7.2 Electrochemical Behaviour

$LiCoPO_4$ has an attractive first discharge capacity of 130 mAh/g with a plateau at 4.6V. The high redox potential of this material pushes the stability window of the electrolyte to its limits, which inhibits the cycling performance of this material. The $LiBF_4$/TMS electrolyte showed the best electrochemical performance. Attempts to improve the electrochemical performance of this material by improving the electronic conductivity were unsuccessful. Further experiments utilising the enhanced conductivity of the 5 mol% vanadium doped $LiCoPO_4$ should be performed. This may help to minimise kinetic problems associated with poor conductivity and large particle size.

$LiNiPO_4$ could not be charge to accessible voltages due to oxidation of the electrolyte. The material could only be reduced with a discharge capacity of 300 mAh/g in a plateau at 1.4V. However, this capacity corresponds to the decomposition of $LiNiPO_4$ to Li_3PO_4 and Ni metal. The major factor limiting the performance of this material is that the lithium binding potential is higher than the oxidative stability of the electrolyte. The high redox potential in the presence of the PO_4 complex is unattainable. Until a very high voltage stable electrolyte is found, $Li_{1-x}Ni_{1-x}M_xPO_4$ materials will not be viable as cathodes in lithium secondary batteries.

$Li_{2.70}Fe_{1.70}Ti_{0.30}(PO_4)_3$ showed a discharge capacity of 60 mAh/g which was considerably less than theoretical. The shape of the discharge curve resembles that of $LiFe_2PO_4(SO_4)_2$ with no distinct plateaus, unlike $Li_3Fe_2(PO_4)_3$ which has plateaus at 2.85 and 2.70V corresponding to the reduction of two crystallographically distinct Fe^{3+} ions to Fe^{2+}. The 65 mAh/g discharge capacity of rhombohedral $LiFe_2PO_4(SO_4)_2$ corresponds to the extraction of lithium with a solid solution type behaviour. The partial substitution of $(SO_4)^{2-}$ for $(PO_4)^{3-}$ results in a 0.5 eV difference in the redox potential of $LiFe_2PO_4(SO_4)_2$ and $Li_3Fe_2(PO_4)_3$.

The first charge of approximately 135 mAh/g for $Li_3V_2(PO_4)_3$ corresponds to the extraction of three lithiums per unit formula from $Li_3V_2(PO_4)_3$ oxidising first the two V^{3+} ions to V^{4+}, and then one V^{4+} to V^{5+}, if one assumes that not all the material is in contact with the current collector. The first discharge with a capacity of 130 mAh/g inserts most of the lithium back into the structure and reduces both vanadiums back to the 3+ state. Continued cycling of this material showed a irreversible capacity loss with each cycle, most likely due to the breakdown of electrical contact between particles in the cathode. The first charge curve of $Li_{2.60}V_{1.60}Ti_{0.40}(PO_4)_3$ was similar to that of $Li_3V_2(PO_4)_3$ with three distinct plateaus and a capacity of 130 mAh/g. The first discharge capacity of 110 mAh/g was similar to that of $Li_3V_2(PO_4)_3$ but the shape of the curve was different, indicating a different type of lithium transport behaviour. A reversible capacity loss was observed with increasing current densities, and this capacity was recovered upon lowering the current density, again indicating the material is diffusion limited. The attempted substitution of vanadium for iron in $Li_{1+x}Fe_2(PO_4)(SO_4)_2$ resulted in a mixed phase material consisting of $LiVOPO_4$ and V_2O_5. The high open circuit voltage achieved results from the V^{5+}/V^{4+} redox couple instead of the expected $(SO_4)^{2-}$ substitution. The mixed phase material performed quite well as a cathode in a lithium button cell, with high capacity discharge characteristics and good cycling performance. However, this material was also diffusion limited. The $LiVOPO_4$ phase in this material warrants further investigation.

7.3 Recommendations

Alternative synthesis routes for all materials may help to optimise particle size, surface area and the interfacial contact between particles. Soft chemistry routes such as ion exchange processes or co-precipitation may help to improve the electrochemical performance.

Padhi et al[1] report the Ni^{3+}/Ni^{2+} redox couple in $LiNiPO_4$ should lie at approximately 0.6 eV below that of the Co^{3+}/Co^{2+} couple in $LiCoPO_4$. This requires a possible value of 5.4V to extract lithium from $LiNiPO_4$. If a suitable electrolyte is found, this material may have similar properties to $LiCoPO_4$ but with an even higher voltage.

$LiCoPO_4$ shows excellent potential as a high voltage cathode material but is limited by this high voltage in the electrolyte it can utilise. The high charge capacities shown by this material are most likely due to electrolyte decomposition at the voltages employed. An electrolyte that is more stable within the voltage window 4 – 5.5V would be desirable. Due to materials and equipment constraints, it was not possible to utilise 5 mol% vanadium $LiCoPO_4$ as a cathode material. With a jump of two orders of magnitude in conduction it would be interesting to determine if there is an improved performance as a result of the enhanced conductivity.

The AC impedance measurements were limited in accuracy due to the shape and size of the impedance rig used. The conductivity values for all the phosphates were rather low; any inaccuracies will be exacerbated at the high impedances measured. This could be improved by the following:

- Using a three-point measuring rig, which uses a reference electrode imbedded in the sample.[2]
- Minimising pellet width. Materials with low bulk density tend to be very fragile. Only materials with very high bulk density could be manufactured with a thickness of less than 1 or 2mm. Polishing of the resulting thin pellets to avoid capacitance effects due to possible pellet/air/electrode interfaces is difficult for the same reasons.
- Maximising pellet diameter. The silica/quartz tube used to hold the pellet had a maximum diameter of approximately 14mm. Maximising the diameter maximises the sample surface area available for impedance measurement which provides better defined spectra.[3]
- Increase the frequency of the data points.

The iron analogues of the NASICON structure show interesting performance. Use of soft chemistry synthesis, especially ion exchange routes, may improve the performance of these materials via particle size, particle distribution, and the potential for synthesising the rhombohedral phase, which has higher lithium transport and better reversible capacities. Iron would be provide an excellent low cost alternative to the more expensive materials currently being used.

$Li_3V_2(PO_4)_3$ shows interesting potential with good initial capacity and a reasonable discharge voltage. However, cycling performance of this material is poor. Further experiments should include the cycling of cells using the 2.7 – 4.2V window only to determine if a high charge voltage contributes to the irreversible capacity loss. Further testing on the higher 4.2 – 5V window may determine the viability of reversibly inserting and extracting the third lithium in the structure. Titanium doped $Li_3V_2(PO_4)_3$ shows similar behaviour to $Li_3V_2(PO_4)_3$ but with better cycling performance. There is a capacity loss due to diffusion limitations at higher current densities but this is reversible. Further investigation into the cycling of both titanium doped $Li_3V_2(PO_4)_3$ and $Li_3V_2(PO_4)_3$ with a more stable electrolyte should be performed. It was not possible to perform the Raman experiments on these materials due to equipment availability. However, these experiments should be performed, as the differences between the monoclinic and orthorhombic symmetries in the iron analogue were easier to distinguish in comparison to Rietveld refinement of the XRD data. It is expected Raman experiments for these materials would show similar behaviour, and would help to confirm the room temperature stabilisation of the doped materials in the high temperature γ-phase as shown by the AC impedance data.

Investigation into the electrochemical properties of $LiVOPO_4$ should be undertaken. A low temperature synthesis similar to that of $LiFe_2PO_4(SO_4)_2$ may be possible. The vanadium substitution into the $LiFe_2PO_4(SO_4)_2$ to achieve a high OCV should be attempted using a low temperature synthesis such as an ion exchange process to avoid SO_2 volatisation.

7.4 References

---

[1] A. K. Padhi, K. S. Nanjundaswamy and J. B. Goodenough, *J. Electrochem. Soc.*, 144, (4), p1188, **1997.**

[2] G. Hsieh, S. J. Ford, T. O. Mason and L. R. Pederson, *Solid State Ionics*, 91, p191, **1996.**

[3] G. Hsieh, T. O. Mason, E. J. Gaboczi and L. R. Pederson, *Solid State Ionics*, 96, p153, **1997.**

Appendices

Appendix I– Kröger-Vink Notation

The Superscript symbols $^{/}$, $^{\cdot}$ and ^{x} represent negative charge, positive charge and neutral charge respectively.

The subscript symbol denotes the lattice site label, that is, either a chemical symbol, or the small letter 'i' for an interstitial site.

The main capitalised symbol designates the species occupying the site, or the capitalised letter 'V' for a vacancy on the labelled site.

For example:

$Y_{Zr}^{/}$ represents an yttrium 3+ (Y^{3+}) on a zirconium 4+ (Zr^{4+}) site with an effective charge of -1.

$V_{o}^{\cdot\cdot}$ implies an oxygen vacancy with an effective charge of +2

O_{o}^{x} indicates an occupied oxygen vacancy with no charge, i.e. neutral.

Appendix II – X-Ray Diffraction Data

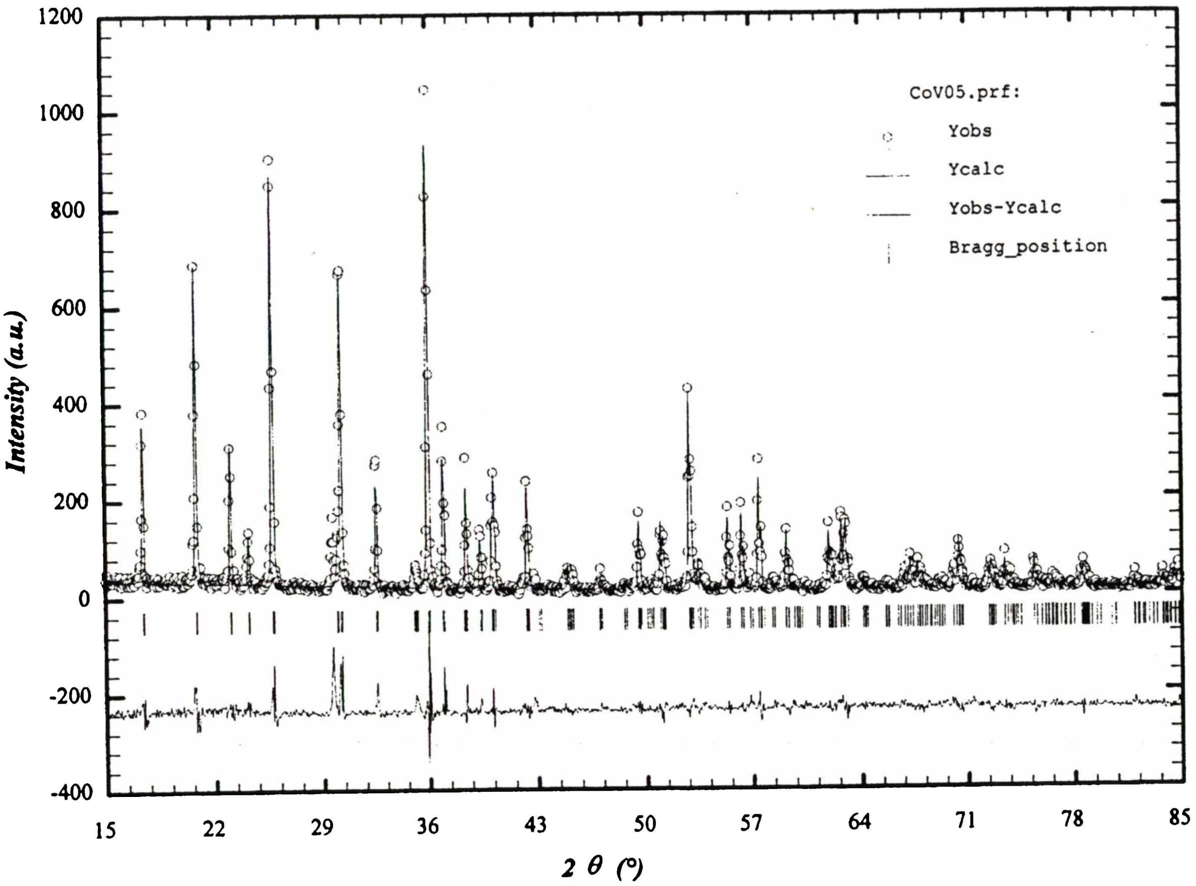

Rietveld Refinement of $Li_{0.95}Co_{0.95}V_{0.05}PO_4$

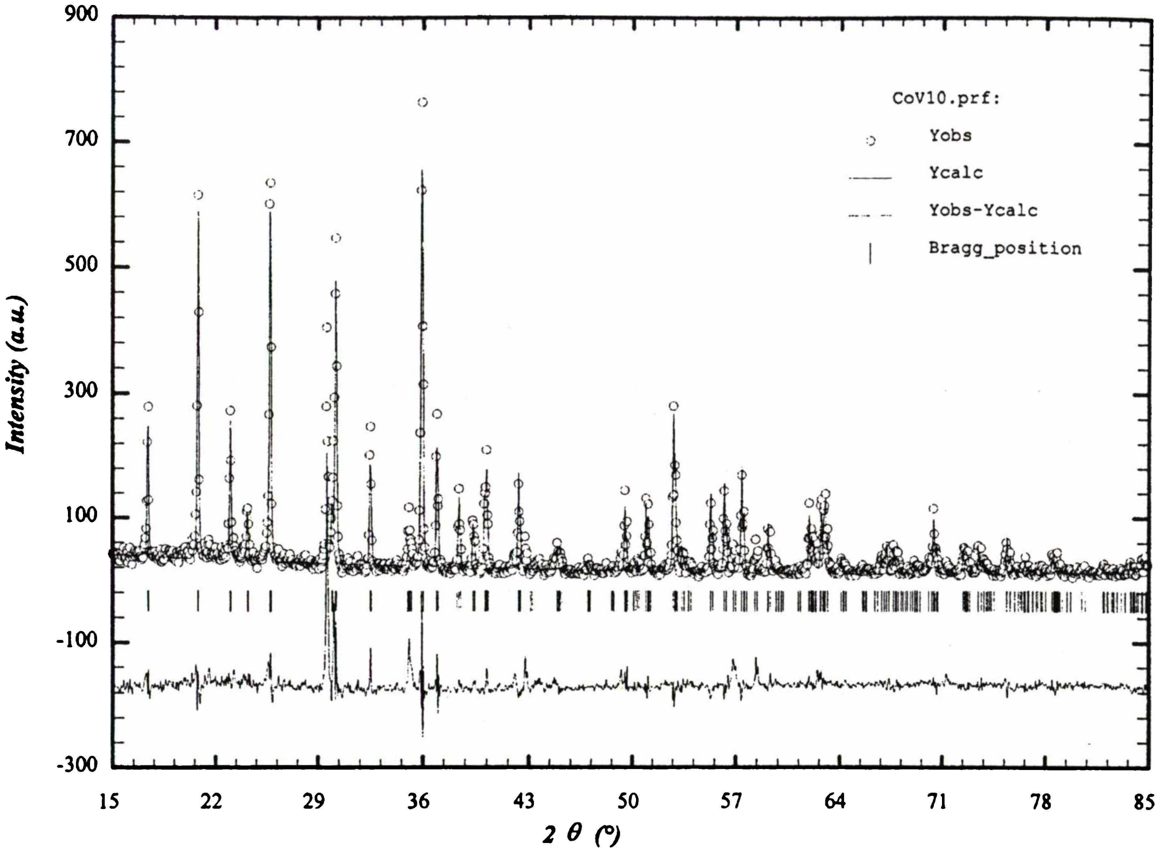

Rietveld Refinement of $Li_{0.90}Co_{0.90}V_{0.10}PO_4$

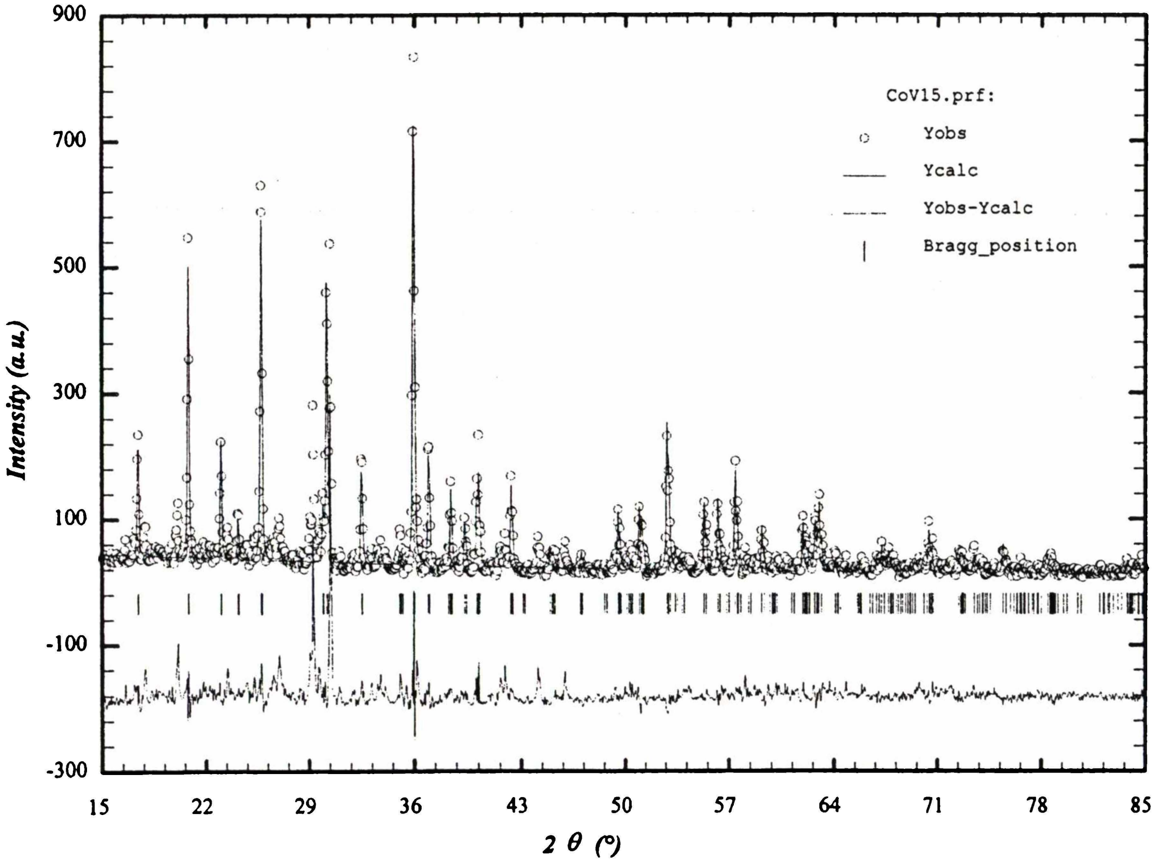

Rietveld Refinement of $Li_{0.85}Co_{0.85}V_{0.15}PO_4$

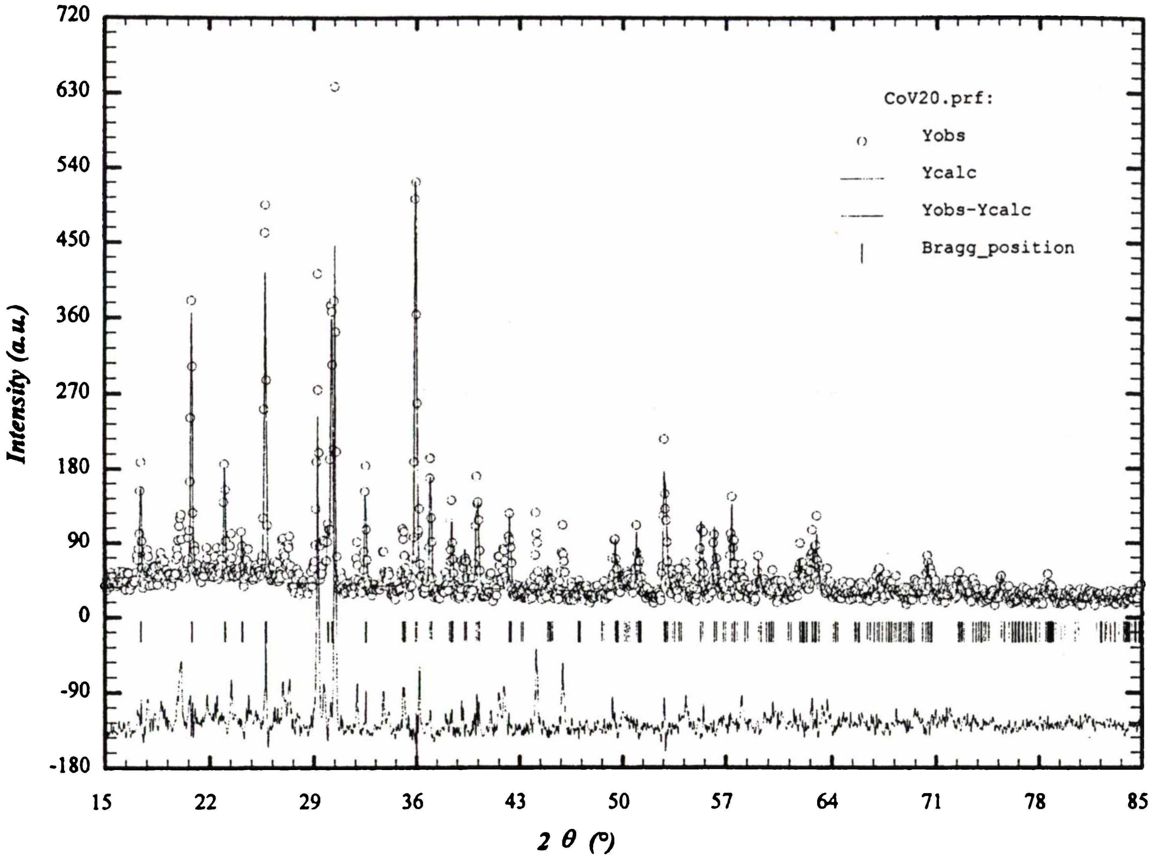

Rietveld Refinement of $Li_{0.80}Co_{0.80}V_{0.20}PO_4$

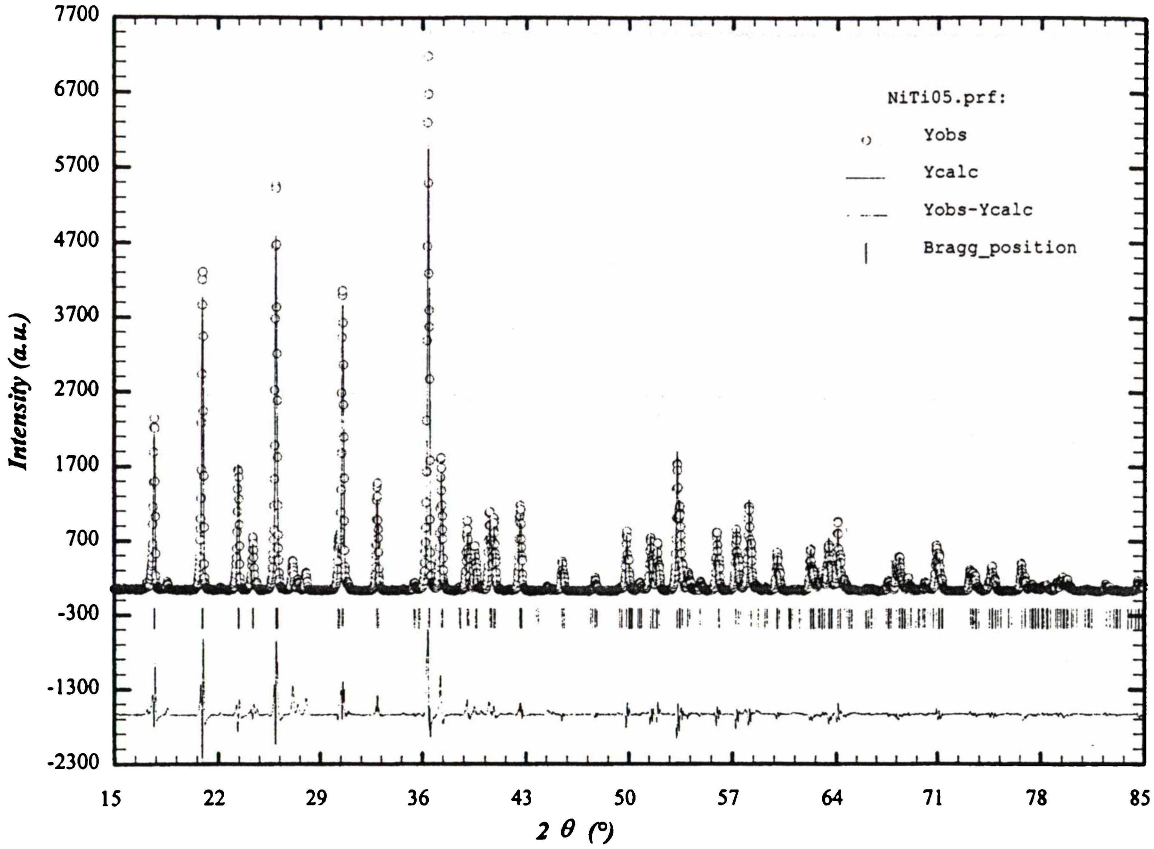

Rietveld Refinement of $Li_{0.95}Ni_{0.95}Ti_{0.05}PO_4$

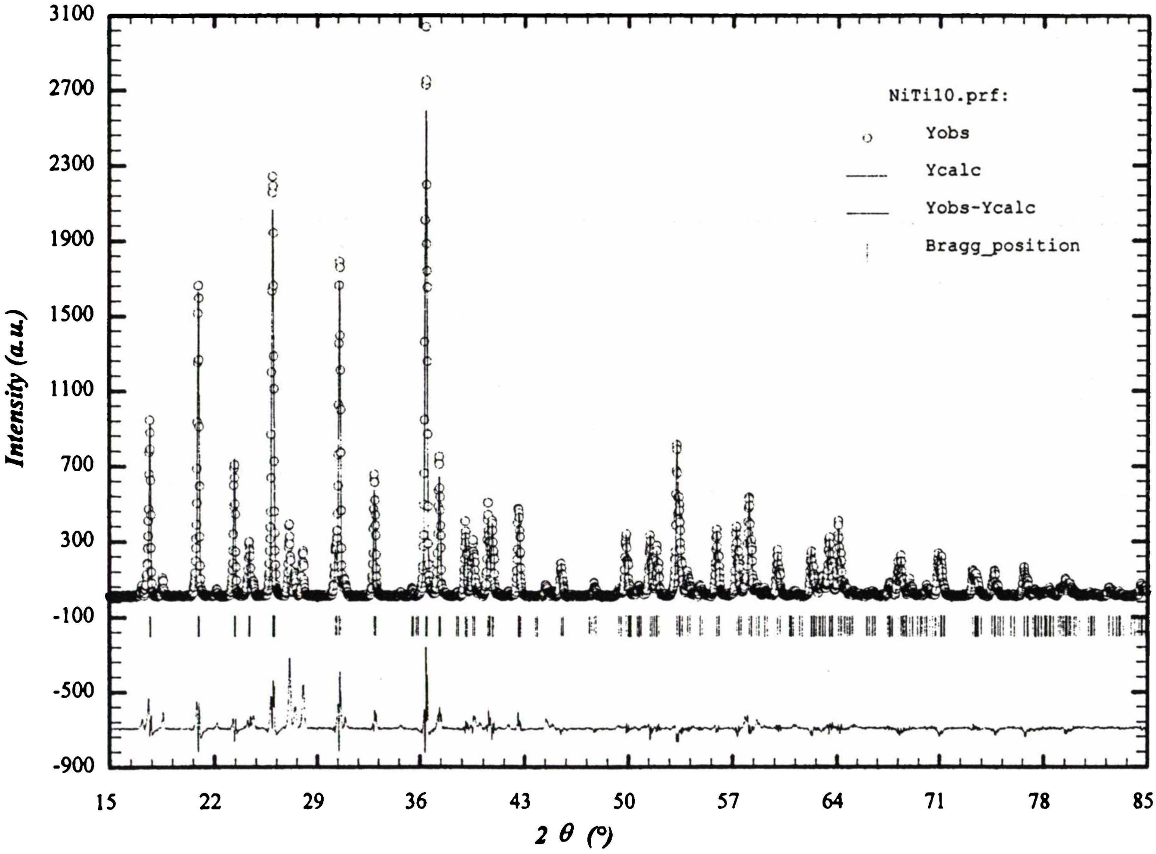

Rietveld Refinement of $Li_{0.90}Ni_{0.90}Ti_{0.10}PO_4$

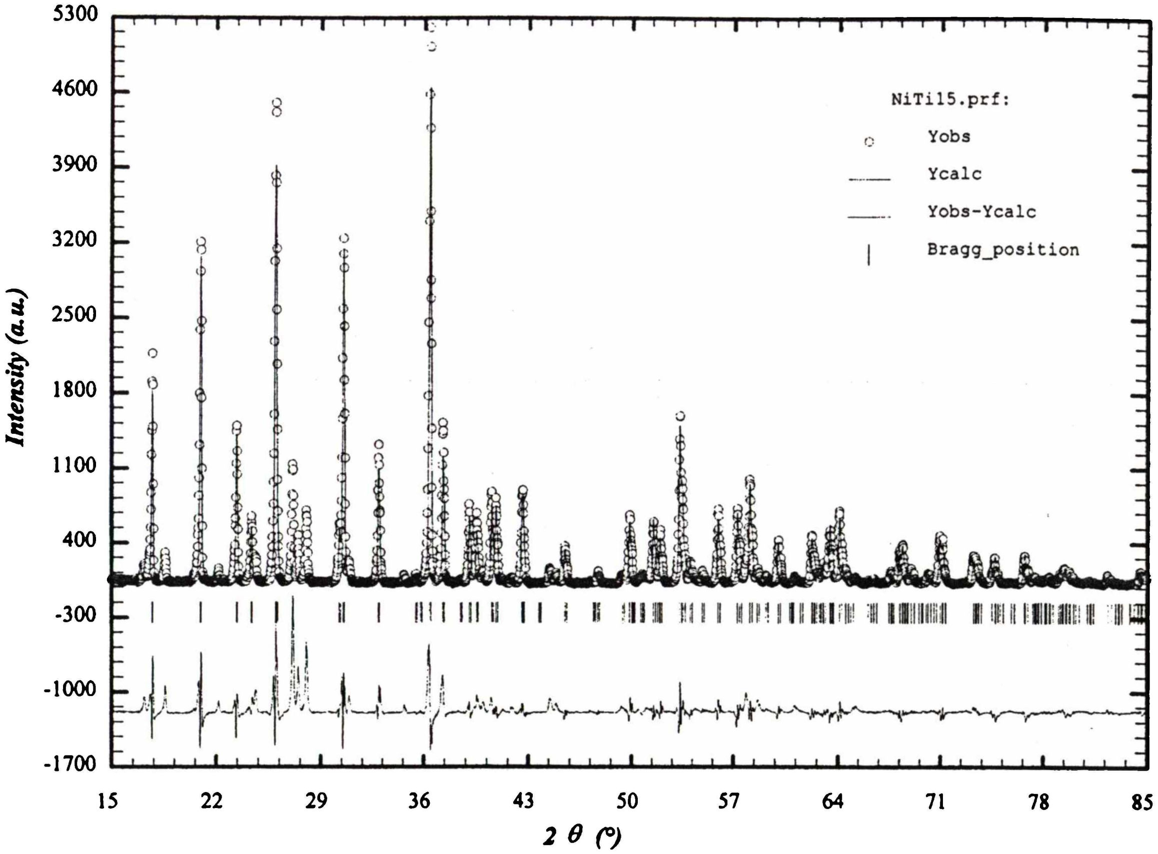

Rietveld Refinement of $Li_{0.85}Ni_{0.85}Ti_{0.15}PO_4$

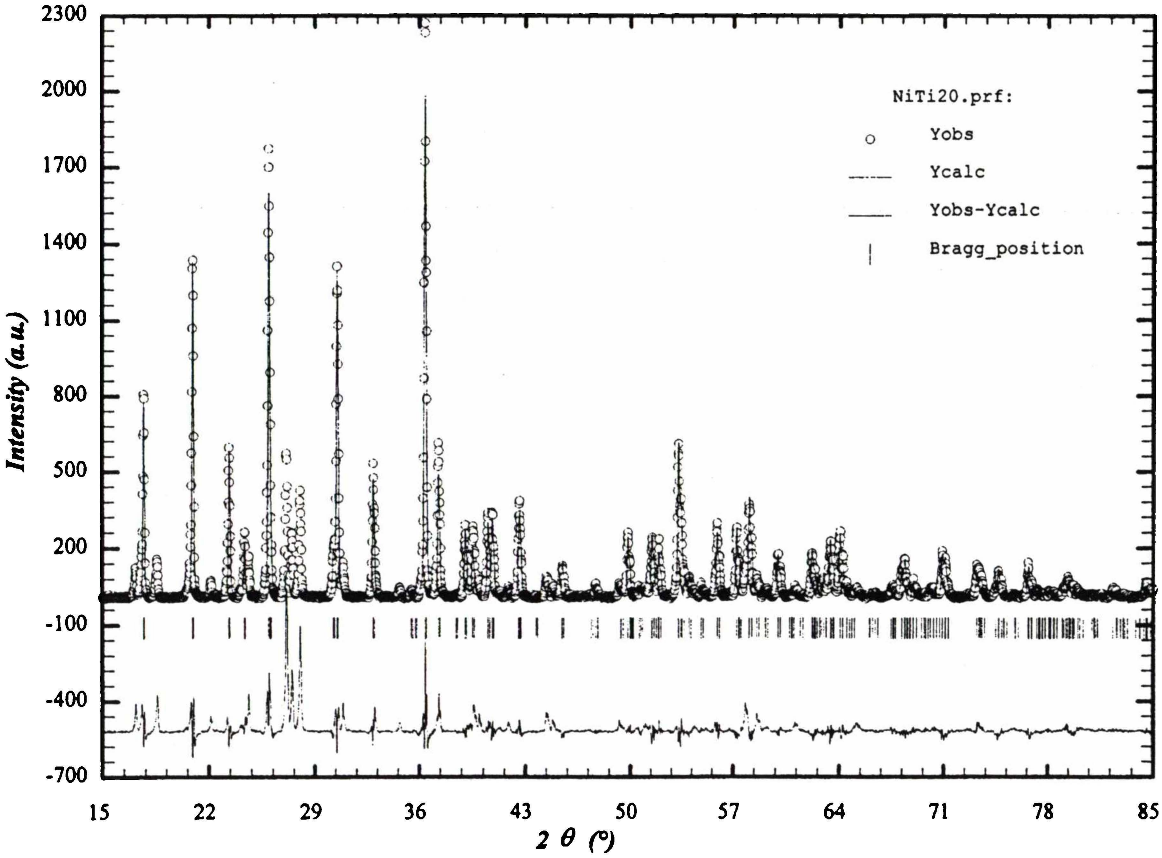

Rietveld Refinement of $Li_{0.80}Ni_{0.80}Ti_{0.20}PO_4$

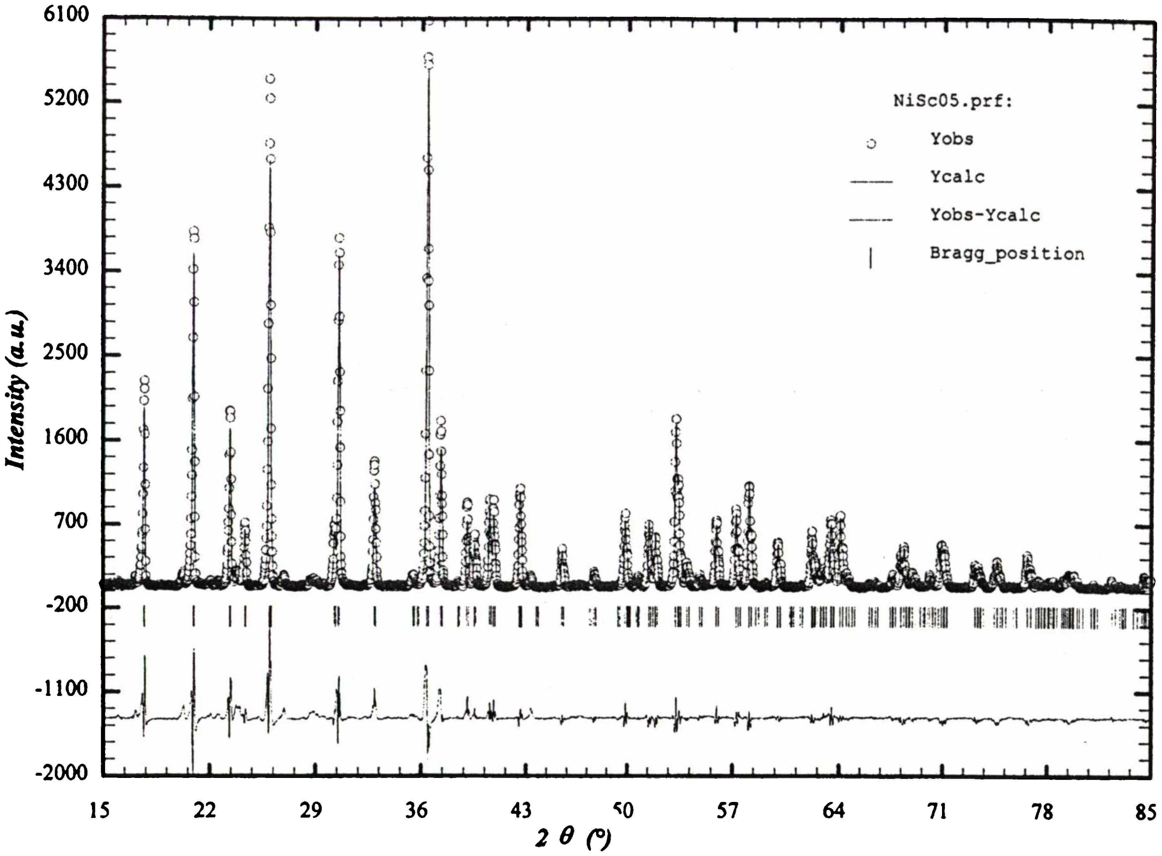

Rietveld Refinement of $Li_{0.95}Ni_{0.95}Sc_{0.05}PO_4$

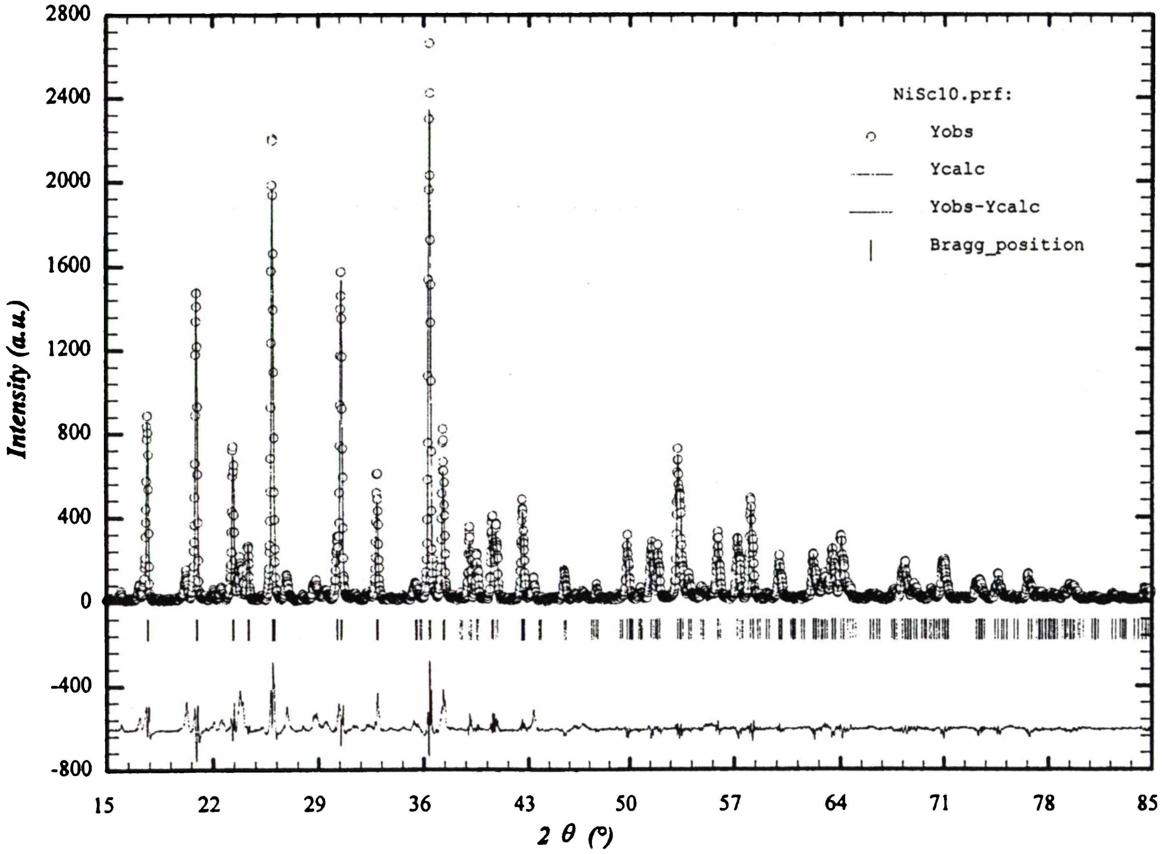

Rietveld Refinement of $Li_{0.90}Ni_{0.90}Sc_{0.10}PO_4$

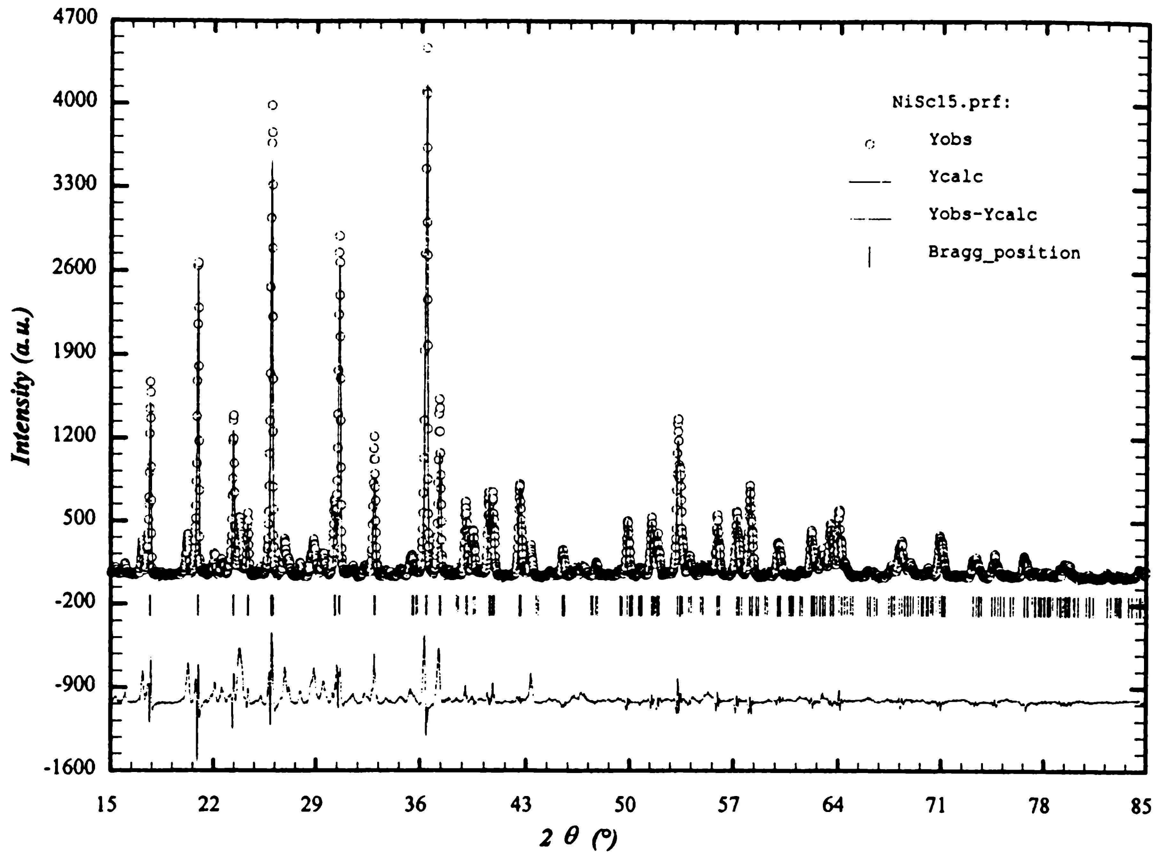

Rietveld Refinement of $Li_{0.85}Ni_{0.85}Sc_{0.15}PO_4$

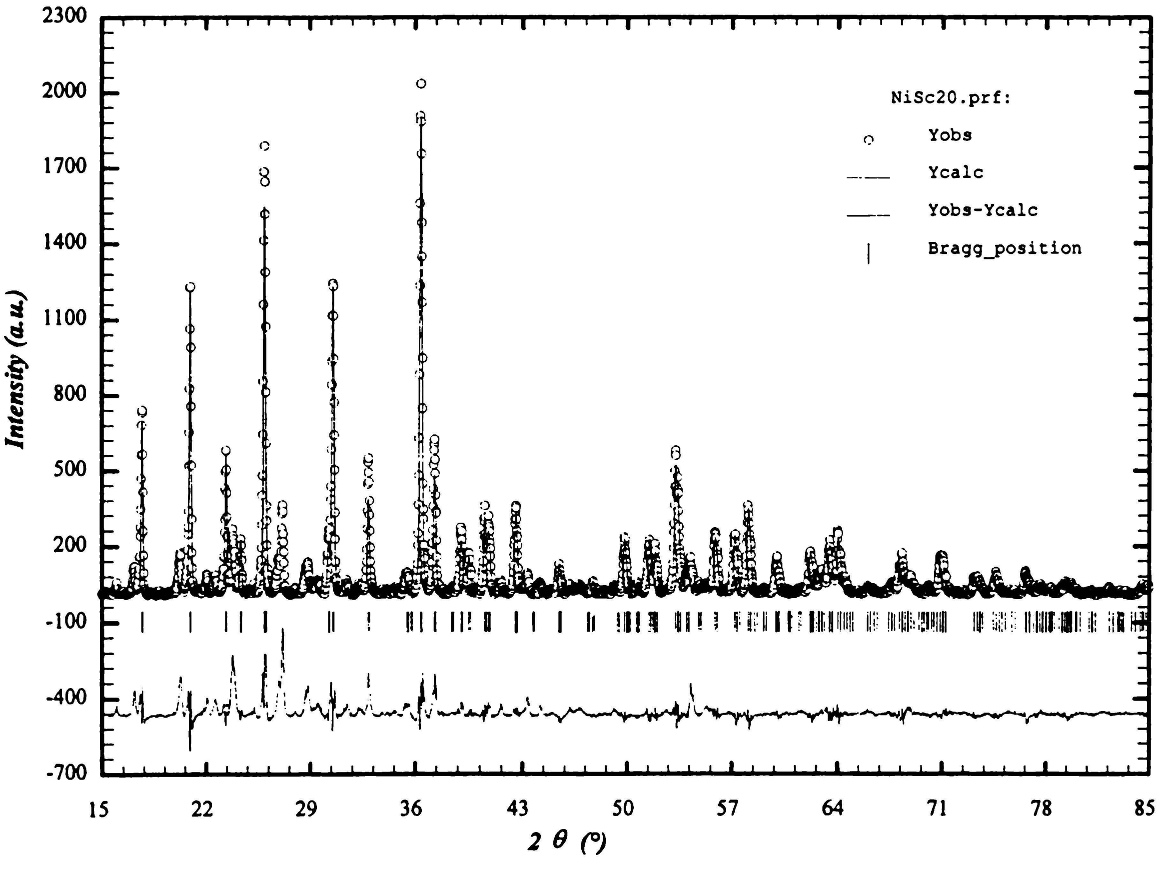

Rietveld Refinement of $Li_{0.80}Ni_{0.80}Sc_{0.20}PO_4$

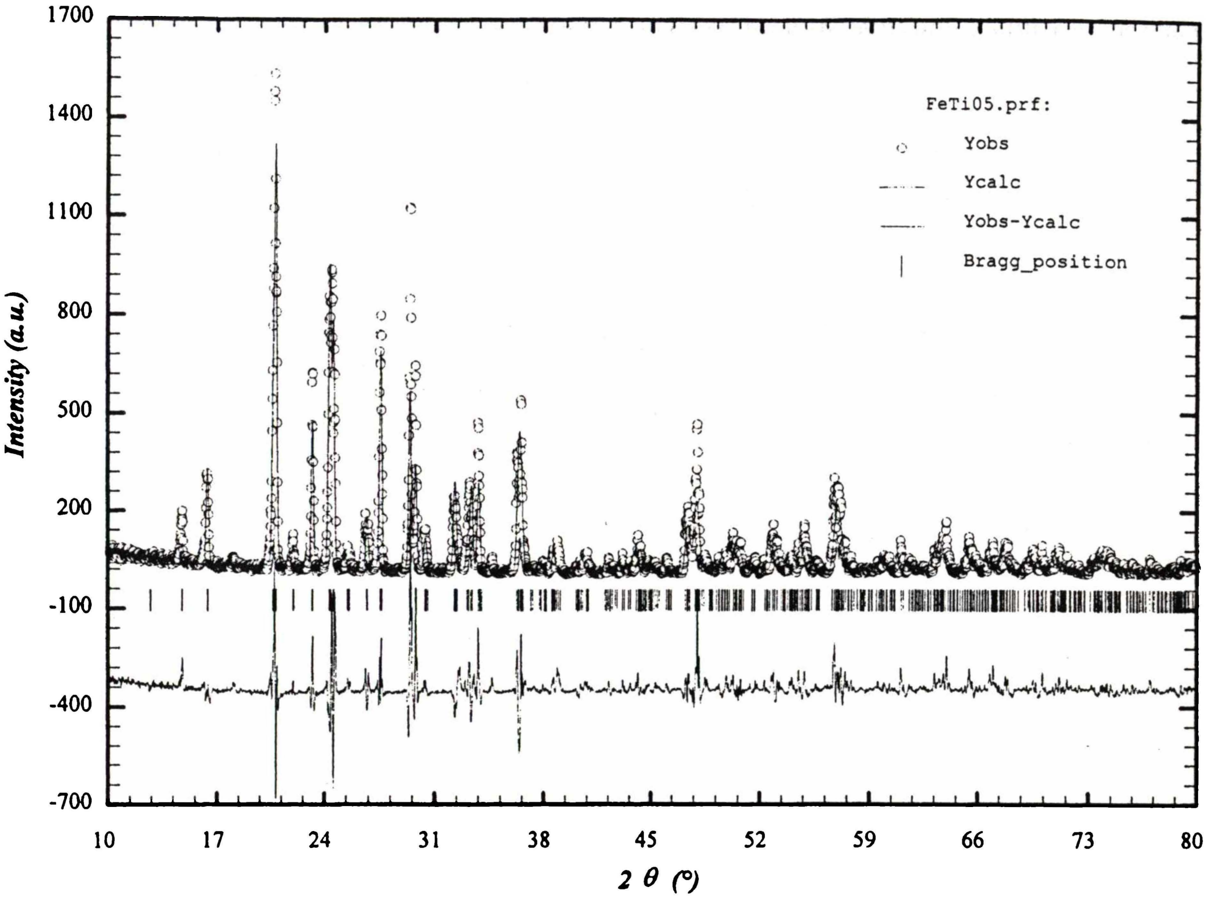

Rietveld Refinement of $Li_{2.90}Fe_{1.90}Ti_{0.10}(PO_4)_3$

Refined Crystallographic Parameters for $Li_{2.90}Fe_{1.90}Ti_{0.10}(PO_4)_3$ (P*can*) - X-ray diffraction data for 711 reflections and 38 variables

Atom	*x*	*y*	*z*	Occupancy	B_{iso} (Å^2)
Fe	0.2410 (10)	0.1064 (5)	0.4642 (7)	1.913 (21)	0.61 *
P	0.1122 (15)	0.1422 (11)	0.0978 (14)	2.000 *	0.58 *
P	0.0345 (21)	0.5000 *	0.2500 *	1.000 *	0.62 *
O	0.4234 (29)	0.3474 (22)	0.0927 (26)	2.000 *	1.10 *
O	0.3157 (29)	0.2753 (19)	0.4664 (27)	2.000 *	1.29 *
O	0.1444 (30)	0.0354 (21)	0.0731 (28)	2.000 *	1.53 *
O	0.4368 (24)	0.0931 (18)	0.3582 (26)	2.000 *	1.17 *
O	0.1451 (28)	0.4303 (18)	0.1424 (27)	2.000 *	1.32 *
O	0.1514 (28)	0.1776 (21)	0.2432 (28)	2.000 *	1.03 *
Li	0.2950 *	0.3220 *	0.2760 *	1.000 *	1.50 *
Li	0.5770 *	0.1930 *	0.4210 *	1.000 *	2.40 *
Li	0.9120 *	0.2410 *	0.2970 *	1.000 *	4.10 *
a = 8.5591, (14) b = 11.9928, (17) c = 8.6008 (13), * = Fixed Parameters V =882.851 (222) Å^3 , wRp = 34.6, Rp =27.8 , $\chi 2$ =6.63					

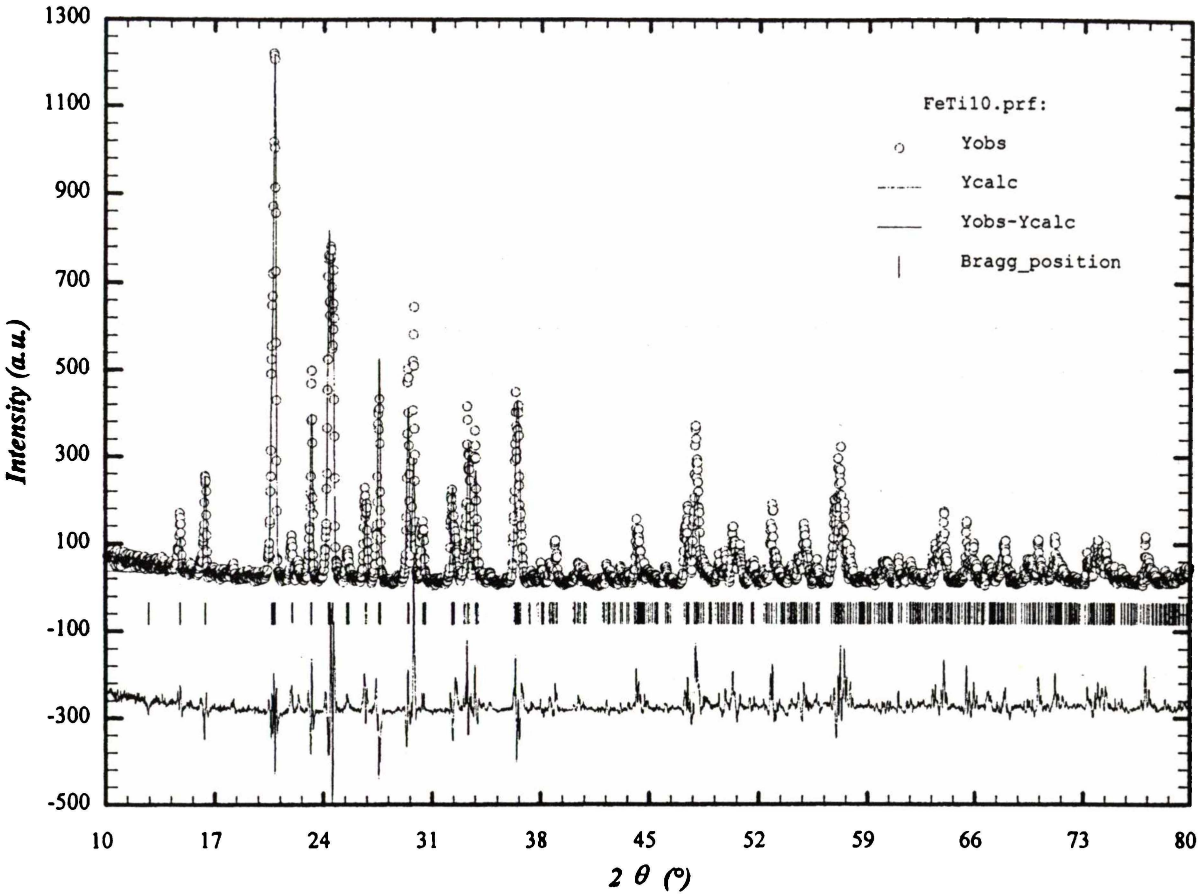

Rietveld Refinement of $Li_{2.80}Fe_{1.80}Ti_{0.20}(PO_4)_3$

Refined Crystallographic Parameters for $Li_{2.80}Fe_{1.80}Ti_{0.20}(PO_4)_3$ (P*can*) - X-ray diffraction data for 711 reflections and 38 variables

Atom	*x*	*y*	*z*	Occupancy	B_{iso} ($Å^2$)
Fe	0.2443 (11)	0.1091 (5)	0.4597 (7)	1.956 (22)	0.61 *
P	0.1100 (17)	0.1476 (11)	0.1018 (16)	2.000 *	0.58 *
P	0.0339 (23)	0.5000 *	0.2500 *	1.000 *	0.62 *
O	0.4206 (30)	0.3496 (23)	0.0908 (30)	2.000 *	1.10 *
O	0.3249 (33)	0.2945 (22)	0.4762 (33)	2.000 *	1.29 *
O	0.1187 (30)	0.0157 (26)	0.0557 (30)	2.000 *	1.53 *
O	0.4354 (25)	0.0831 (18)	0.3624 (27)	2.000 *	1.17 *
O	0.1569 (29)	0.4243 (19)	0.1547 (30)	2.000 *	1.32 *
O	0.1510 (29)	0.1662 (22)	0.2557 (32)	2.000 *	1.03 *
Li	0.2950 *	0.3220 *	0.2760 *	1.000 *	1.50 *
Li	0.5770 *	0.1930 *	0.4210 *	1.000 *	2.40 *
Li	0.9120 *	0.2410 *	0.2970 *	1.000 *	4.10 *

a = 8.5536, (14) b = 11.9889, (17) c = 8.6107 (13), * = Fixed Parameters

V =882.086 (225) $Å^3$, wRp = 33.5, Rp =26.7 , $\chi2$ =5.81

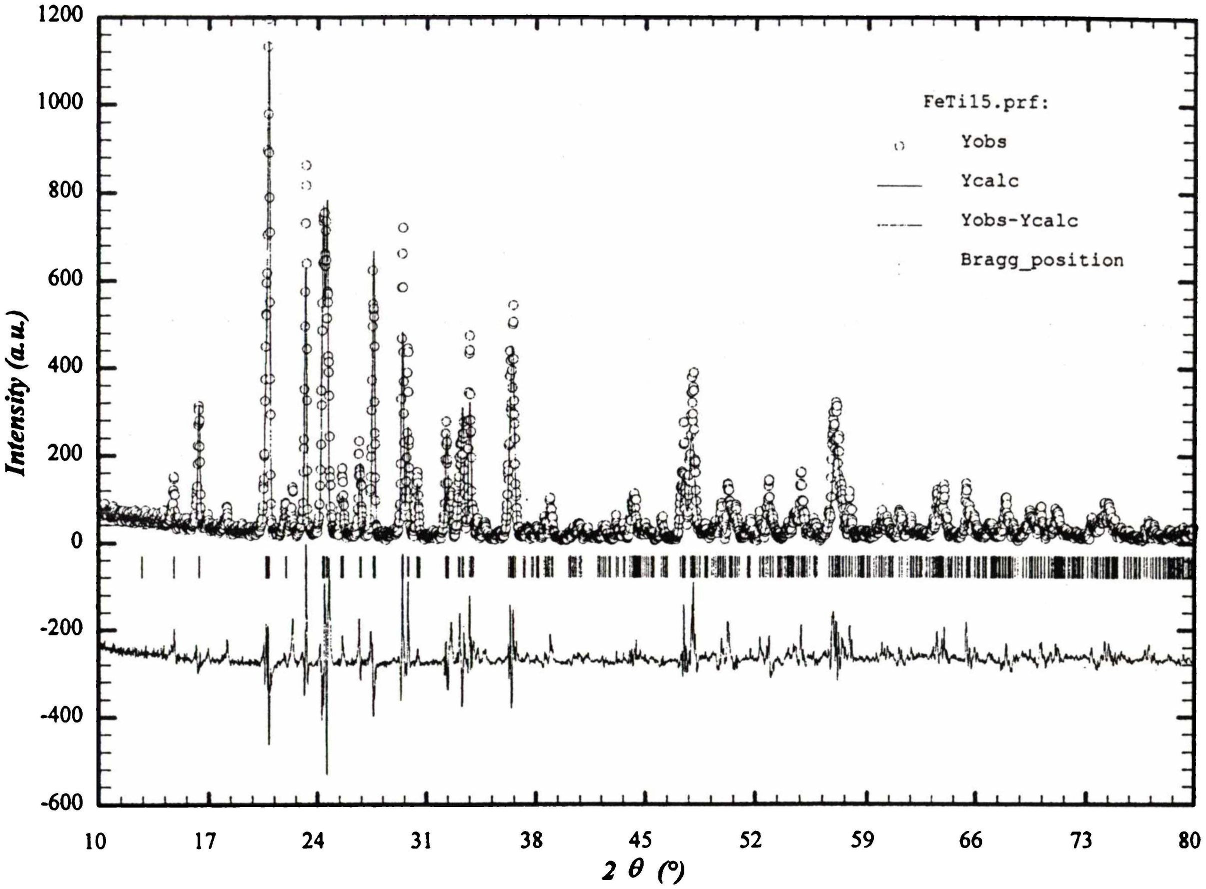

Rietveld Refinement of $Li_{2.70}Fe_{1.70}Ti_{0.30}(PO_4)_3$

Refined Crystallographic Parameters for $Li_{2.70}Fe_{1.70}Ti_{0.30}(PO_4)_3$ (P*can*) - X-ray diffraction data for 711 reflections and 38 variables

Atom	*x*	*y*	*z*	Occupancy	B_{iso} (Å^2)
Fe	0.2479 (13)	0.1085 (5)	0.4647 (7)	1.876 (19)	0.61 *
P	0.1178 (16)	0.1496 (10)	0.1011 (15)	2.000 *	0.58 *
P	0.0360 (21)	0.5000 *	0.2500 *	1.000 *	0.62 *
O	0.4386 (30)	0.3459 (23)	0.0862 (25)	2.000 *	1.10 *
O	0.2974 (29)	0.2819 (18)	0.4627 (27)	2.000 *	1.29 *
O	0.1360 (30)	0.0306 (23)	0.0955 (28)	2.000 *	1.53 *
O	0.4502 (26)	0.0823 (18)	0.3536 (24)	2.000 *	1.17 *
O	0.1450 (29)	0.4204 (18)	0.1626 (27)	2.000 *	1.32 *
O	0.1618 (29)	0.1839 (22)	0.2542 (27)	2.000 *	1.03 *
Li	0.2950 *	0.3220 *	0.2760 *	1.000 *	1.50 *
Li	0.5770 *	0.1930 *	0.4210 *	1.000 *	2.40 *
Li	0.9120 *	0.2410 *	0.2970 *	1.000 *	4.10 *

a = 8.5508, (13) b = 11.9904, (16) c = 8.6047 (11), * = Fixed Parameters

V =882.230 (203) Å^3 , wRp = 31.9, Rp =25.2 , $\chi 2$ =5.51

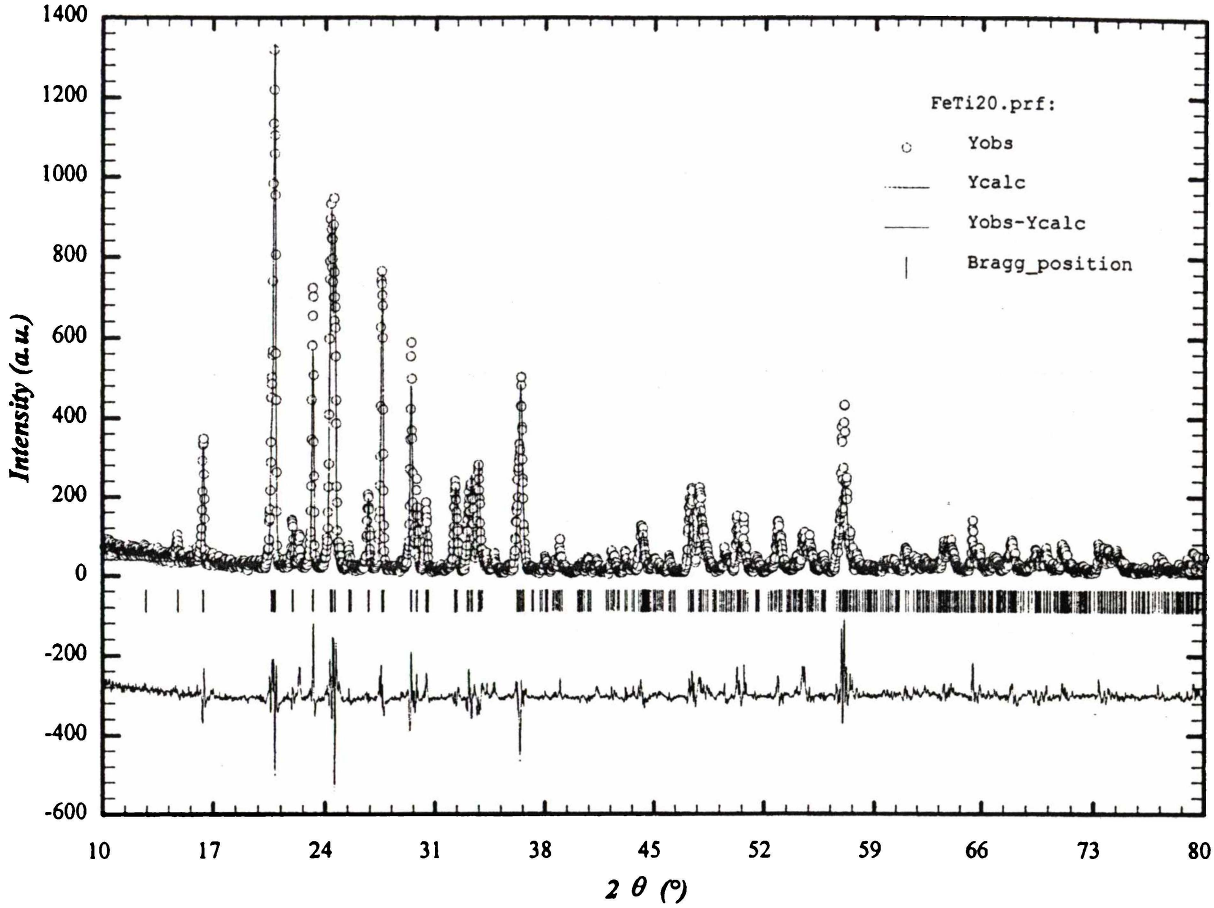

Rietveld Refinement of $Li_{2.60}Fe_{1.60}Ti_{0.40}(PO_4)_3$

Refined Crystallographic Parameters for $Li_{2.60}Fe_{1.60}Ti_{0.40}(PO_4)_3$ (P*can*) - X-ray diffraction data for 712 reflections and 38 variables

Atom	*x*	*y*	*z*	Occupancy	B_{iso} (Å^2)
Fe	0.2530 (11)	0.1076 (4)	0.4680 (6)	1.824 (16)	0.61 *
P	0.1104 (13)	0.1469 (8)	0.1042 (12)	2.000 *	0.58 *
P	0.0373 (17)	0.5000 *	0.2500 *	1.000 *	0.62 *
O	0.4354 (25)	0.3417 (18)	0.0970 (22)	2.000 *	1.10 *
O	0.3322 (24)	0.2694 (16)	0.4724 (23)	2.000 *	1.29 *
O	0.1446 (24)	0.0305 (17)	0.0927 (23)	2.000 *	1.53 *
O	0.4405 (21)	0.0848 (14)	0.3591 (21)	2.000 *	1.17 *
O	0.1430 (25)	0.4306 (15)	0.1494 (22)	2.000 *	1.32 *
O	0.1583 (22)	0.1926 (18)	0.2570 (23)	2.000 *	1.03 *
Li	0.2950 *	0.3220 *	0.2760 *	1.000 *	1.50 *
Li	0.5770 *	0.1930 *	0.4210 *	1.000 *	2.40 *
Li	0.9120 *	0.2410 *	0.2970 *	1.000 *	4.10 *
a = 8.5528, (10) b = 11.9955, (13) c = 8.6108 (9), * = Fixed Parameters V =883.423 (162) Å^3 , wRp = 28.0, Rp =21.1 , $\chi 2$ =4.02					

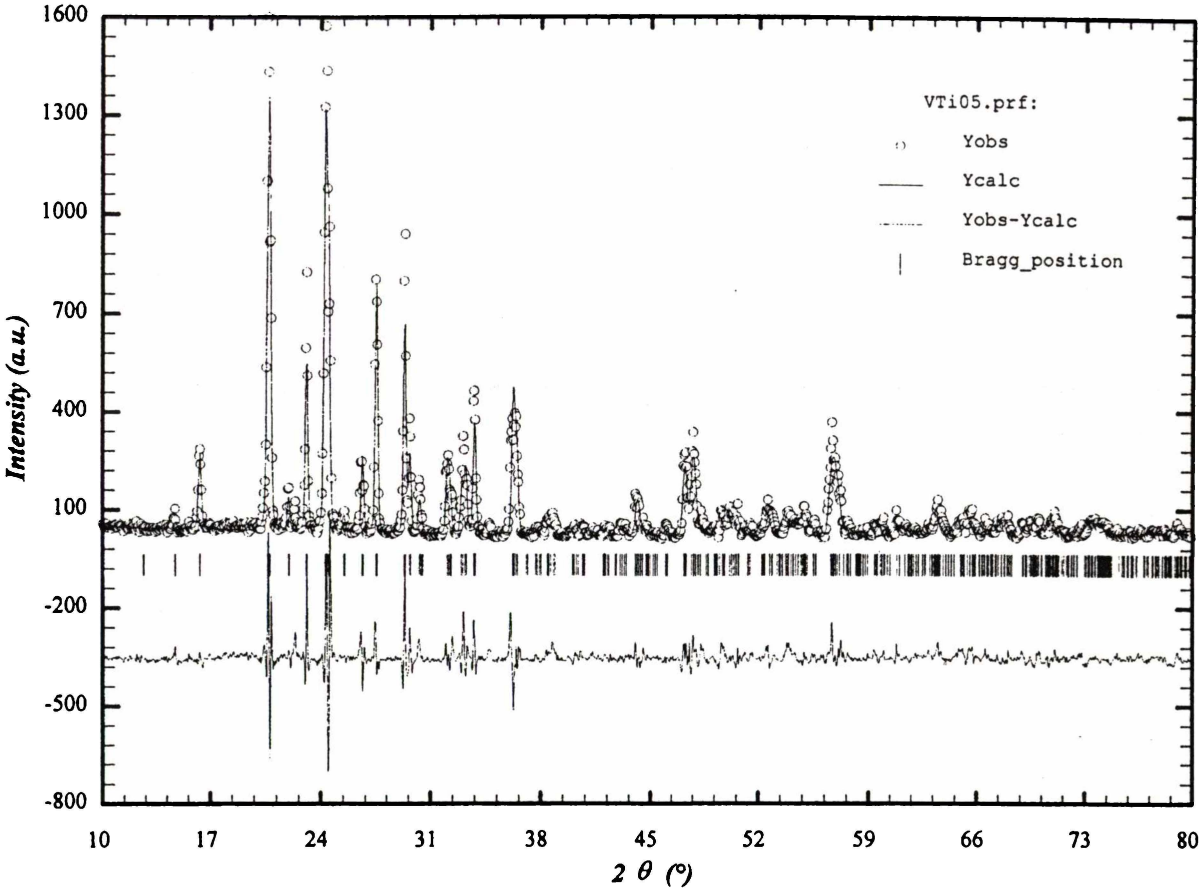

Rietveld Refinement of $Li_{2.90}V_{1.90}Ti_{0.10}(PO_4)_3$

Refined Crystallographic Parameters for $Li_{2.90}V_{1.90}Ti_{0.10}(PO_4)_3$ (P*can*) - X-ray diffraction data for 540 reflections and 38 variables.

Atom	*x*	*y*	*z*	Occupancy	B_{iso} (Å^2)
V	0.2412 (14)	0.1094 (7)	0.4671 (10)	1.984 (28)	0.61 *
P	0.1139 (21)	0.1462 (15)	0.1022 (22)	2.000 *	0.58 *
P	0.0345 (30)	0.5000 *	0.2500 *	1.000 *	0.62 *
O	0.4324 (42)	0.3426 (31)	0.0925 (38)	2.000 *	1.10 *
O	0.3135 (38)	0.2682 (26)	0.4774 (41)	2.000 *	1.29 *
O	0.1578 (38)	0.0394 (29)	0.0639 (39)	2.000 *	1.53 *
O	0.4333 (33)	0.0880 (24)	0.3503 (42)	2.000 *	1.17 *
O	0.1450 (41)	0.4262 (24)	0.1569 (40)	2.000 *	1.32 *
O	0.1574 (38)	0.1943 (30)	0.2520 (43)	2.000 *	1.03 *
Li	0.2950 *	0.3220 *	0.2760 *	1.000 *	1.50 *
Li	0.5770 *	0.1930 *	0.4210 *	1.000 *	2.40 *
Li	0.9120 *	0.2410 *	0.2970 *	1.000 *	4.10 *
a = 8.6082, b = 12.0326, c = 8.5981, * = Fixed Parameters V =890.588 (323) Å^3 , wRp = 25.2, Rp =19.8 , $\chi 2$ =4.97					

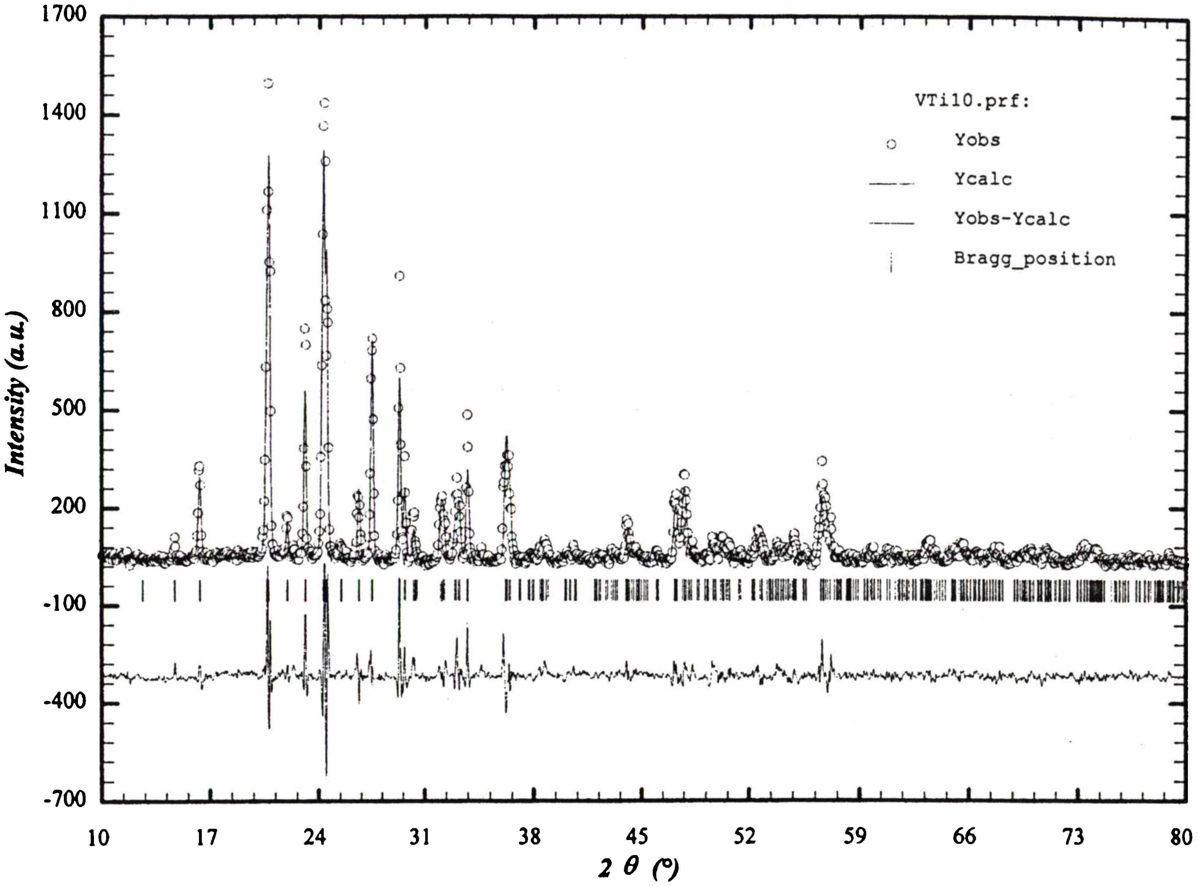

Rietveld Refinement of $Li_{2.80}V_{1.80}Ti_{0.20}(PO_4)_3$

Refined Crystallographic Parameters for $Li_{2.80}V_{1.80}Ti_{0.20}(PO_4)_3$ (P*can*) - X-ray diffraction data for 715 reflections and 38 variables.

Atom	*x*	*y*	*z*	Occupancy	B_{iso} (Å^2)
V	0.2448 (16)	0.1104 (7)	0.4654 (9)	1.908 (26)	0.61 *
P	0.1130 (20)	0.1487 (14)	0.1011 (21)	2.000 *	0.58 *
P	0.0387 (29)	0.5000 *	0.2500 *	1.000 *	0.62 *
O	0.4292 (40)	0.3335 (30)	0.0893 (36)	2.000 *	1.10 *
O	0.3243 (35)	0.2657 (25)	0.4780 (40)	2.000 *	1.29 *
O	0.1543 (36)	0.0351 (28)	0.0678 (37)	2.000 *	1.53 *
O	0.4334 (31)	0.0876 (23)	0.3500 (39)	2.000 *	1.17 *
O	0.1398 (42)	0.4253 (23)	0.1449 (40)	2.000 *	1.32 *
O	0.1519 (36)	0.1890 (29)	0.2515 (41)	2.000 *	1.03 *
Li	0.2950 *	0.3220 *	0.2760 *	1.000 *	1.50 *
Li	0.5770 *	0.1930 *	0.4210 *	1.000 *	2.40 *
Li	0.9120 *	0.2410 *	0.2970 *	1.000 *	4.10 *

a = 8.6142, b = 12.0368, c = 8.6085, * = Fixed Parameters

V =892.590 (309) Å^3 , wRp = 21.5, Rp =17.2 , $\chi 2$ =3.51

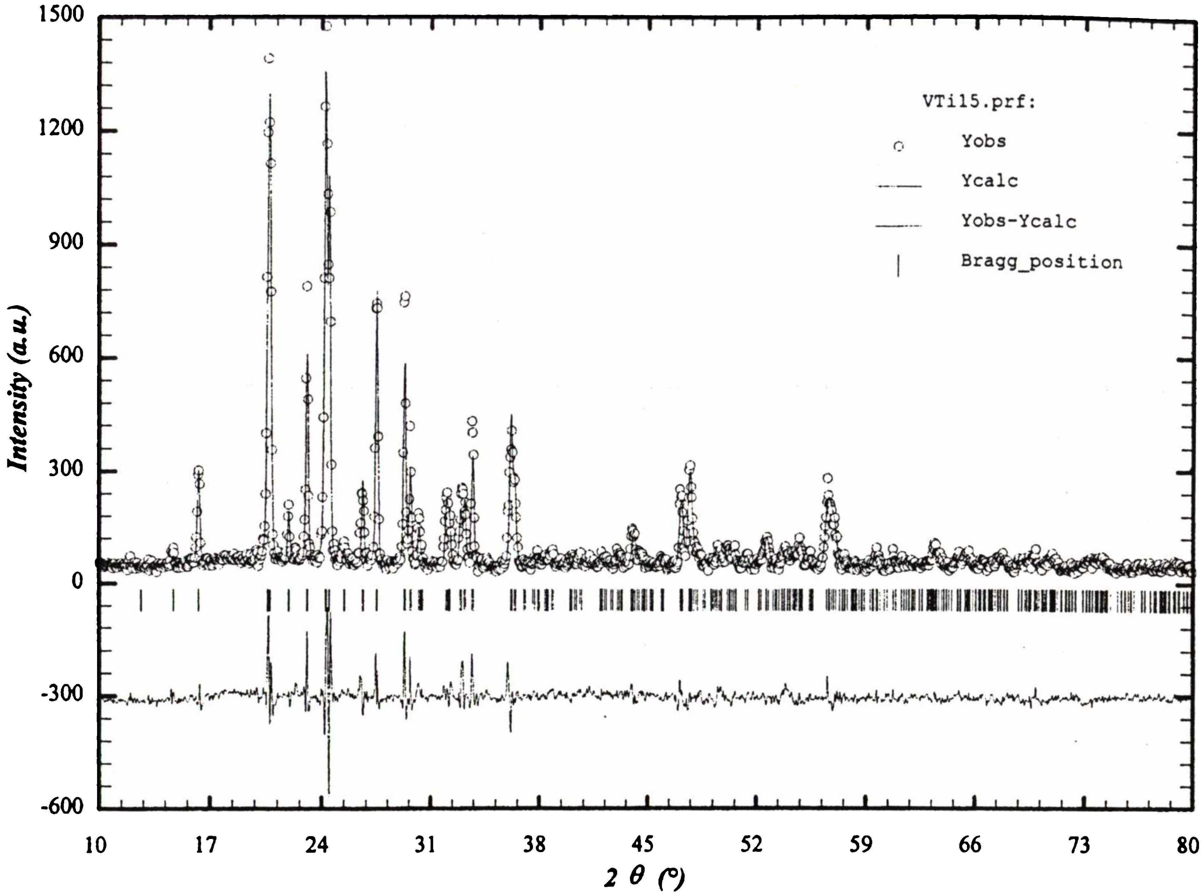

Rietveld Refinement of $Li_{2.70}V_{1.70}Ti_{0.30}(PO_4)_3$

Refined Crystallographic Parameters for $Li_{2.70}V_{1.70}Ti_{0.30}(PO_4)_3$ (P*can*) - X-ray diffraction data for 716 reflections and 38 variables.

Atom	*x*	*y*	*z*	Occupancy	B_{iso} ($Å^2$)
V	0.2448 (15)	0.1108 (6)	0.4662 (8)	1.883 (23)	0.61 *
P	0.1074 (17)	0.1464 (12)	0.1025 (18)	2.000 *	0.58 *
P	0.0423 (25)	0.5000 *	0.2500 *	1.000 *	0.62 *
O	0.4287 (37)	0.3427 (27)	0.0821 (32)	2.000 *	1.10 *
O	0.3258 (32)	0.2678 (22)	0.4810 (36)	2.000 *	1.29 *
O	0.1617 (32)	0.0348 (24)	0.0595 (32)	2.000 *	1.53 *
O	0.4309 (28)	0.0843 (20)	0.3534 (35)	2.000 *	1.17 *
O	0.1394 (39)	0.4207 (21)	0.1477 (35)	2.000 *	1.32 *
O	0.1548 (33)	0.1848 (26)	0.2446 (35)	2.000 *	1.03 *
Li	0.2950 *	0.3220 *	0.2760 *	1.000 *	1.50 *
Li	0.5770 *	0.1930 *	0.4210 *	1.000 *	2.40 *
Li	0.9120 *	0.2410 *	0.2970 *	1.000 *	4.10 *

a = 8.6217, b = 12.0368, c = 8.6177, * = Fixed Parameters

V =894.325 (257) $Å^3$, wRp = 17.7, Rp =14.1 , $\chi2$ =2.58

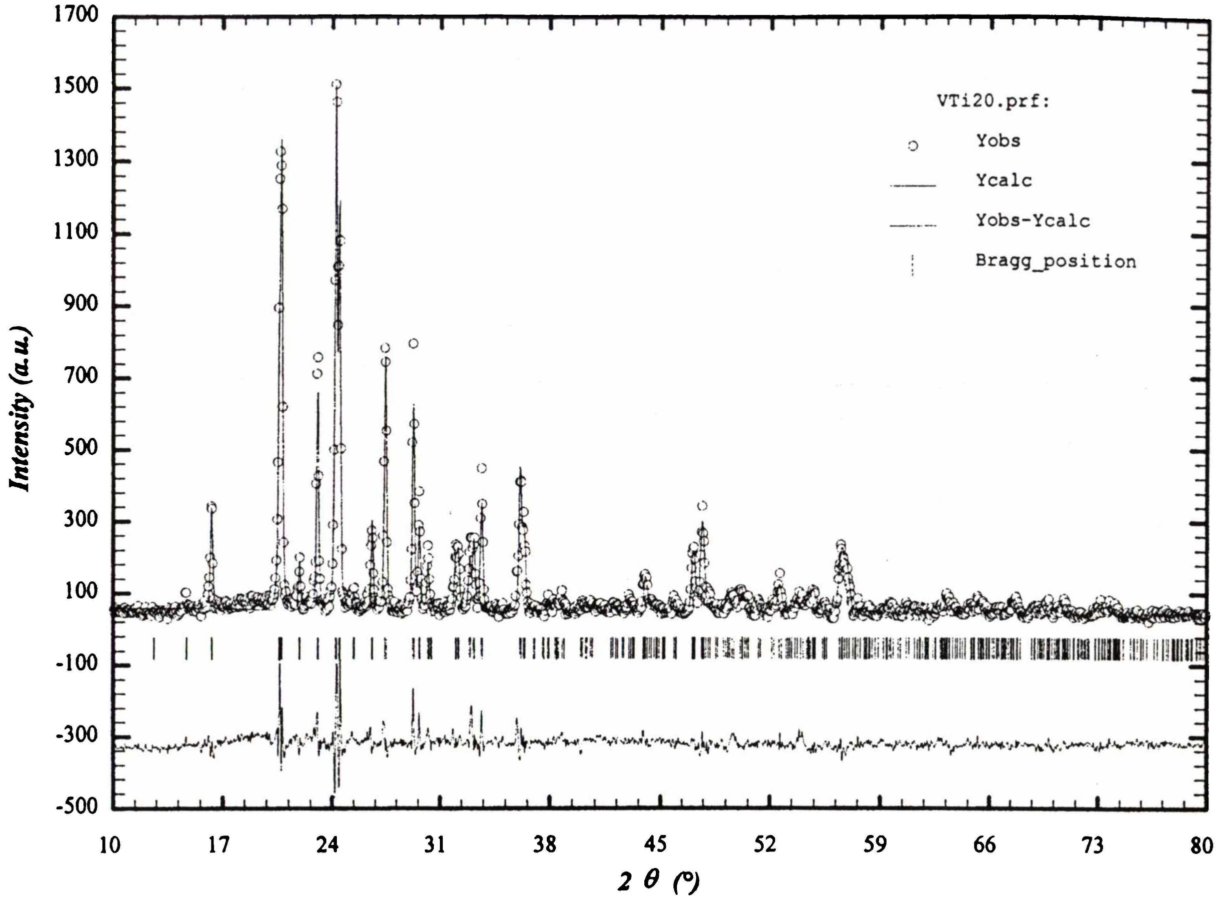

Rietveld Refinement of $Li_{2.60}V_{1.60}Ti_{0.40}(PO_4)_3$

Refined Crystallographic Parameters for $Li_{2.60}V_{1.60}Ti_{0.40}(PO_4)_3$ (P*can*) - X-ray diffraction data for 718 reflections and 38 variables.

Atom	*x*	*y*	*z*	Occupancy	B_{iso} (Å^2)
V	0.2460 (15)	0.1105 (6)	0.4656 (9)	1.845 (23)	0.61 *
P	0.1058 (18)	0.1473 (12)	0.1047 (18)	2.000 *	0.58 *
P	0.0406 (25)	0.5000 *	0.2500 *	1.000 *	0.62 *
O	0.4354 (38)	0.3405 (27)	0.0784 (32)	2.000 *	1.10 *
O	0.3212 (33)	0.2687 (22)	0.4828 (36)	2.000 *	1.29 *
O	0.1566 (32)	0.0341 (24)	0.0542 (32)	2.000 *	1.53 *
O	0.4292 (29)	0.0803 (20)	0.3568 (35)	2.000 *	1.17 *
O	0.1408 (40)	0.4201 (21)	0.1461 (34)	2.000 *	1.32 *
O	0.1508 (33)	0.1861 (26)	0.2529 (36)	2.000 *	1.03 *
Li	0.2950 *	0.3220 *	0.2760 *	1.000 *	1.50 *
Li	0.5770 *	0.1930 *	0.4210 *	1.000 *	2.40 *
Li	0.9120 *	0.2410 *	0.2970 *	1.000 *	4.10 *

a = 8.6265 (15), b = 12.0432 (18), c = 8.6273 (14), * = Fixed Parameters

V =896.292 (244) Å^3 , wRp = 16.8, Rp =13.4 , $\chi 2$ =2.43

Appendix III– TMS Performance

The data for the following cyclic voltammograms was scanned at a rate of $5mVs^{-1}$ in three cycles; the first between 1.5 and 4.5V, the second between 2.0 and 5.0V, and the last between 2.5 and 5.5V.

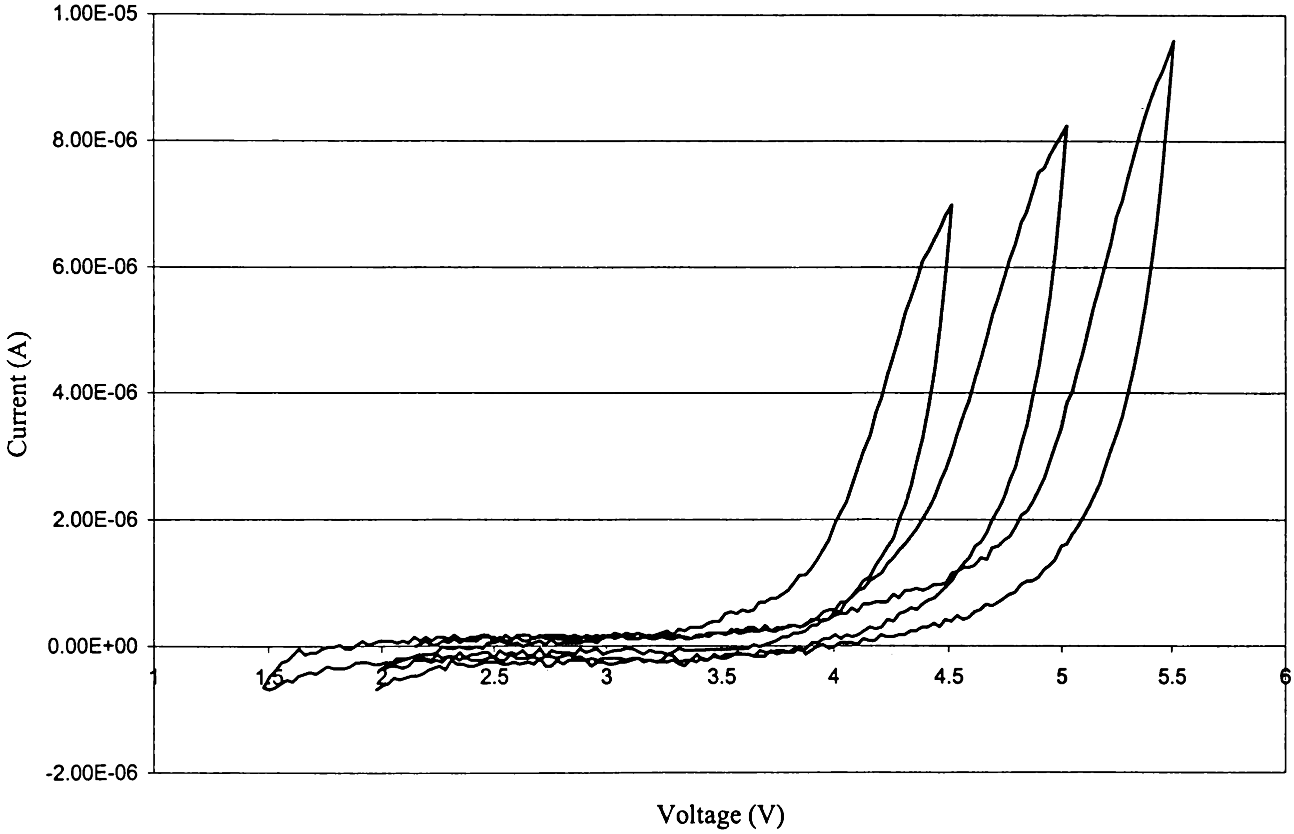

Cyclic Voltammetry of TMS/$LiBF_4$ with Scanning Rate of $5mVs^{-1}$.

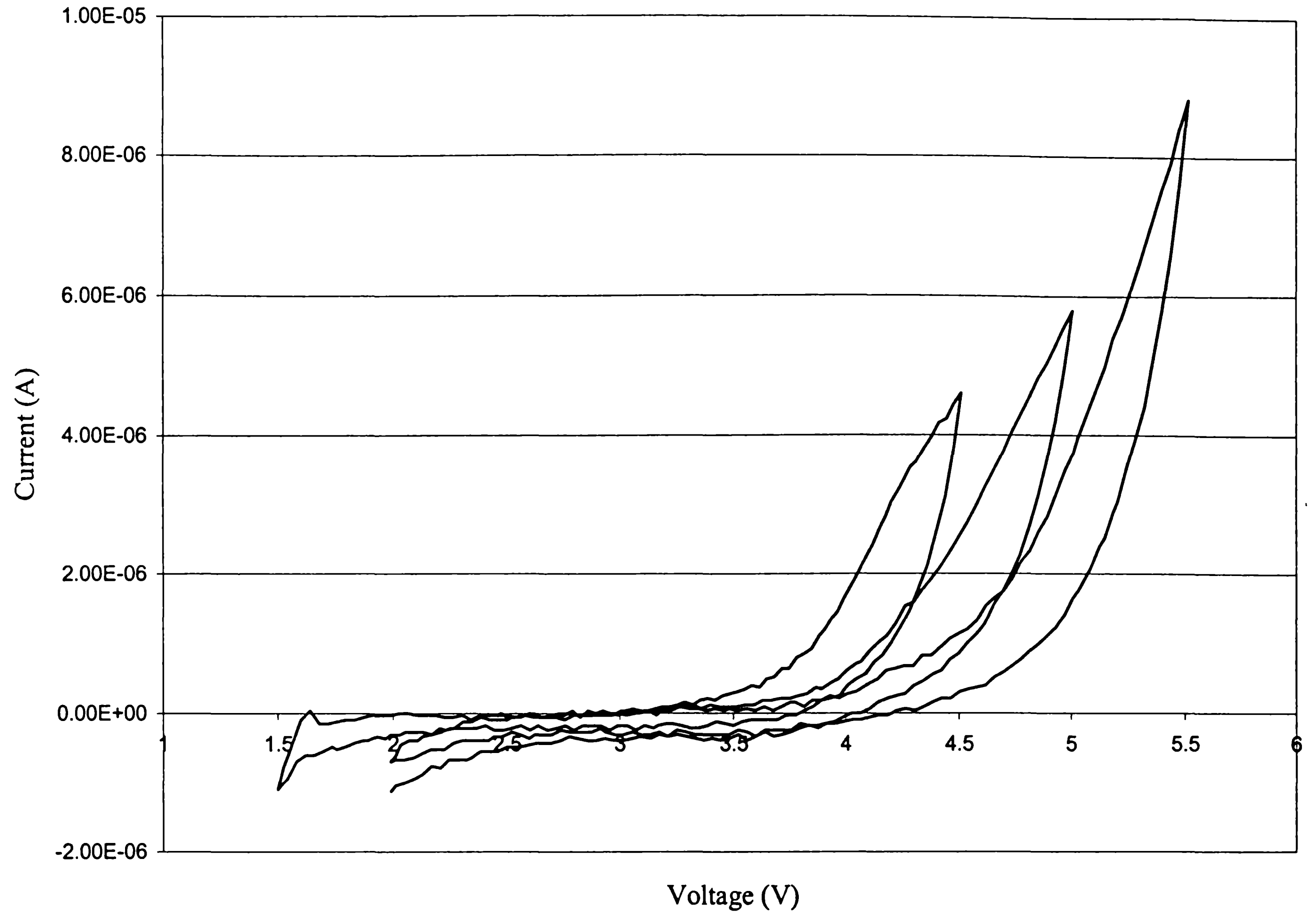

Cyclic Voltammetry of TMS/3M with Scanning Rate of 5mVs^{-1}.